LEAST SQUARES BASED FINITE ELEMENT FORMULATIONS AND THEIR APPLICATIONS IN FLUID MECHANICS

A Dissertation

by

VIVEK PRABHAKAR

Submitted to the Office of Graduate Studies of
Texas A&M University
in partial fulfillment of the requirements for the degree of

DOCTOR OF PHILOSOPHY

December 2006

Major Subject: Mechanical Engineering

LEAST SQUARES BASED FINITE ELEMENT FORMULATIONS AND THEIR APPLICATIONS IN FLUID MECHANICS

A Dissertation

by

VIVEK PRABHAKAR

Submitted to the Office of Graduate Studies of
Texas A&M University
in partial fulfillment of the requirements for the degree of

DOCTOR OF PHILOSOPHY

Approved by:

Chair of Committee,	J. N. Reddy
Committee Members,	H. C. Chen
	S. S. Girimaji
	K. R. Rajagopal
Head of Department,	Dennis L. O'Neal

December 2006

Major Subject: Mechanical Engineering

ABSTRACT

Least Squares Based Finite Element Formulations
and Their Applications in Fluid Mechanics. (December 2006)
Vivek Prabhakar, B. Tech., Indian Institute of Technology, Kanpur
Chair of Advisory Committee: Dr. J. N. Reddy

In this research, least-squares based finite element formulations and their applications in fluid mechanics are presented. Least-squares formulations offer several computational and theoretical advantages for Newtonian as well as non-Newtonian fluid flows. Most notably, these formulations circumvent the inf-sup condition of Ladyzhenskaya-Babuska-Brezzi (LBB) such that the choice of approximating space is not subject to any compatibility condition. Also, the resulting coefficient matrix is symmetric and positive-definite. It has been observed that pressure and velocities are not strongly coupled in traditional least-squares based finite element formulations. Penalty based least-squares formulations that fix the pressure-velocity coupling problem are proposed, implemented in a computational scheme, and evaluated in this study. The continuity equation is treated as a constraint on the velocity field and the constraint is enforced using the penalty method. These penalty based formulations produce accurate results for even low penalty parameters (in the range of 10-50 penalty parameter). A stress based least-squares formulation is also being proposed to couple pressure and velocities. Stress components are introduced as independent variables to make the system first order. The continuity equation is eliminated from the system with suitable modifications. Least-squares formulations are also developed for viscoelastic flows and moving boundary flows. All the formulations developed in this study are tested using several benchmark problems. All of the finite element models developed in this study performed well in all cases.

A method to exploit orthogonality of modal bases to avoid numerical integration and

have a fast computation is also developed during this study. The entries of the coefficient matrix are calculated analytically. The properties of Jacobi polynomials are used and most of the entries of the coefficient matrix are recast so that they can be evaluated analytically.

To my parents for their love, encouragement and belief in me

ACKNOWLEDGMENTS

I would like to express my gratitude to my advisor Professor J. N. Reddy for his support and guidance throughout my Ph.D. studies. I have learned so many valuable things from him, not just in the field of our endeavor, but on all aspects of life. His patience, generosity, and humbleness I admire the most. He has been an exemplary guide, motivator, and mentor. He has shown complete faith in me and always let me do the things in my way, which was instrumental in completing the Ph.D. With him, I always felt protected. I would also thank committee members for their input and the time they spent serving on my committee.

Special thanks to Dr. J. P. Pontaza (former doctoral student of Professor Reddy) for all enlightening discussions and fruitful arguments regarding the least-squares method. He has been a mentor and always helped me whenever I needed it. I would like to thank my undergraduate advisor Professor G. Biswas for introducing me to this field and for the valuable knowledge and experience I received working under him. I also thank my friends (late) Mayank and Nitya for their support and help. I learned a lot from them. They were always there when I needed them.

On the social scale, I would like to thank my friends, especially Blanca and Misael for keeping me at least partially sane and making my stay in College Station very enjoyable.

I also offer my deep gratitude to my parents for providing me the best opportunities in school and college education. I have great admiration for them, who have sacrificed a lot to help me achieve my goals in life thus far. My PhD would not have been possible without their support, love, and encouragement. I am what I am today because of them. I believe that my words to acknowledge their love and support will never be enough. I would like to thank my sister Kalpana, my brother-in-law Ashutosh, and brother Kanak for their love

and support. They always encouraged me and helped me stay focused. Lastly, I would also like to thank my wife, who has been an unending source of strength and inspiration. She always motivated me to improve and do better.

TABLE OF CONTENTS

CHAPTER Page

CHAPTER Page

LIST OF TABLES

LIST OF FIGURES

FIGURE Page

FIGURE Page

FIGURE Page

FIGURE Page

FIGURE Page

FIGURE Page

CHAPTER I

INTRODUCTION

A. Background

The past two decades have witnessed a great deal of progress in the area of computational fluid dynamics (CFD). A large number of methods have been proposed for the numerical solution of the Navier-Stokes equations governing flows of viscous incompressible fluids. Direct discretization methods include finite difference and finite volume techniques, the finite element method using conformal and nonconformal elements, and spectral methods. The finite element method is considered to be the most effective method for solving solid mechanics problems, but the method has not achieved the same level of acceptance in CFD compared to the finite difference or finite volume techniques. This is primarily due to two reasons: (1) CFD is dominated by researchers whose primary education and background is in fluid mechanics and, consequently, they are exposed to finite difference techniques early in their education, and (2) finite difference and finite volume techniques are very simple in concept when compared to the finite element method, which involves considerable formulating effort and computational time due to non-segregated approach used to solve the finite element equations. However, the finite element method enjoys the generality of application to geometrically complex problems as well as to multiphysics problems. The method is gaining popularity in CFD.

The Navier-Stokes equations can be expressed in terms of the primitive variables (e.g., velocities and pressure), secondary variables (velocity gradients, vorticity, stream function, stresses, etc.), or a combination of the two. The finite element model depends on the choice of variables as well as on the method (e.g., Galerkin, collocation, least-squares, and so on)

This dissertation follows the style of *IEEE Transactions on Automatic Control.*

used to satisfy the equations. Often, the finite element model is based on weighted-integral formulations where the choice of the weight function gives rise to different models.

Among the finite element models that involve primitive variables, the pressure-velocity finite element formulation is the most common one. The pressure-velocity formulation has several disadvantages. When the standard weak form Galerkin formulation is used, the biggest problem to be faced is the use of compatible approximation spaces for the velocity field and pressure variable. The choice must be such that they satisfy the inf-sup (or LBB) condition. Also, for nonlinear equations, coefficient matrix is nonsymmetric and computational cost is high.

In the past few years, finite element models based on least-squares variational principles have drawn considerable attention for the solution of Stokes and Navier-Stokes equations ([1]-[7]). Least-squares based finite element formulations offer several theoretical and computational advantages. Most notably, such formulations circumvent the inf-sup condition of Ladyzhenskaya-Babuska-Brezzi (LBB). As a result, equal order interpolation functions can be used for all field variables. They also yield symmetric, positive-definite coefficient matrix and, therefore, robust iterative solvers can be used to solve the resulting system of algebraic equations.

Previous studies [8, 9] showed that mass conservation is not very good in least-squares based formulations. Chang and Nelson [8] suggested that this is because the error is minimized on a global scale, allowing errors of significant size to remain on a local scale, especially in areas in which the gradients of the variables are of significant size. They also proposed a remedy, which consists of enforcing the continuity equation as an explicit constraint through the use of Lagrange multipliers, negates one of the main advantages of the least-squares methods, namely, the positive-definiteness of resulting coefficient matrix. Deang and Gunzburger [10] also studied mass conservation in least-squares formulations and analyzed weighted least-squares functionals. These formulations have better mass

conservation than unweighted formulations but conditioning number of the resultant coefficient matrix becomes high. Bolton and Thatcher also addressed this problem for Stokes [9] and Navier-Stokes equations [11] and proposed weighting of particular terms in the least-squares functional. Pontaza and Reddy [5, 12] used high order basis functions and they did not observe problems with mass conservation. However, for unsteady problems, numerical solutions became unstable if sufficiently high p-level was not used.

Another problem associated with least-squares formulations is an ill-behaved temporal evolution of pressure field. In least-squares based finite element formulations, the divergence-free constraint on the velocity field is enforced directly through the least-squares functional and, thus, the pressure does not have a well-defined role in these formulations. Unsteady problems, especially with inflow/outflow boundaries, produce spurious pressure evolution with time due to this lack of strong pressure velocity coupling.

B. Present study

In this work we present penalty based least-squares finite element formulations for fluid flow problems. We combine the idea of least-squares variational principles with the penalty method. Least-squares formulations result in a symmetric, positive-definite coefficient matrix, which can be solved using robust iterative methods like preconditioned conjugate gradient method. The least-squares formulation results in a minimization problem rather than a saddle point problem and the choice of approximations used for the field variables is not subjected to the LBB condition. High-order element expansions are used to construct the discrete model, which does not experience locking. Equal-order integration is used for all variables in this study. We implement iterative penalty method proposed by Gunzberger [13]. The best feature of present formulation is that it requires very small penalty parameter, Re$= 10 - 40$, to yield very accurate solution. For such small penalty parameters, the coef-

ficient matrix is better conditioned and convergence is not slow as in the traditional penalty finite element model. Due to the use of high-order expansions, we also obtain very accurate velocity as well as pressure fields. Thus, the disadvantages of the weak form penalty finite element model are overcome by the penalty least-squares finite element model.

We present this formulation as an alternative to the spectral/hp least-squares finite element model presented by Pontaza and Reddy [5, 12] for steady and unsteady problems. In their formulation the divergence-free constraint on the velocity field is enforced directly through the least-squares functional, and pressure is retained as an independent variable. For unsteady problems, this approach seems to have disadvantages as the time-evolution of the pressure field is not well-behaved. It is believed that it lacks a strong pressure-velocity coupling. The present formulation avoids this problem altogether by eliminating pressure via Eq. (2.7).

The present penalty least-squares finite element models are better alternative to traditional weak form penalty finite element model also. Advantage of the present models are that they produce very accurate results for very low penalty parameters. In addition, there is no need to under-integrate penalty terms of the coefficient matrix. We note that the computed pressure fields are continuous in this formulation as opposed to weak form penalty finite element formulation, and their values are found to be in excellent agreement with published results. This penalty least-squares formulation produces a symmetric positive-definite coefficient matrix while the weak form penalty finite element formulation produces unsymmetric coefficient matrix.

The p-version of the finite element method is known to possess superior convergence characteristics compared with the h-version. Nevertheless, most of the current finite element research has involved the use of low-order finite element approximation mainly because of low computational cost associated with h-version. In this study we implement the penalty least-squares formulation using bilinear basis functions also, which are widely

used in practice. When using bilinear basis functions a least-squares collocation approach is appropriate [14], which we adopt here.

Another way to couple pressure and velocity is to eliminate the continuity equation and include it in the Navier-Stokes equations implicitly. In this work, we present a stress based least-squares finite element formulation in an attempt to couple velocity and pressure by eliminating continuity equation. In the proposed formulation, continuity equation is eliminated from the system of governing equations with suitable modifications.

We extend least-squares based formulations to viscoelastic flows and use Oldroyd-B constitutive model. We develop basic least-squares formulation and penalty least-squares formulation for viscoelastic flows. The second order governing equations are recast as first order equations by introducing components of stress tensor. The benchmark problem chosen to test the formulations is transient plane Poiseuille flow in a channel bounded by two parallel fixed plates. Weissenberg number varies between 1 and 10.

Another topic which we address in this study is computational cost associated with p-methods. Most of the finite element implementations use low order expansions because they require less computational cost per degree of freedom, and convergence is achieved by refining the mesh. On the other hand, high order expansions demonstrate exponential convergence. If high accuracy is required, then we can justify using high-order methods by the fact that the error will converge at a faster rate than the increase in operation count. Therefore, it will ultimately be more efficient to use high order methods. Nevertheless, the cross-over point between the required accuracy and relative cost of low and high order methods for a given application is a point of much debate. A further argument which can be presented for using high order methods is the numerical diffusion and the enhance phase properties that these schemes demonstrate [12]. In this study, we implement also hierarchical modal bases. In addition to the flexibility in handling nonuniform resolution requirements, hierarchical bases can lead to better conditioning of mass and coefficient

matrices [15]. We implement these bases in the context of least-squares finite element model [5, 12]. As described earlier, high order expansions require more computational time per degree of freedom (during Gauss quadrature to evaluate coefficient matrices). We exploit orthogonality of Jacobi polynomials, and evaluate the coefficient matrices without using any quadrature. We recast the terms of the coefficient matrix using the properties of Jacobi polynomial and evaluate them exactly. For orthogonal elements, coefficient matrix entries are written in alternative forms and analytical expressions are developed to calculate them exactly. It is to be mentioned that multidimensional shape functions are constructed using tensor product of one-dimensional shape functions.

Lastly, we present least-squares based finite element method to simulate moving boundary flows. We use the volume of fluid (VOF) method and model surface tension force using the continuum surface force (CSF) model. The two-dimensional Navier-Stokes equations are expressed as an equivalent set of first-order equations by introducing strain rates as additional dependent variables. The hp least-squares method is used to develop the finite element model. We solve the broken dam problem to test this method and compare results with the benchmark results of Martin and Moyce [16].

CHAPTER II

SPECTRAL/HP PENALTY LEAST-SQUARES FINITE ELEMENT FORMULATION FOR THE STEADY INCOMPRESSIBLE NAVIER-STOKES EQUATIONS

A. Introduction

The past two decades have witnessed a great deal of progress in the area of computational fluid dynamics. A large number of methods have been proposed for the numerical solution of the Navier-Stokes equations governing flows of viscous incompressible fluids. Direct discretization methods include finite difference and finite volume techniques, the finite element method using conformal and nonconformal elements, and spectral methods. The finite element method is considered to be the most effective method for solving solid mechanics problems but the method has not achieved the same level of acceptance in the context of fluid flow analysis.

The velocity-pressure finite element formulation of the incompressible Navier-Stokes equations has several disadvantages. When the standard weak form Galerkin formulation is used, the biggest problem to be faced is the use of compatible approximation spaces for the velocity field and pressure variable. The choice must be such that they satisfy the inf-sup (or LBB) condition [17, 18]. The penalty finite element formulation circumvents this problem. It also reduces one independent variable (pressure). However, the penalty formulation has its own disadvantages. In principle, a very high penalty parameter $(10^8 - 10^{12})$ is required to obtain accurate solutions. For high penalty parameters, the contribution from the viscous terms would be negligibly small compared to the penalty terms in the computer,

---

Numerical results reported in this chapter appear in the article "Spectral/hp penalty least-squares finite element formulation for the steady incompressible Navier-Stokes equations" by V. Prabhakar and J. N. Reddy, *J. Comp. Phys.*, vol. 215, pp. 274-297, 2006.

and a trivial solution is obtained. This is termed as "locking". To circumvent locking and to obtain acceptable solution, underintegration (reduced integration) of penalty terms has been proposed [19]. The other problem with this formulation is inaccurate prediction of the pressure, which is calculated using equation

$$p = -\gamma(\nabla \cdot \mathbf{u}) \tag{2.1}$$

When C^0-continuous shape functions are used to interpolate velocities, pressure is discontinuous along element boundaries, and an averaging is needed to obtain *acceptable* pressure field [20]. However, pressure field computed in this manner is not very accurate; a very high penalty parameter is needed to obtain accurate pressure. For large values of penalty parameters, the condition number of the finite element coefficient matrix is very high and hence the convergence of iterative solvers is very poor.

First penalty based finite element formulation for the Navier-Stokes equations was proposed almost three decades ago and there have been subsequent improvements but it did not gain much popularity mainly because of ill-conditioning of coefficient matrix which renders iterative solvers ineffective. Recently, Bochov and Gunzburger [21] proposed least-squares based penalty formulation for Stokes equations but their study was mathematical and no numerical results were reported. Hasthaven and coworkers [22, 23] have proposed spectral/hp penalty methods where they implement boundary conditions using this approach.

In this chapter we present spectral/hp penalty least-squares finite element formulation for fluid flow problems. We combine the idea of least-squares variational principles with penalty method. Least-squares formulations result in a symmetric positive-definite coefficient matrix, which can be solved using robust iterative methods like preconditioned

conjugate gradient method. The least-squares formulation results in a minimization problem rather than a saddle point problem and the choice of elements is not subjected to the LBB condition. High-order element expansions are used to construct the discrete model, which does not experience locking. Equal-order integration is used for all the terms in this study. We implement iterative penalty method proposed by Gunzberger [13]. The best feature of present formulation is that it requires very small penalty parameter, $10 - 40$ to yield very accurate solution. For such small penalty parameters, the coefficient matrix is better conditioned and convergence is not slow as in the traditional penalty finite element model. Due to the use of high-order expansions, we also obtain very accurate velocity as well as pressure fields. Thus, the disadvantages of the weak form penalty finite element model are overcome by the penalty least-squares finite element model.

We present this formulation as an alternative to the spectral/hp least-squares finite element formulation presented by Pontaza and Reddy [5, 12] for steady and unsteady problems. In their formulation the divergence-free constraint on the velocity field is enforced directly through the least-squares functional, and pressure is retained as an independent variable. For unsteady problems, this approach seems to have disadvantages as the time-evolution of the pressure field is not well-behaved. It is believed that it lacks a strong pressure-velocity coupling. The present formulation avoids this problem altogether by eliminating pressure via Eq. (2.7).

The present chapter is organized as follows. In section B, the penalty least-squares finite element model for the steady incompressible Navier-Stokes equations is presented. Numerical results are presented in section C. The spectral convergence is verified using the exact solution of the Kovasznay flow problem. first we present results for 2D lid driven cavity problem at Re=10^4 and compare the results with Jiang et. al [36]. Next, numerical results are presented for the two-dimensional flow over a backward-facing step and results are compared with the benchmark solutions of Gartling [24] and Pontaza and Reddy [5]. Next,

we consider flow past a circular cylinder at low Reynolds number and compare the predicted surface pressure distribution with experimental measurements of Grove et al. [25]. To test mass conservation rigorously, we solved 2D flow past a large circular cylinder in a channel. Lastly, in section D, we extend this formulation to velocity-temperature coupled problems and present results for buoyant flow inside a square enclosure and compare results with the benchmark solution of Davis et al. [26].

B. The incompressible Navier-Stokes equations

Notations: Let Ω denote an open bounded domain in $\mathbb{R}^{\mathrm{n}}$, n=2 or 3, having a sufficiently smooth boundary Γ. Throughout this dissertation, vectors will be denoted by boldface letters, e.g., $\mathbf{u}$, and tensors by underlined boldface capitals, e.g., $\underline{\mathbf{T}}$. We use the standard notation and definition for the Sobolev spaces $H^s(\Omega)$ and $H^s(\Gamma)$, $s \geq 0$, with corresponding inner products denoted by $(\cdot,\cdot)_{s,\Omega}$ and $(\cdot,\cdot)_{s,\Gamma}$. By $\mathbf{H}^s(\Omega)$ we denote the product space $[H^s(\Omega)]^n$; and $H_0^1(\Omega)$ denotes the space of functions from $H^1(\Omega)$ that vanish on the boundary Γ.

The steady Incompressible Navier-Stokes equations in dimensionless form can be written as follows:

$$(\mathbf{u}\cdot\nabla)\,\mathbf{u} + \nabla p - \frac{1}{\mathrm{Re}}\,\nabla\cdot\left[(\nabla\mathbf{u}) + (\nabla\mathbf{u})^{\mathrm{T}}\right] = \mathbf{f} \qquad \text{in } \Omega \tag{2.2}$$

$$\nabla\cdot\mathbf{u} = 0 \qquad \text{in } \Omega \tag{2.3}$$

$$\mathbf{u} = \mathbf{u}^s \qquad \text{on } \Gamma_u \tag{2.4}$$

$$\hat{\mathbf{n}}\cdot\underline{\boldsymbol{\sigma}} = \mathbf{f}^s \qquad \text{on } \Gamma_f \tag{2.5}$$

where $\mathbf{u}(\mathbf{x})$ is the velocity vector, $\underline{\boldsymbol{\sigma}} = -p\,\underline{\mathbf{I}} + 1/\mathrm{Re}\,\left[(\nabla\mathbf{u}) + (\nabla\mathbf{u})^{\mathrm{T}}\right]$ is the total stress,

$p(\mathbf{x})$ is the pressure, $\mathbf{f}$ is a dimensionless force, $\hat{\mathbf{n}}$ is the outward unit normal on the boundary of Ω, $\mathbf{u}^s$ is the prescribed velocity on the boundary Γ_u, and $\mathbf{f}^s$ are the prescribed tractions on the boundary Γ_f, $\Gamma = \Gamma_u \cup \Gamma_f$ and $\Gamma_u \cap \Gamma_f = \emptyset$, and Re is the Reynolds number.

In the penalty method, pressure is eliminated from the Navier-Stokes equations using the following expression, which follows from the application of the penalty method to the Navier-Stokes equations with the divergence-free constraint (see [27], [28], and [29]):

$$p = -\gamma(\nabla \cdot \mathbf{u}) \tag{2.6}$$

Gunzberger [13] proposed an iterative penalty method

$$p^n = p^{n-1} - \gamma(\nabla \cdot \mathbf{u}) \tag{2.7}$$

where n is the nonlinear iteration number. An advantage of this method is that the value of penalty parameter needed to enforce the continuity constraint is equal to the square of the one needed in the non-iterative penalty method [13]. This, in turn, results in a coefficient matrix with smaller conditioning number. In this study we use the iterative penalty method.

Therefore, the problem becomes one of finding the velocity $\mathbf{u}(\mathbf{x})$ such that

$$(\mathbf{u} \cdot \nabla)\,\mathbf{u} - \gamma\nabla(\nabla \cdot \mathbf{u}) - \frac{1}{\mathrm{Re}}\,\nabla \cdot \left[(\nabla\mathbf{u}) + (\nabla\mathbf{u})^{\mathrm{T}}\right] = \mathbf{f} - \nabla p^{n-1} \quad \text{in } \Omega \tag{2.8}$$

$$\mathbf{u} = \mathbf{u}^s \quad \text{on } \Gamma_u \tag{2.9}$$

$$\hat{\mathbf{n}} \cdot \underline{\boldsymbol{\sigma}} = \mathbf{f}^s \quad \text{on } \Gamma_f \tag{2.10}$$

where n in the superscript $(n-1)$ is the nonlinear iteration number. Since the solution at iteration $(n-1)$ is known, ∇p^{n-1} is known and therefore transferred to the right-hand side

of the equation.

1. The velocity-dilatation-vorticity first-order system

To cast the second-order system (2.8)-(2.10) into a first-order system, we introduce the vorticity vector, $\boldsymbol{\omega} = \nabla \times \mathbf{u}$, and use the vector identity

$$\nabla \times \nabla \times \mathbf{u} = -\nabla^2 \mathbf{u} + \nabla (\nabla \cdot \mathbf{u})$$

We introduce another scalar independent variable dilatation, which is defined as

$$D = \nabla \cdot \mathbf{u}$$

Then Eqs. (2.8)-(2.10) can now be replaced by an equivalent system of first-order equations. The problem now can be stated as one of finding the velocity vector $\mathbf{u}(\mathbf{x})$, dilatation $D(\mathbf{x})$, and vorticity $\boldsymbol{\omega}(\mathbf{x})$ such that

$$(\mathbf{u} \cdot \nabla)\mathbf{u} - \gamma \nabla D + \frac{1}{\mathrm{Re}} \nabla \times \boldsymbol{\omega} = \mathbf{f} - \nabla p^{n-1} \qquad \text{in } \Omega \tag{2.11}$$

$$\boldsymbol{\omega} - \nabla \times \mathbf{u} = \mathbf{0} \qquad \text{in } \Omega \tag{2.12}$$

$$D - \nabla \cdot \mathbf{u} = 0 \qquad \text{in } \Omega \tag{2.13}$$

$$\mathbf{u} = \mathbf{u}^s \qquad \text{on } \Gamma_u \tag{2.14}$$

$$\boldsymbol{\omega} = \boldsymbol{\omega}^s \qquad \text{on } \Gamma_\omega \tag{2.15}$$

Typically $\Gamma_u \cap \Gamma_\omega = \emptyset$, i.e., if velocity is specified at a boundary, vorticity need not be specified there.

a. L_2 least-squares formulation

The least-squares functional of the problem can be set up by summing up the squares of the residuals of the new set of equations

$$\mathcal{J}\left(\mathbf{u}, D, \boldsymbol{\omega}; \mathbf{f}\right) = \frac{1}{2}\Big(\left\| \left(\mathbf{u}\cdot\nabla\right)\mathbf{u} - \gamma\nabla D + \frac{1}{\mathrm{Re}}\nabla\times\boldsymbol{\omega} - \mathbf{f} + \nabla p^{n-1} \right\|_0^2 + \left\| \boldsymbol{\omega} - \nabla\times\mathbf{u}\right\|_0^2 + \left\| D - \nabla\cdot\mathbf{u}\right\|_0^2\Big) \tag{2.16}$$

Considering the homogeneous pure velocity boundary condition case, the least-squares principle for functional (2.16) can be stated as:

find the velocity vector $\mathbf{u}\left(\mathbf{x}\right)$, dilatation $D\left(\mathbf{x}\right)$, and vorticity $\boldsymbol{\omega}\left(\mathbf{x}\right)$ such that

$$\mathcal{J}\left(\mathbf{u}, D, \boldsymbol{\omega}; \mathbf{f}\right) \leq \mathcal{J}\left(\tilde{\mathbf{u}}, \tilde{D}, \tilde{\boldsymbol{\omega}}; \mathbf{f}\right) \qquad \forall\ \left(\tilde{\mathbf{u}}, \tilde{D}, \tilde{\boldsymbol{\omega}}\right) \in \mathbf{X} \tag{2.17}$$

i.e.,

$$seek\ \left(\mathbf{u}, D, \boldsymbol{\omega}\right)\ such\ that\ \mathcal{J}\left(\mathbf{u}, D, \boldsymbol{\omega}; \mathbf{f}\right)\ is\ minimized\ over\ X.$$

where we use the space

$$\mathbf{X} = \left\{ \left(\mathbf{u}, D, \boldsymbol{\omega}\right) \in \mathbf{H}_0^1\left(\Omega\right) \times H^1\left(\Omega\right) \times \mathbf{H}^1\left(\Omega\right) \right\}$$

The variational problem (after linearization using Newton's method)corresponding to the least-squares principle is given by

$$\mathcal{B}\left(\left(\mathbf{u}, D, \boldsymbol{\omega}\right), \left(\tilde{\mathbf{u}}, \tilde{D}, \tilde{\boldsymbol{\omega}}\right)\right) = \mathcal{F}\left(\left(\tilde{\mathbf{u}}, \tilde{D}, \tilde{\boldsymbol{\omega}}\right)\right) \qquad \forall\ \left(\tilde{\mathbf{u}}, \tilde{D}, \tilde{\boldsymbol{\omega}}\right) \in \mathbf{X} \tag{2.18}$$

where

$$\mathcal{B}\left((\mathbf{u},D,\boldsymbol{\omega}),\left(\tilde{\mathbf{u}},\tilde{D},\tilde{\boldsymbol{\omega}}\right)\right)=\int_{\Omega}\left((\mathbf{u}\cdot\nabla)\,\mathbf{u}_0+(\mathbf{u}_0\cdot\nabla)\,\mathbf{u}-\gamma D+\frac{1}{\mathrm{Re}}\nabla\times\boldsymbol{\omega}\right)\cdot$$
$$\left((\tilde{\mathbf{u}}\cdot\nabla)\,\mathbf{u}_0+(\mathbf{u}_0\cdot\nabla)\,\tilde{\mathbf{u}}-\gamma\tilde{D}+\frac{1}{\mathrm{Re}}\nabla\times\tilde{\boldsymbol{\omega}}\right)\,d\Omega$$
$$+\int_{\Omega}(\boldsymbol{\omega}-\nabla\times\mathbf{u})\cdot(\tilde{\boldsymbol{\omega}}-\nabla\times\tilde{\mathbf{u}})\,d\Omega$$
$$+\int_{\Omega}(D-\nabla\cdot\mathbf{u})\left(\tilde{D}-\nabla\cdot\tilde{\mathbf{u}}\right)\,d\Omega$$

and

$$\mathcal{F}\left(\left(\tilde{\mathbf{u}},\tilde{D},\tilde{\boldsymbol{\omega}}\right)\right)=\int_{\Omega}\left(\mathbf{f}-\nabla p^{n-1}+(\mathbf{u}_0\cdot\nabla)\,\mathbf{u}_0\right)\cdot\left((\tilde{\mathbf{u}}\cdot\nabla)\,\mathbf{u}_0+(\mathbf{u}_0\cdot\nabla)\,\tilde{\mathbf{u}}-\gamma\tilde{D}+\frac{1}{\mathrm{Re}}\nabla\times\tilde{\boldsymbol{\omega}}\right)\,d\Omega$$

Let $\mathbf{X}_{hp}$ denote a finite-dimensional subspace of $\mathbf{X}$. Then the least-squares discretized model of the Navier-Stokes equations is defined by the following discrete variational problem: find $\left(\mathbf{u}^{hp},D^{hp},\boldsymbol{\omega}^{hp}\right)\in\mathbf{X}_{hp}$ such that

$$\mathcal{B}\left(\left(\mathbf{u}^{hp},D^{hp},\boldsymbol{\omega}^{hp}\right),\left(\tilde{\mathbf{u}}^{hp},\tilde{D}^{hp},\tilde{\boldsymbol{\omega}}^{hp}\right)\right)=\mathcal{F}\left(\left(\tilde{\mathbf{u}}^{hp},\tilde{D}^{hp},\tilde{\boldsymbol{\omega}}^{hp}\right)\right)\forall\ \left(\tilde{\mathbf{u}}^{hp},\tilde{D}^{hp},\tilde{\boldsymbol{\omega}}^{hp}\right)\in\mathbf{X}_{hp}\tag{2.19}$$

b. Expansion bases

Having defined the finite element framework in terms of the penalty least-squares formulation, we need to choose proper basis functions to interpolate dependent variables. Almost all the penalty finite element implementations use low order expansions, linear or quadratic, and perform different order integration to integrate penalty terms and rest of the terms in the coefficient matrix. In this study, we use high order interpolation functions that give p-convergence but computational work associated per degree of freedom is more compared

to that of low order interpolation functions. One way to tackle the computational problem is to use expansion bases that are orthogonal. We use spectral bases that give exponential convergence and, the same time, satisfy orthogonality conditions. It is to be mentioned that all the variables are be approximated using the same interpolation functions since there is no compatibility condition such as LBB condition in this formulation.

Nodal expansion: In the standard interval $\Omega_{st} = \{\xi | -1 < \xi < 1\}$ nodal expansions are defined as

$$\psi_i(\xi) = \frac{(\xi - 1)(\xi + 1)L'_p(\xi)}{p(p+1)L_p(\xi_i)(\xi - \xi_i)} \tag{2.20}$$

In Eq. (2.20), $L_p = P_p^{0,0}$ is the Legendre polynomial of order p and ξ_i denotes the location of the roots of $(\xi - 1)(\xi + 1)L'_p(\xi) = 0$ in the interval $[-1, 1]$. Nodal expansion follows discrete orthogonality i.e., $\psi_p(\xi_q) = \delta_{pq}$. This property has been exploited during the calculation of conjugate gradient residual, which makes computations very fast. Details on the multidimensional construction of nodal expansions can be found in Ref. [30].

The integrals in Eq. (2.19) are evaluated using Gauss quadrature rules. In the computer implementation, Gauss-Lobatto-Legendre rule is used, which is imperative to exploit discrete orthogonality of nodal basis functions. This integration is not full integration still for the sake of fast numerical integration we use this. We would like to mention that this integration gives identically same results as full integration (Gauss-Legendre) gives and unlike in traditional penalty finite element formulation where coefficient matrix is almost singular and reduced integration is imperative to obtain acceptable solution. For details on standard finite element computer implementation, such as mapping $\bar{\Omega}_e \rightleftarrows \hat{\Omega}_e$, numerical integration in $\hat{\Omega}_e$, and assembly using the direct stiffness approach, see Reddy [27, 28]. For linearization, we use Newton's method, details of which can be found in [31].

2. The stress based first-order system

To define the first-order velocity-stress system, 'scaled' stress tensor (symmetric part of velocity gradient tensor) is introduced

$$\underline{\mathbf{T}} = \left[(\nabla \mathbf{u}) + (\nabla \mathbf{u})^{\mathrm{T}} \right] \tag{2.21}$$

Then Eqs. (2.8)-(2.10) can now be replaced by an equivalent system of first-order equations. The problem now can be stated as one of finding the velocity vector $\mathbf{u}(\mathbf{x})$ and stress tensor $\underline{\mathbf{T}}(\mathbf{x})$ such that

$$(\mathbf{u} \cdot \nabla)\,\mathbf{u} - \gamma \nabla \left[\frac{1}{2} \operatorname{tr}(\underline{\mathbf{T}}) \right] - \frac{1}{\mathrm{Re}} \nabla \cdot \underline{\mathbf{T}} = \mathbf{f} - \nabla p^{n-1} \qquad \text{in } \Omega \tag{2.22}$$

$$\underline{\mathbf{T}} - \left[(\nabla \mathbf{u}) + (\nabla \mathbf{u})^{\mathrm{T}} \right] = \underline{\mathbf{0}} \qquad \text{in } \Omega \tag{2.23}$$

$$\mathbf{u} = \mathbf{u}^s \qquad \text{on } \Gamma_u \tag{2.24}$$

$$\hat{\mathbf{n}} \cdot \underline{\mathbf{T}} = \mathbf{T}^s \qquad \text{on } \Gamma_T \tag{2.25}$$

Typically $\Gamma_u \cap \Gamma_T = \emptyset$, i.e., if velocity is specified at a boundary, and stress need not be specified there. The L_2 least-squares formulation and finite element model proceed in a similar manner as that described for the dilatation-vorticity based first-order system.

3. Implementation of boundary conditions

In general, in a given problem we have boundary conditions on the primary variables and/or secondary variables [27]. Boundary conditions on the primary variables can be implemented easily in the strong sense by restricting the value of corresponding degree of freedom. Symmetry boundary conditions in 2D are $v = 0$ and $\omega = 0$ (at the wall $y =$constant).

Boundary conditions on the secondary variables (typically, they involve derivatives of the primary variables) are imposed in a weak sense through the least-squares functional.

For example, the outflow boundary condition, $\hat{\mathbf{n}} \cdot \tilde{\boldsymbol{\sigma}} = \hat{\mathbf{n}} \cdot (-p\mathbf{I} + (1/\mathrm{Re})\ \nabla\mathbf{u}) = 0$ is implemented by modifying the L_2 least-squares functional to be

$$\mathcal{J}(\mathbf{u}, D, \boldsymbol{\omega}; \mathbf{f}) = \frac{1}{2}\Big(\big\| (\mathbf{u}\cdot\nabla)\,\mathbf{u} - \gamma\nabla D + \frac{1}{\mathrm{Re}}\nabla\times\boldsymbol{\omega} - \mathbf{f} + \nabla p^{n-1} \big\|_0^2 + \big\| \boldsymbol{\omega} - \nabla\times\mathbf{u} \big\|_0^2 + \big\| D - \nabla\cdot\mathbf{u} \big\|_0^2 + \| \hat{\mathbf{n}}\cdot\tilde{\boldsymbol{\sigma}} \|^2_{0,\,\Gamma_{\text{outflow}}} \Big) \tag{2.26}$$

In the boundary term, pressure p is replaced by ($p^{n-1} - \gamma D$). For long domains, the strong outflow boundary condition $p = 0$ also gives good results [5].

4. Solution of algebraic equations

In this study, we use both direct as well as iterative solvers. We use Schur complement method [32, 30] and condense out all interior degrees of freedom. Fig. 9 shows one such mesh with interface nodes shown by square symbols and interior nodes shown by triangles. Since interior nodes of an element are not connected to other elements, coefficient matrix entries of corresponding degrees of freedom get contribution only from the nodes of that element and hence can be expressed in terms of interface nodes of that element. In this way, all interior degrees of freedom are eliminated and the system of equations is solved for interface degrees of freedom. Details of Schur complement can be found in [32, 30]. While generating the mesh, one should number global interface degrees of freedom first, followed by global interior degrees of freedom. In addition, the global interior degrees of freedom should be numbered consecutively to maximize the benefit of this procedure.

The Schur complement method has two-fold benefit. First, if coefficient matrix is stored, then one needs to store coefficient matrix corresponding to interface degrees of freedom. This saves tremendous amount of memory and one needs to solve for only the interface degrees of freedom. Secondly, conditioning number of new coefficient matrix is significantly lower than that of original matrix and iterative solvers converge faster [30].

To construct Schur complement, we need to invert elemental coefficient matrices which is computationally very cheap. Once Schur complement matrix is constructed, direct or iterative solvers can be used to solve this system. We note that Schur complement method can also be implemented in 'element by element' PCG method, where the global coefficient matrix is not stored (see [1] for details on 'element by element' solution algorithm). This is particularly desirable for large problems where even coefficient matrix corresponding to interface degrees of freedom requires large memory.

a. Direct solvers

Schur complement eliminates all interior degrees of freedom and therefore memory storage required to save coefficient matrix is significantly low and direct solvers can be used for relatively large problems. Given a SPD coefficient matrix, N_{dof} by N_{dof} with bandwidth B, banded Cholesky factorization is an effective direct solver provided $N_{dof} >> B$. The amount of work required for this factorization is approximately $N_{dof}(B^2 + 3B)$ flops and N_{dof} square roots. We store only the nonzero lower triangular part in a $(B + 1)$ by N_{dof} array. At this point we caution the reader that because of round-off errors Cholesky factorization may not be stable (square-root of negative numbers may arise); see [33]. In particular, for high penalty parameters, Cholesky factorization may be unstable. But the present formulation requires very low value of penalty parameter and hence we did not face this problem.

b. Iterative solvers

For large problems, direct solvers are not a good choice both in terms of computer memory and CPU time. For SPD coefficient matrix, preconditioned conjugate gradient (PCG) methods are optimal choice. In this study we use Jacobi preconditioner as only diagonal entries of coefficient matrix are needed to be stored as opposed to other preconditioners

which require partial or full storage of coefficient matrix.

5. Calculation of pressure

Unlike the non-iterative penalty method, in the iterative penalty method, pressure is calculated (actually updated) in every nonlinear iteration through the following equation

$$p^n = p^{n-1} - \gamma D^n \tag{2.27}$$

Thus no post-processing is needed in this formulation to compute pressure. Unlike penalty finite element formulations where pressure is not continuous, this formulation gives smooth and very accurate pressure field.

C. Numerical results

In this section, numerical results obtained with the penalty least-squares finite element model are presented for a number of benchmark problems. First, spectral convergence of the proposed algorithm is verified for both vorticity-dilatation and stress based least-squares finite element formulations. Next, results are presented for 2D lid driven cavity flow, flow over a backward facing step, and flow past a circular cylinder at low Reynolds number. To test mass conservation rigourously we solve 2D flow past a large circular cylinder in a channel. We use vorticity-dilatation based first order system in this study because it carries lesser degrees of freedom compared to stress based first order system and gives equally accurate results. We also investigate accuracy of the formulation with respect to the penalty parameter for these problems.

In this study, both direct and iterative solvers are used. All results presented are ob-

tained using direct solver (banded Cholesky factorization) unless stated otherwise. Real world fluid mechanics problems are generally big in size requiring large number of degrees of freedom. For such problems direct solvers are not efficient because of both memory required and CPU time taken. Therefore, all problems are also solved using iterative solver (PCG), and PCG convergence history is reported, which show that present formulation is free from ill-conditioning problem. Dilatation contours are presented for all problems apart from reporting L_2-norm of the residual of continuity equation (dilatation) as L_2-norm gives global picture only. The L_2-norm of the least-squares functional and other variables are defined as

$$\|\mathcal{J}\|_0 = \Big[\frac{1}{2}\sum_{e=1}^{Nem}\int_{\Omega^e}\left(R_1^2 + R_2^2 + R_3^2 + R_4^2\right) d\Omega^e\Big]^{\frac{1}{2}}$$

$$\|D\|_0 = \Big(\sum_{e=1}^{Nem}\int_{\Omega^e} D^2\, d\Omega^e\Big)^{\frac{1}{2}}$$

where R_i is residual of ith partial differential equation of the system and D is an independent variable (dilatation, vorticity, etc.). Some authors report square of these values. Nevertheless spectral convergence is important. L_2-norm of the residual should decay exponentially with p-level.

For all the problems considered in this chapter, non-linear convergence is declared when the relative norm of the residual, $\|\Delta\mathbf{U}\|/\|\mathbf{U}\|$ is less than 10^{-3} unless mentioned, where $\mathbf{U}$ is the solution vector (includes all degrees of freedom at a node). Convergence of conjugate gradient is declared when L_2-norm of error is less than 10^{-6}.

1. Verification problem: Kovasznay flow

The benchmark problem to be used for the purpose of verification of the least-squares based finite element models is an analytical solution to the two-dimensional steady incom-

pressible Navier-Stokes due to Kovasznay [34]. Domain of interest is $\bar{\Omega} = [-0.5, 1.5] \times [-0.5, 1.5]$. The solution is given by

$$u = 1 - e^{\lambda x} \cos(2\pi y) \tag{2.28}$$

$$v = \frac{\lambda}{2\pi} e^{\lambda x} \sin(2\pi y) \tag{2.29}$$

$$p = p_0 - \frac{1}{2} e^{2\lambda x} \tag{2.30}$$

where $\lambda = \mathrm{Re}/2 - [(\mathrm{Re}^2/4) + 4\pi^2]^{1/2}$ and p_0 is a reference pressure (an arbitrary constant).

Drichlet boundary conditions on velocities are specified using the exact solution given by Eqs. (2.28) and (2.29). The discrete system is linearized using Newton's method and resulting symmetric positive-definite (SPD) system of equations has been solved using the Choleski factorization. A uniform mesh of 64 quadrilateral elements is used for spatial discretization. Newton's convergence is declared when the relative norm of the residual is less than 10^{-10}. Penalty parameter used is 10^2 for which L_2-norm of the residual of continuity equation is below 10^{-12} for all p-levels used here and does not interfere with the spectral convergence.

Streamlines obtained with the present formulation for the Kovasznay flow are shown in Fig. 1(a). and Fig. 1(b) contains dilatation contours.

To verify spectral convergence, L_2 norm of least-square functional $\mathcal{J}$ and L_2 error of the velocity, pressure and vorticity fields are plotted against polynomial order in Fig. 2 for the dilatation-vorticity based first-order formulation. On logarithmic-linear scale we obtain almost straight line for all the variables verifying exponential decay with respect to the polynomial degree used.

Next, spectral convergence of stress based first order system is verified. Fig. 3 shows that formulation achieves spectral convergence for all variables including pressure. The fact that functionals are not H^1-norm equivalent and hence define non-equivalent formulations

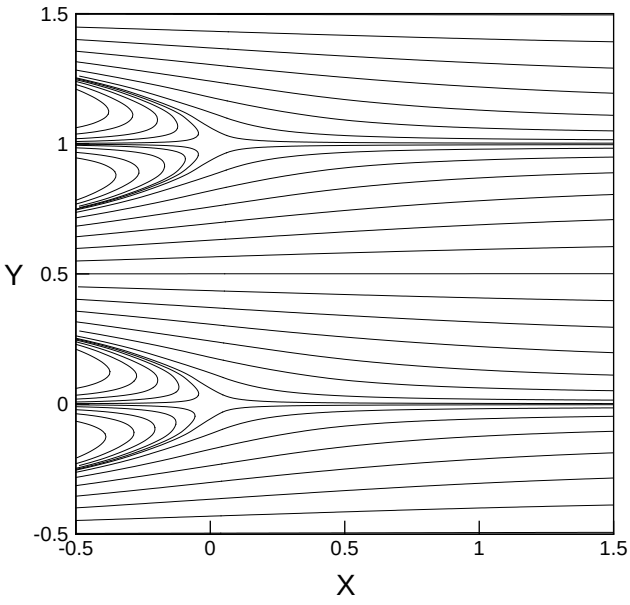

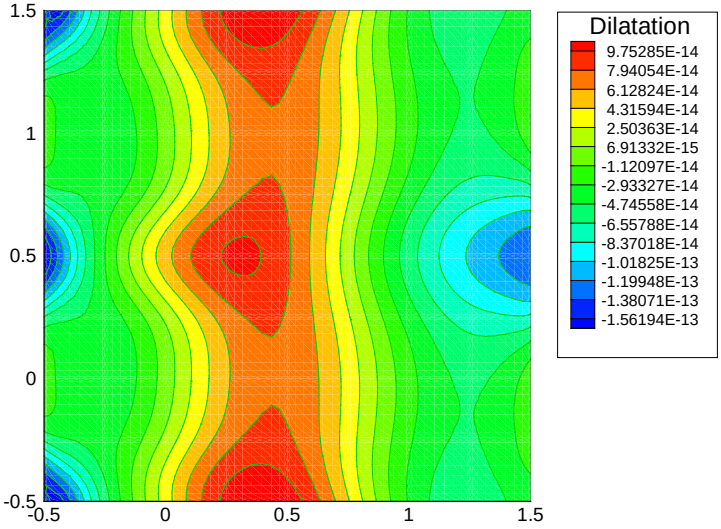

Fig. 1. (a) Kovasznay flow: Streamlines for Re = 40 (b) Kovasznay flow: Dilation contours for Re =40

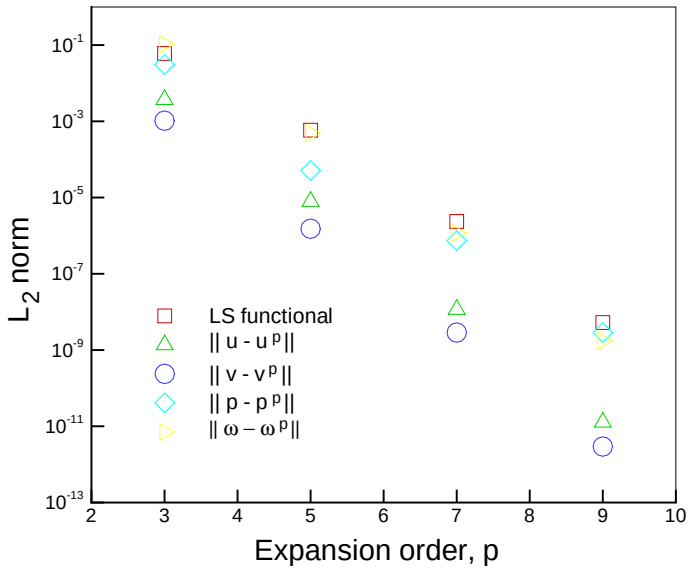

Fig. 2. Convergence of the least-squares functional, velocity, pressure and vorticity fields to the exact Kovasznay solution in the L_2 norm

does not imply that the method is not optimal. It simply means that optimality of the resulting method can not be established a priori using standard elliptic theory.

Simulations are carried out for various values of penalty parameters. The p-level used is 9. Newton's iteration does not converge for penalty parameters less than one. For penalty parameter greater than one, non-linear convergence depends on the value of penalty parameter as shown in Table I. Newton's convergence is declared when the relative norm of the residual is less than 10^{-10}. The L_2 norm of least-square functional remains almost the same (5×10^{-9}) and L_2-norm of the residual of continuity equation is below 10^{-12} for all these penalty parameters.

2. 2D Lid-driven cavity flow

Next, the two-dimensional lid-driven cavity problem is analyzed to test our formulation. The flow is driven by the translation of the top boundary. No slip boundary condition

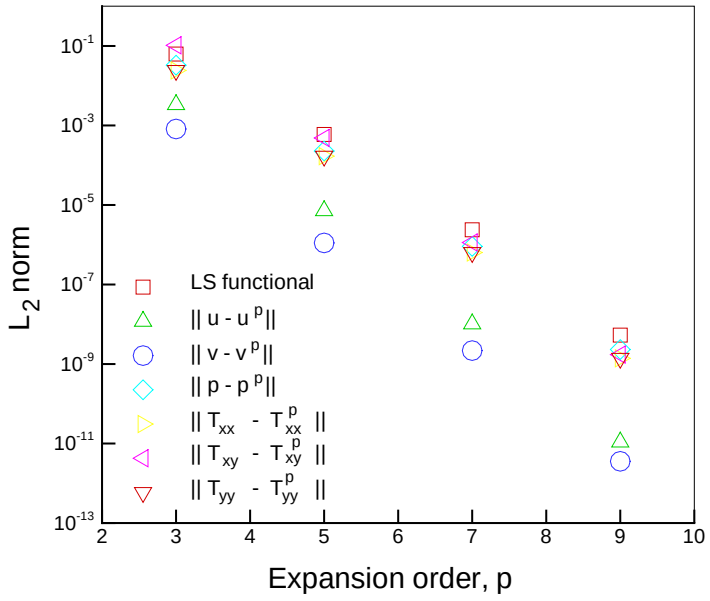

Fig. 3. Convergence of the least-squares functional, velocity, pressure and stress fields to the exact Kovasznay solution in the L_2 norm

is imposed on all solid walls. On the top wall ($y = 1.0$) boundary conditions are $u = u(x)$, $v = 0$. To avoid singularity in the boundary condition, we specify a hyperbolic tangent u-velocity distribution on the top wall:

$$u(x) = \begin{cases} \tanh(\beta\, x) & 0 \le x \le 0.5 \\ -\tanh(\beta\,(x-1)) & 0.5 < x \le 1.0 \end{cases}$$

with $\beta > 0$. In the present study, $\beta = 100$ and 500 are used, which give a smooth but at the same time sharp transition from $u = 0.0$ to $u = 1.0$ near the walls of the driven surface. This boundary condition results in a well posed boundary condition as singularities at the corners are eliminated. The standard boundary condition ($u = 1$ everywhere) would destroy the high accuracy properties associated with high-order expansions by polluting the solution near the corners. High order methods are sensitive to these types of singularities.

Table I. Number of Newton's iterations required for nonlinear convergence.

Penalty parameter	No. of Newtons itr.
1	23
5	14
10	13
50	11
100	11

These singularities render the computational method unstable.

We use 18×18 nonuniform mesh which is graded towards the wall; corner elements have the dimension of 0.008×0.008. The 8th order nodal expansion is used in each element and there are total of $84,100$ degrees of freedom in the mesh. All internal degrees of freedom are condensed out, resulting in 20,596 interface degrees of freedom with a band-width of 1148. The banded Cholesky factorization is used to solve for the interface degrees of freedom. In this study, the global nodes are numbered in a natural order and no effort is made to reduce the band-width. Band-width can be reduced with a suitable choice of a node numbering scheme. An alternate approach to minimize the bandwidth is by using the graph-theory. A popular choice is the Reverse Cuthill-McKee permutation [35]. This problem has been solved for the penalty parameter varying from 5 to 40. We use Re continuation method and start with Re=100 and march till Re=10^4 at the increment of 300. Results are presented for $\beta = 100$.

Fig. 4(a) contains plots of streamline at Re=10^4. Results match qualitatively very well with the published results of Jiang et al. [36], who used least-squares finite element formulation with an almost uniform 400×408 mesh of bi-linear elements and one-point quadrature. A penalty parameter of 10 is used for these results. The value of the L_2 least-

squares functional remains below 1.1×10^{-2} and L_2-norm of the residual of continuity equation is below 3.1×10^{-6} for these computations. Typically it takes two Newton's iterations to converge for every Re step. Fig. 4(b) shows pressure contours and Fig. 4(c) contains dilatation contours. Dilatation contours show that mass conservation is satisfied very well locally at all points in the domain with a maximum value of dilatation around 6×10^{-6} near the top corner. Penalty parameter used is only 10 and it works very well for even for this high Reynolds number. This problem is not a very good example to judge required penalty parameter at high Re, as there is no mass coming in or going out, problems of flow over a backward facing step and flow past circular cylinder will test it better.

The u-velocity profiles along the vertical mid-line of the cavity $x = 0.5$ is shown in Fig. 5(a) for various values of the penalty parameter and the results are compared with those of Jiang et al. [36]. Again, we see excellent agreement between the two results even for $\gamma = 5$. In Fig. 5(b) v-velocity profiles are plotted along the horizontal mid-line of the cavity $y = 0.5$ for various values of the penalty parameter. We note that boundary conditions are different for the two studies. Jiang et al. [36] used lid velocity of 1 everywhere while in our case lid velocity varies with x.

Next, PCG convergence history is plotted for four Newton's iterations for Re=100 in Fig. 6. We use 10×10 grid with the corner element having dimension of 0.05×0.05. The p-level used is 7 and the penalty parameter is taken to be 10. Zero initial guess is used for all variables including pressure. There are no pronounced fluctuation.

As Fig. 5(a) and 5(b) show, formulation gives very accurate results for even penalty parameter of 5. Typical penalty parameter values used in the traditional penalty finite element formulation are in the range of $10^8 - 10^{12}$. For such a high penalty parameter, conditioning number of the resulting coefficient matrix becomes very high and different order integration rule is used to integrate penalty terms to obtain *acceptable* solution. Some explanations have been given in literature to justify the use of different order integration

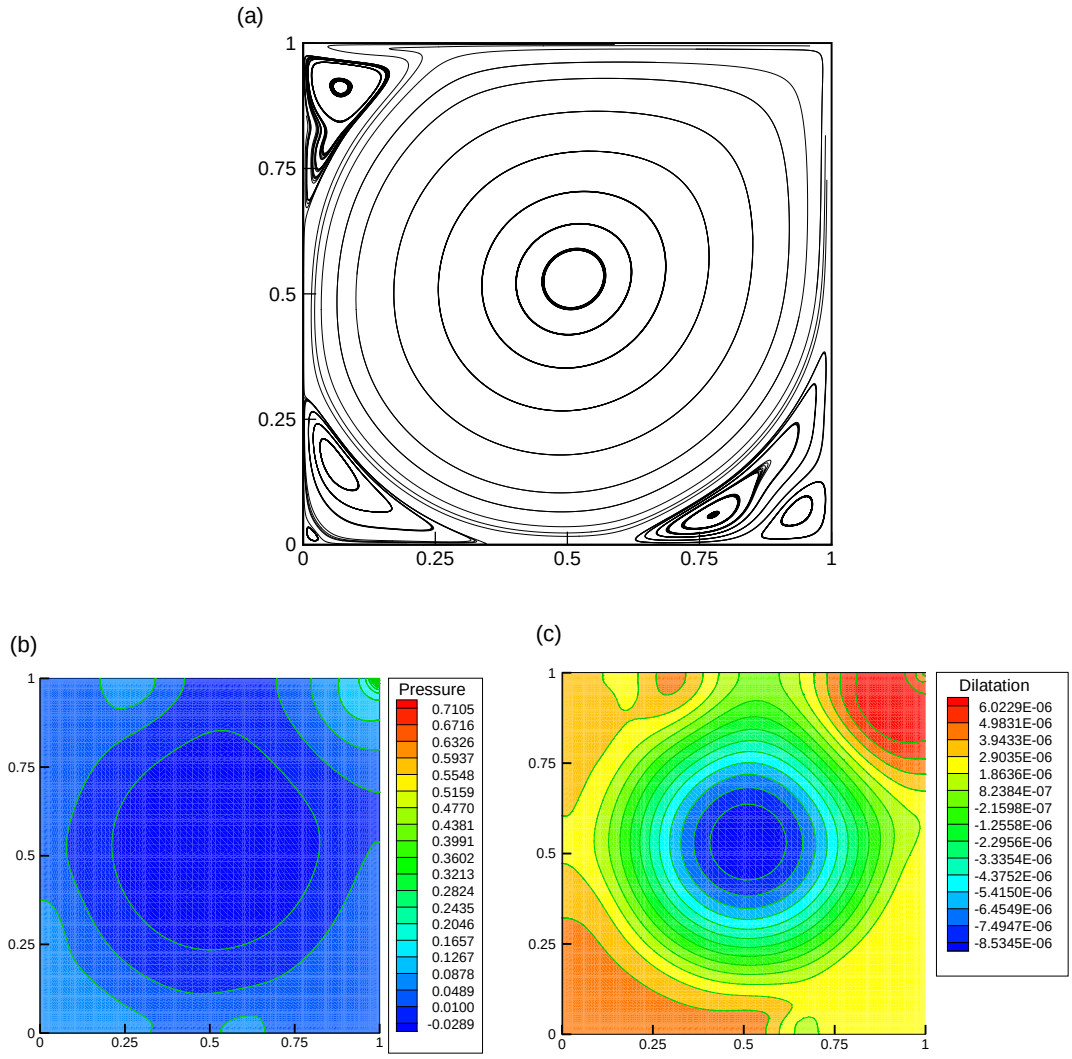

Fig. 4. Numerical results for 2D cavity flow at $Re = 10^4$ (a) Streamlines (b) Pressure Contours (c) Dilation Contours

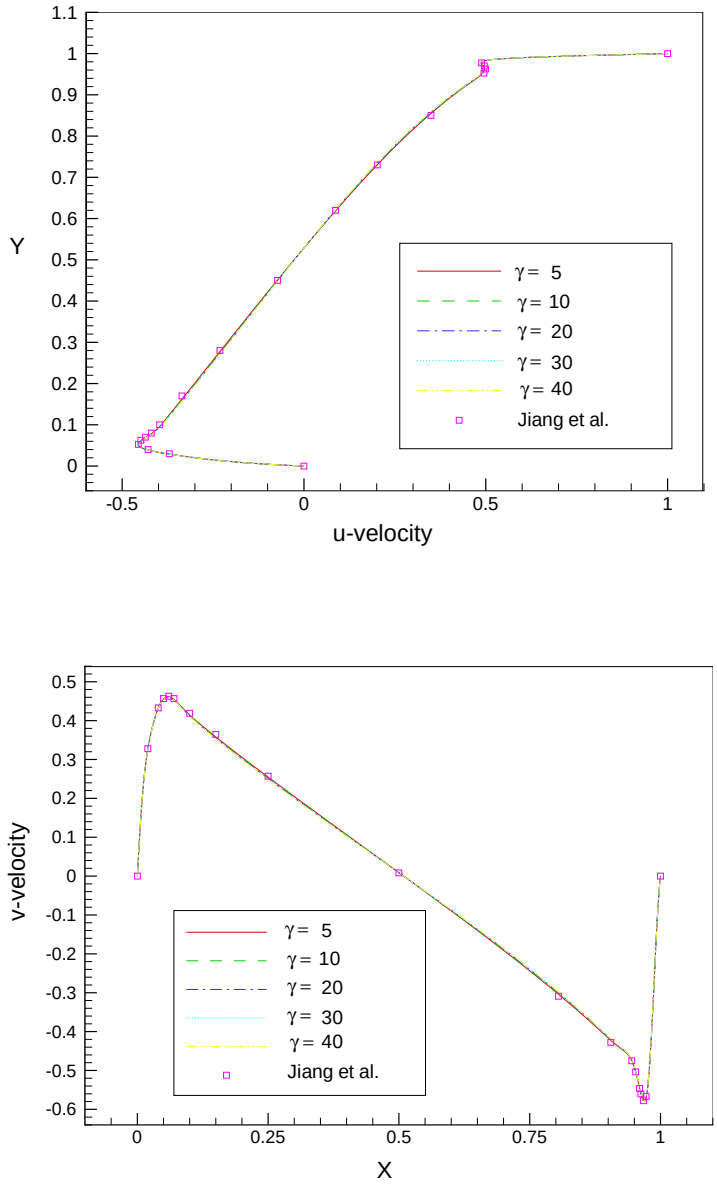

Fig. 5. 2D cavity flow for $Re = 10^4$ (a) variation of u-velocity with y for various penalty parameters (b) variation of v-velocity with x for various penalty parameters: comparision with benchmark results

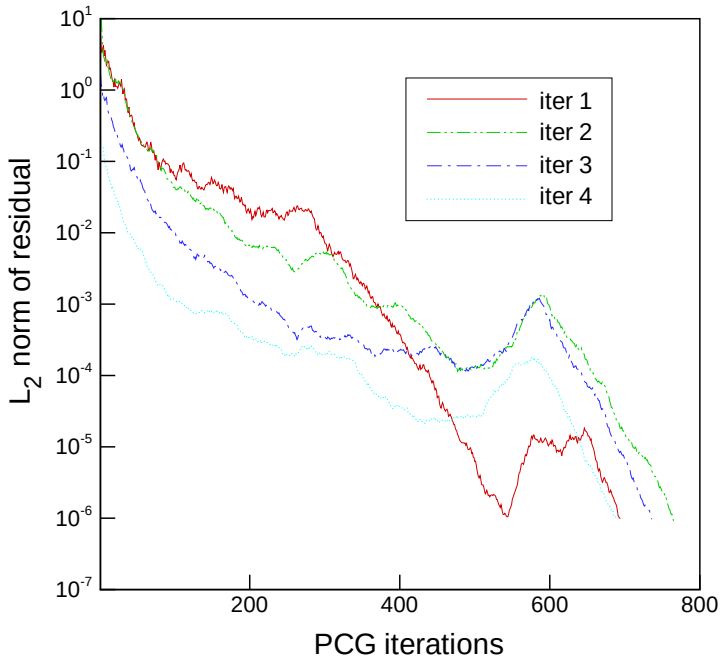

Fig. 6. Convergence history of preconditioned conjugate gradient solver (PCG) for 2D cavity flow

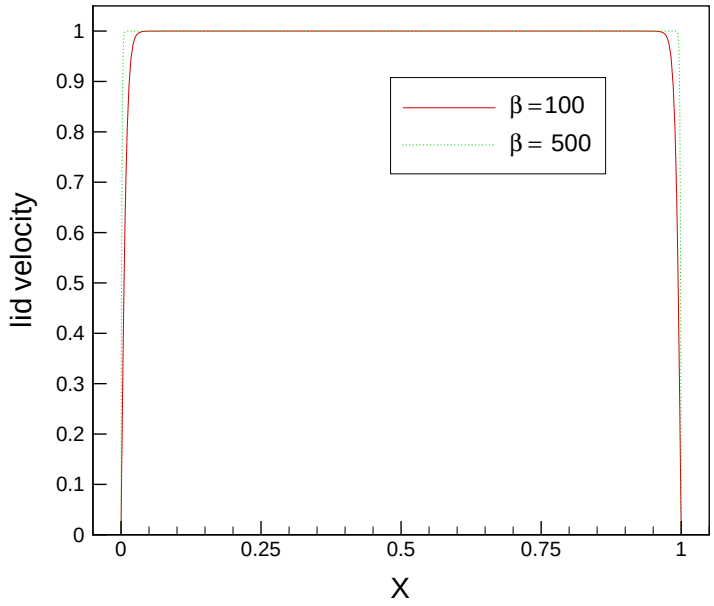

Fig. 7. Variation of lid velocity with parameter β

schemes for various terms of the coefficient matrix. In this study we have used equal order integration for all terms.

We solve this problem for $\beta = 500$ also on two different grids 18×18 and 22×22 with corner element having dimension 0.008×0.008 and 0.007×0.007 respectively with 8th order nodal expansion in each element ($\gamma = 20$). Variation of lid velocity with x for $\beta = 100$ and 500 is shown in Fig. 7.

They closely emulate the standard ill-posed boundary condition. As Fig. 8(a) and 8(b) show that on 18×18 mesh results are not satisfactory while results are accurate on 22×22 mesh. We see that even for singular boundary conditions (close to 1) accurate results can be obtained with h-refinement. For singular boundary conditions simulation becomes unstable (Newton's iterations do not converge) around Reynolds number of 7100 for 18×18 mesh. The Reynolds number at which the simulation becomes unstable depends

on the h-refinement used.

3. Flow over a backward-facing step

Next, we consider two-dimensional steady flow over a backward-facing step at Re $= 800$. The geometry and boundary conditions, taken from the benchmark solution of Gartling [24], are shown in Fig. 9. No-slip boundary condition is imposed on all walls. Boundary condition of $u(y) = 0$ is imposed for $-0.5 \leq y \leq 0.0$. A parabolic velocity profile given by $u(y) = 24y(0.5 - y)$ is specified at the inlet for $0.0 \leq y \leq 0.5$. This produces a maximum inflow velocity of $u_{max} = 1.5$ and a mean inflow velocity of $u_{avg} = 1.0$. The Reynolds number is based on the mean inflow velocity. At the outflow, boundary condition is implemented as described earlier in section 3. The domain, $\bar{\Omega} = [0, 30] \times [-0.5, 0.5]$, is discretized using 32 elements as shown in Fig. 9. To accurately resolve primary and secondary circulation zones, a non-uniform mesh is used. Interface nodes are shown with squares while interior nodes are shown with triangles. We use 11^{th} order nodal expansion in each element. There are $16,284$ degrees of freedom in the mesh. We condense out all interior degrees of freedom, resulting in $3,434$ interface degrees of freedom and a bandwidth of 260. In this case, the nodes are numbered in the y-direction first to reduce the bandwidth. One might think to use a very high order p-level to reduce interface degrees of freedom and bandwidth (which will also reduce memory storage) but in that case cost of elemental matrix inversion will be high to construct the Schur complement. Simulations are carried out for penalty parameter of 5 to 30. We use Re continuation method and start with Re=100 and march till Re=800 with an increment of 100.

Fig. 10(a), 10(b) and 10(c) contain plots of streamlines, pressure and dilatation contours for the penalty parameter of 20. Results match qualitatively very well with the published results of Pontaza and Reddy [5]. After reattachment of the upper wall eddy, the flow slowly recovers towards a fully developed Poiseuille flow. Flow is almost fully de-

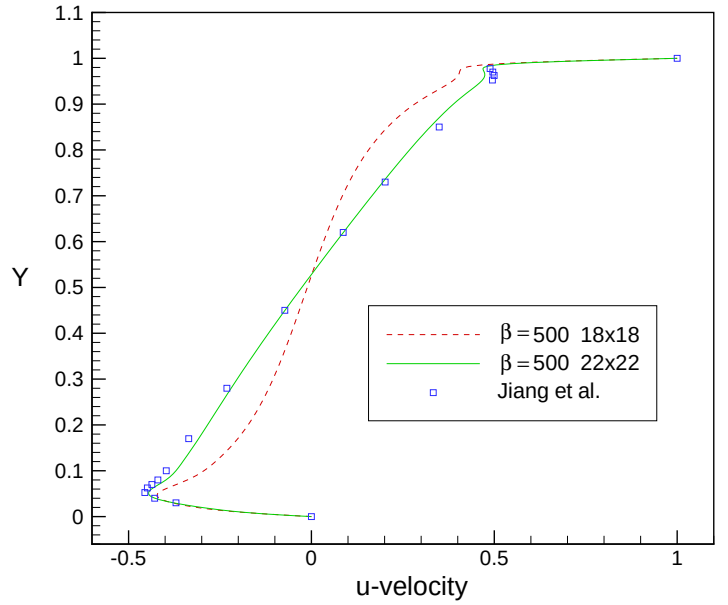

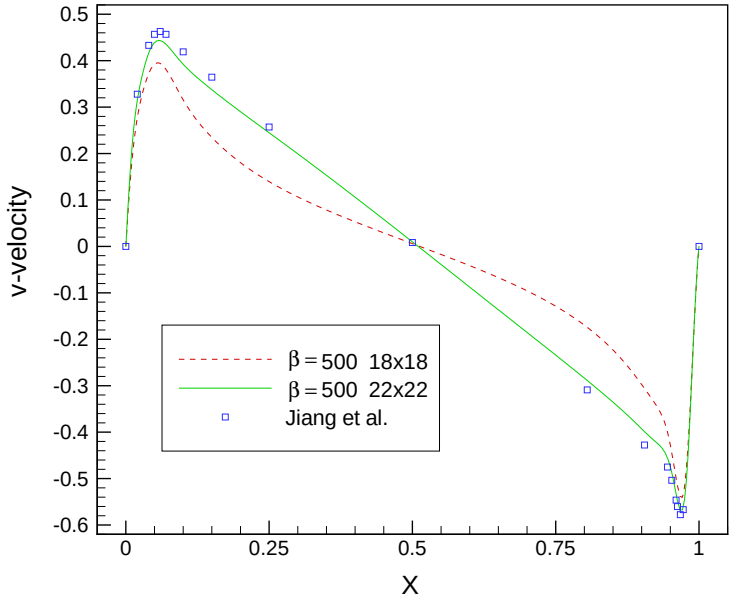

Fig. 8. (a) Variation of u-velocity with y for two different meshes (b) Variation of v-velocity with x for two different meshes

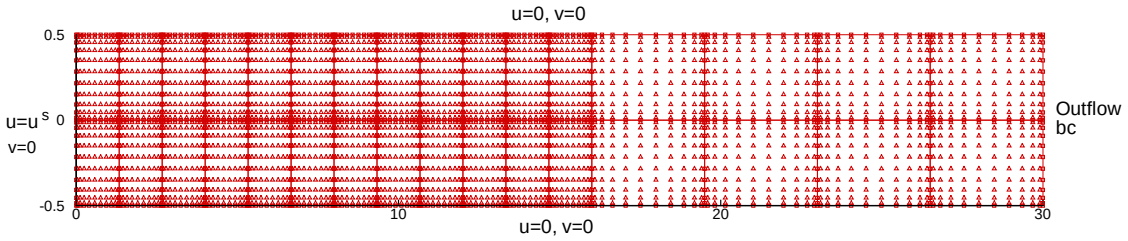

Fig. 9. Mesh and boundary conditions for flow over a backward facing step

veloped at the exit ($x = 30$) with no pressure gradient in the direction of flow. This is because outlet boundary condition of $p = 0$ also gives good results. The value of the L_2 least-squares functional remains below 3×10^{-2} and L_2-norm of the residual of continuity equation is below 1.1×10^{-5} for these computations. Fig. 10(c) shows dilatation contours, which are similar to the pressure contours. Dilatation has a high value in the reattachment zone where there are sharp gradients.

The u-velocity profiles along the channel height at $x = 7$ and $x = 15$ are compared with the benchmark results of Gartling [24] in Fig. 11for penalty parameter of 20. We find excellent agreement.

Pressure profiles along the length of the channel are plotted in Fig. 12 for penalty parameters of 5, 10, 20 and 30 and compared with the result of Pontaza and Reddy [5]. They give identically same results and match well with that of [5]. A comparison of primary reattachment length (S_1), secondary separation length (S_2), and secondary reattachment length (S_3) for various values of penalty parameter is presented in Table II. Accurate values of reattachment lengths are found by running stress based formulation where stresses are primary variables.

Next, PCG convergence history is plotted in Fig. 13. We present this formulation as an alternative to hp least-square formulation of Pontaza and Reddy [5, 12]. To compare PCG history, we run the simulation on 10×2 uniform grid and use 11th order polynomial

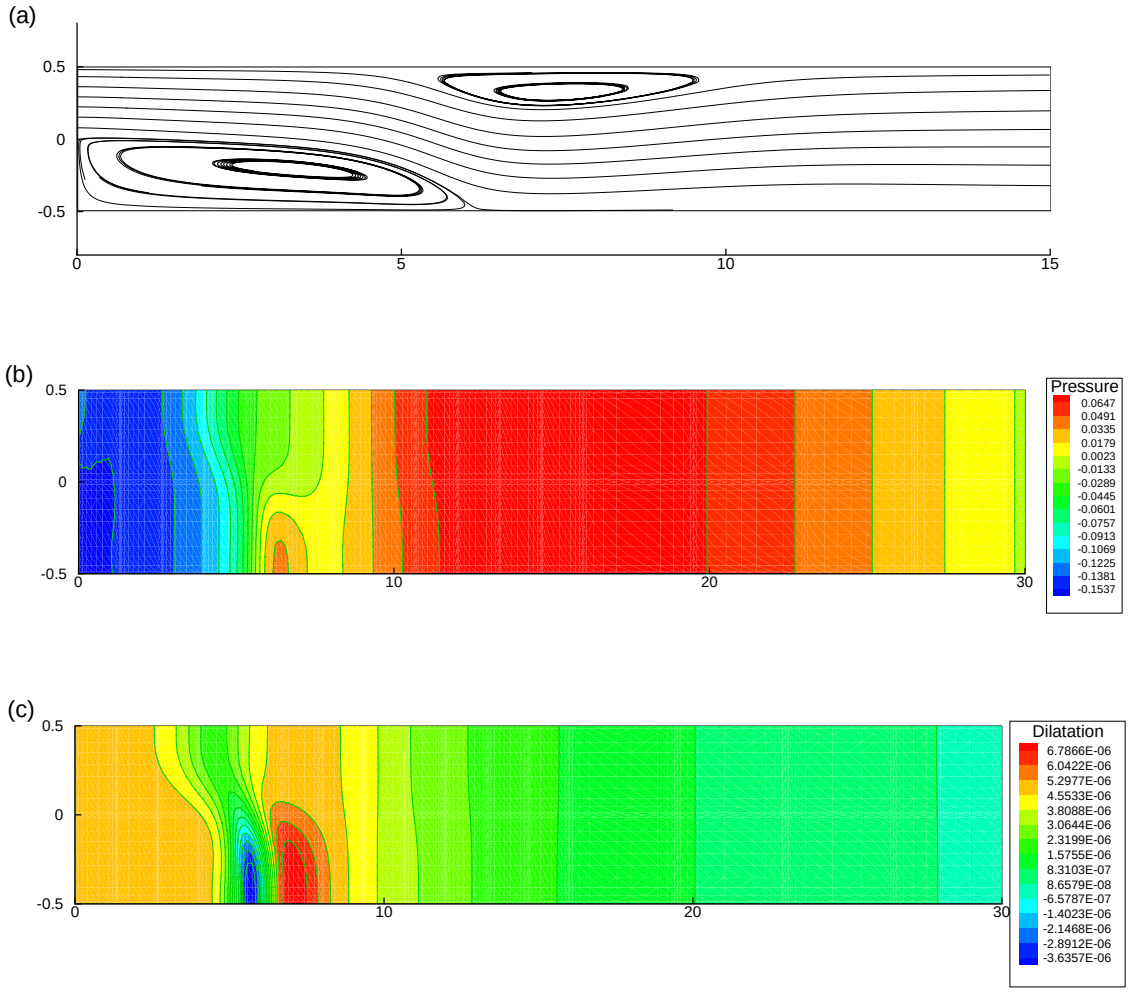

Fig. 10. Flow over a backward facing step at Re = 800 (a) Streamlines (b) Pressure contours (c) Dilatation contours

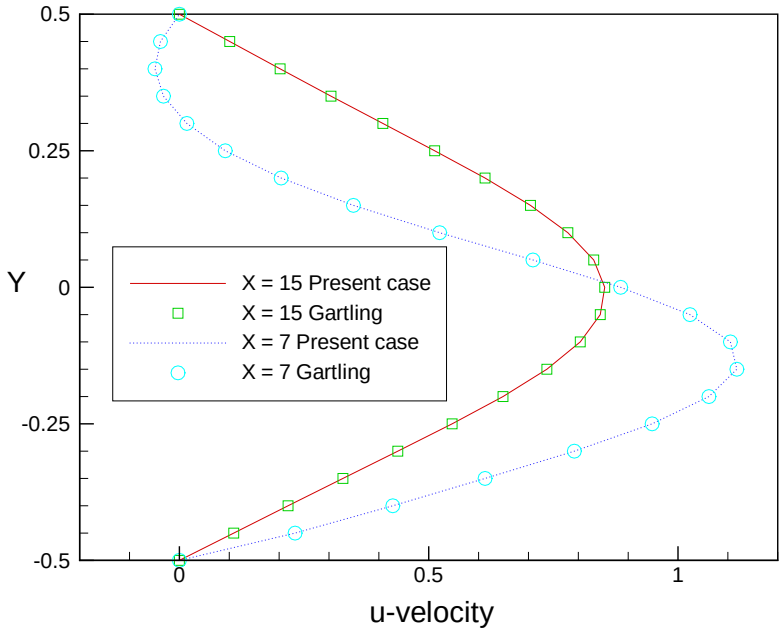

Fig. 11. Flow over a backward facing step at $Re = 800$: horizontal velocity profiles along the height of the channel

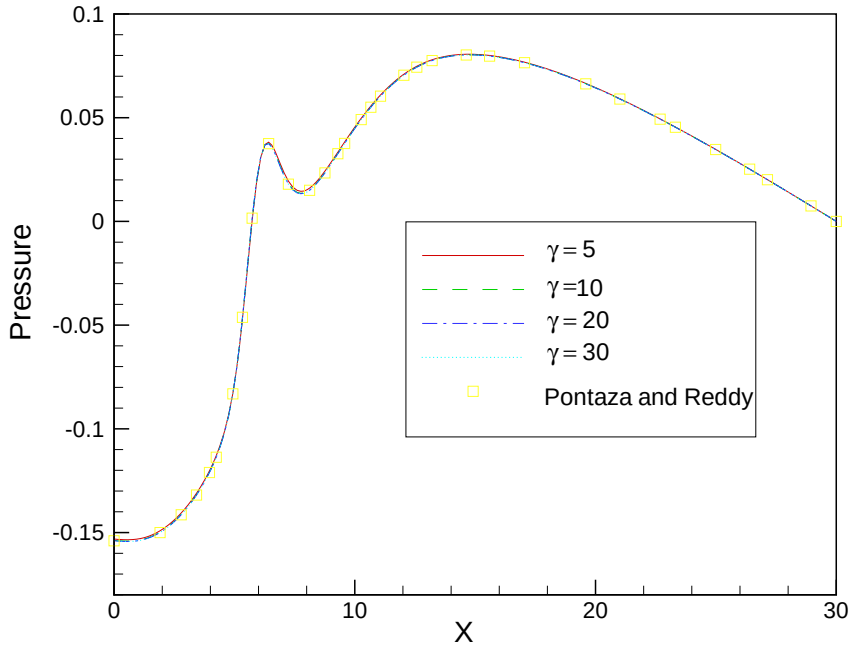

Fig. 12. Variation of lower wall pressure with horizontal position for different values of penalty parameter : Comparison with Pontaza et. al [1]

Table II. Separation and reattachment lengths for flow over a backward facing step Re = 800.

	$\gamma = 5$	$\gamma = 10$	$\gamma = 20$	$\gamma = 30$	Gartling [24]
S_1	6.17	6.11	6.10	6.10	6.10
S_2	4.93	4.87	4.86	4.85	4.85
S_3	10.43	10.47	10.48	10.48	10.48

expansion (same as used in [5]). They reported that for Re=800 with solution of Re=700 as initial guess, it takes 4 Newton's iterations to converge and it takes approximately 4500, 3500, 2500 and 700 PCG iterations to converge when the Jacobi preconditioner is used.

In our case for penalty parameter of 40, it takes six Newton's iterations to converge and it takes approximately 1850, 1600, 1850, 1850, 1800 and 1500 iterations to converge; PCG convergence is declared when L_2-norm of residual is below 10^{-6} in both the cases. The only difference is that Pontaza and Reddy did not use Schur complement method. Another small difference is that they used modal basis but modal basis has, in general, sightly better conditioning than the nodal basis. Both formulations have the same number of independent variables (4). Its clear from this plot that conditioning of coefficient matrix is almost the same as that produced by hp least-squares formulation of Pontaza and Reddy [5].

4. Flow past a circular cylinder at low Reynolds number

The third benchmark problem considered here is the steady two-dimensional flow of an incompressible fluid past a circular cylinder. The Reynolds number is taken to be 40, for which a steady-state solution exists. Domain of interest is $[-10.0, 15.0] \times [-10.0, 10.0]$. The x-component of inlet velocity (u) is specified to be 1.0 and the y-component (v) is set to zero. Symmetry boundary conditions, $\omega = 0$ and $v = 0$, are imposed on the top and

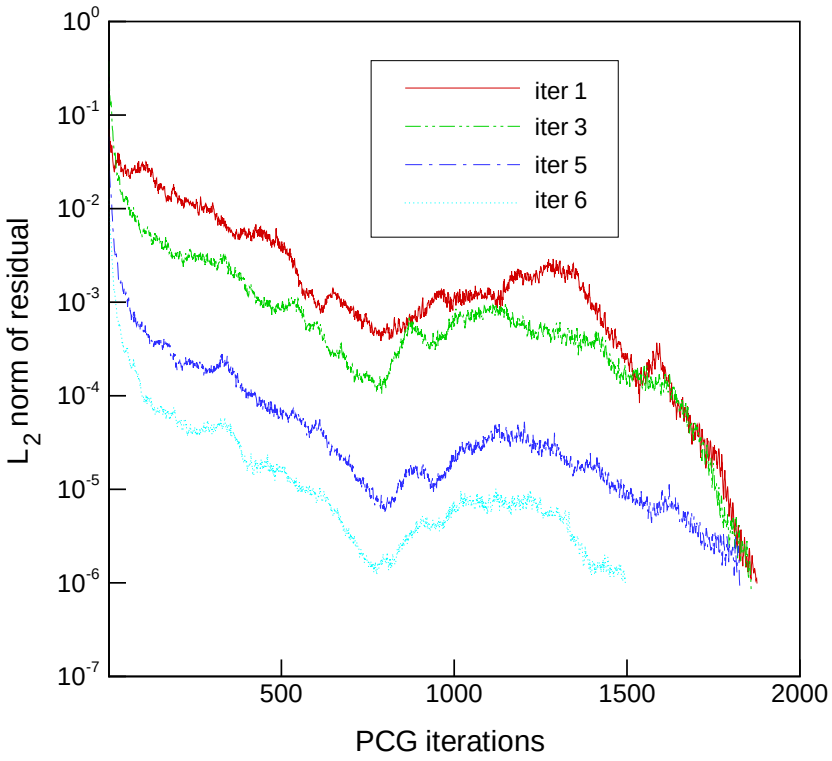

Fig. 13. Convergence history of preconditioned conjugate gradient solver (PCG) for flow over a backward facing step

bottom walls. The outflow boundary conditions are imposed in a weak sense through the least-squares functional.

Fig. 14 contains a close-up view of the geometric discretization around the circular cylinder. We generate orthogonal mesh using rectangular elements everywhere in the domain except around the cylinder. One layer of body fitting mesh is generated around the cylinder. At this point we will digress a bit and talk about reducing computational cost for high order finite element based formulations. For rectangular elements jacobian matrix is

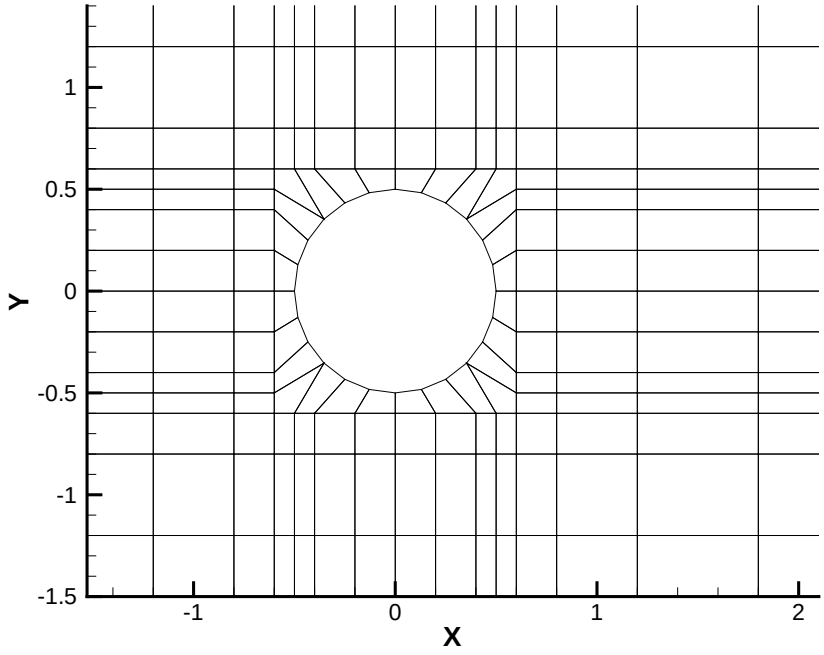

Fig. 14. Closeup view of the geometric discretization around the cylinder

of the form (see Reddy [27, 28])

$$J = \begin{pmatrix} \frac{h_1}{2} & 0 \\ 0 & \frac{h_2}{2} \end{pmatrix}$$

and global derivatives of shape functions are

$$\begin{pmatrix} \frac{\partial \psi_i^e}{\partial x} \\ \frac{\partial \psi_i^e}{\partial y} \end{pmatrix} = J^{-1} \begin{pmatrix} \frac{\partial \psi_i^e}{\partial \xi} \\ \frac{\partial \psi_i^e}{\partial \eta} \end{pmatrix} = \begin{pmatrix} \frac{2}{h_1} \frac{\partial \psi_i^e}{\partial \xi} \\ \frac{2}{h_2} \frac{\partial \psi_i^e}{\partial \eta} \end{pmatrix}$$

where $\frac{\partial \psi_i^e}{\partial \xi}$ and $\frac{\partial \psi_i^e}{\partial \eta}$ are local derivatives of shape functions. Therefore, calculation of global derivatives of the shape functions is straight forward. In the case of curved elements, we need to calculate jacobian matrix for each element and carry out matrix multiplications to obtain global derivatives of the shape functions, which is computationally costly (see Reddy [27]). Such grids reduce a lot of computational time. It is to be mentioned that even for moderate size problems we cannot store global derivatives of shape functions for all elements of the mesh. In order to accurately represent the curved boundary, we implement an isoparametric formulation; i.e., we use the same expansion order to interpolate dependent variables and the geometry.

We use two-dimensional incompressible Navier-Stokes equations in the dilatation-vorticity first-order form. There are 424 quadrilateral elements in the mesh. The 7th order nodal expansions are used in each element. Discrete model contains $84,644$ degrees of freedom. We condense out all interior degrees of freedom. There are $23,588$ interface degrees of freedom and bandwidth of the system is 1256.

Fig. 15(a) and 15(b) contain plots of streamlines and pressure contours and dilatation contours for Re $= 40$ and $\gamma = 20$. The value of the recirculation length is found to be 4.55 cylinder radii. Our result is in good agreement with the numerical value of 4.50 cylinder radii by Kawaguti and Jain [37], whereas Dennis and Chang [38] reported a recirculation

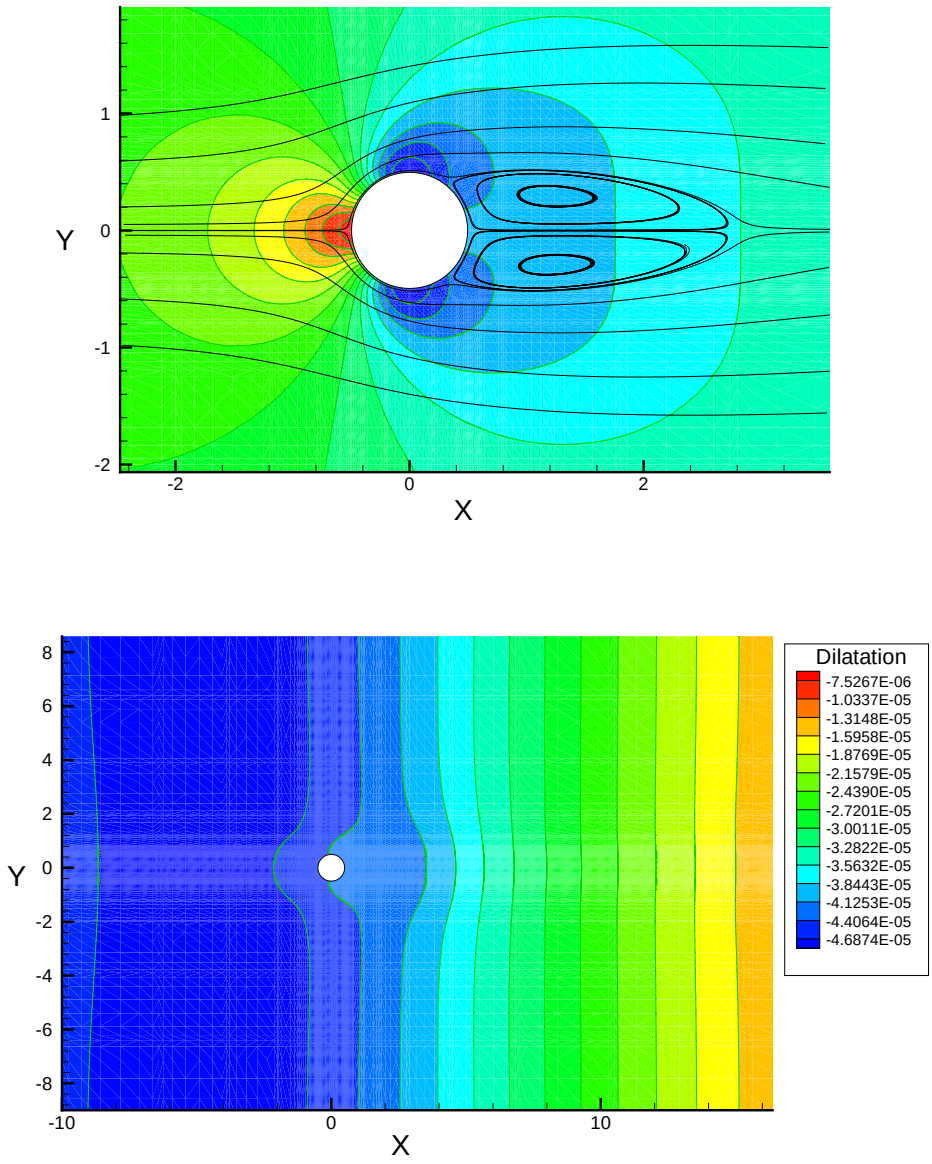

Fig. 15. Flow past a circular cylinder at Re = 40 (a) Streamlines and pressure contours (b) Dilatation contours

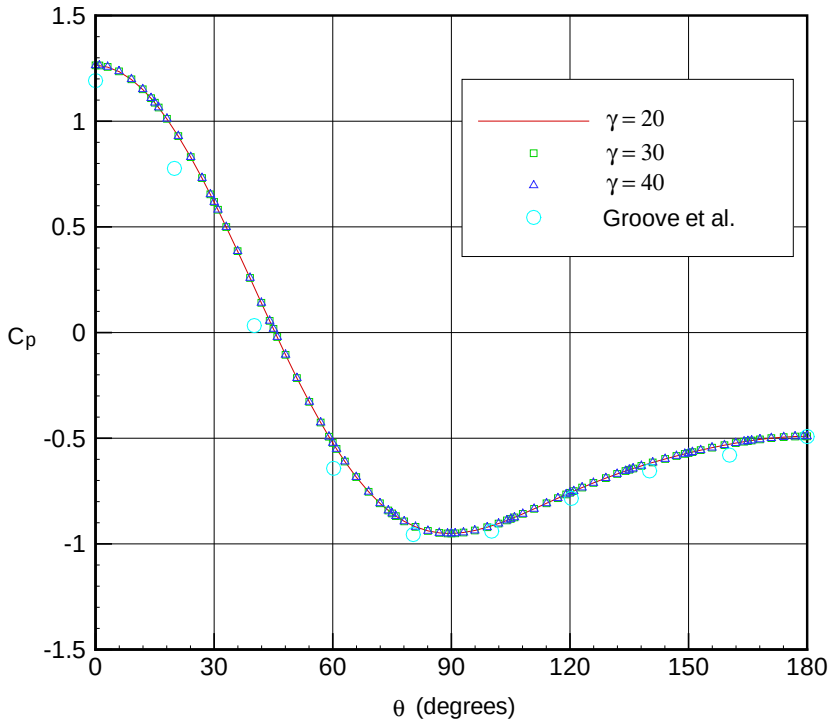

Fig. 16. Pressure coefficient distribution along the cylinder surface for various values of penalty parameter

length of 4.69 cylinder radii. The value of the L_2 least-squares functional remains below 1.3×10^{-2}.

A comparison of the experimental values of the surface pressure coefficient distribution along the cylinder surface with the computed values is shown in Fig. 16 for the penalty parameters of $20, 30,$ and 40. Experimental values are taken from Grove et al. [25]. Our results are in good agreement with the experimental measurements. Pressure coefficient distribution is almost same for the all the penalty parameters considered here. Drag coefficient is $C_D = 1.55$ which is in good agreement with the published results of Tritton [39], who reported it to be 1.56.

It has been seen earlier that nonlinear convergence is dependent on penalty parameter.

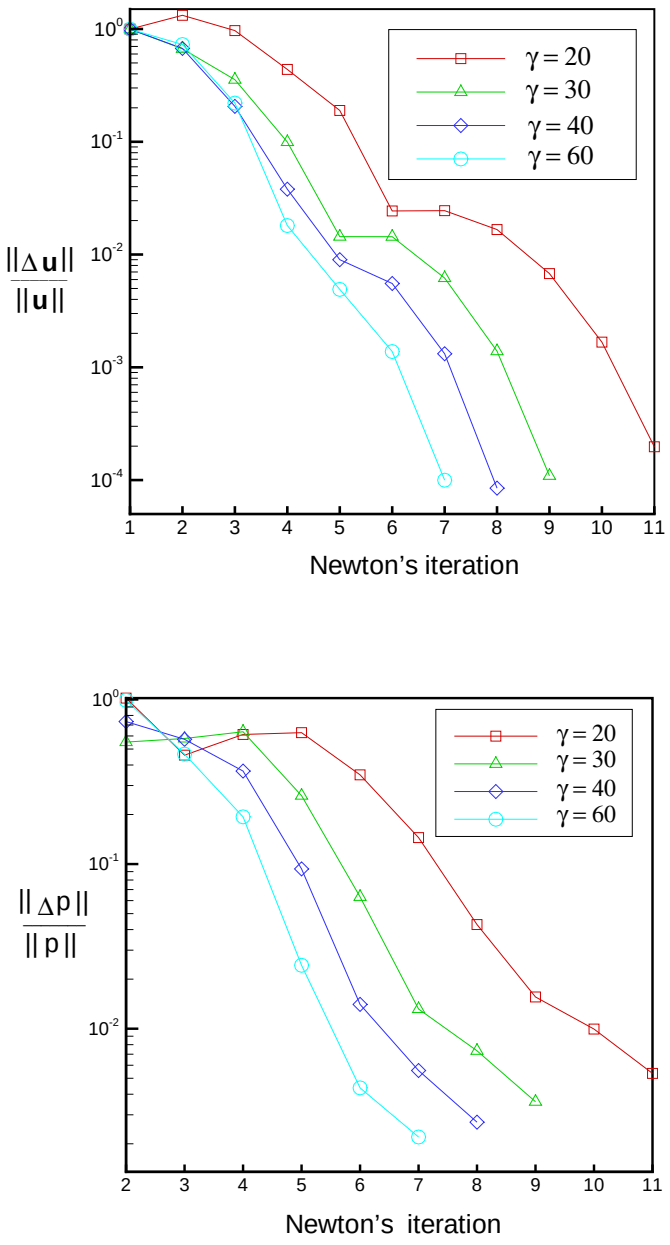

Fig. 17. (a) Nonlinear convergence for various values of penalty parameter (b) Pressure convergence for various values of penalty parameter

For very low value of penalty parameter (1-10) Newton's convergence is slow (this value is problem dependent). In Fig. 17(a) nonlinear convergence is plotted for various values of penalty parameter. As plot reveals that convergence is slow for $\gamma = 20$. In Fig. 17(b) we plot pressure convergence history. For all the problem solved in this chapter pressure convergence is almost the same as the nonlinear convergence but one needs to make sure that pressure also converges. For very low value of the penalty parameter, pressure convergence is slow, which in turn slows nonlinear convergence.

5. Flow past a large circular cylinder in a channel

We tested this formulation for various problems but they do not test mass conservation rigorously. To test mass conservation rigorously, we solve flow past a large circular cylinder in a channel with blockage ratio of 2 (H/D = 2). Chang and Nelson [8] used similar problem to test mass conservation for Stokes flow. Domain of interest is $[-5.0, 10.0] \times [-1.0, 1.0]$. Cylinder has unit diameter and it is centered at $(0.0, 0.0)$. We use similar grid as used earlier for flow past a circular cylinder. A p-level of 6 is used and there are $76,584$ degrees of freedom in the mesh. Mesh is fine near the cylinder. No-slip boundary conditions are imposed on side walls. At inlet $u = 1.0$ and $v = 0.0$. The outflow boundary conditions are imposed in a weak sense through the least-squares functional. Reynolds number considered here is 40 for which steady state solution exists.

Fig. 18(a) shows streamline plot. In this case separation delayed. u-velocity contours around the cylinder are shown in Fig. 18(b). We calculate mass flow rate at the inlet, outlet and section $x = 0$ and we find very good mass conservation as shown by Table III. We solved this problem using hp least-squares formulation [5] also (under same conditions) and calculated mass flow rates. Even for low values of penalty parameter, present formulation conserves mass better than hp least-squares formulation [5] does.

In Fig. 19 we plot dilatation contours for penalty parameter of 40. Mass conservation

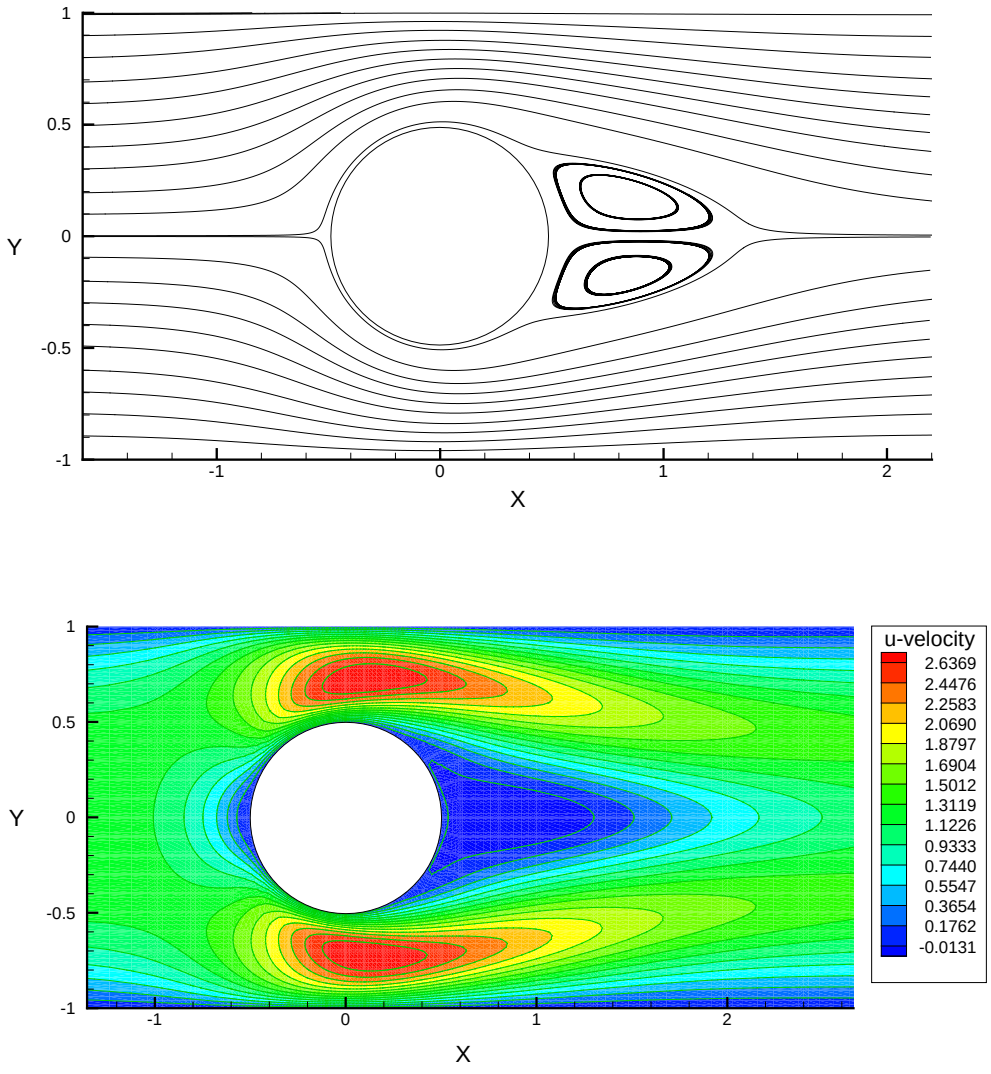

Fig. 18. Flow past a large circular cylinder in a channel (a) Streamlines (b) u-velocity contours

Table III. Mass flow rate for various values of penalty parameter.

	$\gamma = 40$	$\gamma = 70$	hp Least-squares
Inlet	2.000	2.000	2.000
x = 0	1.982	1.986	1.974
Outlet	1.987	1.991	1.975

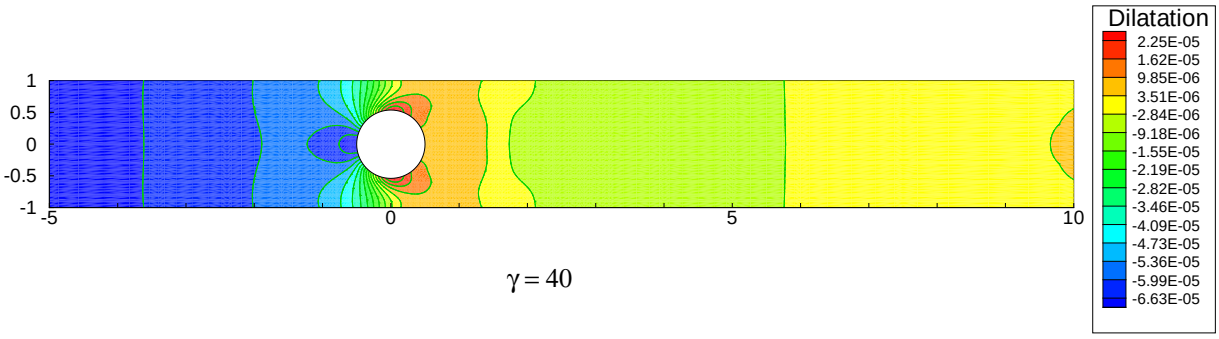

Fig. 19. Dilatation contours for flow past a large circular cylinder

is satisfied to a very good extent as shown by this plot. It requires a bit higher value of penalty parameter compared to the last example. Dilatation values are a bit high at the inlet. This might be because we use very coarse grid at the inlet. This example shows that even for very low value of the penalty parameter, mass conservation is satisfied to a very good extent in this formulation.

6. 3D Lid-driven cavity flow

Next, the three-dimensional lid-driven cavity problem is analyzed to further test our formulation. The flow is driven by the translation of the top boundary. Projection of the grid on the xy-plane is shown in Fig. 20. Grid is stacked in the z-direction. A non-uniform

mesh of $6 \times 6 \times 3$ cubic finite elements is used to discretize the domain. Reynolds number considered here is 100. We model only a half of the domain as flow is symmetric about the plane $z = 0.5$ for this Reynolds number [36, 40]. No slip boundary condition is imposed on all solid walls. On the symmetry plane, boundary conditions used are $\partial u/\partial z = 0$, $\partial v/\partial z = 0$ and $w = 0$ which are equivalent to $\sigma_{xz} = 0$, $\sigma_{yz} = 0$ and $w = 0$. On the top wall ($y = 1.0$) boundary conditions are $u = u^s(x, z)$, $v = w = 0$. To avoid singularity in the boundary condition, we specify a hyperbolic tangential u-velocity distribution on the top wall: $u^s = g(x)\, g(z)$, where

$$g(s) = \begin{cases} \tanh(\beta\, s) & 0 \leq s \leq 0.5 \\ -\tanh(\beta\,(s-1)) & 0.5 < s \leq 1.0 \end{cases}$$

with $\beta > 0$. In the present study we took $\beta = 50$, which gave a smooth but at the same time sharp transition from $u = 0.0$ to $u = 1.0$ near the walls of the driven surface. To recast the second order PDEs into first order PDEs, we introduce stress tensor as independent variable. We use a 5th order nodal expansion in each element and there are total of $138,384$ degrees of freedom in the mesh. This problem has been solved for the penalty parameter of 10 to 30. The value of the L_2 least-squares functional remains below 10^{-3} for these computations.

Fig. 21 contains plots of streamline and pressure contours at various planes. Results match qualitatively well with the published results of Jiang et al. [36], who used least-squares finite element formulation with an almost uniform $50 \times 52 \times 25$ mesh of tri-linear elements and one-point quadrature (which reduces the least-squares model to a collocation model). A penalty parameter of 20 is used. The u-velocity profiles along the vertical mid-line of the plane $z = 0.5$ are compared with those of Jiang et al. [36] in Fig. 22. Again, we see excellent agreement between the two results.

Next, we investigate accuracy of the present formulation with respect to the magnitude

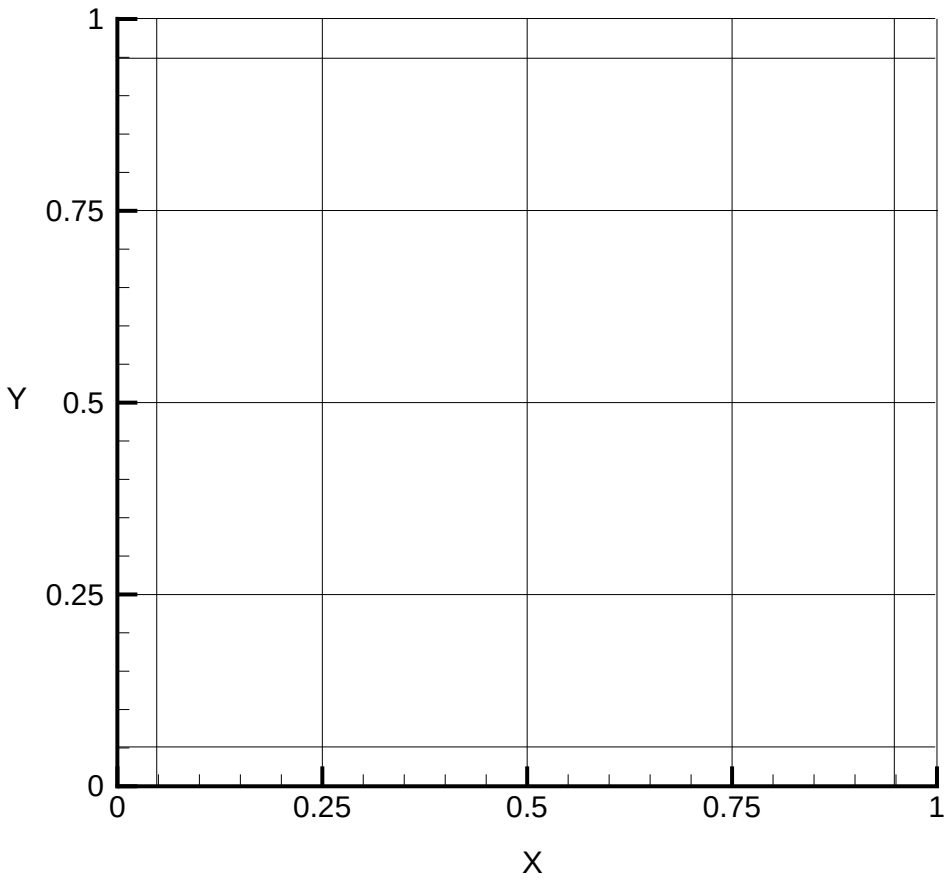

Fig. 20. The schematic of the grid on XY plane

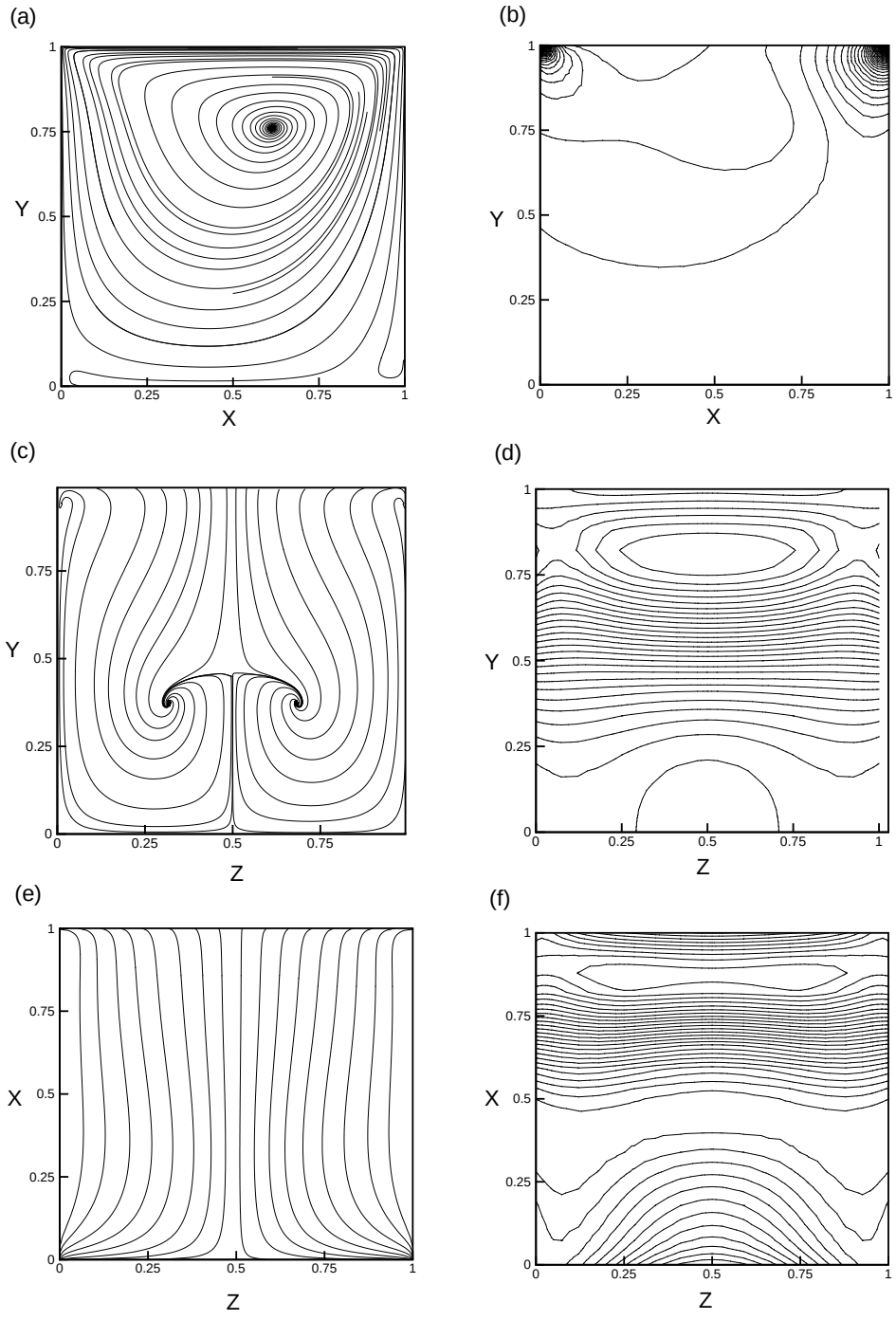

Fig. 21. Numerical results for 3D cavity flow at Re = 100. (a) Streamlines at z = 0.5 (b) pressure contours at z = 0.5 (c) streamlines at x = 0.5 (d) pressure at x = 0.5 (e) streamlines at y = 0.5 (f) pressure contours at y = 0.5

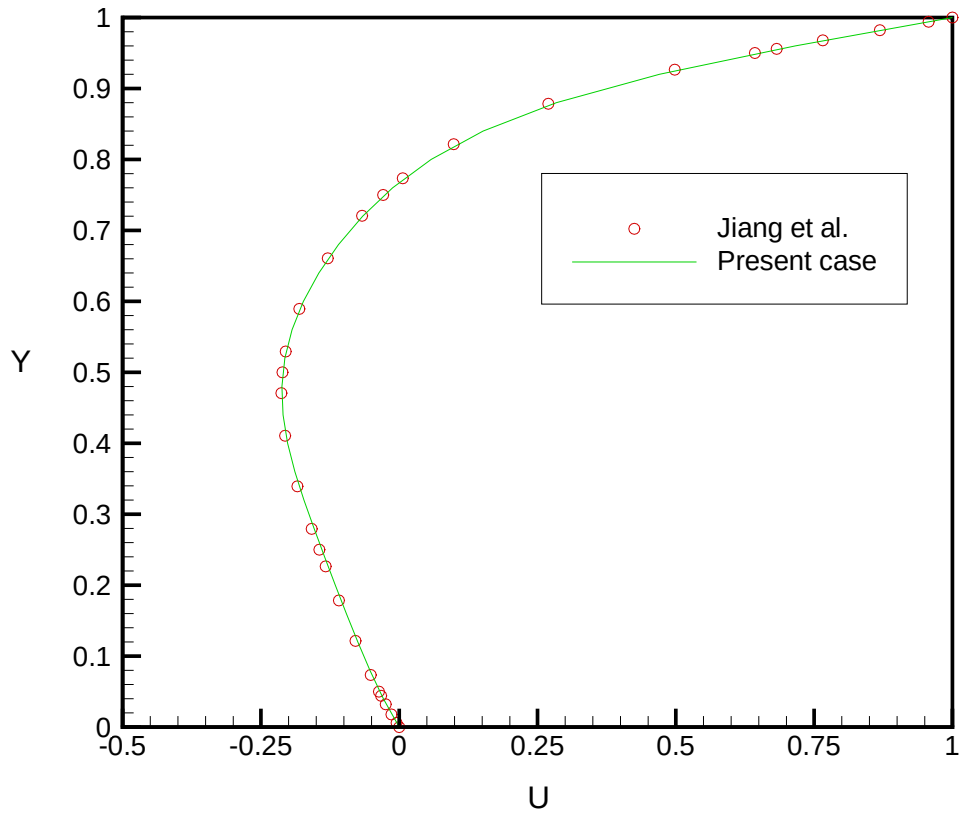

Fig. 22. Profiles of u-velocity along the vertical mid-line of the plane z = 0: Comparison with benchmark result

of the penalty parameter. For this purpose we solve the 3D lid-driven problem for the penalty parameter of 10 to 30. Fig. 23 contains a comparison of u-velocity profiles along the vertical mid-line of the plane $z = 0.5$ for these two penalty parameters. Maximum difference in u-velocities is less than 1 percent. We can conclude that for this problem penalty parameter of 10 gives sufficiently accurate results.

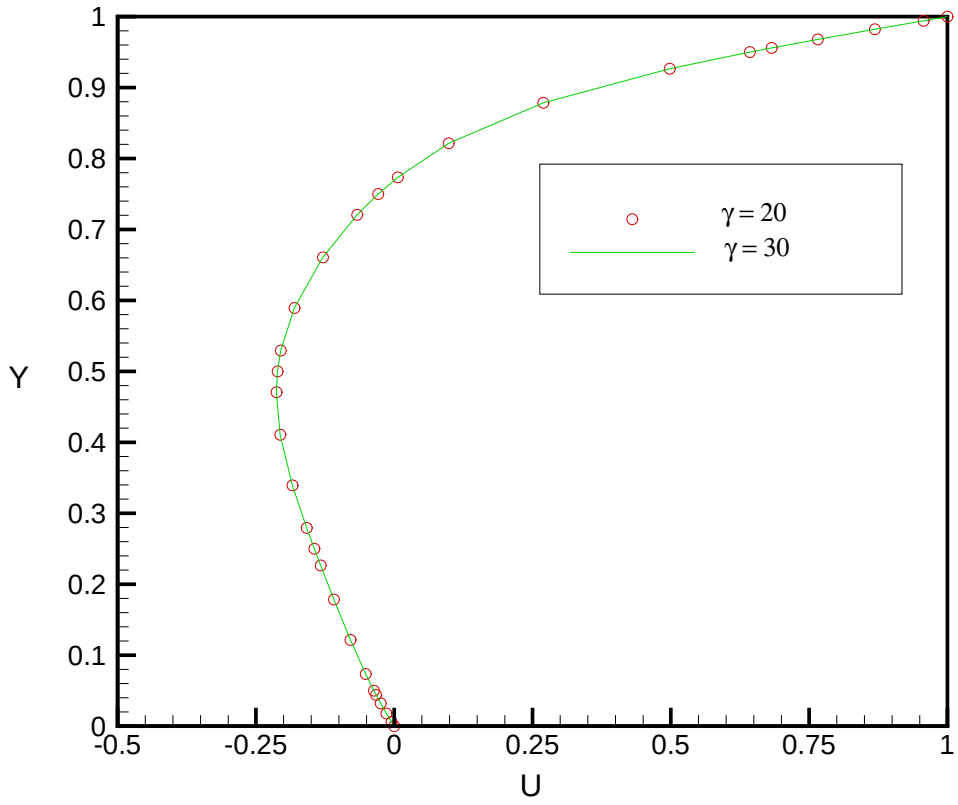

Fig. 23. Profiles of u-velocity along the vertical mid-line of the plane z = 0.5 for two different values of penalty parameters

D. Temperature-Velocity coupled problem

Here, we consider steady incompressible fluid flow in a domain $\Omega \subset \mathbb{R}^2$ bounded by $\Gamma = \Gamma_\theta \cup \Gamma_q$ where Γ_θ and Γ_q are the isothermal and the adiabatic boundaries as well as $\Gamma_\theta \cap \Gamma_q = \emptyset$. The fluid motion is induced by the temperature gradient across the vertical walls. The buoyancy effect is approximated by the Boussinesq assumption. The Navier-Stokes equations and the energy equation in dimensionless form are given below.

Find the velocity $\mathbf{u}(\mathbf{x})$, pressure $p(\mathbf{x})$ and temperature $\theta(\mathbf{x})$ such that

$$(\mathbf{u}\cdot\nabla)\,\mathbf{u} + \nabla p - \frac{1}{\mathrm{Re}}\nabla\cdot\left[(\nabla\mathbf{u}) + (\nabla\mathbf{u})^{\mathrm{T}}\right] + \theta\frac{\mathbf{g}}{|\mathbf{g}|} = \mathbf{0} \qquad \text{in } \Omega \tag{2.31}$$

$$\nabla\cdot\mathbf{u} = 0 \qquad \text{in } \Omega \tag{2.32}$$

$$(\mathbf{u}\cdot\nabla)\,\theta - \frac{1}{\mathrm{Pe}}\nabla^{\mathbf{2}}\theta = 0 \qquad \text{in } \Omega \tag{2.33}$$

$$\mathbf{u} = \mathbf{u}^s \qquad \text{on } \Gamma_u \tag{2.34}$$

$$\hat{\mathbf{n}}\cdot\boldsymbol{\sigma} = \mathbf{f}^s \qquad \text{on } \Gamma_f \tag{2.35}$$

$$\theta = \theta^s \qquad \text{on } \Gamma_\theta \tag{2.36}$$

$$\hat{\mathbf{n}}\cdot\mathbf{q} = q^s \qquad \text{on } \Gamma_q \tag{2.37}$$

where $\mathbf{g}$ is gravitational acceleration vector which is acting in negative y-direction. Here we take the cavity wall length and buoyant speed ($(|\mathbf{g}|\alpha\Delta\theta l)^{1/2}$) as characteristic length and velocity, respectively. The characteristic numbers are Re = $(\mathrm{Ra}/\mathrm{Pr})^{1/2}$, Pe $= (\mathrm{Ra}\ \mathrm{Pr})^{1/2}$, Ra $= \alpha|\mathbf{g}|l^3\Delta\theta/(\kappa\nu)$ and Pr $= \nu/\kappa$, where α is the volumetric thermal expansion coefficient, l is the characteristic length, $\Delta\theta$ is the characteristic temperature, κ is the thermal diffusivity, and $\nu = \mu/\rho$ is the kinematic viscosity.

1. The vorticity-dilatation/heat flux based first-order system

To make the system first-order, we introduce vorticity-dilatation and heat flux vector as independent variables. The resulting first-order system in dimensionless form can be stated as follows:

Find the velocity $\mathbf{u}(\mathbf{x})$, dilatation $D(\mathbf{x})$, vorticity $\boldsymbol{\omega}(\mathbf{x})$, temperature $\theta(\mathbf{x})$ and heat flux $\mathbf{q}(\mathbf{x})$ such that

$$(\mathbf{u}\cdot\nabla)\,\mathbf{u} - \gamma\nabla D + \frac{1}{\mathrm{Re}}\nabla\times\boldsymbol{\omega} + \theta\frac{\mathbf{g}}{|\mathbf{g}|} + \nabla p^{n-1} = \mathbf{0} \qquad \text{in } \Omega \tag{2.38}$$

$$\boldsymbol{\omega} - \nabla\times\mathbf{u} = \mathbf{0} \qquad \text{in } \Omega \tag{2.39}$$

$$D - \nabla\cdot\mathbf{u} = 0 \qquad \text{in } \Omega \tag{2.40}$$

$$(\mathbf{u}\cdot\nabla)\,\theta + \nabla\cdot\mathbf{q} = 0 \qquad \text{in } \Omega \tag{2.41}$$

$$\mathbf{q} + \frac{1}{\mathrm{Pe}}\nabla\theta = \mathbf{0} \qquad \text{in } \Omega \tag{2.42}$$

$$\mathbf{u} = \mathbf{u}^s \qquad \text{on } \Gamma_u \tag{2.43}$$

$$\boldsymbol{\omega} = \boldsymbol{\omega}^s \qquad \text{on } \Gamma_\omega \tag{2.44}$$

$$\theta = \theta^s \qquad \text{on } \Gamma_\theta \tag{2.45}$$

$$\hat{\mathbf{n}}\cdot\mathbf{q} = q^s \qquad \text{on } \Gamma_q \tag{2.46}$$

The L_2 least-squares formulation and finite element model development proceed in a similar manner as described for the incompressible Navier-Stokes equations.

2. Numerical example: Buoyancy-driven flow inside a square enclosure

As a numerical example, we consider two-dimensional, steady, buoyancy-driven flow in a square enclosure with differentially heated vertical walls. The square enclosure is taken

to be the unit square, $\bar{\Omega} = [0,1] \times [0,1]$. A finite element mesh of 10×10 nonuniform quadrilateral finite elements is used to discretize the domain with the corner element having dimension 0.02×0.02. No slip velocity boundary condition is imposed on all solid walls. q_y is 0 at the top and bottom walls while left side wall is kept at $\theta = 1$ and right side wall at $\theta = 0$.

Computations have been performed for Rayleigh numbers of 10^4, 10^5, 10^6. Air is taken as the working fluid with Prandtl number 0.71; 7th order nodal expansion is used. There are seven degrees of freedom at each node. There are total $35,287$ degrees of freedom in the mesh. We condense out all interior degrees of freedom. There are $10,087$ interface degrees of freedom and bandwidth of the system is 1015. The discrete model is linearized using Newton's method and algebraic equations are solved using the banded Cholesky factorization. Computations have been performed for penalty parameters of 10, 20, and 30.

The Nusselt number on the vertical boundary at x = 0 is calculated as

$$Nu(y) = q_x(y)\,\text{Pe}$$

and the average Nusselt number (at x = 0) is calculated as

$$\overline{Nu} = \int_0^1 Nu(y)dy$$

Components of heat flux are taken to be the primary variables. Therefore, in spite of using C^0 continuous basis functions, we obtain smooth solution for heat fluxes. The average Nusselt number on the boundary is calculated using numerical integration using 8-point Gauss quadrature. We use Ra continuation method, start with Ra = 10^5 and proceed till 10^6 with Ra increment of 10^5. Zero initial guess is used for Ra = 10^5. It takes 10 Newton's iterations to converge for Ra = 10^5. Subsequent Rayleigh numbers take 2-3 Newton's

iterations to converge. The value of the L_2 least-squares functional remains below 1×10^{-4} for all Rayleigh numbers.

Fig. 24 contains plots of streamlines of the flow field and temperature distribution for Rayleigh numbers of 10^5 and 10^6. The patterns exhibit the required centrosymmetry and are in qualitative agreement with previously reported numerical results of Davis [26]. Fig. 24(e) shows vorticity contours which match well qualitatively with that of [26]. In Fig. 24(f) dilatation contours are plotted. Mass conservation is satisfied to very good extent. Maximum dilatation value is of the order 10^{-6}. Fig. 25(a) contains the plot of u-velocity profile along the vertical mid-line for penalty parameters of 10, 20 and 30. All three penalty parameters give identical values. Fig. 25(b) contains plots of temperature distributions along the vertical mid-line for three penalty parameters. Although the penalty parameter does not appear directly in the energy equation, there will be an effect of it on the temperature field since the temperature field depends on the velocity field for both coupled and decoupled formulations. Again all three penalty parameters give identical values. The average Nusselt number on the vertical boundary of the cavity at x = 0 for three Rayliegh numbers are compared with the benchmark result of Davis [26] in Table IV.

Table IV. Average Nusselt number at $x = 0$ for various values of penalty parameter and Rayleigh number.

	$\gamma = 5$	$\gamma = 10$	$\gamma = 20$	Davis [26]
Ra $= 10^4$	2.244	2.244	2.244	2.238
Ra $= 10^5$	4.521	4.522	4.522	4.509
Ra $= 10^6$	8.824	8.824	8.825	8.817

In Fig. 26 we plot PCG convergence history for Ra = 10^4. Zero initial guess is used. It takes six Newton's iterations to converge. Penalty parameter is 10. Again PCG converges

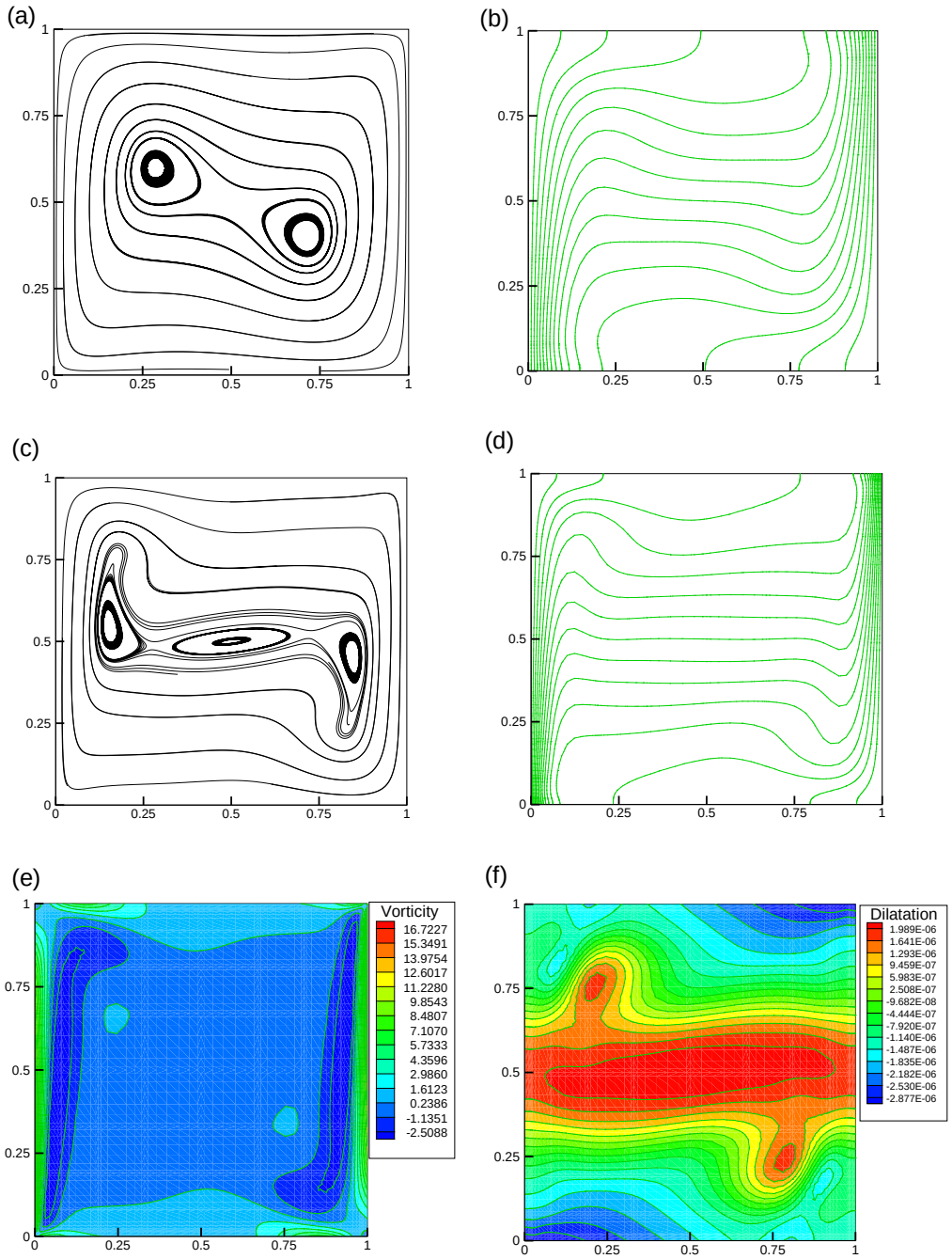

Fig. 24. Numerical results for 2D thermal cavity flow. (a) Streamlines at $Ra = 10^5$ (b) temperature contours for $Ra = 10^6$, (c) streamlines for $Ra = 10^6$ (d) temperature contours for $Ra = 10^6$, (e) vorticity contours for $Ra = 10^6$ (f) dilatation contours for $Ra = 10^6$

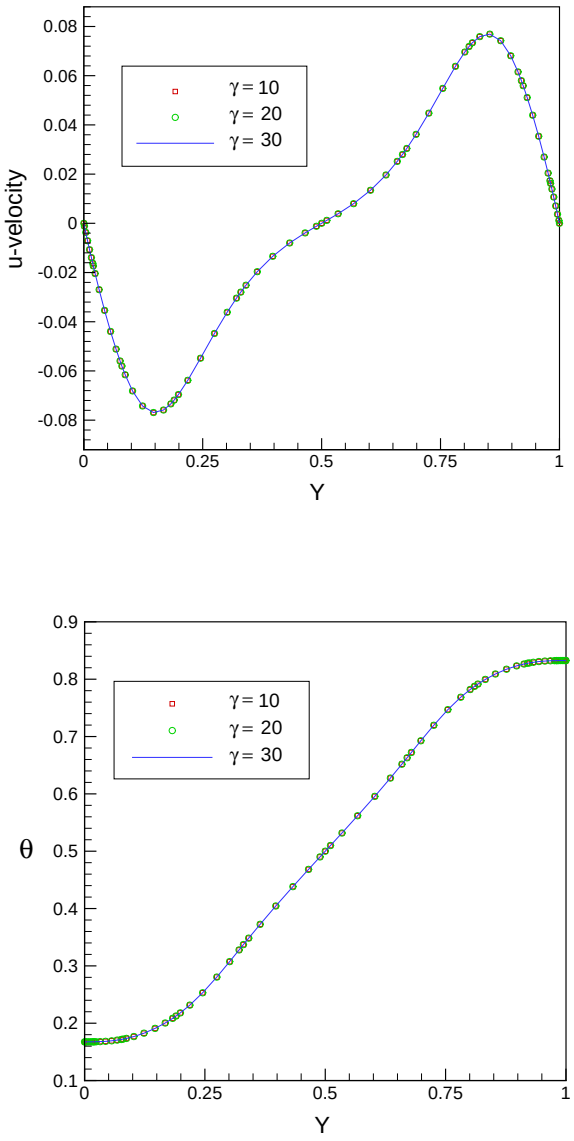

Fig. 25. (a) u-velocity (b)temperature along the vertical midline of the enclosure $Ra = 10^6$

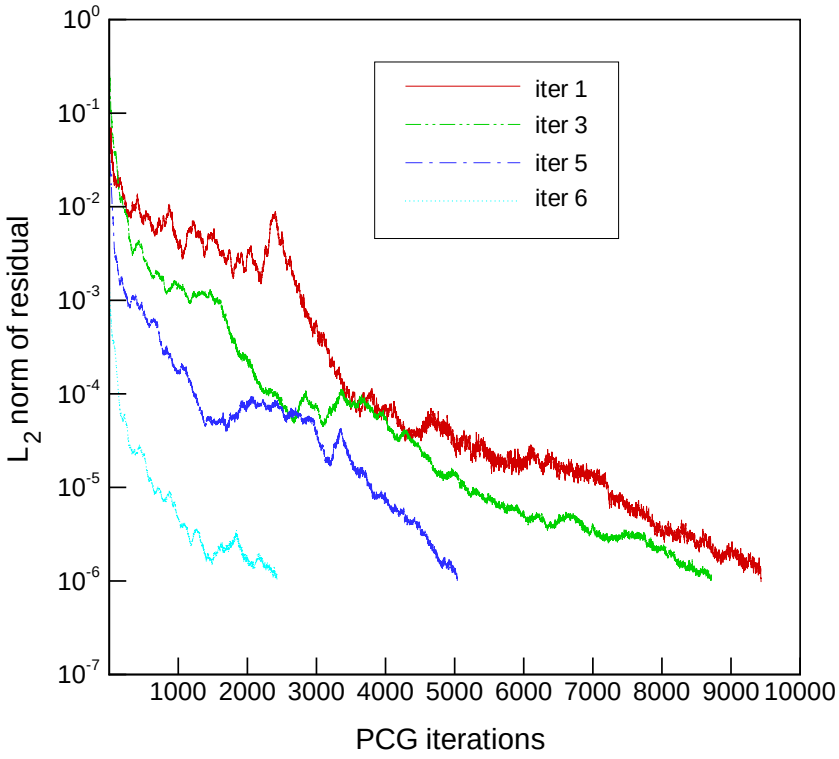

Fig. 26. Convergence history of preconditioned conjugate gradient solver (PCG) for thermal cavity problem

steadily without much fluctuations.

CHAPTER III

SPECTRAL/HP PENALTY LEAST-SQUARES FINITE ELEMENT FORMULATION FOR UNSTEADY INCOMPRESSIBLE FLOWS

A. Introduction

In the past few years, finite element models based on least-squares functionals have drawn considerable attention ([1]-[7]). Given a set of partial differential equations, the least-squares method allows us to define an unconstrained minimization problem. These formulations have several advantages over the traditionally used weak form Galerkin formulations. Most notably, the least-squares formulations circumvent the inf-sup condition of Ladyzhenskaya-Babuska-Brezzi (LBB). So the choice of approximating space is not subject to LBB conditions. Also, the resulting algebraic system is symmetric and positive-definite.

Previous study of Pontaza and Reddy [12] showed that in these formulations, temporal evolution of pressure field ill-behaves, which in turn leads to spurious solutions in many cases. Unsteady problems, especially with inflow/outflow boundaries, produce spurious pressure evolution with time, mainly due to the lack of strong pressure velocity coupling. In these formulations, the divergence-free constraint on the velocity field is enforced directly through the least-squares functional and pressure does not play a role in enforcing divergence free constraint.

Recently, Prabhakar and Reddy [6] presented a spectral/hp penalty least-squares finite element formulation for steady incompressible Navier-Stokes equations. For steady-state flows, pressure evolution does not pose any problem. In the present study, we extend this formulation to unsteady problems. For time integration, space-time decoupled formulations are popular, where discretization in space and time are carried out separately.

In space-time decoupled formulations, least-squares variational principles are applied in space only. Pontaza and Reddy [12] and Surana et al. [31] implemented space-time coupled least-squares formulations. These formulations have higher accuracy than decoupled formulations but associated computational costs are very high. A two-dimensional problem becomes a three-dimensional problem, with time as the additional dimension. In this study, we implement space-time decoupled time integration schemes, namely Crank-Nicholson scheme and backward multi-step scheme (BDF2).

In another study Prabhakar et al. [41] extended this idea for unsteady problems and implemented it using low order basis functions (bilinear) with one-point Gauss quadrature, which is equivalent to the collocation approach. The p-version of the finite element method is known to possess superior convergence characteristics compared with the h-version. Nevertheless, most of the current finite element research has involved the use of low-order approximations, mainly because of low computational cost associated with the h-version. If high accuracy is required, then we may justify using high-order methods by the fact that the error will converge at a faster rate than the operation count increases. Therefore , it will ultimately be more efficient to use high-order methods. Nevertheless, the cross-over point between the required accuracy and relative computational cost of low and high order methods for a given application is a point of much debate.

Several studies have been reported on penalty models implemented in the context of weak form Galerkin formulation. They achieved some popularity mainly because they circumvent LBB stability condition. Also there is a reduction in number of independent variables. Almost all these studies use low order basis functions and reduced order integration for penalty terms to circumvent locking. Also, the penalty parameter used is of the order 10^8 to 10^{12}. For such penalty parameter, the coefficient matrix is ill-conditioned and iterative solvers do not perform well. In this study, high-order element expansions are used to construct the discrete model, which does not experience locking. Equal-order integration

is used for all the terms of the coefficient matrix.

The present chapter is organized as follows. In Section B, the penalty least-squares finite element model for the incompressible Navier-Stokes equations is presented. Numerical results are presented in Section C. First, the second-order accuracy of the time integration scheme is established using method of manufactured solution. Next, we present results for 2D impulsively started lid-driven cavity at Reynolds number of 5,000. Lastly, numerical results are presented for the transient two-dimensional flow over a backward-facing step. Simulations for various penalty parameters are carried out and evolution of velocity and pressure fields with time are reported.

B. The incompressible Navier-Stokes equations

The unsteady incompressible Navier-Stokes equations in dimensionless form can be written as follows:

$$\frac{\partial \mathbf{u}}{\partial t} + (\mathbf{u} \cdot \nabla)\,\mathbf{u} + \nabla p - \frac{1}{\mathrm{Re}}\,\nabla \cdot \left[(\nabla \mathbf{u}) + (\nabla \mathbf{u})^{\mathrm{T}}\right] = \mathbf{f} \qquad \text{in } \Omega \times (0, \tau] \tag{3.1}$$

$$\nabla \cdot \mathbf{u} = 0 \qquad \text{in } \Omega \times (0, \tau] \tag{3.2}$$

$$\mathbf{u} = \mathbf{u}_0(\mathbf{x}) \qquad \text{on } \Omega \tag{3.3}$$

$$\mathbf{u} = \mathbf{u}^s \qquad \text{on } \Gamma_u \times (0, \tau] \tag{3.4}$$

$$\hat{\mathbf{n}} \cdot \underline{\boldsymbol{\sigma}} = \mathbf{f}^s \qquad \text{on } \Gamma_f \times (0, \tau] \tag{3.5}$$

where $\mathbf{u}\,(\mathbf{x})$ is the velocity vector, $\underline{\boldsymbol{\sigma}} = -p\,\underline{\mathbf{I}} + 1/\mathrm{Re}\,\left[(\nabla \mathbf{u}) + (\nabla \mathbf{u})^{\mathrm{T}}\right]$ is the total stress, $p\,(\mathbf{x})$ is the pressure, $\mathbf{f}$ is a dimensionless force, $\hat{\mathbf{n}}$ is the outward unit normal on the boundary of Ω, $\mathbf{u}^s$ is the prescribed velocity on the boundary Γ_u, and $\mathbf{f}^s$ are the prescribed tractions on the boundary Γ_f, $\Gamma = \Gamma_u \cup \Gamma_f$ and $\Gamma_u \cap \Gamma_f = \emptyset$, and Re denotes the Reynolds

number.

In the penalty method, the continuity equation is treated as a constraint, which is included back into the formulation in a least-squares sense. This amounts to replacing pressure in the Navier-Stokes equations with the following expression (see [27], [28], and [29] for additional details):

$$p = -\gamma(\nabla \cdot \mathbf{u}) \tag{3.6}$$

Gunzberger [13] proposed an iterative penalty method in which the pressure is updated using the formula

$$p^n = p^{n-1} - \gamma(\nabla \cdot \mathbf{u}) \tag{3.7}$$

where n is the iteration number during the solution of nonlinear equations. An advantage of this method is that the value of the penalty parameter needed to enforce the continuity constraint is equal to the square-root of the one needed in the non-iterative penalty method [13]. This, in turn, results in a coefficient matrix with smaller conditioning number. In this study, we use the iterative penalty method.

The problem at hand can now be stated as one of finding the velocity $\mathbf{u}(\mathbf{x})$ such that

$$\frac{\partial \mathbf{u}}{\partial t} + (\mathbf{u}\cdot\nabla)\,\mathbf{u} - \gamma\nabla(\nabla\cdot\mathbf{u}) - \frac{1}{\mathrm{Re}}\,\nabla\cdot\left[(\nabla\mathbf{u}) + (\nabla\mathbf{u})^{\mathrm{T}}\right] = \mathbf{f} - \nabla p^{n-1} \qquad \text{in } \Omega\times(0,\tau] \tag{3.8}$$

$$\mathbf{u} = \mathbf{u}_0(\mathbf{x}) \qquad \text{in } \Omega \tag{3.9}$$

$$\mathbf{u} = \mathbf{u}^s \qquad \text{on } \Gamma_u\times(0,\tau] \tag{3.10}$$

$$\hat{\mathbf{n}}\cdot\underline{\boldsymbol{\sigma}} = \mathbf{f}^s \qquad \text{on } \Gamma_f\times(0,\tau] \tag{3.11}$$

Since the solution at iteration $(n-1)$ is known, ∇p^{n-1} is known and, therefore, transferred to the right-hand side of the equation.

1. The velocity-dilatation-vorticity first-order system

In the interest of reducing the order of the equations to avoid C^k-approximation ($k \geq 1$) of the filed variables, we cast the second-order system (3.8)-(3.11) as a set of first-order equations by introducing the vorticity vector, $\boldsymbol{\omega} = \nabla\times\mathbf{u}$, and dilatation, $D = \nabla\cdot\mathbf{u}$, as independent dependent variables. Then the problem can be stated as one of finding the

velocity vector $\mathbf{u}(\mathbf{x})$, dilatation $D(\mathbf{x})$, and vorticity $\boldsymbol{\omega}(\mathbf{x})$ such that

$$\frac{\partial \mathbf{u}}{\partial t} + (\mathbf{u} \cdot \nabla)\,\mathbf{u} - \gamma \nabla D + \frac{1}{\mathrm{Re}} \nabla \times \boldsymbol{\omega} = \mathbf{f} - \nabla p^{n-1} \qquad \text{in } \Omega \times (0, \tau] \tag{3.12}$$

$$\boldsymbol{\omega} - \nabla \times \mathbf{u} = \mathbf{0} \qquad \text{in } \Omega \times (0, \tau] \tag{3.13}$$

$$D - \nabla \cdot \mathbf{u} = 0 \qquad \text{in } \Omega \times (0, \tau] \tag{3.14}$$

$$\mathbf{u} = \mathbf{u}_0(\mathbf{x}) \qquad \text{on } \Gamma_u \tag{3.15}$$

$$\mathbf{u} = \mathbf{u}^s \qquad \text{on } \Gamma_u \times (0, \tau] \tag{3.16}$$

$$\boldsymbol{\omega} = \boldsymbol{\omega}^s \qquad \text{on } \Gamma_\omega \times (0, \tau] \tag{3.17}$$

Typically, $\Gamma_u \cap \Gamma_\omega = \emptyset$, i.e., if velocity is specified at a boundary, vorticity need not be specified there.

a. L_2 least-squares formulation

The least-squares functional of the problem can be set up by summing up the squares of the residuals of the new set of equations. For time integration, space-time decoupled formulations are used. In space-time decoupled formulations, discretizations in space and time are introduced independently. Generally, the temporal operators are represented by truncated Taylor series expansions in time domain. We use Crank-Nicholson or backward multi-step scheme (BDF2). Least-square functional for backward multi-step schemes can be written as

$$\mathcal{J}\left(\mathbf{u}, D, \boldsymbol{\omega}; \mathbf{f}\right) = \frac{1}{2}\Big(\Big\| \frac{\gamma_0}{\Delta t}\mathbf{u}^{s+1} - \sum_{q=0}^{M_\alpha} \frac{\beta_q}{\Delta t}\mathbf{u}^{s-q} + \left(\mathbf{u}\cdot\nabla\right)\mathbf{u} - \gamma\nabla D + \frac{1}{\mathrm{Re}}\nabla\times\boldsymbol{\omega}$$

$$- \mathbf{f} + \nabla p^{n-1} \Big\|^2_{0,\Omega\times(0,\tau]} + \Big\| \boldsymbol{\omega} - \nabla\times\mathbf{u}\Big\|^2_{0,\Omega\times(0,\tau]}$$

$$+ \Big\| D - \nabla\cdot\mathbf{u}\Big\|^2_{0,\Omega\times(0,\tau]}\Big) \tag{3.18}$$

where $\gamma_0 = \sum_{q=0}^{M_\alpha}\beta_q$ for consistency, β_q are weights associated with a particular multi-step scheme, and $\Delta t = t_{s+1} - t_s$ is the time increment.

Considering the homogeneous, pure velocity, boundary condition case, the least-squares principle for functional (3.18) can be stated as follows:
find $(\mathbf{u}, D, \boldsymbol{\omega}) \in \mathbf{X}$, $\mathbf{u}(\mathbf{x}, 0)$=$\mathbf{u}_0(\mathbf{x})$ such that

$$\mathcal{J}\left(\mathbf{u}, D, \boldsymbol{\omega}; \mathbf{f}\right) \leq \mathcal{J}\left(\tilde{\mathbf{u}}, \tilde{D}, \tilde{\boldsymbol{\omega}}; \mathbf{f}\right) \qquad \forall\ \left(\tilde{\mathbf{u}}, \tilde{D}, \tilde{\boldsymbol{\omega}}\right) \in \mathbf{X} \tag{3.19}$$

where we use the space

$$\mathbf{X} = \Big\{ \left(\mathbf{u}, D, \boldsymbol{\omega}\right) \in \mathbf{H}^1_0\left(\Omega\right) \times H^1\left(\Omega\right) \times \mathbf{H}^1\left(\Omega\right) \Big\}$$

The variational problem (after linearization using Newton's method) corresponding to the least-squares principle is given by: find $(\mathbf{u}, D, \boldsymbol{\omega}) \in \mathbf{X}$, $\mathbf{u}(\mathbf{x}, 0)$=$\mathbf{u}_0(\mathbf{x})$ such that

$$\mathcal{B}\left(\left(\mathbf{u}, D, \boldsymbol{\omega}\right), \left(\tilde{\mathbf{u}}, \tilde{D}, \tilde{\boldsymbol{\omega}}\right)\right) = \mathcal{F}\left(\left(\tilde{\mathbf{u}}, \tilde{D}, \tilde{\boldsymbol{\omega}}\right)\right) \qquad \forall\ \left(\tilde{\mathbf{u}}, \tilde{D}, \tilde{\boldsymbol{\omega}}\right) \in \mathbf{X} \tag{3.20}$$

Let $\mathbf{X}_h$ denote a finite-dimensional subspace of $\mathbf{X}$. Then the least-squares discretized model of the Navier-Stokes equations is defined by the following discrete variational problem: find $\left(\mathbf{u}^h, D^h, \boldsymbol{\omega}^h\right) \in \mathbf{X}_h$, $\mathbf{u}(\mathbf{x}, 0)$=$\mathbf{u}_0(\mathbf{x})$ such that

$$\mathcal{B}\left(\left(\mathbf{u}^h, D^h, \boldsymbol{\omega}^h\right), \left(\tilde{\mathbf{u}}^h, \tilde{D}^h, \tilde{\boldsymbol{\omega}}^h\right)\right) = \mathcal{F}\left(\left(\tilde{\mathbf{u}}^h, \tilde{D}^h, \tilde{\boldsymbol{\omega}}^h\right)\right) \forall\ \left(\tilde{\mathbf{u}}^h, \tilde{D}^h, \tilde{\boldsymbol{\omega}}^h\right) \in \mathbf{X}_h \tag{3.21}$$

b. Expansion bases

Nodal expansion: In the standard interval $\Omega_{st} = \{\xi | -1 < \xi < 1\}$ nodal expansions are defined as

$$\psi_i(\xi) = \frac{(\xi - 1)(\xi + 1)L'_p(\xi)}{p(p+1)L_p(\xi_i)(\xi - \xi_i)} \tag{3.22}$$

In Eq. (3.22), $L_p = P_p^{0,0}$ is the Legendre polynomial of order p and ξ_i denotes the location of the roots of $(\xi - 1)(\xi + 1)L'_p(\xi) = 0$ in the interval $[-1, 1]$. Details on the multidimensional construction of nodal expansions can be found in Ref. [30]. The integrals in Eq. (3.21) are evaluated using Gauss-Lobatto-Legendre quadrature rule. For details on standard finite element computer implementation, such as mapping $\bar{\Omega}_e \rightleftarrows \hat{\Omega}_e$, numerical integration in $\hat{\Omega}_e$, and assembly using the direct stiffness approach, see Reddy [27, 28]. For linearization, we use Newton's method, details of which can be found in [31].

C. Numerical results

In this section, numerical results obtained with the present least-squares finite element model are presented. First, second-order accuracy of the time integration scheme used is verified. Next, results are presented for impulsively started lid-driven cavity problem and transient flow over a backward facing step problem.

For all the problems considered in this chapter, non-linear convergence is declared when the relative norm of the residual, $\|\Delta\mathbf{U}\|/\|\mathbf{U}\|$ is less than 10^{-3}, unless mentioned otherwise, where **U** is the solution vector (includes all degrees of freedom at a node). Convergence of the conjugate gradient method to solve the equations is declared when the L_2-norm of error is less than 10^{-6}.

1. Verification problem

In the first numerical example, we establish the second-order accuracy of the time integration scheme used. We use the method of manufactured solutions. The idea behind manufactured solutions is to come up with an exact solution to the, preferably one that is infinitely differentiable, not trivially reproduced by the element approximation functions and utilize all terms of the governing equation. We consider a unit square and take the exact solution of the incompressible Navier-Stokes equations to be of the form:

$$u(x,y,t) = \pi sin^2(\pi x) sin(\pi y) cos(\pi y) sin(t)$$
$$v(x,y,t) = -\pi sin(\pi x) cos(\pi x) sin^2(\pi y) sin(t)$$
$$p(x,y,t) = cos(\pi x) sin(\pi y) sin(t)$$

The prescribed velocity field satisfies continuity equation and the source term $\mathbf{f}$ of the momentum equations represents the residual of the differential equations such that the prescribed solution is the exact solution to the problem.

The Dirichlet boundary conditions on velocities are specified using the exact solution given above. The discrete system is linearized using Newton's method and resulting symmetric positive-definite (SPD) system of equations has been solved using the Choleski factorization. A 4×4 uniform mesh of quadrilateral elements is used for spatial discretization. Newton's convergence is declared when the relative norm of the residual is less than 10^{-10}. Penalty parameter used is 10^2 for which L_2-norm of the residual of continuity equation is below 10^{-12}, and does not interfere with the convergence.

The time evolution of fields is computed for $t \in [0, 20]$ for decreasing time step size varying from 10^{-1} to 10^{-3}. The L_2 error in v-velocity, pressure, and vorticity is recorded at $t = 5$ and plotted in Fig. 27 as a function of time step on log-log scale. The errors decay

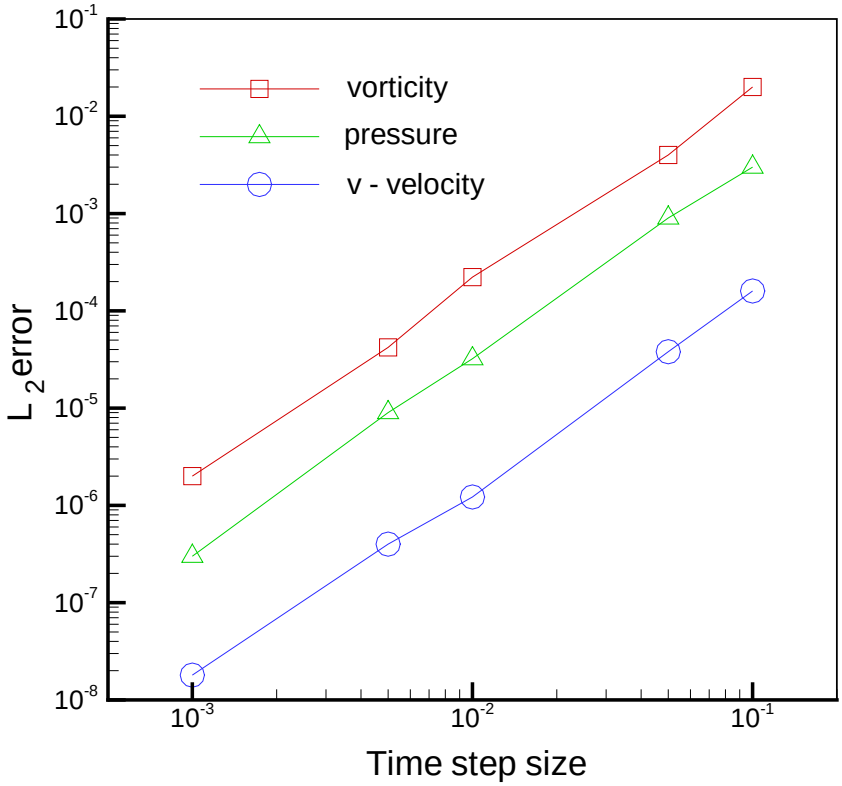

Fig. 27. Convergence of the velocity, pressure and vorticity fields in the L_2 norm for decreasing time step size.

at an algebraic rate with slope 2, as expected for the second-order accurate time integration scheme.

2. 2D Lid-driven cavity flow

Next, the two-dimensional lid-driven cavity problem is analyzed to test the presented formulation. The flow is driven by the translation of the top boundary. No slip boundary condition is imposed on all solid walls. On the top wall ($y = 1.0$), the boundary conditions are taken as $u = \hat{u}(x,t)$, $v = 0$. To avoid singularity in the boundary condition, we specify

a hyperbolic tangent u-velocity distribution on the top wall:

$$u(x) = \begin{cases} \tanh(\beta\, x) & 0 \le x \le 0.5 \\ -\tanh(\beta\,(x-1)) & 0.5 < x \le 1.0 \end{cases}$$

with $\beta > 0$. In the present study, $\beta = 50$ is used, which gives a smooth but at the same time sharp transition from $u = 0.0$ to $u = 1.0$ is represented near the walls of the driven surface. This boundary condition results in a well-posed boundary condition as singularities at the corners are eliminated. The standard boundary condition ($u = 1$ everywhere) would make the problem singular and destroys the high accuracy properties associated with high-order expansions by polluting the solution near the corners. High order methods are sensitive to these types of singularities.

The u-velocity of the driven surface also varies in time according to a hyperbolic tangent distribution. So lid velocity is given by $u_{lid}(x,t) = u_{lid}(x)$tanh(t).

We use 14×14 nonuniform mesh that is graded towards the wall; the corner elements have the dimension of 0.01×0.01. The 7th-order nodal expansion is used in each element, and there are a total of $39,204$ degrees of freedom in the mesh. All internal degrees of freedom are condensed out using Schur complement method (see [6] for details), resulting in $10,980$ interface degrees of freedom with a bandwidth of 788. The preconditioned conjugate gradient is used to solve for the interface degrees of freedom. This problem has been solved for the penalty parameters 10 and 30. Reynolds number is taken to be Re = 5,000. Initial velocity conditions are taken to be zero everywhere. The Crank-Nicholson scheme is used for time marching, and a time increment of 0.2 has been used for all results reported in this section.

Fig. 28 contains streamline plots for various times. Upon start-up a long narrow vortex forms close to the lid. The vortex gradually moves to the right and begins to grow.

Streamlines at the steady state are shown in Fig. 29. At the steady state, there is

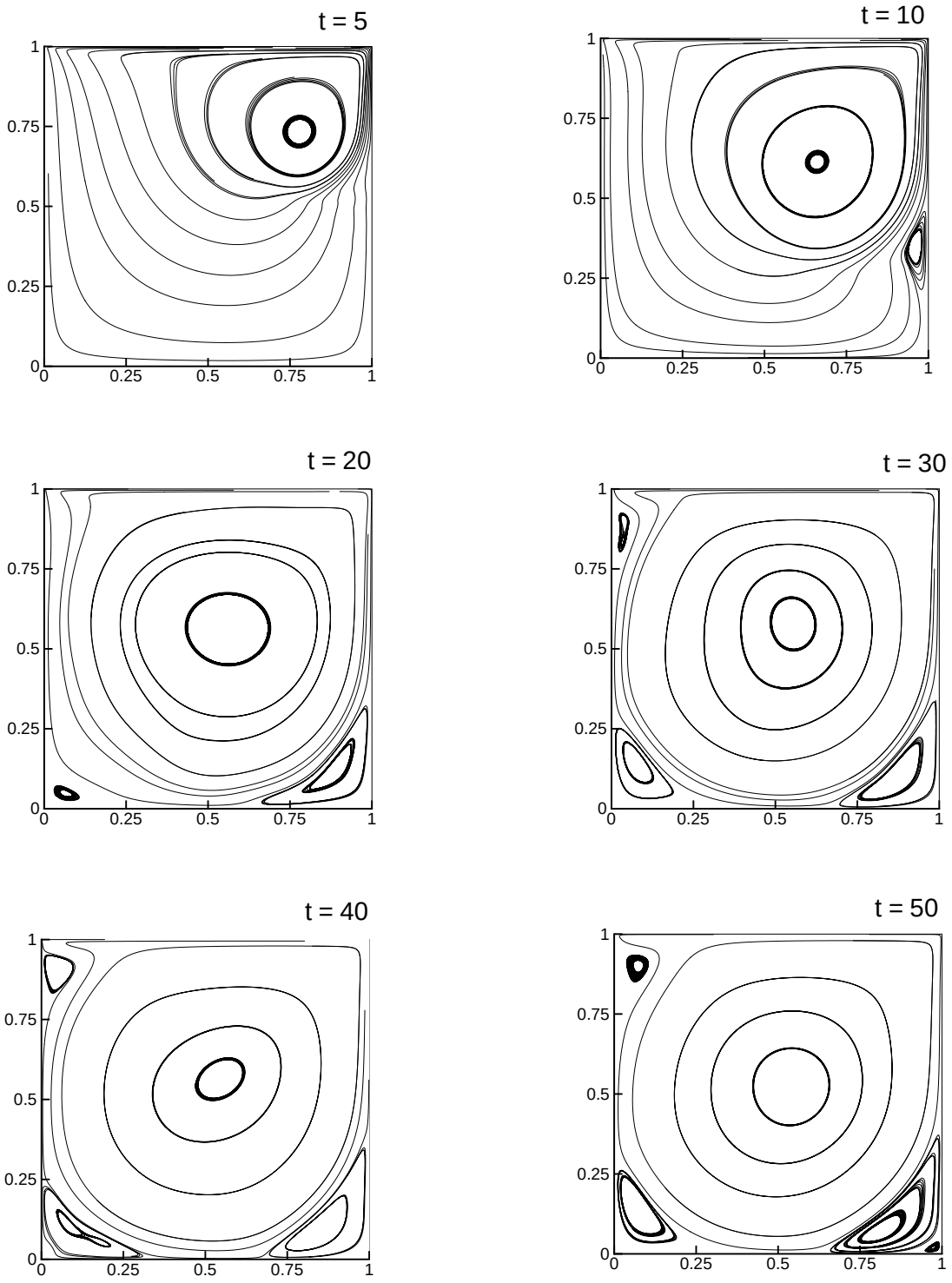

Fig. 28. Time history of streamline plots for impulsively started lid-driven cavity flow at Re = 5000

one primary vortex, three first vortices, at left and right bottom corners, named BR and BL, and the top left corner is named TL; and two second vortices appear at left and right bottom corners. Centers of these vortices are reported in Table V and compared with the benchmark values of Ghia et al. [42]. These values match well with the corresponding values of Ghia et al. [42]. A penalty parameter of 10 is used for these results. The value of the L_2 least-squares functional remains below 3.4×10^{-2} and L_2-norm of the residual of continuity equation is below 10^{-5} at all times for the penalty parameter of 30. Typically, it takes two Newton's iterations to converge for every time step. Fig. 30 shows pressure contours. Pressure $p = 0$ is specified at the center of the cavity.

Table V. Location of Vortices: comparison with the benchmark results of Ghia.

	Present	Ghia et al. [42]
Primary	0.5147,0.5341	0.5117,0.5352
First BR	0.8085,0.0725	0.8086,0.0742
First BL	0.0743,0.1347	0.0703,0.1367
First TL	0.0640,0.9107	0.0625,0.9102
Second BR	0.9801,0.0166	0.9805,0.0195
Second BL	0.0073,0.0074	0.0117,0.0078

Dilatation contours are shown in Fig. 31; it is clear that mass conservation is satisfied very well locally at all points in the domain, with a maximum value of dilatation approximately 1×10^{-5} near the top corner. Penalty parameter used in this case is only 10, and it works very well for even for this high Reynolds number.

The u-velocity profiles along the vertical middle line of the cavity $x = 0.5$ at steady state are shown in Fig. 32(a) for various values of the penalty parameter, and the results are compared with those of Ghia et al. [42]. Again, we see excellent agreement between the

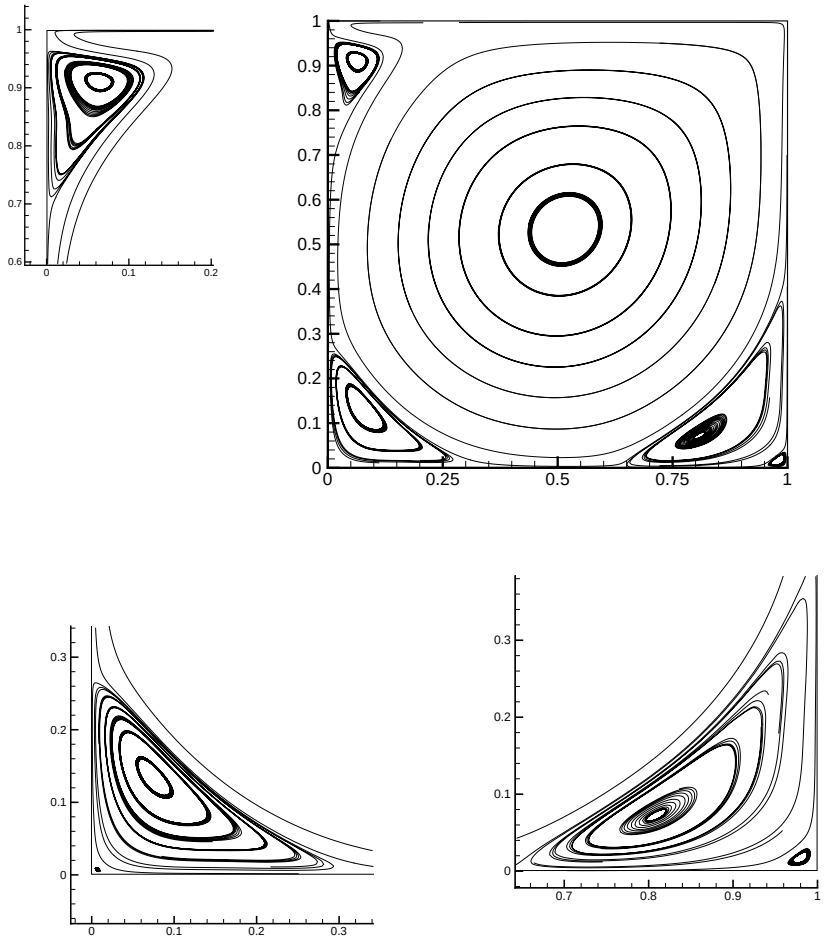

Fig. 29. Streamlines at steady state for lid-driven cavity flow

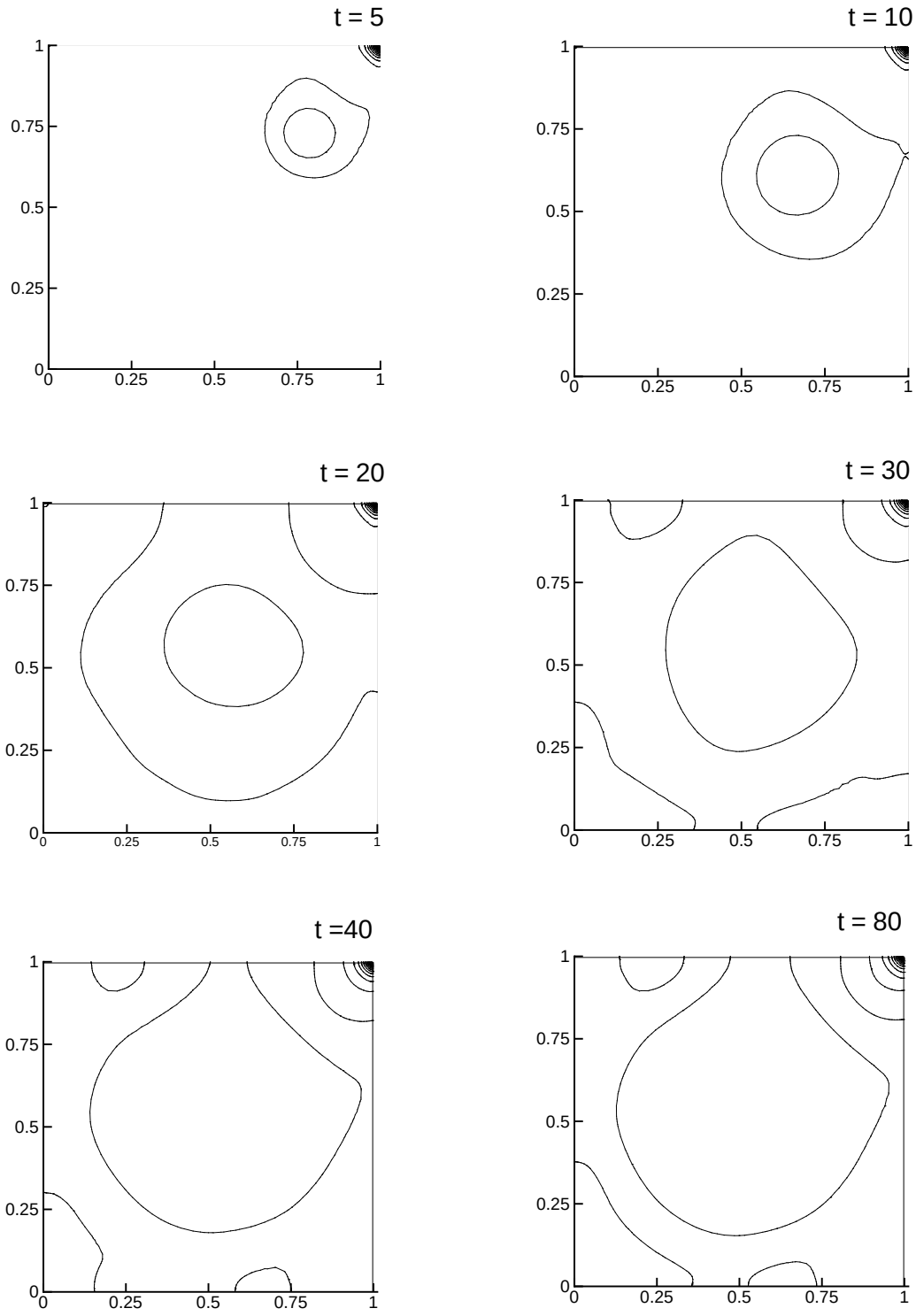

Fig. 30. Time history of pressure contours for impulsively started lid-driven cavity flow

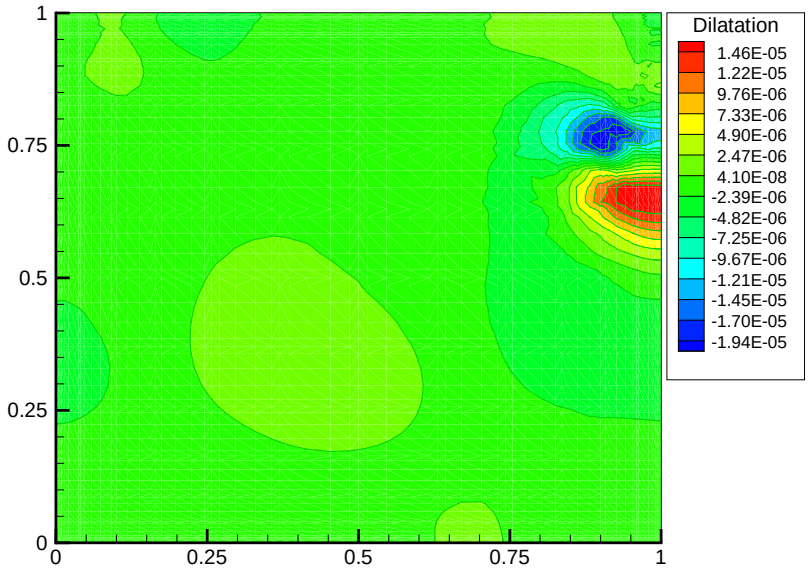

Fig. 31. Dilatation contours at t=100

two solutions even for $\gamma = 10$.

In Fig. 32(b) v-velocity profiles are plotted along the horizontal middle line of the cavity $y = 0.5$ for various values of the penalty parameter. We note that boundary conditions are slightly different for the two studies. Ghia et al. [42] used lid velocity of 1.0 everywhere on the top wall while in our case lid velocity varies with x and time.

Time history of v-velocity at (0.5,0.2) is plotted in Fig. 33 for penalty parameters of 10 and 30. All three penalty parameters give identical time evolution of the velocity field. Steady state is reached around $t = 120$ nondimensional time.

Next, number of PCG iterations required for the convergence of PCG solver is plotted against time in Fig. 34. Each data point in the plot represents the sum of PCG iterations at each Newton step, thus indicating the total number of PCG iterations required to converge at a time step. The penalty parameter used is 10 in this case.

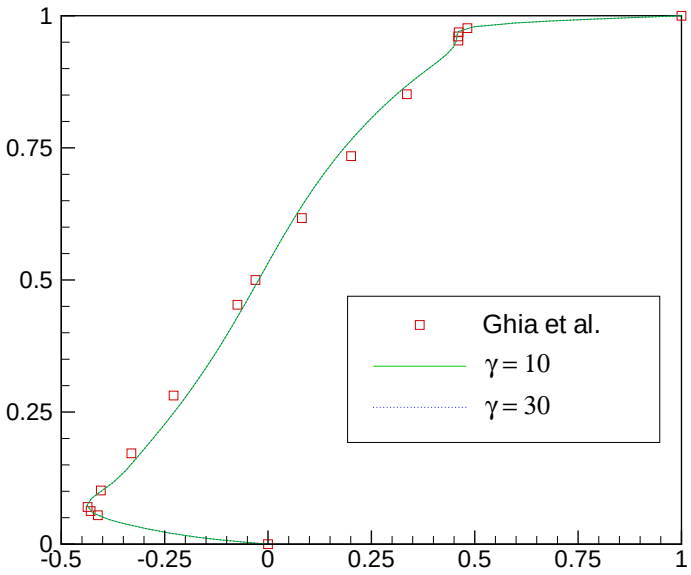

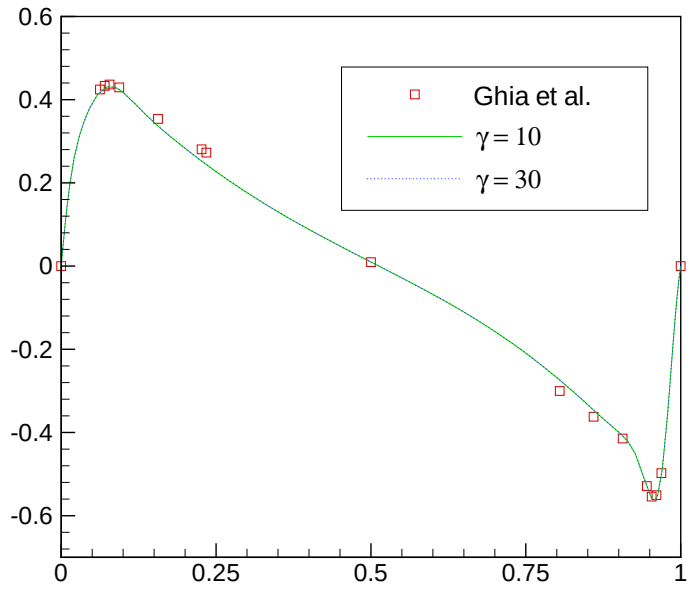

Fig. 32. (a) Steady state u-velocity profile along the vertical middle line of the cavity (b) Steady state v-velocity profile along the horizontal middle line of the cavity: comparison with Ghia et al. [42]

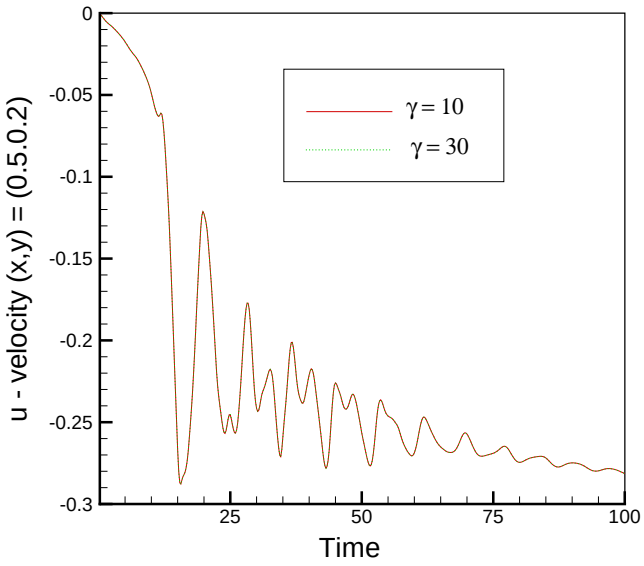

Fig. 33. Time history of the u-velocity component.

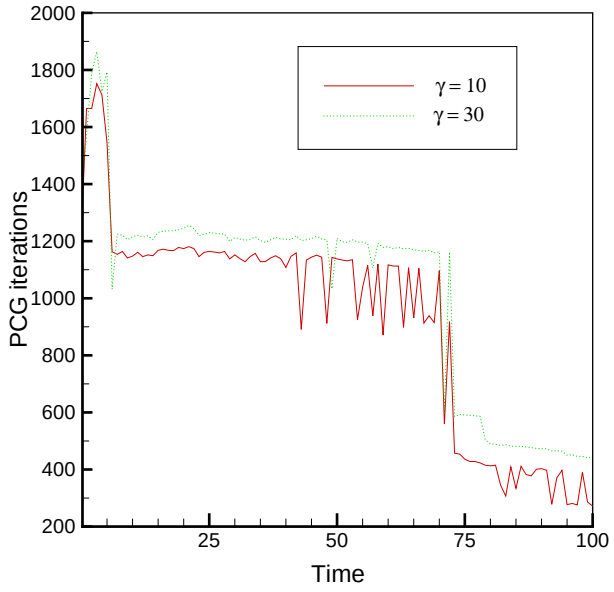

Fig. 34. Time history of PCG iterations for impulsively started lid-driven cavity flow

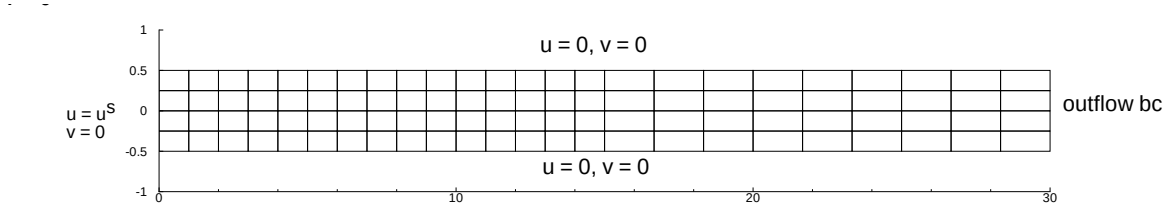

Fig. 35. Geometry and boundary conditions for flow over a backward-facing step

As Figs. 32(a) and Fig. 32(b) indicate, the present model gives very accurate results for even penalty parameter of 10. Typical penalty parameter values used in the traditional penalty finite element model are in the range of 10^8 to 10^{12}. For such a high penalty parameter, conditioning number of the resulting coefficient matrix becomes very high and different order integration rule is used to integrate penalty terms to obtain *acceptable* solution. In this study we have used equal order integration for all terms.

3. Transient flow over a backward-facing step

Next, we consider transient flow over a two-dimensional backward-facing step at Re $= 800$. The domain of interest is $\bar{\Omega} = [0, 30] \times [-0.5, 0.5]$. Mesh and boundary conditions are shown in Fig. 35. The boundary and initial conditions used here are the same as those used in the works of Gresho et al. [43] and Pontaza and Reddy [12]: $u = v = 0$ on the horizontal walls, $-p + \mu\partial u/\partial n = 0$ and $\partial v/\partial n = 0$ on the outflow boundary, and $u = [\tanh(t/4)]u_b(y) + [1 - \tanh(t/4)]u_p(y)$ and $v = 0$ on the inflow boundary. Here $u_b(y) = \max[0, 24y(0.5 - y)]$ is the true inlet boundary condition and $u_p(y) = 3(0.5 - y)(0.5 + y)$ is the Poiseuille flow observed infinitely far downstream at steady-state. The initial velocity field is set to $u = u_p(y)$ and $v = 0$ everywhere in the computational domain. The inlet condition is varied fast but smoothly from Poisuille flow to flow over a backward facing step.

To accurately resolve primary and secondary circulation zones, a nonuniform mesh

is used. We use 7^{th} order nodal expansion in each element (Mesh A). There are $19,604$ degrees of freedom in the mesh. We condense out all interior degrees of freedom, resulting in $5,780$ interface degrees of freedom and a bandwidth of 268. Simulations are carried out for penalty parameter of 30, 50, and 100. The Crank-Nicholson scheme is used for time marching, and a time increment of $\Delta t = 0.2$ has been used for all the results reported in this section.

Fig. 36 shows the evolution of the velocity flow field during initial stage. The main flow coming from the inlet follows a sinuous path, forming a series of eddies along the upper and lower wall. At the steady state, two eddies (primary and secondary separation zones) remain, all other eddies die out. These plots match qualitatively well with the published results of Prabhakar and Reddy [41].

In the steady state, the primary reattachment length is around 6.10, while secondary separation and reattachment lengths are approximately 4.9 and 10.4, respectively. Fig. 37 shows the evolution of pressure field. In this formulation pressure field evolves smoothly. The pressure gradient caused by eddies can be seen in these plots. Dilatation contours at steady state are plotted in Fig. 38 for three penalty parameters. Maximum value of the dilatation is around 10^{-6}, showing that mass conservation is very good.

Time history of v-velocity signal at two locations (10,0) and (13,0) are plotted in Fig. 39 for three penalty parameters and compared with the results of Prabhakar et al. [41], who used collocation penalty least-squares (bilinear shape functions with one-point Gauss quadrature). Results match well for all three penalty parameters. For all the penalty parameters, we obtain smooth and monotonic decay of the transient. There are no fluctuations in the v-velocity field, showing that mesh resolution is adequate.

In Figs. 40(a) and 40(b) mass flow rate across sections $x = 5$ and $x = 10$ are plotted with time for three penalty parameters considered here. There is less than 0.5% of mass loss for these penalty parameters, showing that mass conservation is very good even for

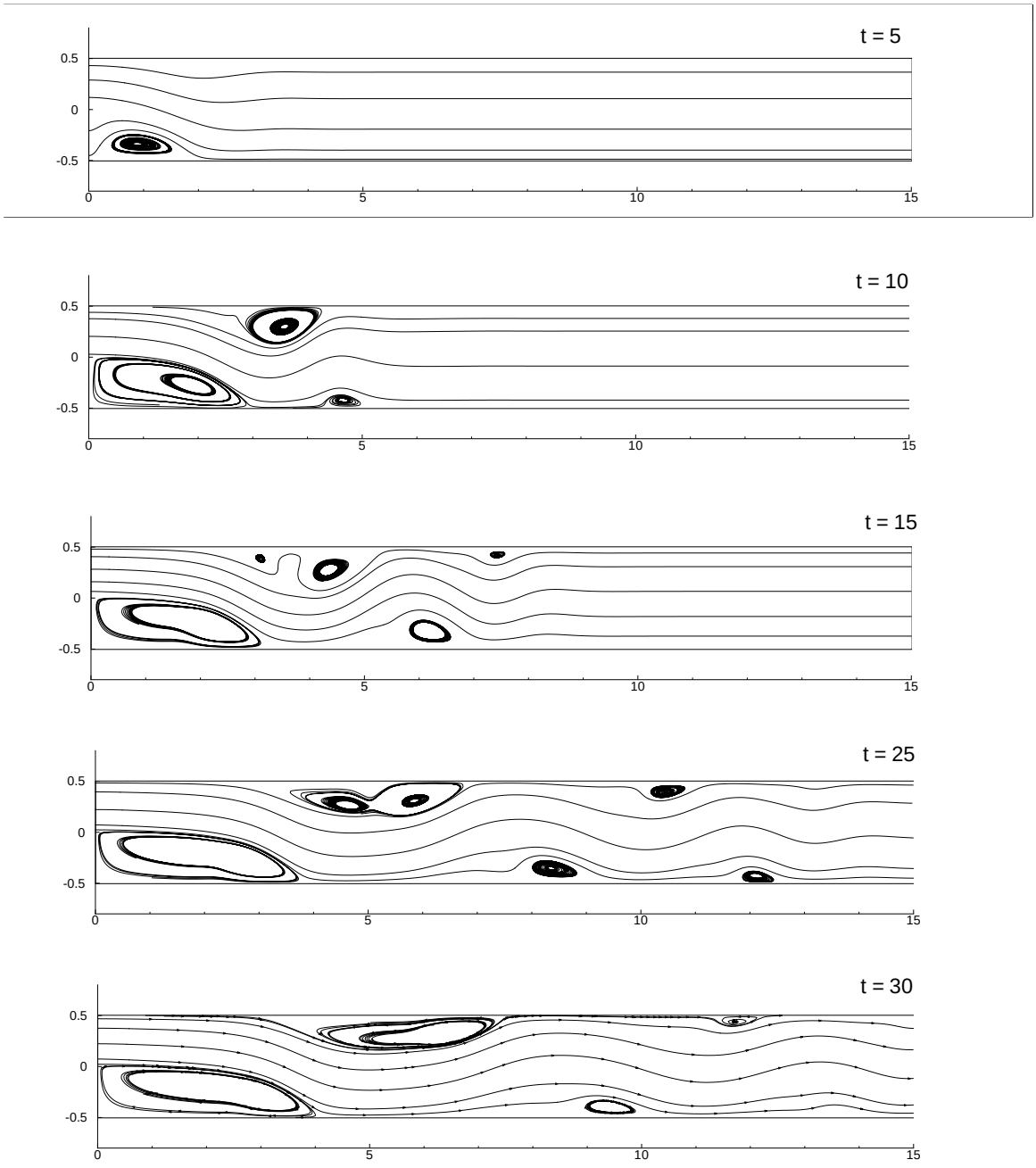

Fig. 36. Time history of streamline plots for flow over a backward facing step

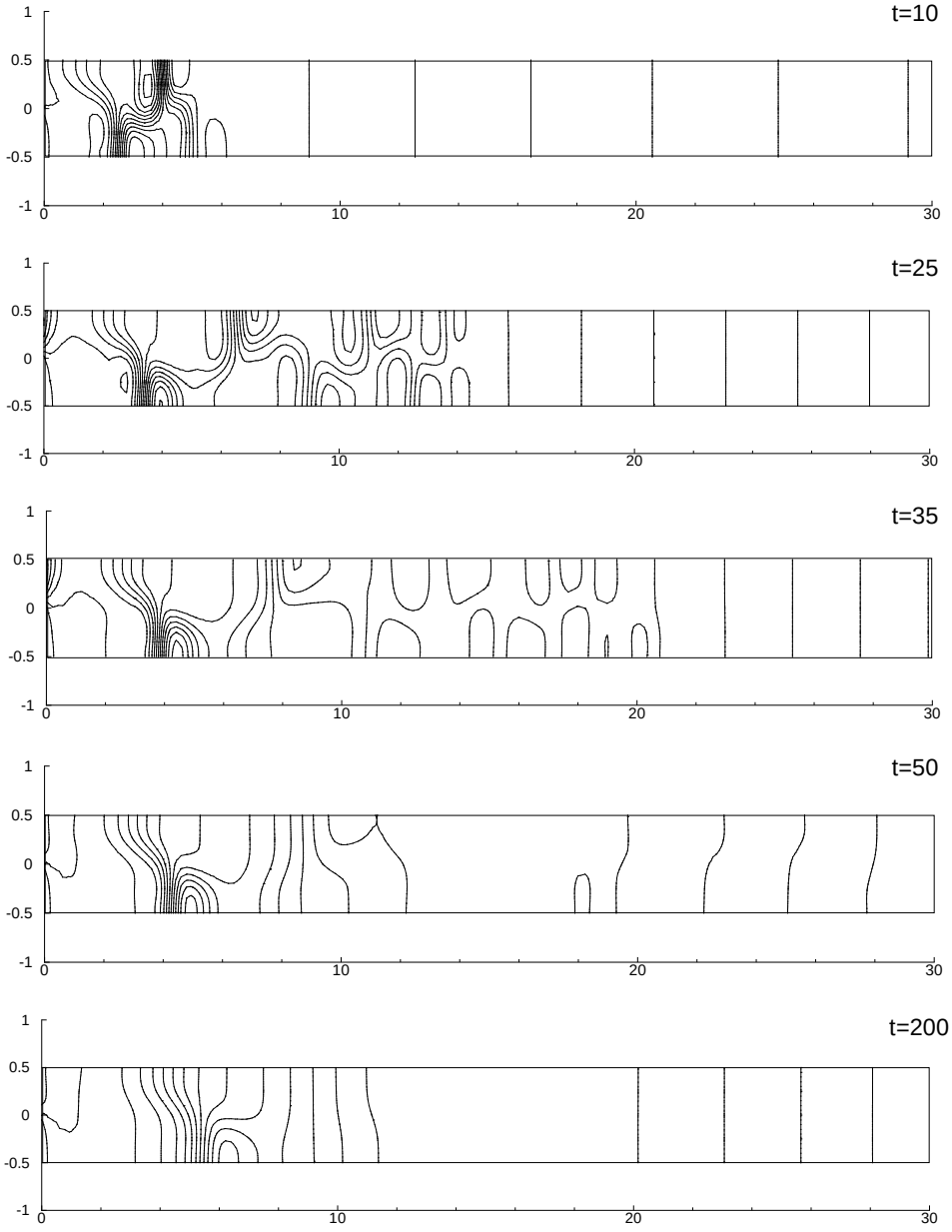

Fig. 37. Time history of pressure contours for flow over a backward facing step

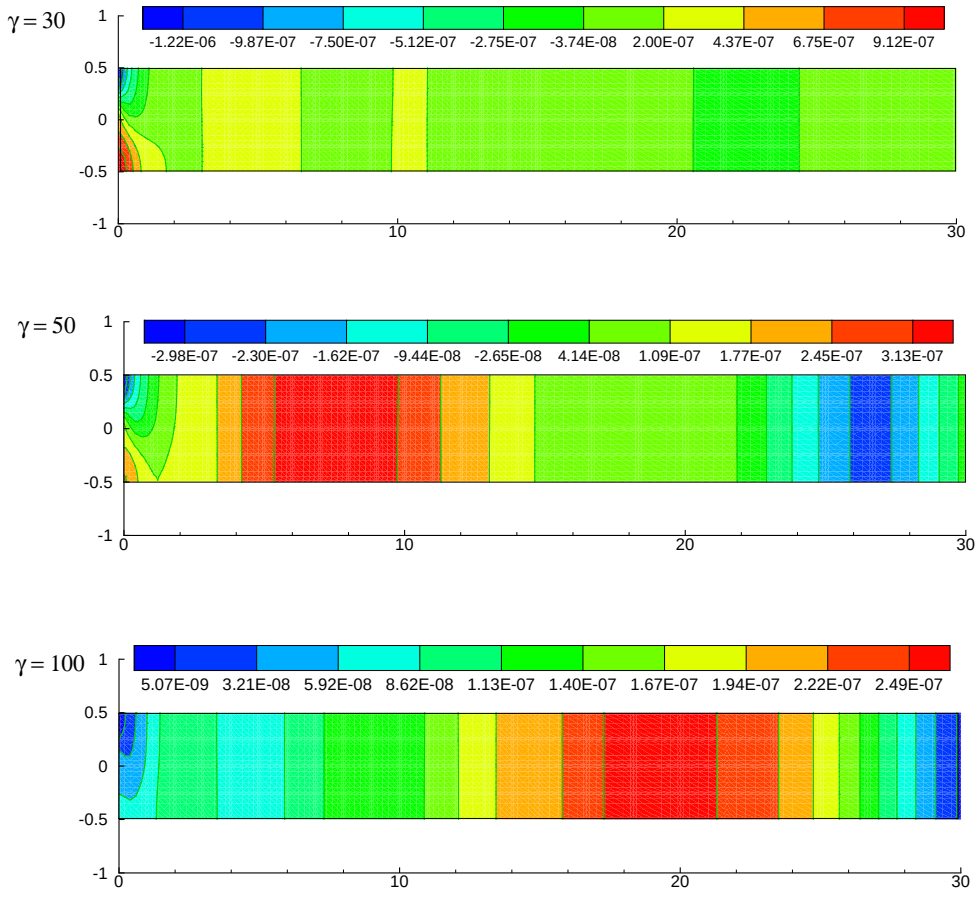

Fig. 38. Dilatation contours at steady state for three penalty parameters

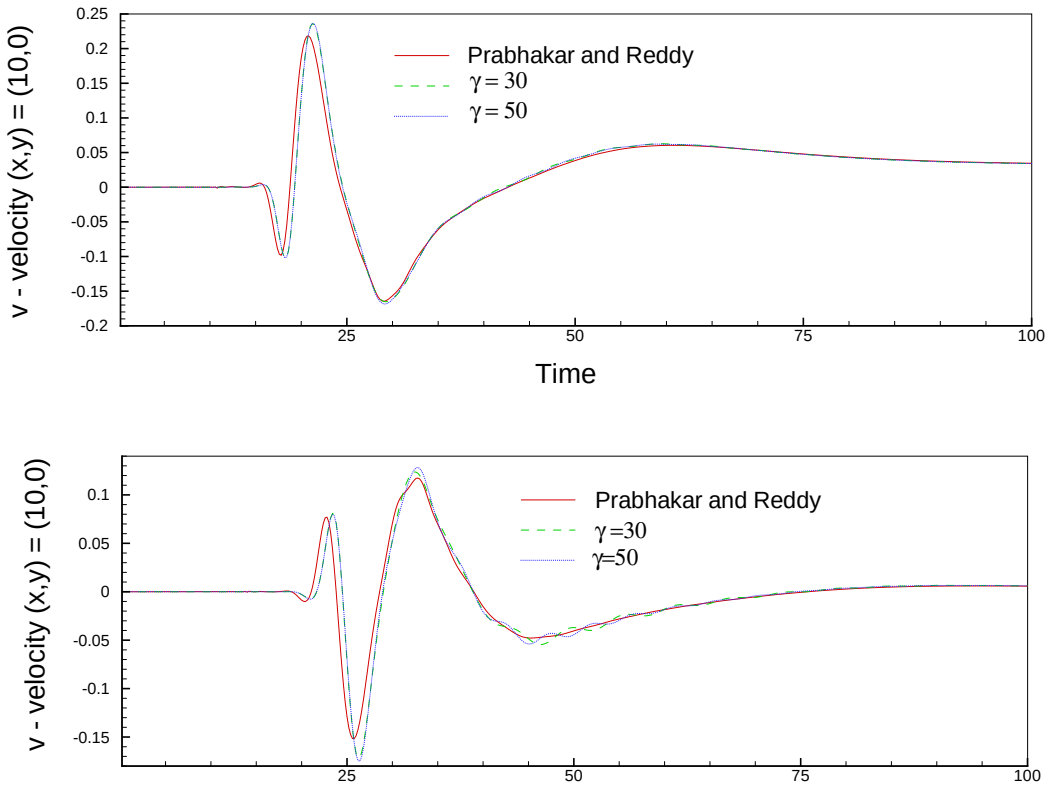

Fig. 39. Time history of the v-velocity component at two selected locations: $P = 7$

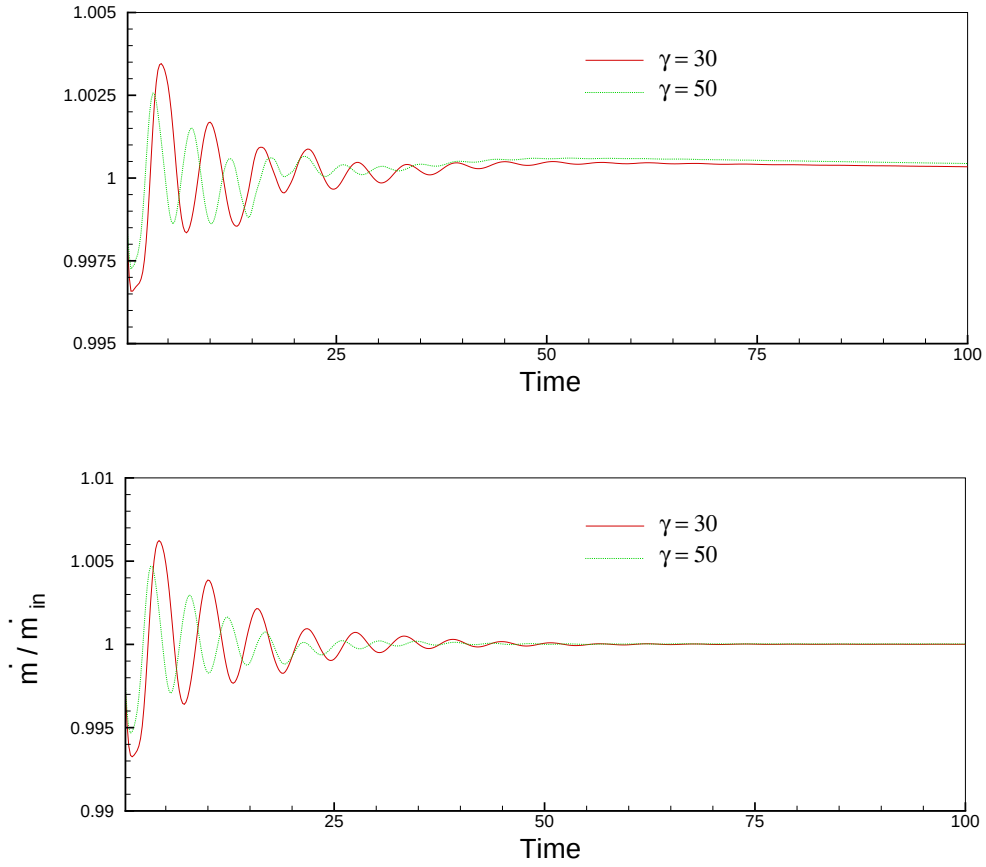

Fig. 40. Time history of mass flow rate at (a) $x = 5$ (b) $x = 10;\ P = 7$

low values of penalty parameters.

Next, the number of PCG iterations required are plotted against time in Fig. 41. The PCG solver converges steadily without much fluctuation (not shown here) indicating good conditioning of coefficient matrix. The penalty parameter is taken to be 30 in this case.

The previous works of Gresho et al. [43], Torczynski [44], and Pontaza and Reddy [12] showed that lack of spatial resolution induces unrealistic temporal chaotic behavior, resulting in an erroneous prediction of the long-term behavior of the flow. In such cases, either simulation diverges or the velocities fluctuate with time if it converges to steady state [12]. Pontaza and Reddy [12] reported that simulations diverge for p level less than 9

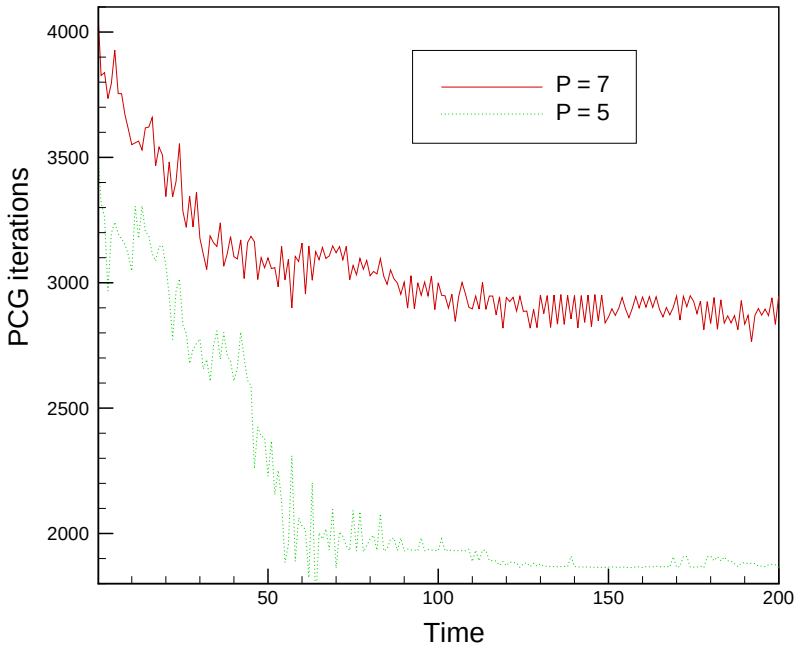

Fig. 41. Time history of PCG iterations for flow over a backward facing step

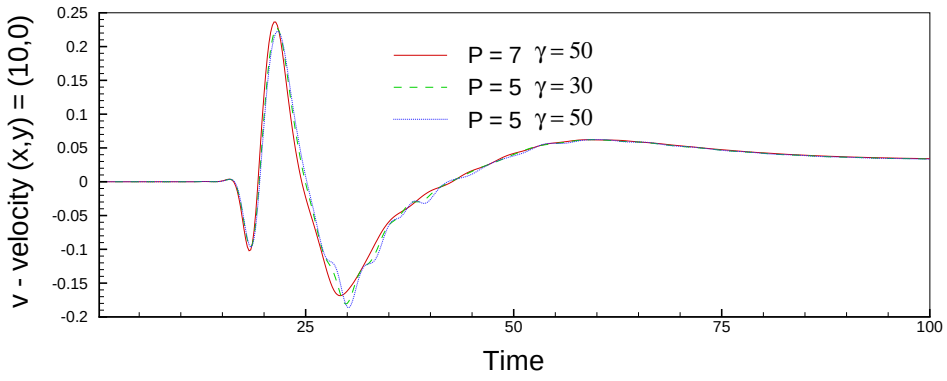

Fig. 42. Time history of the v-velocity component at two selected locations: $P = 5$

on 30×4 mesh, when space-time decoupled formulations are used. In our case, mesh is coarser than the one used in [12], but still simulations predict correct evolution of field and reach the steady state. To examine sensitivity of accuracy on p-level, simulations are run for $p = 5$ on 24×4 mesh (Mesh B) for penalty parameters of 30, 50, and 100. Time evolution of v-velocity at two locations (10,0) and (13,0) are plotted in Fig. 42 and compared with the results obtained using $p = 7$. Even for this p-level, velocity evolution is quite accurate.

The L_2-norm of least-squares functional and dilatation are plotted in Figs. 43(a) and 43(b) for p levels of 5 and 7 and penalty parameter of 30. These plots show monotonic convergence to steady state.

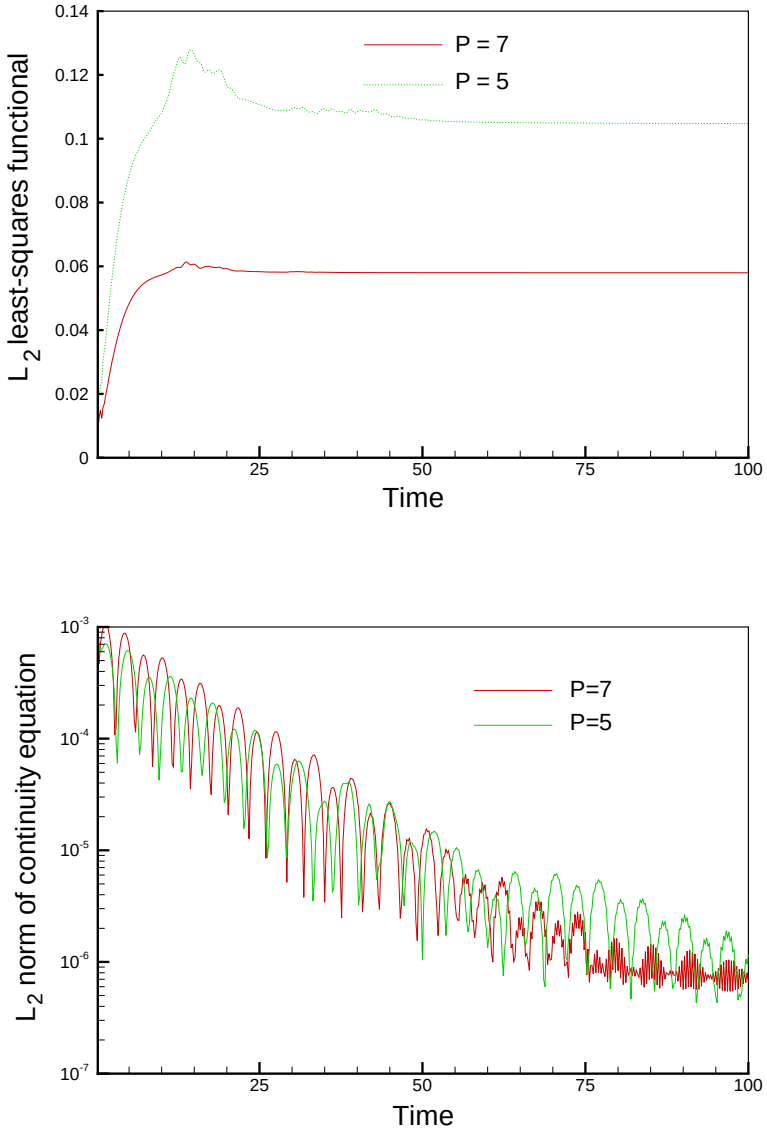

Fig. 43. (a) Time history of the L_2 least-squares functional for $P = 5$ and $P = 7$ (b) Time history of L_2 norm of the continuity equation for $P = 5$ and $P = 7$

CHAPTER IV

A COLLOCATION PENALTY LEAST-SQUARES FINITE ELEMENT FORMULATION FOR INCOMPRESSIBLE FLOWS

A. Introduction

Recently, there has been substantial interest in the use of least-squares based finite element formulations for the numerical solution of Stokes and Navier-Stokes equations [1, 2, 3, 4, 5, 6]. They offer several theoretical and computational advantages. Most notably, such formulations circumvent the inf-sup condition of Ladyzhenskaya-Babuska-Brezzi (LBB). So the choice of approximating spaces is not subject to any condition, and a single continuous piecewise polynomial space can be used for the approximation of all unknowns. They also yield symmetric positive-definite coefficient matrix and robust iterative solvers can be used to solve resulting system of linear equations.

Previous studies [8, 9] showed that mass conservation is not very good in least-squares based formulations when low order basis functions are used. Chang and Nelson [8] suggested that this is because the error is minimized on a global scale, allowing errors of significant size to remain on a local scale, especially in areas in which the gradients of the variables are of significant size. They also proposed a remedy. Unfortunately, this remedy, which consists of enforcing the continuity equation as an explicit constraint through the use of Lagrange multipliers, negates one of the main advantages of the least-squares methods, namely, the positive-definiteness of resulting coefficient matrix. Deang and Gunzburger [10] also studied mass conservation in least-squares formulations and analyzed weighted least-squares functionals. These formulations showed better mass conservation than unweighted formulations but conditioning number of the resultant coefficient matrix became high. Bolton and Thatcher also addressed this problem for Stokes [9] and Navier-Stokes

equations [11] and proposed weighting of particular terms in the least-squares functional.

Another problem associated with least-squares formulations is an ill-behaved temporal evolution of pressure field. In least-squares based finite element formulations, the divergence-free constraint on the velocity field is enforced directly through the least-squares functional and pressure does not play a role in enforcing it. Thus, the pressure does not have a well-defined role in these formulations. Unsteady problems, especially with inflow/outflow boundaries, produce spurious pressure evolution with time due to this lack of strong pressure velocity coupling.

Recently, Pontaza [45] proposed the use of a regularized divergence-free constraint to improve the velocity-pressure coupling. In the resulting variational problem the pressure is readily identified as an enforcer of the divergence-free constraint. The formulation was shown to give a smooth and accurate temporal evolution of the pressure field and excellent conservation of mass in time.

Penalty based finite element formulations for the Navier-Stokes equations were proposed almost three decades ago and there have been subsequent improvements. The penalty methods did not gain much popularity mainly because of ill-conditioning of the coefficient matrix, which renders iterative solvers ineffective. Prabhakar and Reddy [6] proposed a least-squares based penalty formulation for the steady incompressible Navier-Stokes equations where the pressure degree of freedom is eliminated using an iterative penalization. This eliminates the issue of proper velocity-pressure coupling, as the pressure is no longer explicitly present in the formulation. They used spectral high-order basis functions to construct the discrete models. This formulation gave accurate numerical results and good conservation of mass for low penalty parameters (10-40).

In this chapter we implement the penalty least-squares formulation using bi-linear basis functions, which are widely used in practice. Further, we extend the implementation to simulate unsteady flows. When using bi-linear basis functions a least-squares collocation

approach is appropriate [14], which we adopt here.

The present chapter is organized as follows. In section B, the penalty based least-squares finite element model for the incompressible Navier-Stokes equations is presented. Numerical results are presented in section C. The h-convergence is verified using the exact solution of the Kovasznay flow problem. We then present results for 2D flow past a large circular cylinder in a channel. We check the dependence of mass conservation on penalty parameter and mesh size. Next, numerical results are presented for the transient two-dimensional flow over a backward-facing step. We run simulations for various penalty parameters and report the evolution of velocity and pressure field with time. Lastly, in section D, we extend this formulation to velocity-temperature coupled problems and present results for buoyant flow inside a square enclosure and compare results with benchmark solution of Davis et al. [26] and Prabhakar and Reddy [6].

B. The incompressible Navier-Stokes equations

The unsteady Incompressible Navier-Stokes equations in dimensionless form can be written as follows:

$$\frac{\partial \mathbf{u}}{\partial t} + (\mathbf{u}\cdot\nabla)\,\mathbf{u} + \nabla p - \frac{1}{\mathrm{Re}}\,\nabla\cdot\left[(\nabla\mathbf{u}) + (\nabla\mathbf{u})^{\mathrm{T}}\right] = \mathbf{f} \qquad \text{in } \Omega\times(0,\tau] \tag{4.1}$$

$$\nabla\cdot\mathbf{u} = 0 \qquad \text{in } \Omega\times(0,\tau] \tag{4.2}$$

$$\mathbf{u} = \mathbf{u}_0(\mathbf{x}) \qquad \text{on } \Omega \tag{4.3}$$

$$\mathbf{u} = \mathbf{u}^s \qquad \text{on } \Gamma_u\times(0,\tau] \tag{4.4}$$

$$\hat{\mathbf{n}}\cdot\underline{\boldsymbol{\sigma}} = \mathbf{f}^s \qquad \text{on } \Gamma_f\times(0,\tau] \tag{4.5}$$

where $\mathbf{u}(\mathbf{x})$ is the velocity vector, $\underline{\boldsymbol{\sigma}} = -p\underline{\mathbf{I}} + 1/\mathrm{Re}\left[(\nabla\mathbf{u}) + (\nabla\mathbf{u})^{\mathrm{T}}\right]$ is the total stress, $p(\mathbf{x})$ is the pressure, $\mathbf{f}$ is a dimensionless force, $\hat{\mathbf{n}}$ is the outward unit normal on the boundary of Ω, $\mathbf{u}^s$ is the prescribed velocity on the boundary Γ_u, and $\mathbf{f}^s$ are the prescribed tractions on the boundary Γ_f, $\Gamma = \Gamma_u \cup \Gamma_f$ and $\Gamma_u \cap \Gamma_f = \emptyset$, and Re is the Reynolds number.

In the penalty method, pressure is eliminated from the Navier-Stokes equations using the following expression (see [27], [28], and [29]):

$$p = -\gamma(\nabla \cdot \mathbf{u}) \tag{4.6}$$

Gunzburger [13] proposed an iterative penalty method

$$p^n = p^{n-1} - \gamma(\nabla \cdot \mathbf{u}) \tag{4.7}$$

where n is the nonlinear iteration number. An advantage of this method is that the value of penalty parameter needed to enforce the continuity constraint is equal to the square-root of the one needed in the non-iterative penalty method [13]. This, in turn, results in a coefficient matrix with smaller conditioning number. In this study we use the iterative penalty method.

Therefore, the problem becomes one of finding the velocity $\mathbf{u}(\mathbf{x})$ such that

$$\frac{\partial \mathbf{u}}{\partial t} + (\mathbf{u}\cdot\nabla)\,\mathbf{u} - \gamma\nabla(\nabla\cdot\mathbf{u}) - \frac{1}{\mathrm{Re}}\nabla\cdot\left[(\nabla\mathbf{u}) + (\nabla\mathbf{u})^{\mathrm{T}}\right] = \mathbf{f} - \nabla p^{n-1} \qquad \text{in } \Omega\times(0,\tau] \tag{4.8}$$

$$\mathbf{u} = \mathbf{u}_0(\mathbf{x}) \qquad \text{in } \Omega \tag{4.9}$$

$$\mathbf{u} = \mathbf{u}^s \qquad \text{on } \Gamma_u\times(0,\tau] \tag{4.10}$$

$$\hat{\mathbf{n}}\cdot\underline{\boldsymbol{\sigma}} = \mathbf{f}^s \qquad \text{on } \Gamma_f\times(0,\tau] \tag{4.11}$$

where n in the superscript $(n-1)$ is the nonlinear iteration number. Since the solution at iteration $(n-1)$ is known, ∇p^{n-1} is known and therefore transferred to the right-hand side of the equation.

1. The velocity-dilatation-vorticity first-order system

To cast the second-order system (4.8)-(4.11) into a first-order system, we introduce the vorticity vector, $\boldsymbol{\omega} = \nabla \times \mathbf{u}$, and dilatation, $D = \nabla \cdot \mathbf{u}$, as independent variables. Then the problem can be stated as one of finding the velocity vector $\mathbf{u}(\mathbf{x})$, dilatation $D(\mathbf{x})$, and vorticity $\boldsymbol{\omega}(\mathbf{x})$ such that

$$\frac{\partial \mathbf{u}}{\partial t} + (\mathbf{u} \cdot \nabla)\,\mathbf{u} - \gamma \nabla D + \frac{1}{\mathrm{Re}} \nabla \times \boldsymbol{\omega} = \mathbf{f} - \nabla p^{n-1} \qquad \text{in } \Omega \times (0, \tau] \tag{4.12}$$

$$\boldsymbol{\omega} - \nabla \times \mathbf{u} = \mathbf{0} \qquad \text{in } \Omega \times (0, \tau] \tag{4.13}$$

$$D - \nabla \cdot \mathbf{u} = 0 \qquad \text{in } \Omega \times (0, \tau] \tag{4.14}$$

$$\mathbf{u} = \mathbf{u}_0(\mathbf{x}) \qquad \text{on } \Gamma_u \tag{4.15}$$

$$\mathbf{u} = \mathbf{u}^s \qquad \text{on } \Gamma_u \times (0, \tau] \tag{4.16}$$

$$\boldsymbol{\omega} = \boldsymbol{\omega}^s \qquad \text{on } \Gamma_\omega \times (0, \tau] \tag{4.17}$$

Typically $\Gamma_u \cap \Gamma_\omega = \emptyset$, i.e., if velocity is specified at a boundary, vorticity need not be specified there.

a. L_2 least-squares formulation

The least-squares functional of the problem can be set up by summing up the squares of the residuals of the new set of equations. In this study, we use space time decoupled formulation. In space-time decoupled formulations, discretization in space and time are done independently. Generally, the temporal operators are represented by truncated Taylor

series expansions in time domain. We use a Crank-Nicholson or a backward multi-step scheme (BDF2) in this study. Least-square functional for backward multi-step schemes can be written as

$$\mathcal{J}\left(\mathbf{u}, D, \boldsymbol{\omega}; \mathbf{f}\right) = \frac{1}{2}\Big(\Big\| \frac{\gamma_0}{\Delta t}\mathbf{u}^{s+1} - \sum_{q=0}^{M_\alpha} \frac{\beta_q}{\Delta t}\mathbf{u}^{s-q} + \left(\mathbf{u}\cdot\nabla\right)\mathbf{u} - \gamma\nabla D + \frac{1}{\mathrm{Re}}\nabla\times\boldsymbol{\omega}$$
$$- \mathbf{f} + \nabla p^{n-1}\Big\|^2_{0,\Omega\times(0,\tau]} + \Big\|\boldsymbol{\omega} - \nabla\times\mathbf{u}\Big\|^2_{0,\Omega\times(0,\tau]}$$
$$+ \Big\| D - \nabla\cdot\mathbf{u}\Big\|^2_{0,\Omega\times(0,\tau]}\Big) \tag{4.18}$$

where $\gamma_0 = \sum_{q=0}^{M_\alpha}\beta_q$ for consistency, β_q are weights associated with a particular multi-step scheme, $\Delta t = t_{s+1} - t_s$ is the time increment.

Considering the homogeneous pure velocity boundary condition case, the least-squares principle for functional (4.18) can be stated as:
find $(\mathbf{u}, D, \boldsymbol{\omega}) \in \mathbf{X}$, $\mathbf{u}(\mathbf{x}, 0)$=$\mathbf{u}_0(\mathbf{x})$ such that

$$\mathcal{J}\left(\mathbf{u}, D, \boldsymbol{\omega}; \mathbf{f}\right) \leq \mathcal{J}\left(\tilde{\mathbf{u}}, \tilde{D}, \tilde{\boldsymbol{\omega}}; \mathbf{f}\right) \qquad \forall\ \left(\tilde{\mathbf{u}}, \tilde{D}, \tilde{\boldsymbol{\omega}}\right) \in \mathbf{X} \tag{4.19}$$

where we use the space

$$\mathbf{X} = \Big\{ \left(\mathbf{u}, D, \boldsymbol{\omega}\right) \in \mathbf{H}^1_0\left(\Omega\right) \times H^1\left(\Omega\right) \times \mathbf{H}^1\left(\Omega\right) \Big\}$$

The variational problem (after linearization using Newton's method)corresponding to the least-squares principle is given by: find $(\mathbf{u}, D, \boldsymbol{\omega}) \in \mathbf{X}$, $\mathbf{u}(\mathbf{x}, 0)$=$\mathbf{u}_0(\mathbf{x})$ such that

$$\mathcal{B}\left(\left(\mathbf{u}, D, \boldsymbol{\omega}\right), \left(\tilde{\mathbf{u}}, \tilde{D}, \tilde{\boldsymbol{\omega}}\right)\right) = \mathcal{F}\left(\left(\tilde{\mathbf{u}}, \tilde{D}, \tilde{\boldsymbol{\omega}}\right)\right) \qquad \forall\ \left(\tilde{\mathbf{u}}, \tilde{D}, \tilde{\boldsymbol{\omega}}\right) \in \mathbf{X} \tag{4.20}$$

Let $\mathbf{X}_h$ denote a finite-dimensional subspace of $\mathbf{X}$. Then the least-squares discretized model of the Navier-Stokes equations is defined by the following discrete variational prob-

lem: find $\left(\mathbf{u}^h, D^h, \boldsymbol{\omega}^h\right) \in \mathbf{X}_h$, $\mathbf{u}(\mathbf{x}, 0)$=$\mathbf{u}_0(\mathbf{x})$ such that

$$\mathcal{B}\left(\left(\mathbf{u}^h, D^h, \boldsymbol{\omega}^h\right), \left(\tilde{\mathbf{u}}^h, \tilde{D}^h, \tilde{\boldsymbol{\omega}}^h\right)\right) = \mathcal{F}\left(\left(\tilde{\mathbf{u}}^h, \tilde{D}^h, \tilde{\boldsymbol{\omega}}^h\right)\right) \forall \ \left(\tilde{\mathbf{u}}^h, \tilde{D}^h, \tilde{\boldsymbol{\omega}}^h\right) \in \mathbf{X}_h \quad (4.21)$$

Having defined the finite element framework in terms of the penalty least-squares formulation, we need to choose proper basis functions to interpolate dependent variables. We use bi-linear basis functions in this study. The integrals in Eq. (4.21) are evaluated using one point Gauss quadrature rules, which is equivalent to adopting a least-squares collocation approach [14]. For details on standard finite element computer implementation, such as mapping $\bar{\Omega}_e \rightleftarrows \hat{\Omega}_e$, numerical integration in $\hat{\Omega}_e$, and assembly using the direct stiffness approach, see Reddy [27, 28]. For linearization, we use Newton's method, details of which can be found in [31].

C. Numerical results

In this section, numerical results obtained with the present least-squares finite element model are presented. First, h-convergence of the proposed formulation are verified. Next, results are presented for steady flow past a large circular cylinder in a channel, transient flow over a backward facing step and unsteady flow past circular cylinder.

For all the problems considered in this chapter, non-linear convergence is declared when the relative norm of the residual, $\|\Delta\mathbf{U}\|/\|\mathbf{U}\|$ is less than 10^{-3} unless mentioned, where **U** is the solution vector (includes all degrees of freedom at a node). Convergence of conjugate gradient is declared when L_2-norm of error is less than 10^{-6}.

1. Verification problem: Kovasznay flow

Kovasznay flow problem is used for the purpose of verification of the penalty least-squares based finite element model. Domain of interest is $\bar{\Omega} = [-0.5, 1.5] \times [-0.5, 1.5]$. The

analytical solution is given by [34]

$$u = 1 - e^{\lambda x}\,\cos(2\pi y) \tag{4.22}$$

$$v = \frac{\lambda}{2\pi}\,e^{\lambda x}\,\sin(2\pi y) \tag{4.23}$$

$$p = p_0 - \frac{1}{2}\,e^{2\lambda x} \tag{4.24}$$

where $\lambda = \mathrm{Re}/2 - [(\mathrm{Re}^2/4) + 4\pi^2]^{1/2}$ and p_0 is a reference pressure (an arbitrary constant).

Drichlet boundary conditions on velocities are specified using the exact solution given by Eqs. (4.22) and (4.23). The discrete system is linearized using Newton's method and resulting symmetric positive-definite (SPD) system of equations has been solved using PCG solver. Newton's convergence is declared when the relative norm of the residual is less than 10^{-10}. Convergence of conjugate gradient is declared when L_2-norm of error is less than 10^{-10}.

Streamlines obtained with the present formulation for the Kovasznay flow are shown in Fig. 44. We perform an h-refinement study. For such a study, the p-level of of the element approximation function is fixed, and mesh is refined systematically. The error measures should decay at an algebraic rate as the mesh is refined. On a log-log scale it should be a straight line. We use p-level of 5 for which approximation theory implies that the best convergence rate in the L_2 norm is 6. Penalty parameter used is 10^2.

Four different uniform meshes are used to perform the h-refinement study. The meshes are varied successively from 6×6 to 20×20. In Fig. 45 L_2 norm of least-square functional $\mathcal{J}$ and L_2 error of the velocity, pressure and vorticity fields are plotted against h. An algebraic convergence rate slightly lower than 6 is achieved by least-squares functional and pressure, and an algebraic convergence rate slightly better than 6 is achieved by u, v velocities and vorticity.

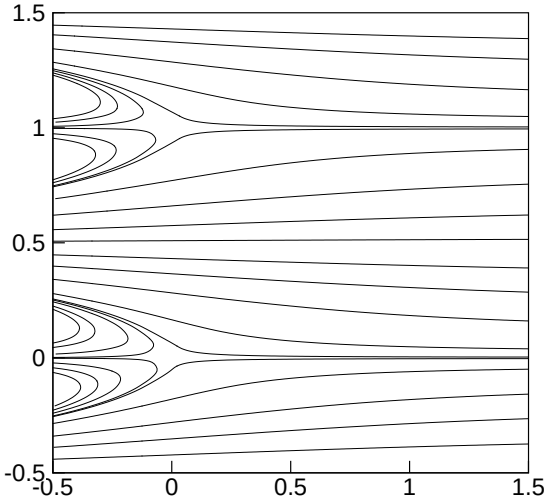

Fig. 44. Streamlines for Kovasznay flow

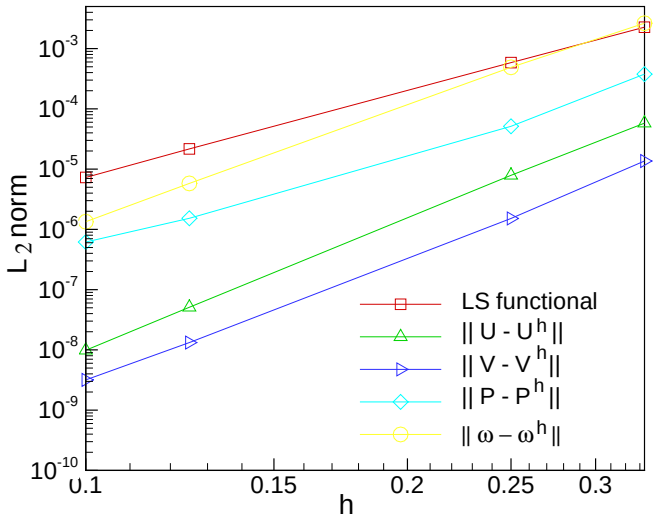

Fig. 45. Convergence of leastsquares functional, velocity, pressure and vorticity field to exact Kovasznay solution

2. Steady flow past a large circular cylinder in a channel

To test mass conservation rigorously, we solve flow past a large circular cylinder in a channel with blockage ratio of 2 (H/D = 2). Domain of interest is $[-10.0, 15.0] \times [-1.0, 1.0]$. Cylinder has unit diameter and it is centered at $(0.0, 0.0)$. No-slip boundary conditions are imposed on side walls. At inlet, boundary conditions are $u = 1.0$ and $v = 0.0$. The outflow boundary conditions are imposed in a weak sense through the least-squares functional. Reynolds number considered here is 40 for which steady state solution exists. Problem is solved for three penalty parameters, 20, 30 and 50.

Fig. 46 contains a close-up view of the geometric discretization around the circular cylinder. We use quadrilateral elements. There are 1824 elements and 1938 nodes in the mesh (Mesh 1). Fig. 47(a) shows streamline plot for the penalty parameter of 30. U-velocity contours around the cylinder are shown in Fig. 47(b). The predicted wake extends 1.68 cylinder radius measured from the back of the cylinder for all three penalty parameters considered here. Next, in Fig. 48(a) and Fig. 48(b), u and v-velocities are plotted along line AB (see Fig. 46). Present results are compared with the results of Prabhakar and Reddy [6] who solved same problem using a spectral/hp penalty least-squares formulation. Present results matches well with the results of Prabhakar and Reddy [6]. Results are almost identical for all three penalty parameters. Mass flow rate at x=0 is calculated and found to be ≈ 2 for all three penalty parameters if Newton's convergence is declared when relative norm of the residual is less than 10^{-6} (it depends on nonlinear convergence).

Next we coarsen the mesh. We generate a similar mesh shown in Fig. 49(a) and Fig. 49(b) with 720 elements and 802 nodes (Mesh 2). U and v-velocities are plotted along line AB and compared with the results obtained with hp penalty least-squares formulation. While u-velocity profile matches to a good extent, v-velocities are quite off. Speculating that till now mass conservation was good because of fine mesh and not because of penalty

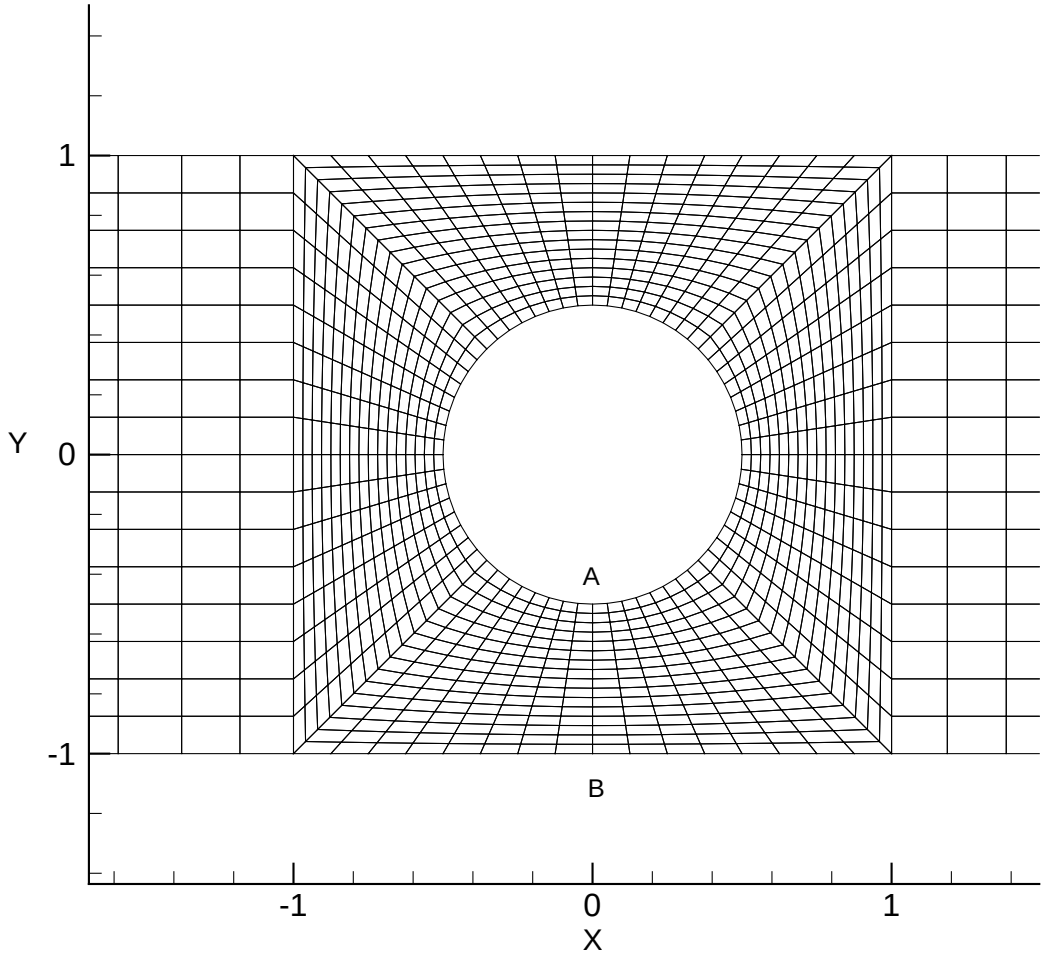

Fig. 46. Close view of geometric discretization around the cylinder

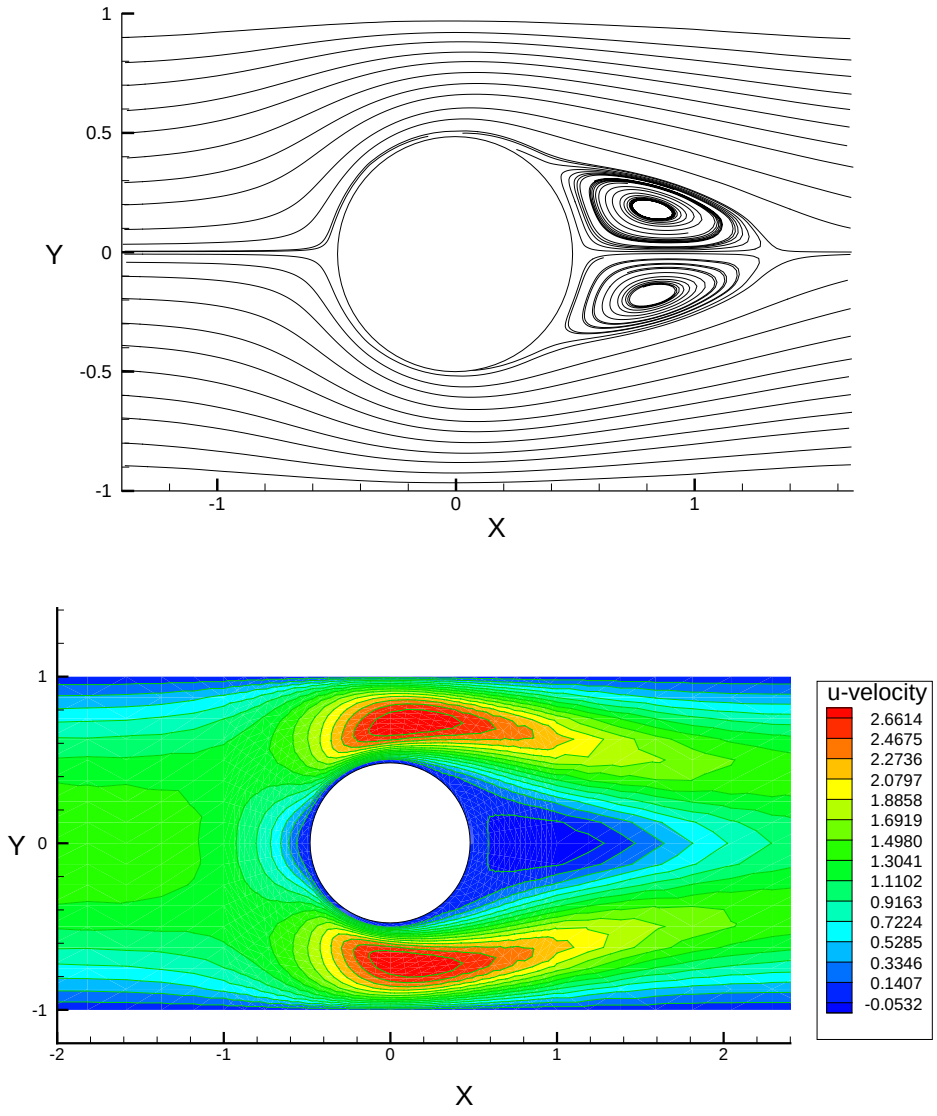

Fig. 47. Flow past a large circular cylinder in a channel (a)Streamlines (b)u-velocity contours

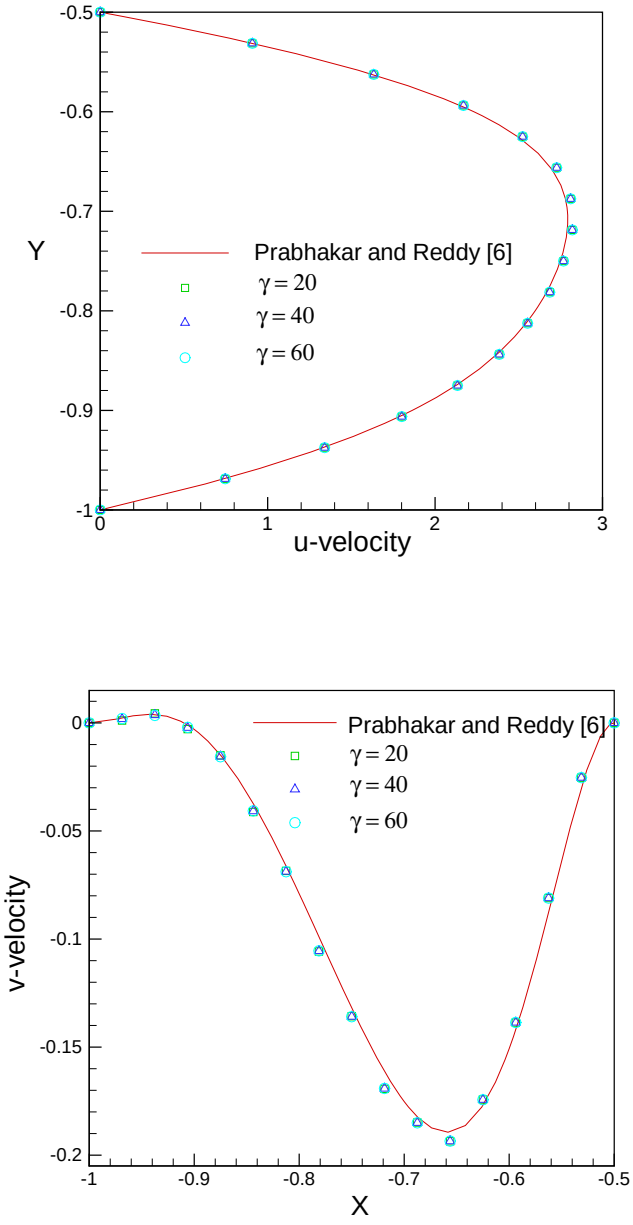

Fig. 48. (a) Variation of u-velocity along AB (b) Variation of vvelocity along AB (Mesh 1)

parameter, we increase penalty parameter in an attempt to get better mass conservation and hence accurate results. But all three penalty parameters (20, 40, 60) produce equally 'inaccurate results' on coarse mesh showing that penalty parameter of 20 is sufficient to enforce continuity constraint and error is because of insufficient mesh resolution and not because of low value of penalty parameter.

3. Transient flow over a backward-facing step

Next, we consider two-dimensional transient flow over a backward-facing step at Re $= 800$. The domain of interest is $\bar{\Omega} = [0, 30] \times [-0.5, 0.5]$. The boundary and initial conditions used here are those used in the work of Gresho et al. [43] and Pontaza and Reddy [12]: u = v = 0 on the horizontal walls, $-p + \mu \partial u/\partial n = 0$ and $\partial v/\partial n = 0$ on the outflow boundary, and u = [tanh(t/4)]u_b(y) + [1-tanh(t/4)]u_p(y) and v=0 on the inflow boundary. Here u_b(y) = max[0,24y(0.5-y)] is the true inlet boundary condition and u_p(y) = 3(0.5-y)(0.5+y) is the Poiseuille flow observed infinitely far downstream at steady flow conditions. The initial velocity field is set to u=u_p(y) and v = 0 everywhere in the computational domain. The inlet condition is varied fast but smoothly from Poisuille flow to flow over a backward facing step.

A 150×50 mesh has been used. Along x direction, there are 90 uniform element till x=15 and 60 uniform element from x=15 to x=30 (Mesh A). Mesh is uniform in y direction. Crank-Nicholson scheme is used for time marching and a time increment of 0.20 has been used for all the results reported in this section.

Fig. 50 shows the evolution of the flow field. The main flow coming from the inlet follows a sinuous path, forming a series of eddies along the upper and lower wall. At the steady state, two eddies (primary and secondary separation zones) remain, all other eddies die out. These plots match qualitatively well with the published results of Pontaza and Reddy [12]. In the steady state, the primary reattachment length is around 6.10, while

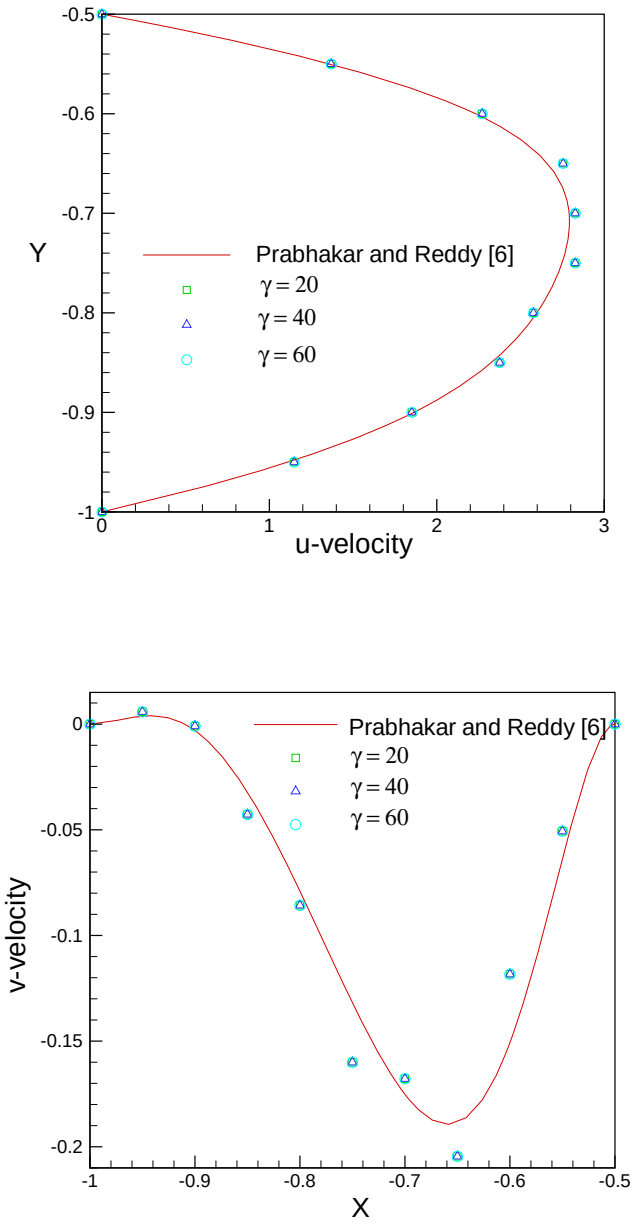

Fig. 49. (a) Variation of u-velocity along AB (b) Variation of vvelocity along AB (Mesh 2)

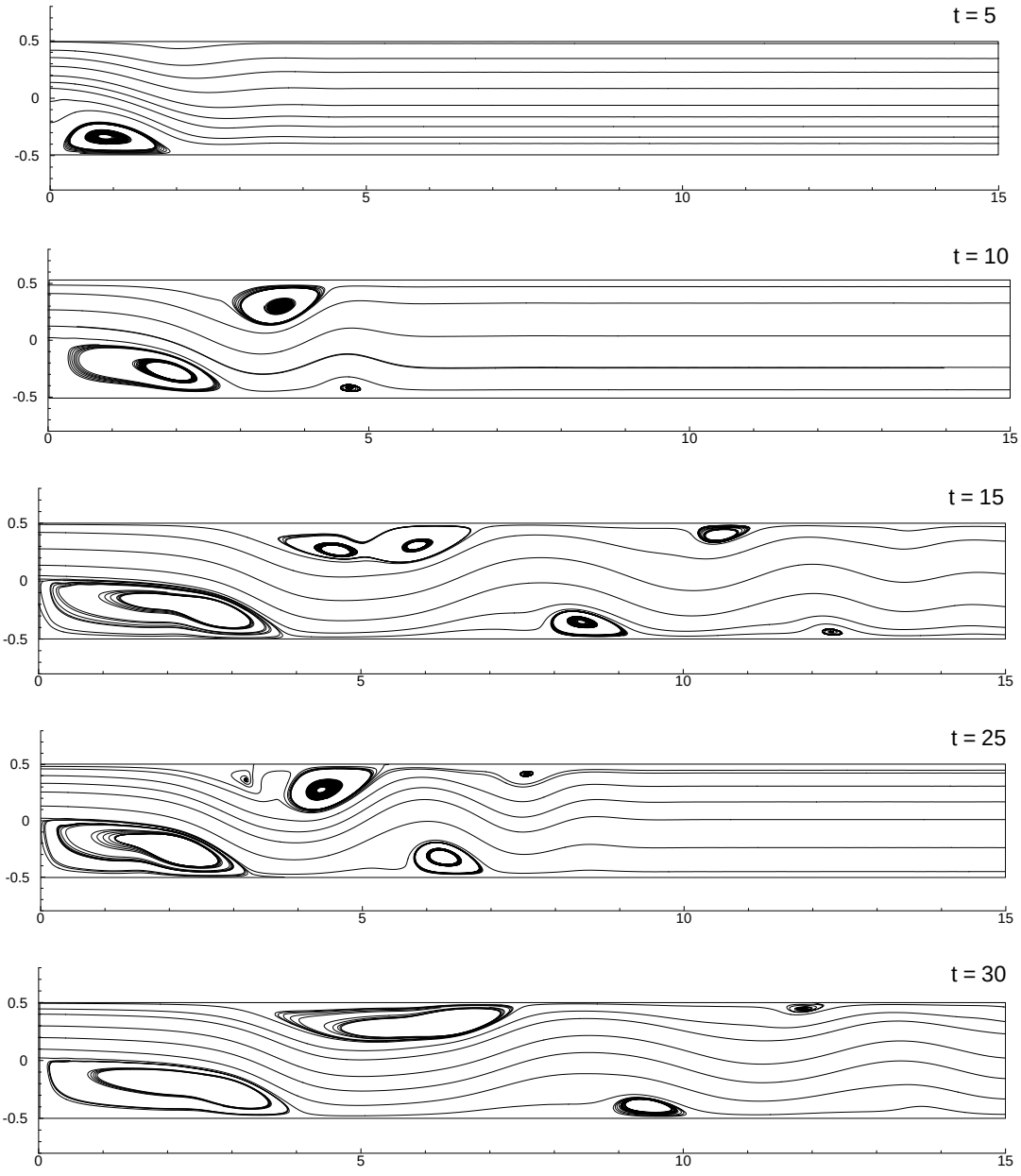

Fig. 50. Time history of streamline plots for flow over a backward facing step

secondary separation and reattachment lengths approximately 4.9 and 10.4 respectively.

Fig. 51 shows the evolution of pressure field. In this formulation pressure field evolves smoothly. The pressure gradient caused by eddies can be seen in these plots. At all time, at the outlet (x=30) there is no pressure gradient in y direction. That's why boundary condition of p=0 also performs well for long domains.

Fig. 52(a) and 52(b) show the time history of the v-velocity component at two locations along the channel's mid-section for the three penalty parameters. For all the penalty parameters, we obtain smooth and monotonic decay of the transient. There are no fluctuations in v-velocity signals showing that mesh resolution is adequate.

Time histories of the mass flow rates across x=5 and x=10 are plotted in Fig. 53 for penalty parameter of 30, 50 and 100. There is less than 1% of mass loss for all three penalty parameters. As expected mass conservation is better for $\gamma = 100$ than $\gamma = 30$ and $\gamma = 50$.

Previous work of Gresho et al. [43], Torczynski [44] and Pontaza and Reddy [12] showed that lack of spatial resolution induces unrealistic temporal chaotic behavior resulting in an erroneous prediction of the long-term behavior of the flow. In such cases either simulation diverges or the velocities fluctuate with time if it converges to steady state [12]. We coarsen the mesh and solve this problem on 100×40 (60+40 in x direction) (Mesh B). This mesh is uniform in y direction. Fig. 54(a) and 54(b) show time history of v-velocity at two locations for various values of penalty parameters. Velocity evolution is slightly off but same for penalty parameters of 50 and 100.

Expecting that penalty parameter is not sufficient to enforce continuity constraint, we increase penalty parameter to 200. Penalty parameter of 200 also produces 'equally inaccurate' showing that inaccuracy in not because of penalty parameter but inadequate mesh resolution. v-signal for $\gamma = 200$ fluctuates more probable because PCG does not converge properly (PCG tolerance of 10^{-6} is used for all simulations). In Fig. 55, time history of mass flow rates are plotted at section x=5 and x=10 for penalty parameters of 50, 100 and

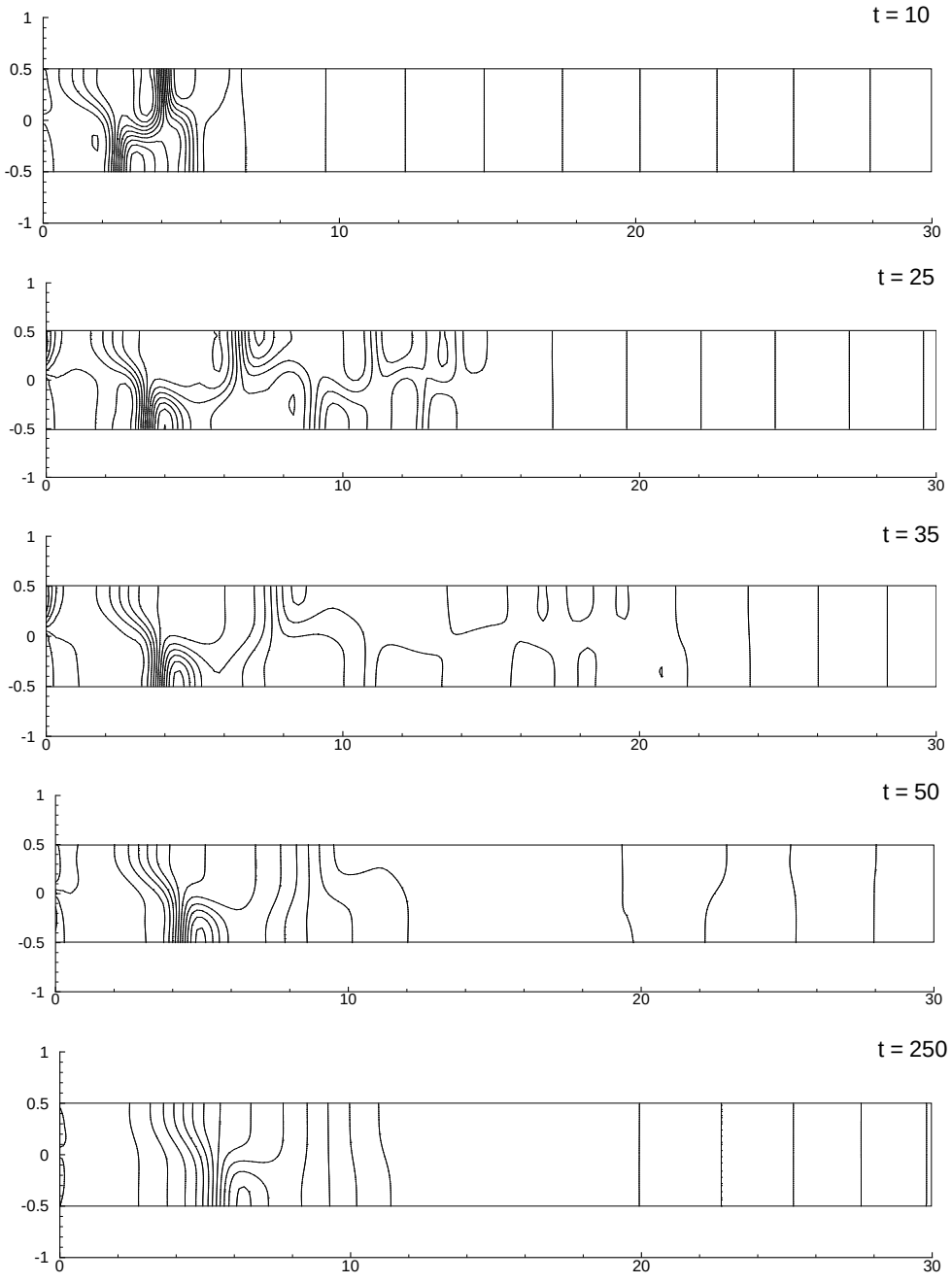

Fig. 51. Time history of pressure contours

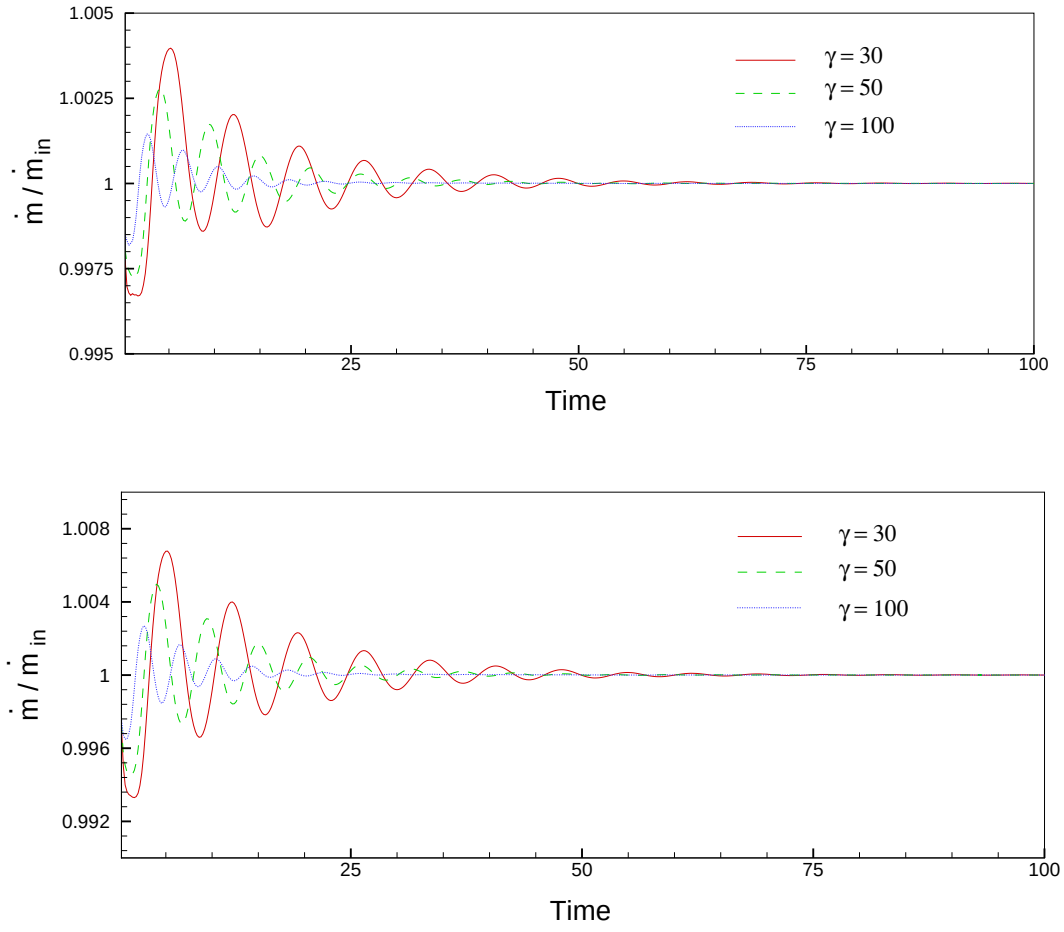

Fig. 52. Time history of mass flow rate at (a) x = 5 (b) x = 10; Mesh A

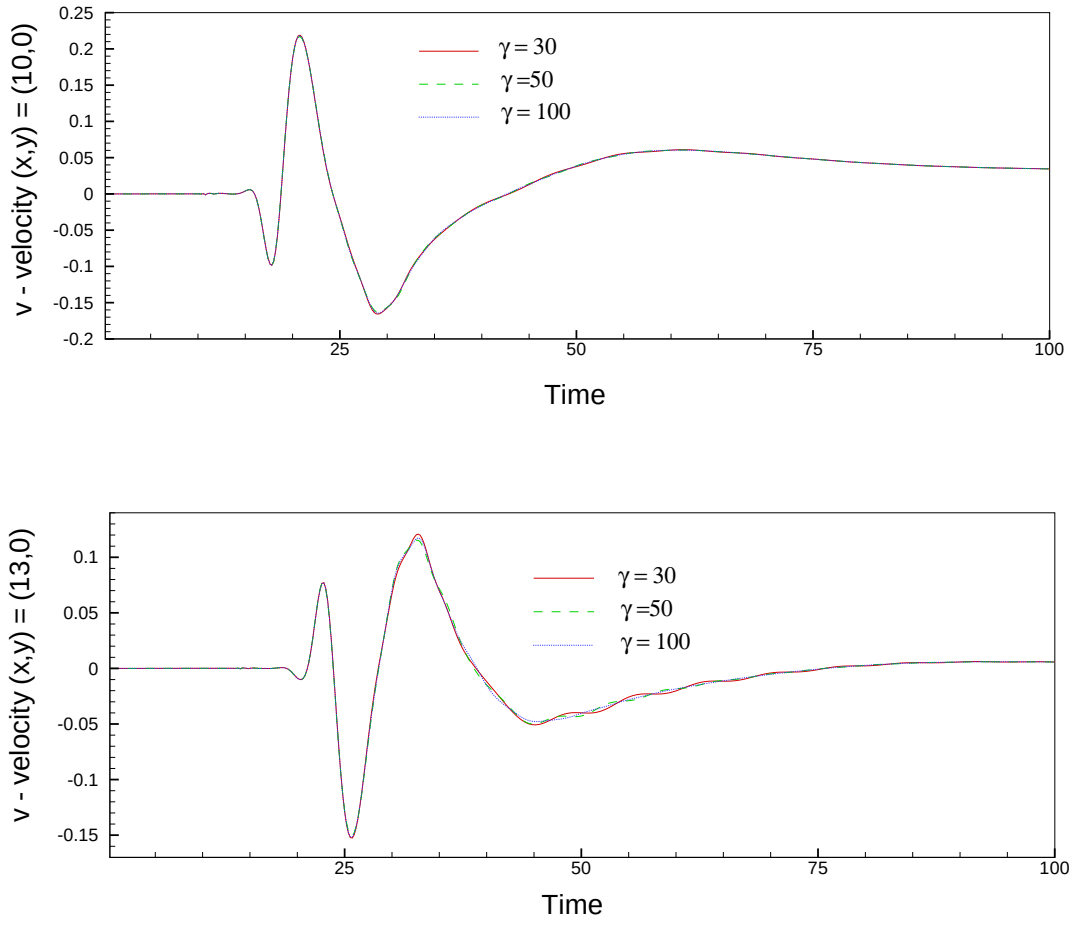

Fig. 53. Time history of the v velocity component at two selected locations : Mesh A

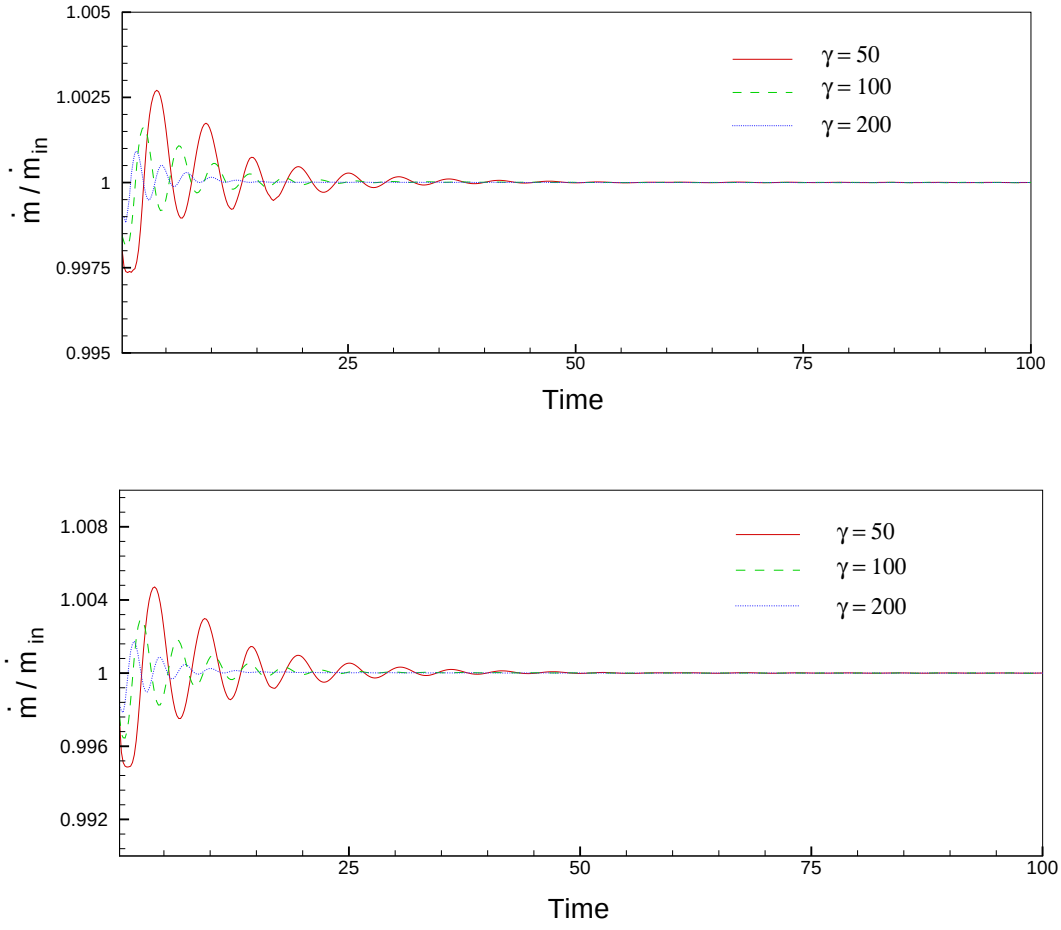

Fig. 54. Time history of mass flow rate at (a) x = 5 (b) x = 10; Mesh B

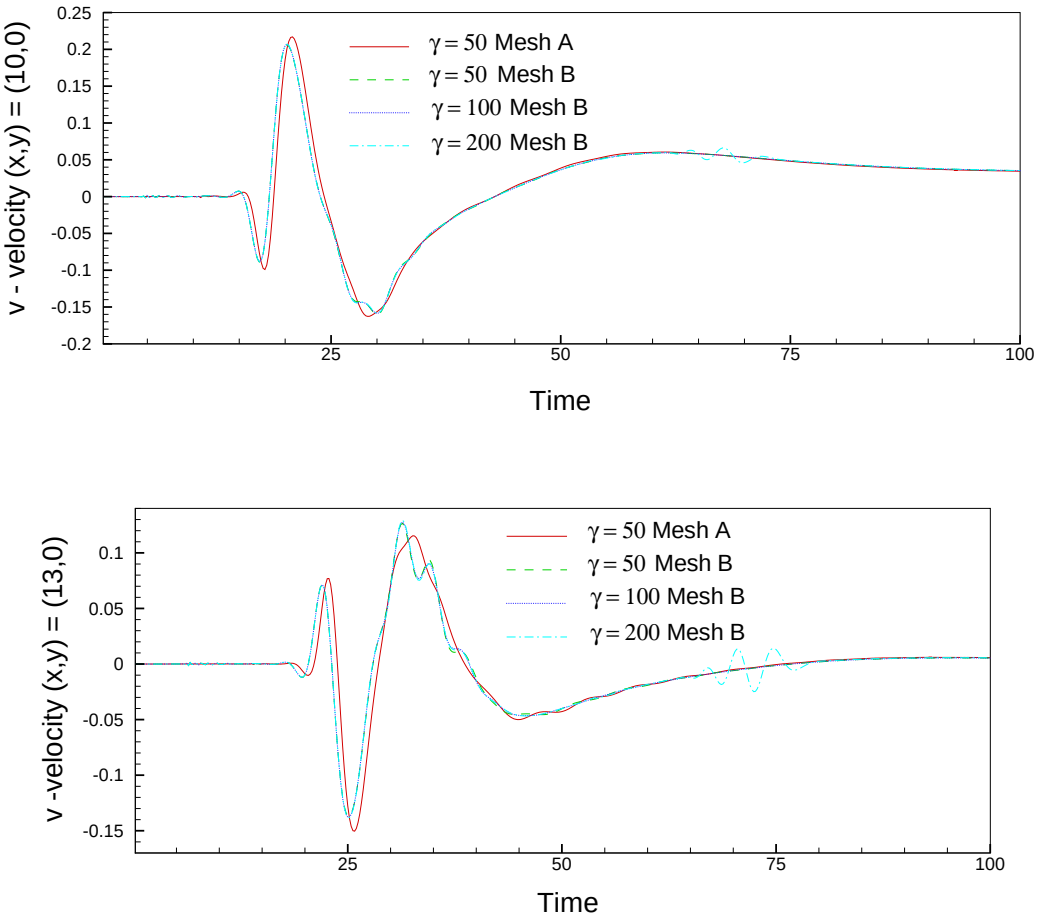

Fig. 55. Time history of the v-velocity component at two selected locations : Mesh B

200. Mass flow rates on this mesh B is almost same as that on mesh A.

D. Temperature-Velocity coupled problem

We consider steady incompressible fluid flow in a domain $\Omega \subset \mathbb{R}^2$ bounded by $\Gamma = \Gamma_\theta \cup \Gamma_q$ where Γ_θ and Γ_q are the isothermal and the adiabatic boundaries as well as $\Gamma_\theta \cap \Gamma_q = \emptyset$. The fluid motion is induced by the temperature gradient across the vertical walls. The buoyancy effect is approximated by the Boussinesq assumption. The Navier-Stokes equations and the energy equation in dimensionless form are given below.

Find the velocity $\mathbf{u}(\mathbf{x})$, pressure $p(\mathbf{x})$ and temperature $\theta(\mathbf{x})$ such that

$$(\mathbf{u}\cdot\nabla)\,\mathbf{u}+\nabla p-\frac{1}{\mathrm{Re}}\nabla\cdot\left[(\nabla\mathbf{u})+(\nabla\mathbf{u})^{\mathrm{T}}\right]+\theta\frac{\mathbf{g}}{|\mathbf{g}|}=\mathbf{0} \qquad \text{in } \Omega \tag{4.25}$$

$$\nabla\cdot\mathbf{u}=0 \qquad \text{in } \Omega \tag{4.26}$$

$$(\mathbf{u}\cdot\nabla)\,\theta-\frac{1}{\mathrm{Pe}}\nabla^{\mathbf{2}}\theta=0 \qquad \text{in } \Omega \tag{4.27}$$

$$\mathbf{u}=\mathbf{u}^{s} \qquad \text{on } \Gamma_u \tag{4.28}$$

$$\hat{\mathbf{n}}\cdot\boldsymbol{\sigma}=\mathbf{f}^{s} \qquad \text{on } \Gamma_f \tag{4.29}$$

$$\theta=\theta^{s} \qquad \text{on } \Gamma_\theta \tag{4.30}$$

$$\hat{\mathbf{n}}\cdot\mathbf{q}=q^{s} \qquad \text{on } \Gamma_q \tag{4.31}$$

where $\mathbf{g}$ is gravitational acceleration vector which is acting in negative y-direction. Here we take the cavity wall length and buoyant speed ($(|\mathbf{g}|\alpha\Delta\theta l)^{1/2}$) as characteristic length and velocity, respectively. The characteristic numbers are Re = $(\mathrm{Ra/Pr})^{1/2}$, Pe $=(\mathrm{Ra\ Pr})^{1/2}$, Ra $=\alpha|\mathbf{g}|l^3\Delta\theta/(\kappa\nu)$ and Pr $=\nu/\kappa$, where α is the volumetric thermal expansion coefficient, l is the characteristic length, $\Delta\theta$ is the characteristic temperature, κ is the thermal diffusivity, and $\nu=\mu/\rho$ is the kinematic viscosity.

1. The vorticity-dilatation/heat flux based first-order system

Vorticity-dilatation and heat flux vector are introduced as independent variables to make the system first order. The resulting first-order system in dimensionless form can be stated as follows:

Find the velocity $\mathbf{u}(\mathbf{x})$, dilatation $D(\mathbf{x})$, vorticity $\boldsymbol{\omega}(\mathbf{x})$, temperature $\theta(\mathbf{x})$ and heat

flux $\mathbf{q}(\mathbf{x})$ such that

$$(\mathbf{u}\cdot\nabla)\,\mathbf{u} - \gamma\nabla D + \frac{1}{\mathrm{Re}}\nabla\times\boldsymbol{\omega} + \theta\frac{\mathbf{g}}{|\mathbf{g}|} + \nabla p^{n-1} = \mathbf{0} \qquad \text{in } \Omega \tag{4.32}$$

$$\boldsymbol{\omega} - \nabla\times\mathbf{u} = \mathbf{0} \qquad \text{in } \Omega \tag{4.33}$$

$$D - \nabla\cdot\mathbf{u} = 0 \qquad \text{in } \Omega \tag{4.34}$$

$$(\mathbf{u}\cdot\nabla)\,\theta + \nabla\cdot\mathbf{q} = 0 \qquad \text{in } \Omega \tag{4.35}$$

$$\mathbf{q} + \frac{1}{\mathrm{Pe}}\nabla\theta = \mathbf{0} \qquad \text{in } \Omega \tag{4.36}$$

$$\mathbf{u} = \mathbf{u}^s \qquad \text{on } \Gamma_u \tag{4.37}$$

$$\boldsymbol{\omega} = \boldsymbol{\omega}^s \qquad \text{on } \Gamma_\omega \tag{4.38}$$

$$\theta = \theta^s \qquad \text{on } \Gamma_\theta \tag{4.39}$$

$$\hat{\mathbf{n}}\cdot\mathbf{q} = q^s \qquad \text{on } \Gamma_q \tag{4.40}$$

The L_2 least-squares formulation and finite element model development proceed in a similar manner as described for the incompressible Navier-Stokes equations.

2. Numerical example: Buoyancy-driven flow inside a square enclosure

As a numerical example, we consider two-dimensional, steady, buoyancy-driven flow in a square enclosure with differentially heated vertical walls. The square enclosure is taken to be the unit square, $\bar{\Omega} = [0,1]\times[0,1]$. A finite element mesh of 100×100 nonuniform quadrilateral finite elements is used to discretize the domain with the corner element having dimension 0.001×0.001. No slip velocity boundary condition is imposed on all solid walls. q_y is 0 at the top and bottom walls while left side wall is kept at $\theta = 1$ and right side wall at $\theta = 0$.

Computations have been performed for Rayleigh numbers of 10^5 and 10^6. Air is taken

as the working fluid with Prandtl number 0.71. Computations have been performed for penalty parameters of 10, 20 and 40.

The Nusselt number on the vertical boundary at x=0 is calculated as

$$Nu(y) = q_x(y)\,\text{Pe}$$

and the average Nusselt number (at x=0) is calculated as

$$\overline{Nu} = \int_0^1 Nu(y)dy$$

Components of heat flux are taken to be the primary variables. Therefore, in spite of using C^0 continuous basis functions, we obtain smooth solution for heat fluxes. The average Nusselt number on the boundary is calculated using numerical integration using 9-point Gauss quadrature. We use Ra continuation method, start with Ra = 10^5 and proceed till 10^6 with Ra increment of 10^5. Zero initial guess is used for Ra = 10^5. It takes 10 Newton's iterations to converge for Ra = 10^5. Subsequent Rayleigh numbers take 2-3 Newton's iterations to converge.

Fig. 56 contains plots of streamlines of the flow field and temperature distribution for Rayleigh numbers of 10^5 and 10^6. The patterns exhibit the required centrosymmetry and are in qualitative agreement with previously reported numerical results of Davis [26]. Fig. 57(a) contains the plot of u-velocity profile along the vertical mid-line for penalty parameters of 10 and 20 for Rayleigh number of 10^6. All three penalty parameters give identical values. Fig 57(b) contains plots of temperature distributions along the vertical mid-line for three penalty parameters. Again all three penalty parameters give identical values. The average Nusselt number on the vertical boundary of the cavity at $x = 0$ for Rayliegh numbers are compared with the benchmark result of Davis [26] in Table VI.

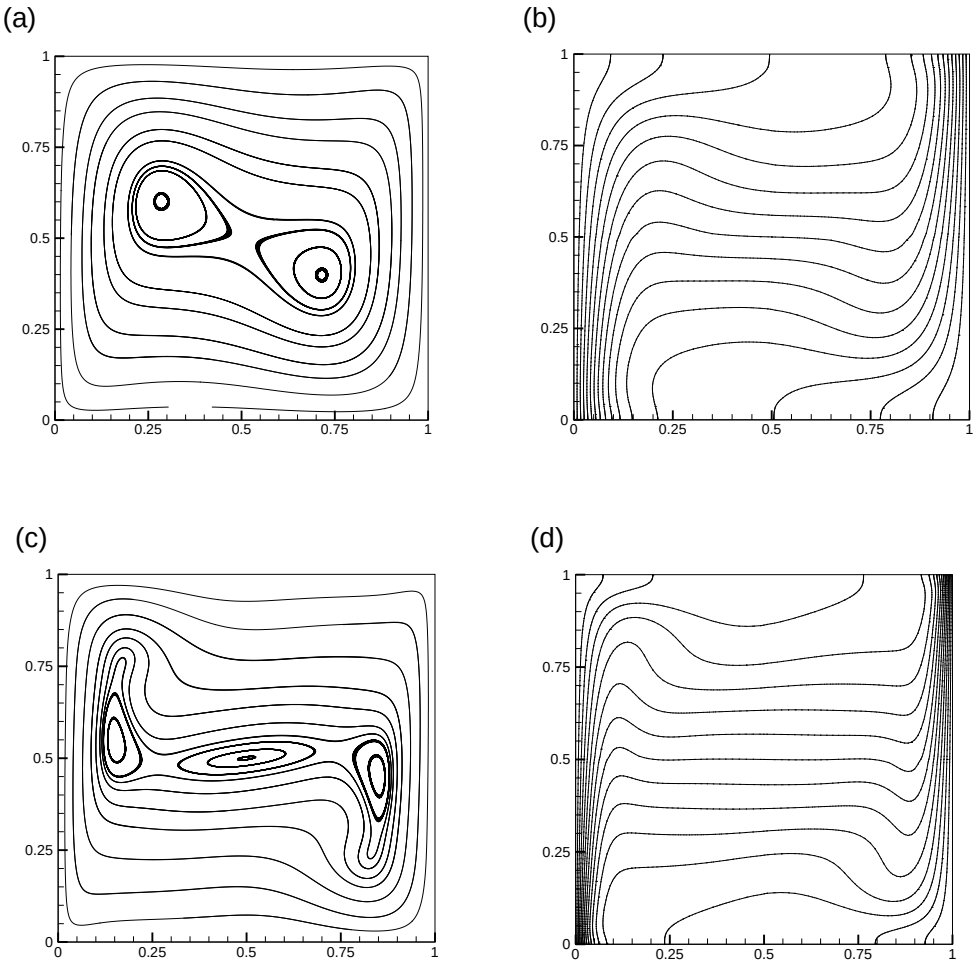

Fig. 56. Numerical results for 2D thermal cavity flow. (a) Streamlines at $Ra = 10^5$ (b) temperature contours for $Ra = 10^6$, (c) streamlines for $Ra = 10^6$ (d) temperature contours for $Ra = 10^6$

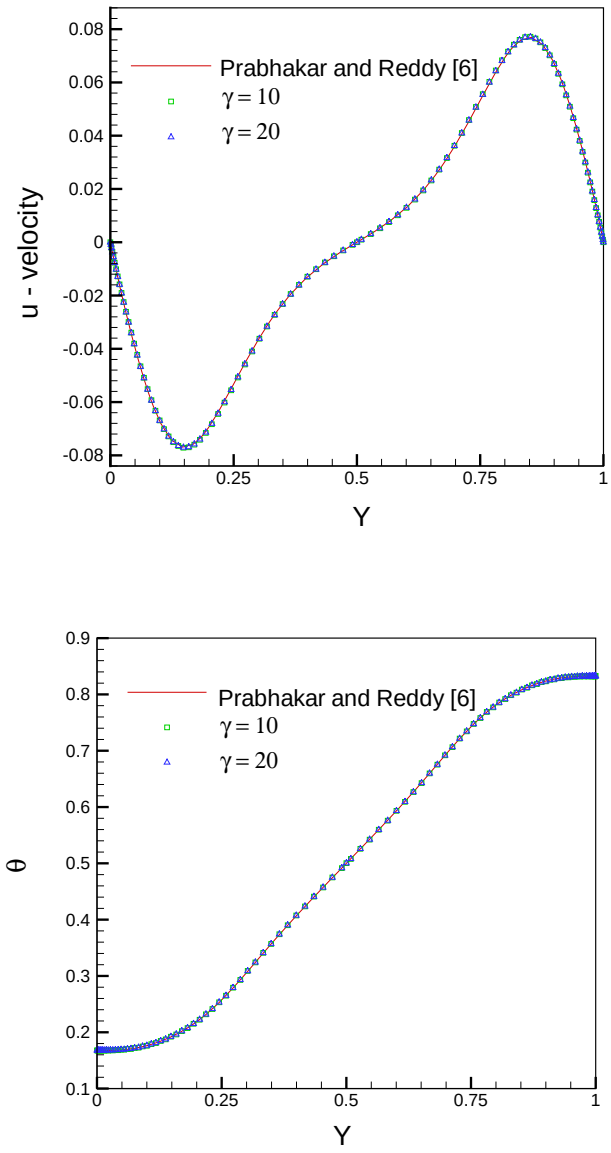

Fig. 57. (a) u-velocity (b)temperature along the vertical midline of the enclosure $Ra = 10^6$

Table VI. Average Nusselt number on the vertical boundary of the cavity at $x = 0$.

	$\gamma = 10$	$\gamma = 20$	$\gamma = 40$	Davis [26]
Ra $= 10^5$	4.517	4.526	4.533	4.509
Ra $= 10^6$	8.833	8.845	8.853	8.817

Next, we coarsen the mesh and solve the problem on 50×50 non-uniform mesh with corner element of size 0.002 (elements sizes are doubled). Temperature and u-velocity profile along vertical midline are plotted in Fig. 58(a) and 58(b). Results are slightly off. In an attempt to fix this, we increase penalty parameter to 60. Still results are 'equally inaccurate' showing that inaccuracy is not because of continuity constraint enforcement and penalty parameter of 20 is sufficient to enforce continuity constraint to a good extent.

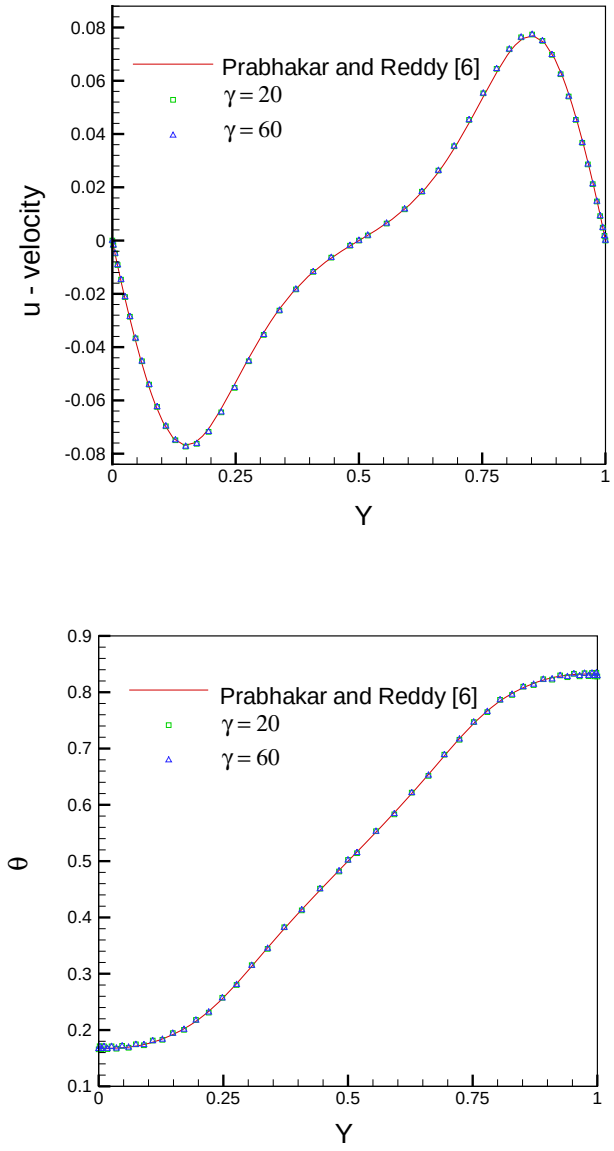

Fig. 58. (a) u-velocity (b)temperature along the vertical midline of the enclosure $Ra = 10^6$: Coarse mesh

CHAPTER V

A STRESS BASED LEAST-SQUARES FINITE ELEMENT MODEL FOR INCOMPRESSIBLE NAVIER-STOKES EQUATIONS

A. Introduction

In the past few years finite element models based on least-squares variational principles have drawn considerable attention for the solution of Stokes and Navier-Stokes equations [1, 2, 3, 4, 5, 6]. Least-squares based finite element formulations offer several theoretical and computational advantages. Most notably, such formulations circumvent the inf-sup condition of Ladyzhenskaya-Babuska-Brezzi (LBB). As a result equal order interpolation functions can be used for all field variables. They also yield symmetric positive-definite coefficient matrix and therefore robust iterative solvers can be used to solve resulting system of algebraic equations.

Vorticity based least-squares formulation is the most popular first order formulation for the solution of Stokes and Navier-Stokes equations since only one additional independent variable is introduced in 2D compared to three in stress based formulation and four in velocity-flux formulation. In this chapter we present a stress based least-squares finite element formulation that carries five independent variables. In the proposed formulation, continuity equation becomes an algebraic equation and is eliminated from the system of governing equations with suitable modifications.

Bochev and Gunzburger [46] studied stress based first order system for the incompressible Stokes equations but retained continuity equation. They analyzed weighted (mesh dependent weights) as well as the unweighted L_2 least-squares functional. They showed that weighted least-squares formulation converges faster but suffers from the problem of bad conditioning of the coefficient matrix. They tested the formulation with several model

problems. However, no detailed numerical results were reported.

Previous studies [8, 9] showed that mass conservation is not very good in least-squares based formulations. Chang and Nelson [8] suggested that this is because the error is minimized on a global scale, allowing errors of significant size to remain on a local scale, especially in areas in which the gradients of the variables are of significant size. They also proposed a remedy. Unfortunately, this remedy, which consists of enforcing the continuity equation as an explicit constraint through the use of Lagrange multipliers, negates one of the main advantages of the least-squares methods, namely, the positive-definiteness of resulting coefficient matrix. Deang and Gunzburger [10] also studied mass conservation in least-squares formulations and analyzed weighted least-squares functionals. These formulations have better mass conservation than un-weighted formulations but conditioning number of the resultant coefficient matrix becomes high. Bolton and Thatcher also addressed this problem for Stokes [9] and Navier-Stokes equations [11] and proposed weighting of particular terms in the least-squares functional. Pontaza and Reddy [5, 12] used high order basis functions and they did not observe problems with mass conservation. However, for unsteady backward facing problem numerical solutions become unstable if sufficiently high p-level was not used. In this study we pay particular attention to mass conservation and solve problems on relatively coarse meshes to check mass conservation. We examine mesh dependence of the solution for transient backward facing step problem.

The chapter is organized as follows. In section B, the stress based least-squares finite element model for the steady incompressible Navier-Stokes equations is presented. Numerical results are presented in section C. The h and p convergence are verified using the exact solution of the Kovasznay flow problem. first we present results for 2D flow past a large circular cylinder in a channel. We check the dependence of mass conservation on mesh size. Next, numerical results are presented for the transient two-dimensional flow over a backward-facing step. We run the simulation for various meshes and report evolu-

tion of velocity field with time. We compare these results with the results obtained using traditional vorticity-pressure formulation. We conclude the chapter with some remarks.

B. The incompressible Navier-Stokes equations

The steady incompressible Navier-Stokes equations in dimensionless form can be written as

$$\nabla \cdot \mathbf{u} = 0 \qquad \text{in } \Omega \tag{5.1}$$

$$(\mathbf{u} \cdot \nabla)\,\mathbf{u} + \nabla p - \frac{1}{\mathrm{Re}}\,\nabla \cdot \left[(\nabla \mathbf{u}) + (\nabla \mathbf{u})^{\mathrm{T}}\right] = \mathbf{f} \qquad \text{in } \Omega \tag{5.2}$$

$$\mathbf{u} = \mathbf{u}^s \qquad \text{on } \Gamma_u \tag{5.3}$$

$$\hat{\mathbf{n}} \cdot \underline{\boldsymbol{\sigma}} = \mathbf{f}^s \qquad \text{on } \Gamma_f \tag{5.4}$$

where $\mathbf{u}(\mathbf{x})$ is the velocity vector, $\underline{\boldsymbol{\sigma}} = -p\,\underline{\mathbf{I}} + 1/\mathrm{Re}\,\left[(\nabla \mathbf{u}) + (\nabla \mathbf{u})^{\mathrm{T}}\right]$ is the total stress, $p(\mathbf{x})$ is the pressure, $\mathbf{f}$ is a dimensionless force, $\hat{\mathbf{n}}$ is the outward unit normal on the boundary of Ω, $\mathbf{u}^s$ is the prescribed velocity on the boundary Γ_u, and $\mathbf{f}^s$ are the prescribed tractions on the boundary Γ_f, $\Gamma = \Gamma_u \cup \Gamma_f$ and $\Gamma_u \cap \Gamma_f = \emptyset$, and Re is the Reynolds number.

1. The stress based first-order system

To define the first-order velocity-pressure-stress system, 'scaled' stress tensor (symmetric part of velocity gradient tensor) is introduced

$$\underline{\mathbf{T}} = \left[(\nabla \mathbf{u}) + (\nabla \mathbf{u})^{\mathrm{T}}\right] \tag{5.5}$$

Then Eqs. (5.1)-(5.4) can be replaced by an equivalent system of first-order equations. The problem now can be stated as one of finding the velocity vector $\mathbf{u}(\mathbf{x})$, pressure $p(x)$

and stress tensor $\underline{\mathbf{T}}(\mathbf{x})$ such that

$$\nabla \cdot \mathbf{u} = 0 \qquad \text{in } \Omega \tag{5.6}$$

$$(\mathbf{u} \cdot \nabla)\,\mathbf{u} + \nabla p - \frac{1}{\mathrm{Re}}\,\nabla \cdot \underline{\mathbf{T}} = \mathbf{f} \qquad \text{in } \Omega \tag{5.7}$$

$$\underline{\mathbf{T}} - \left[(\nabla \mathbf{u}) + (\nabla \mathbf{u})^{\mathrm{T}}\right] = \underline{\mathbf{0}} \qquad \text{in } \Omega \tag{5.8}$$

$$\mathbf{u} = \mathbf{u}^s \qquad \text{on } \Gamma_u \tag{5.9}$$

$$\hat{\mathbf{n}} \cdot \underline{\mathbf{T}} = \mathbf{T}^s \qquad \text{on } \Gamma_T \tag{5.10}$$

In component form these equations can be written as

$$\frac{\partial u}{\partial x} + \frac{\partial v}{\partial y} = 0 \qquad \text{in } \Omega \tag{5.11}$$

$$u\frac{\partial u}{\partial x} + v\frac{\partial u}{\partial y} + \frac{\partial p}{\partial x} - \frac{1}{\mathrm{Re}}\left[\frac{\partial T_{xx}}{\partial x} + \frac{\partial T_{xy}}{\partial y}\right] = f_x \qquad \text{in } \Omega \tag{5.12}$$

$$u\frac{\partial v}{\partial x} + v\frac{\partial v}{\partial y} + \frac{\partial p}{\partial y} - \frac{1}{\mathrm{Re}}\left[\frac{\partial T_{xy}}{\partial x} + \frac{\partial T_{yy}}{\partial y}\right] = f_y \qquad \text{in } \Omega \tag{5.13}$$

$$T_{xx} - 2\,\frac{\partial u}{\partial x} = 0 \qquad \text{in } \Omega \tag{5.14}$$

$$T_{xy} - \frac{\partial u}{\partial y} - \frac{\partial v}{\partial x} = 0 \qquad \text{in } \Omega \tag{5.15}$$

$$T_{yy} - 2\,\frac{\partial v}{\partial y} = 0 \qquad \text{in } \Omega \tag{5.16}$$

$$\mathbf{u} = \mathbf{u}^s \qquad \text{on } \Gamma_u \tag{5.17}$$

$$\hat{\mathbf{n}} \cdot \underline{\mathbf{T}} = \mathbf{T}^s \qquad \text{on } \Gamma_T \tag{5.18}$$

Continuity equation can be written as

$$\frac{\partial u}{\partial x}+\frac{\partial v}{\partial y}=0 \qquad \text{in } \Omega \tag{5.19}$$

$$\Rightarrow \qquad T_{xx}=-T_{yy} \qquad \text{in } \Omega \tag{5.20}$$

Continuity equation is eliminated and T_{yy} is replaced by -T_{xx} in the system of governing equations. Then Navier-Stokes and continuity equations can now be replaced by an equivalent system of first-order equations. The problem now can be stated as one of finding the velocity vector $\mathbf{u}(\mathbf{x})$ pressure $p(\mathbf{x})$ and stress tensor components T_{xx}, T_{xy} such that

$$u\frac{\partial u}{\partial x}+v\frac{\partial u}{\partial y}+\frac{\partial p}{\partial x}-\frac{1}{\text{Re}}\left[\frac{\partial T_{xx}}{\partial x}+\frac{\partial T_{xy}}{\partial y}\right]=f_x \qquad \text{in } \Omega \tag{5.21}$$

$$u\frac{\partial v}{\partial x}+v\frac{\partial v}{\partial y}+\frac{\partial p}{\partial y}-\frac{1}{\text{Re}}\left[\frac{\partial T_{xy}}{\partial x}-\frac{\partial T_{xx}}{\partial y}\right]=f_y \qquad \text{in}\Omega \tag{5.22}$$

$$T_{xx}-2\frac{\partial u}{\partial x}=0 \qquad \text{in } \Omega \tag{5.23}$$

$$T_{xy}-\frac{\partial u}{\partial y}-\frac{\partial v}{\partial x}=0 \qquad \text{in } \Omega \tag{5.24}$$

$$-T_{xx}-2\frac{\partial v}{\partial y}=0 \qquad \text{in } \Omega \tag{5.25}$$

$$\mathbf{u}=\mathbf{u}^s \qquad \text{on } \Gamma_u \tag{5.26}$$

$$\hat{\mathbf{n}}\cdot\underline{\mathbf{T}}=\mathbf{T}^s \qquad \text{on } \Gamma_T \tag{5.27}$$

a. L_2 least-squares formulation

The least-squares functional of the problem can be set up by summing up the squares of the residual of the new set of equations

$$\mathcal{J}(\mathbf{u},p,T_{xx},T_{xy};\mathbf{f})=\frac{1}{2}\left(\left\|R_1\right\|_0^2+\left\|R_2\right\|_0^2+\left\|R_3\right\|_0^2+\left\|R_4\right\|_0^2+\left\|R_5\right\|_0^2\right) \tag{5.28}$$

where R_1, R_2, R_3, R_4, R_5 are the residuals of Eqs. (5.21)- (5.25).

Considering the homogeneous pure velocity boundary condition case, the least-squares principle for functional (5.28) can be stated as:
find the velocity vector $\mathbf{u}(\mathbf{x})$, pressure $p(x)$ and stress components T_{xx} and T_{xy} such that

$$\mathcal{J}(\mathbf{u}, p, T_{xx}, T_{xy}; \mathbf{f}) \leq \mathcal{J}\left(\tilde{\mathbf{u}}, \tilde{p}, \tilde{T_{xx}}, \tilde{T_{xy}}; \mathbf{f}\right) \qquad \forall \ \left(\tilde{\mathbf{u}}, \tilde{p}, \tilde{T_{xx}}, \tilde{T_{xy}}\right) \in \mathbf{X} \tag{5.29}$$

where we use the space

$$\mathbf{X} = \left\{ (\mathbf{u}, p, T_{xx}, T_{xy}) \in \mathbf{H}_0^1(\Omega) \times H^1(\Omega) \cap \bar{L}_2(\Omega) \times H^1(\Omega) \times H^1(\Omega) \right\}$$

The variational problem and finite element model are constructed in conventional way, details of which can be found in [5].

We use space-time decoupled formulation where discretization in space and time are done independently. The Crank-Nicolson scheme is used for time approximation.

b. Expansion bases

There is no compatibility condition, such as LBB condition, in this formulation so all the variables are approximated using the same interpolation functions. We use low order basis functions (bilinear Lagrange basis functions) in this study except when we verify h and p convergence, we use high order nodal expansion.

Nodal expansion: In the standard interval $\Omega_{st} = \{\xi | -1 < \xi < 1\}$ nodal expansions are defined as

$$\psi_i(\xi) = \frac{(\xi - 1)(\xi + 1)L_p'(\xi)}{p(p+1)L_p(\xi_i)(\xi - \xi_i)} \tag{5.30}$$

In Eq. (5.30), $L_p = P_p^{0,0}$ is the Legendre polynomial of order p and ξ_i denotes the location of the roots of $(\xi - 1)(\xi + 1)L_p'(\xi) = 0$ in the interval $[-1, 1]$. Details on the multidimen-

sional construction of nodal expansions can be found in Ref. [30].

The integrals are evaluated using Gauss quadrature rules. In the computer implementation, one point Gauss quadrature is used for bilinear Lagange basis functions and Gauss-Lobatto-Legendre rule is used for high order basis functions. For details on standard finite element computer implementation, such as mapping $\bar{\Omega}_e \rightleftarrows \hat{\Omega}_e$, numerical integration in $\hat{\Omega}_e$, and assembly using the direct stiffness approach, see Reddy [27, 28]. For linearization, we use Newton's method, details of which can be found in [31].

C. Numerical results

In this section, numerical results obtained with the present least-squares finite element model are presented. First, h and p convergence of the proposed formulation are verified. Next, results are presented for steady flow past a circular cylinder and transient flow over a backward facing step.

For all the problems considered in this chapter, non-linear convergence is declared when the relative norm of the residual, $\|\Delta\mathbf{U}\|/\|\mathbf{U}\|$ is less than 10^{-3} unless mentioned, where **U** is the solution vector (includes all degrees of freedom at a node). Convergence of conjugate gradient is declared when L_2-norm of error is less than 10^{-6}.

1. Verification problem: Kovasznay flow

The benchmark problem to be used for the purpose of verification of the least-squares based finite element model is an analytical solution to the two-dimensional steady incompressible Navier-Stokes due to Kovasznay [34]. Domain of interest is $\bar{\Omega} = [-0.5, 1.5] \times [-0.5, 1.5]$. The solution is given by

$$u = 1 - e^{\lambda x} \cos(2\pi y) \tag{5.31}$$

$$v = \frac{\lambda}{2\pi}\, e^{\lambda x}\, \sin(2\pi y) \tag{5.32}$$

$$p = p_0 - \frac{1}{2}\, e^{2\lambda x} \tag{5.33}$$

where $\lambda = \mathrm{Re}/2 - [(\mathrm{Re}^2/4) + 4\pi^2]^{1/2}$ and p_0 is a reference pressure (an arbitrary constant).

Dirichlet boundary conditions on velocities are specified using the exact solution given by Eqs. (5.31) and (5.32). The discrete system is linearized using Newton's method and resulting symmetric positive-definite (SPD) system of equations has been solved using PCG solver. Newton's convergence is declared when the relative norm of the residual is less than 10^{-10}. Convergence of conjugate gradient is declared when L_2-norm of error is less than 10^{-10}.

An 8×8 uniform mesh is used . To verify spectral convergence (p-convergence), L_2 norm of least-square functional $\mathcal{J}$ and L_2 error of the velocity, pressure and stress fields are plotted against polynomial order in Fig. 59. On logarithmic-linear scale we obtain almost straight line for all the variables verifying exponential decay with respect to the polynomial degree used.

Next, we perform an h-refinement study. For such a study, we fix the p-level of the element approximation functions, and systematically refine the mesh. The error measures should decay at an algebraic rate as the mesh is refined. On a log-log scale it should be a straight line. We use p-level of 3 for which approximation theory implies that the best convergence rate in the L_2 norm is 4.

Five different uniform meshes are used to perform the h-refinement study. The meshes are varied successively from 6×6 to 20×20. In Fig. 60 L_2 norm of least-square functional $\mathcal{J}$ and L_2 error of the velocity, pressure and stress fields are plotted against h. An algebraic convergence rate slightly better than 4 is achieved by u, v and T_{xy} and slightly lower than 4 is achieved by p, T_{xx} and L_2 norm of error.

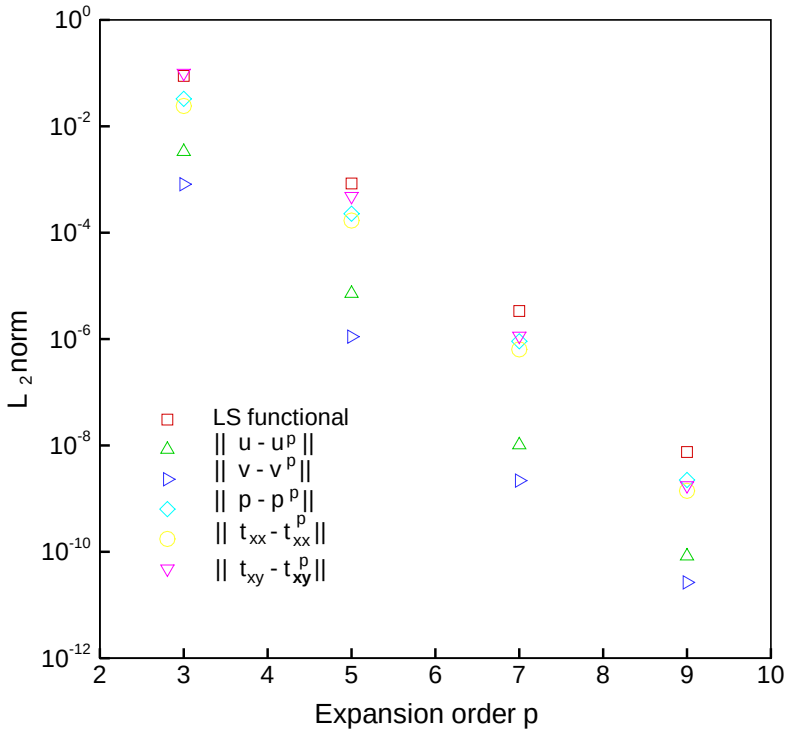

Fig. 59. Convergence of the leastsquares functional, velocity, pressure and stress field to the exact Kovasznzy solution: p-convergence

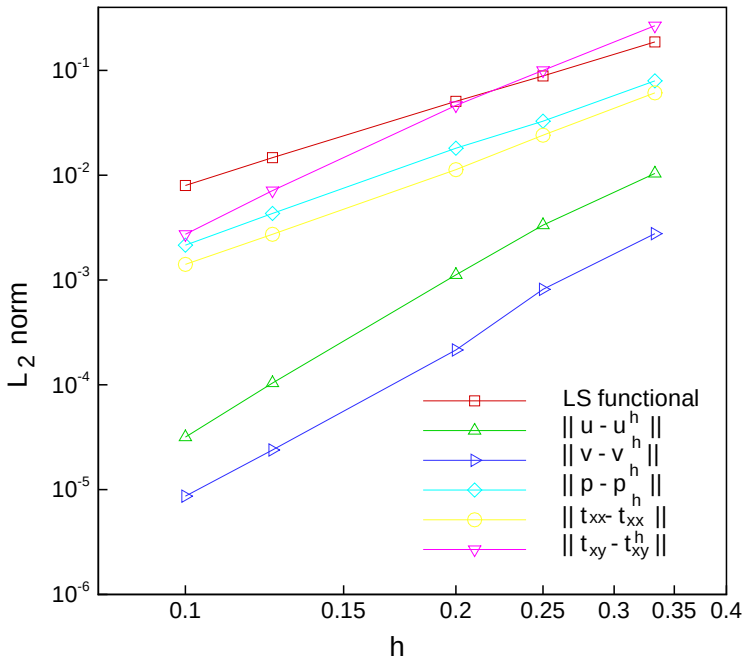

Fig. 60. Convergence of the leastsquares functional, velocity, pressure and stress field to the exact Kovasznay solution: h-convergence

2. Flow past a large circular cylinder in a channel

To test mass conservation rigorously, we solve flow past a large circular cylinder in a channel with blockage ratio of 2 ($H/D = 2$). Chang and Nelson [8] used similar problem to test mass conservation for Stokes flow. Domain of interest is $[-10.0, 15.0] \times [-1.0, 1.0]$. Cylinder has unit diameter and it is centered at $(0.0, 0.0)$. No-slip boundary conditions are imposed on side walls. At inlet boundary conditions are $u = 1.0$ and $v = 0.0$. The outflow boundary conditions are imposed in a weak sense through the least-squares functional. Reynolds number considered here is 40 for which steady state solution exists.

Fig. 61 contains a close-up view of the geometric discretization around the circular cylinder. We use quadrilateral elements. There are 1824 element in the mesh and 1938 nodes (Mesh 1). Fig. 62(a) shows streamline plot. In this case separation delayed. u-velocity contours around the cylinder are shown in Fig. 62(b). The predicted wake extends 1.68 cylinder radius measured from the back of the cylinder.

Next, u and v-velocities are plotted along line AB (see Fig. 61). Present results are compared with the results of Prabhakar and Reddy [6] who solved same problem using Spectral/hp penalty least-squares formulation. Results in [6] are expected to be accurate to a good extent. Present results match well with the results of Prabhakar and Reddy [6]. Mass flow rate at $x = 0$ is calculated and found to be 1.98.

Next we coarsen the mesh. We generate a similar mesh shown in Fig. 61 with 720 elements and 802 nodes (Mesh 2); u and v-velocities are plotted along line AB (see Fig. 64(a) and 64(b)) and compared with the results obtained with hp penalty least-squares formulation. While u-velocity profile matches to a good extent, v-velocities are significantly off.

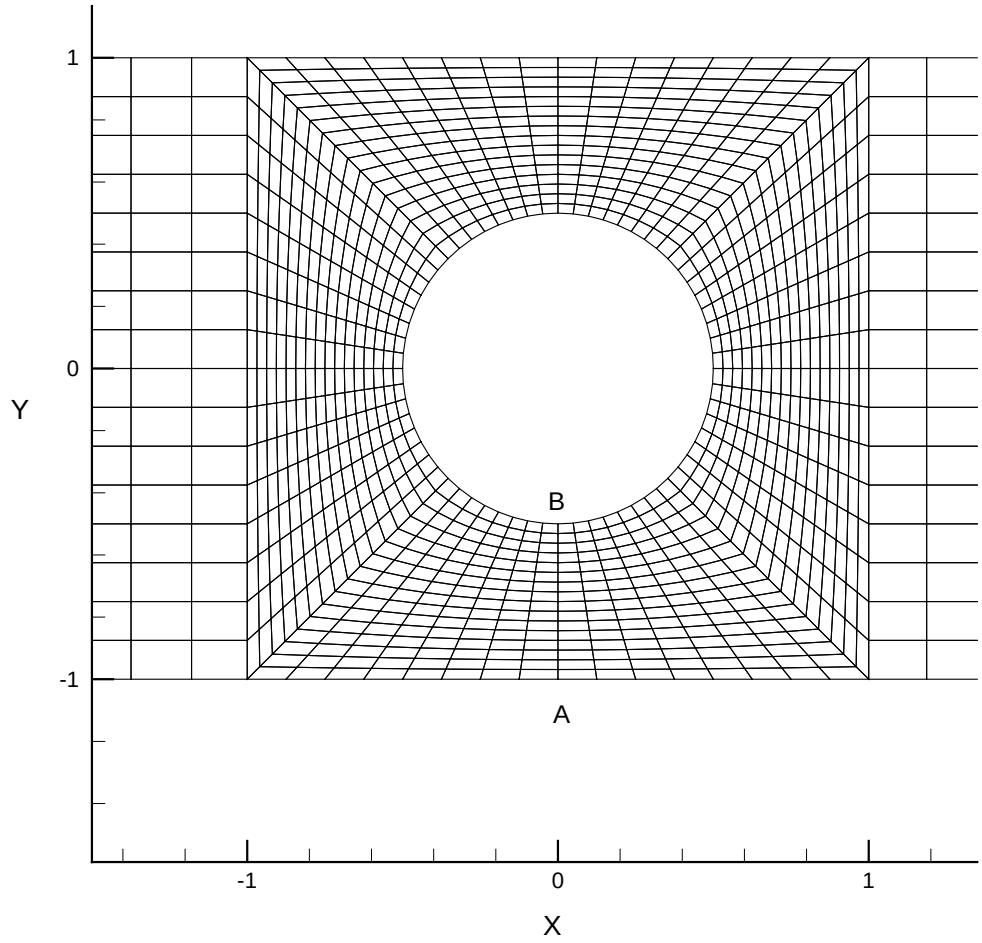

Fig. 61. Close up view of the geometric discretization around the cylinder

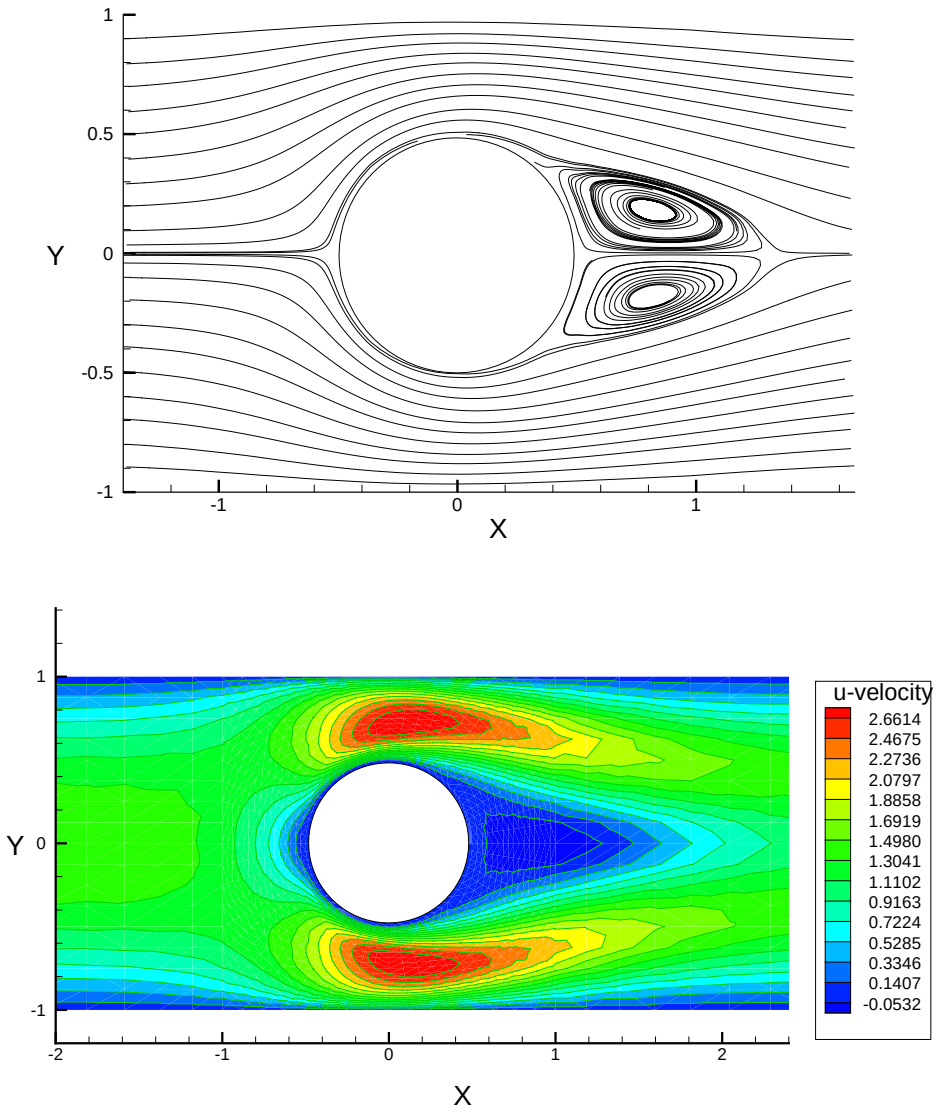

Fig. 62. Flow past a large circular cylinder in a channel (a) Streamlines (b) u-velocity contours

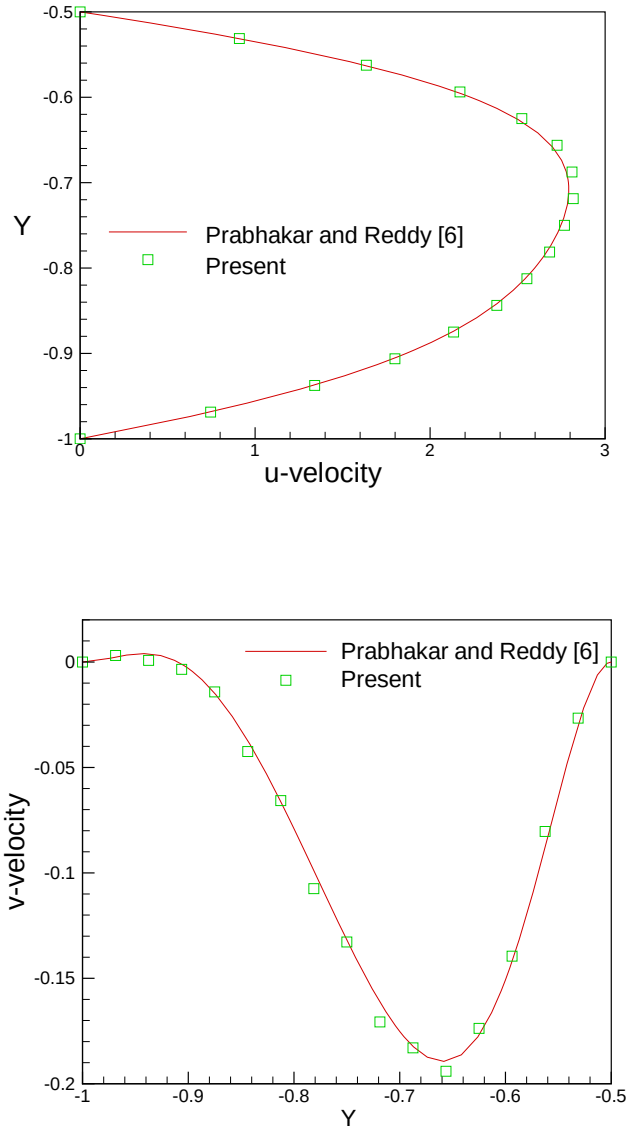

Fig. 63. (a) Variation of u-velocity along AB (b) Variation of v-velocity along AB (Mesh 1)

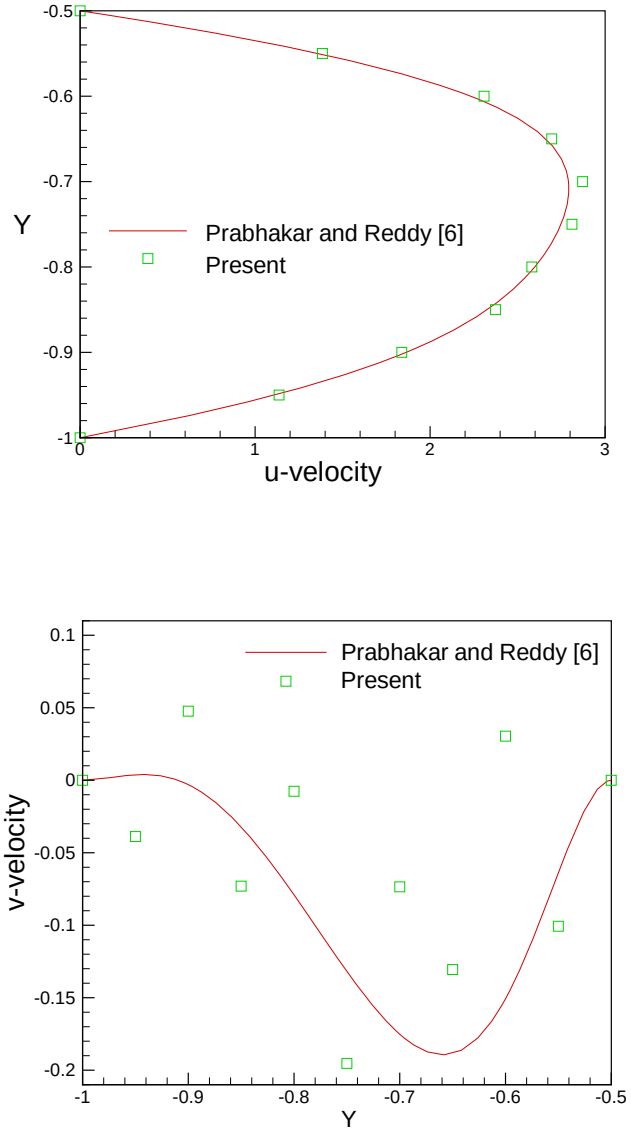

Fig. 64. (a) Variation of u-velocity along AB (b) Variation of v-velocity along AB (Mesh 2)

3. Transient flow over a backward-facing step

Next, we consider two-dimensional transient flow over a backward-facing step at Re $= 800$. The domain of interest is $\bar{\Omega} = [0, 30] \times [-0.5, 0.5]$. The boundary and initial conditions used here are those used in the work of Gresho et al. [43] and Pontaza and Reddy [12]: $u = v = 0$ on the horizontal walls, $-p + \mu \partial u/\partial n = 0$ and $\partial v/\partial n = 0$ on the outflow boundary, and $u = [\tanh(t/4)]u_b(y) + [1 - \tanh(t/4)]u_p(y)$ and $v = 0$ on the inflow boundary. Here $u_b(y) = \max[0, 24y(0.5 - y)]$ is the true inlet boundary condition and $u_p(y) = 3(0.5 - y)(0.5 + y)$ is the Poiseuille flow observed infinitely far downstream at steady flow conditions. The initial velocity field is set to $u = u_p(y)$ and $v = 0$ everywhere in the computational domain. The inlet condition is varied fast but smoothly from Poisuille flow to flow over a backward facing step.

A 150×50 mesh has been used. Along x direction, there are 90 uniform element till $x = 15$ and 60 uniform element from $x = 15$ to $x = 30$. Mesh is uniform in the y direction. A time increment of 0.2 has been used for time marching.

Fig. 65 shows the evolution of the flow field. The main flow coming from the inlet follows a sinuous path, forming a series of eddies along the upper and lower wall. At the steady state, two eddies (primary and secondary separation zones) remain, all other eddies die out. These plots match qualitatively well with the published result of Pontaza and Reddy [12].

We also solve this problem using vorticity based first-order least-squares finite element method under the same conditions. Fig. 66 shows the time history of the v-velocity component at two locations along the channel's mid-section for stress based and vorticity based first order formulations. Both formulations predict same velocity evolution. There are no fluctuations in v-velocity signal showing that mesh resolution is adequate.

Previous work of Gresho et al. [43], Torczynski [44] and Pontaza and Reddy [12]

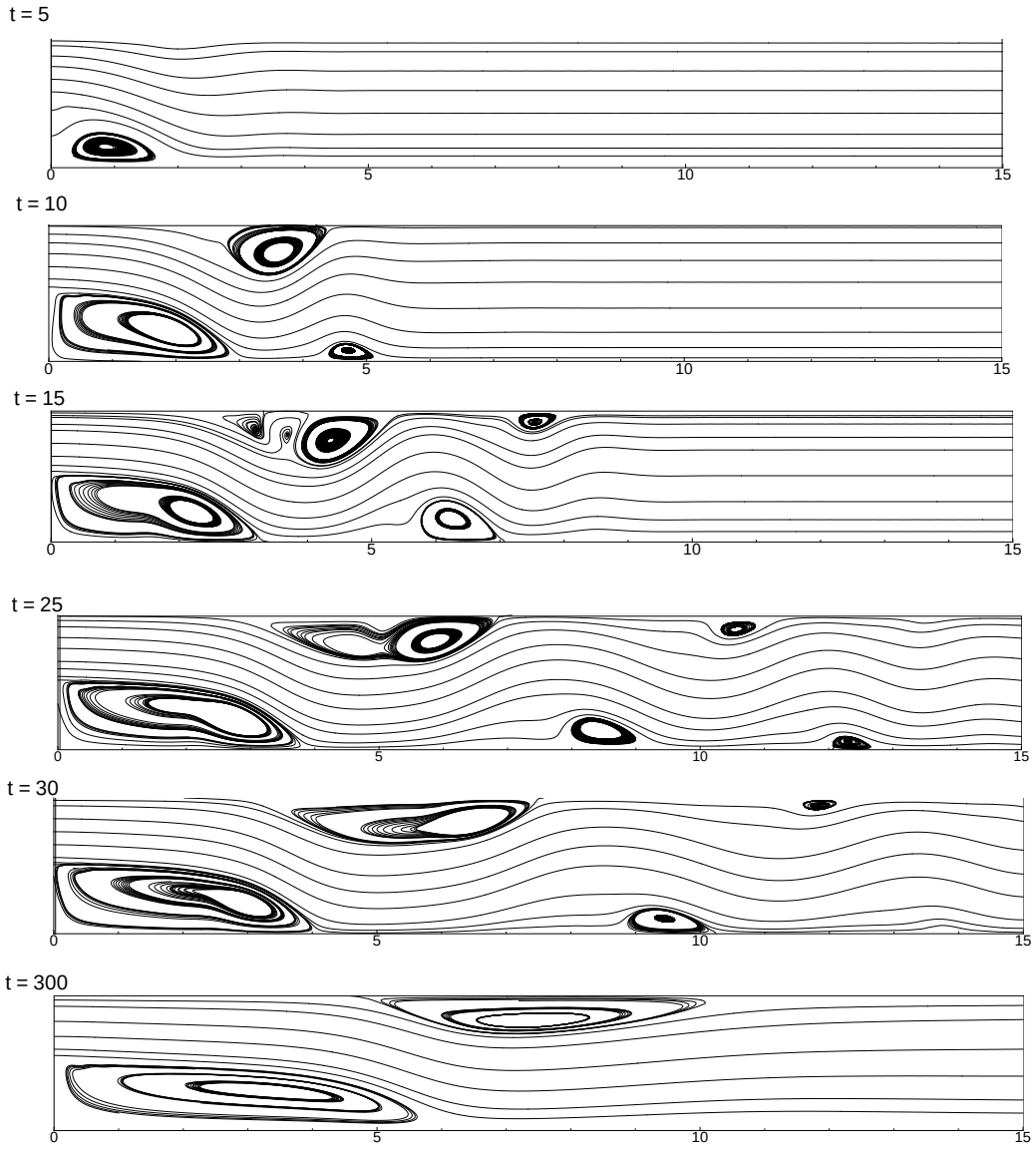

Fig. 65. Time history of streamline plots for flow over a backward facing step

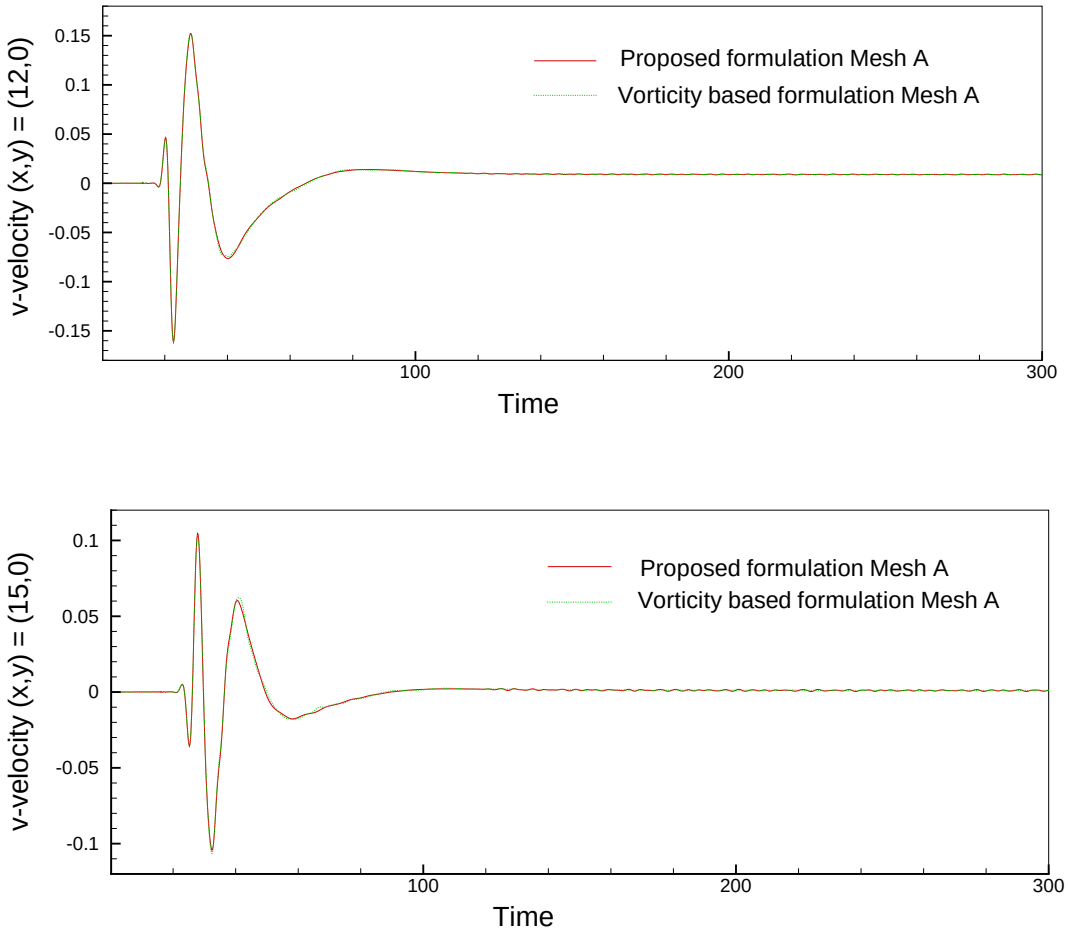

Fig. 66. Time history of the v-velocity component at two selected locations: Mesh A

showed that lack of spatial resolution induces unrealistic temporal chaotic behavior resulting in an erroneous prediction of of the long-term behavior of the flow. In such cases either simulation diverges or the velocities fluctuate with time if it converges to steady state [12].

We coarsen the mesh and solve this problem on 60×20 (40+20 in the x direction) and 40×16 mesh (25+15 in the x direction). These meshes are uniform in the y direction. Fig. 67 shows time history of v-velocity at two locations for both stress based and vorticity based formulations for 60×20 mesh. Stress based formulation does not show much sensitivity towards mesh coarsening and for 60×20 grid results are close to that for

150×50. Vorticity based formulation shows pronounced fluctuation in v-velocity. However simulation does not diverge.

On 40×16 mesh, v-velocity evolutions are same for both the formulations but significantly off from accurate results on 150×50 mesh (Fig. 68). Steady state is achieved in these simulations.

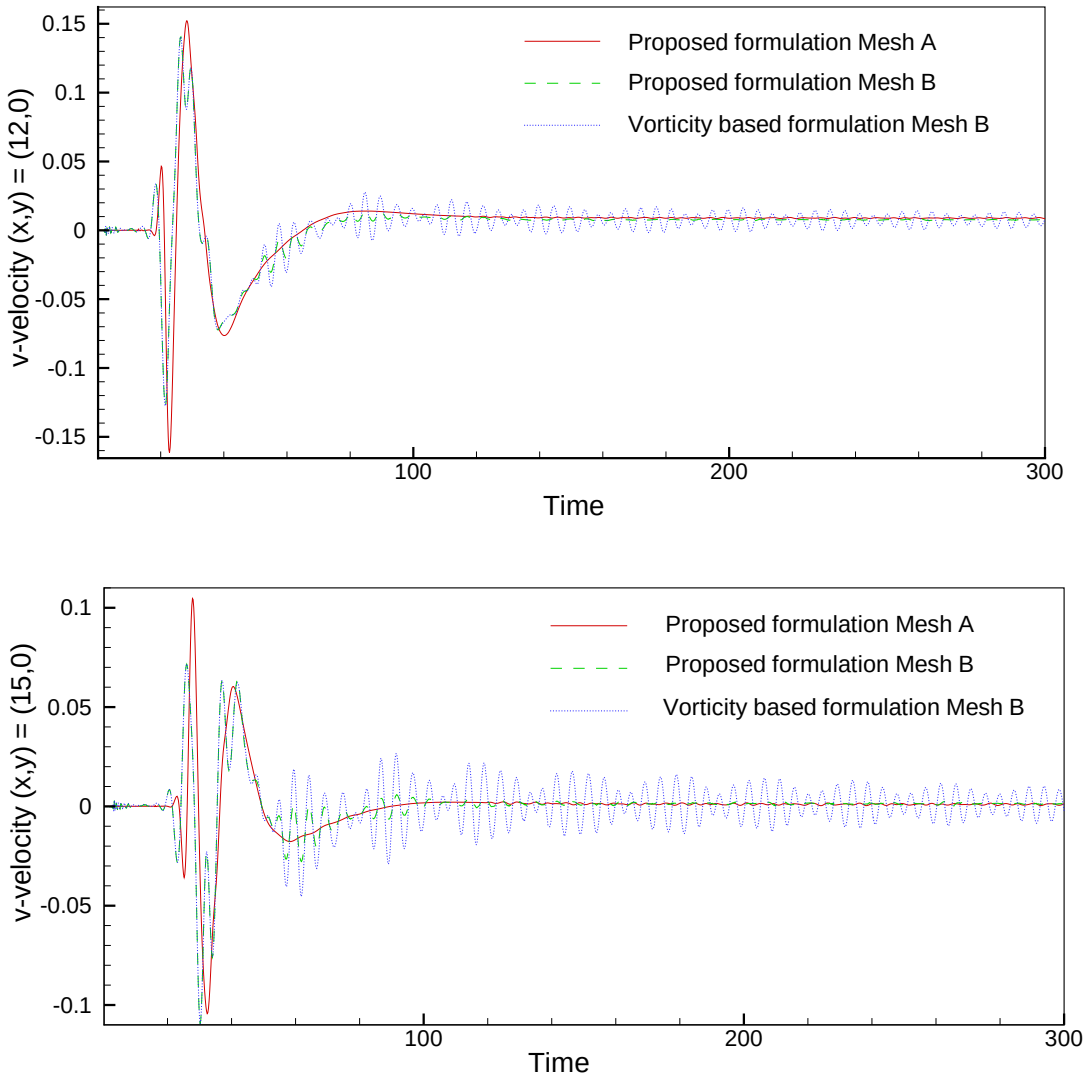

Fig. 67. Time history of the v-velocity component at two selected locations: Mesh B

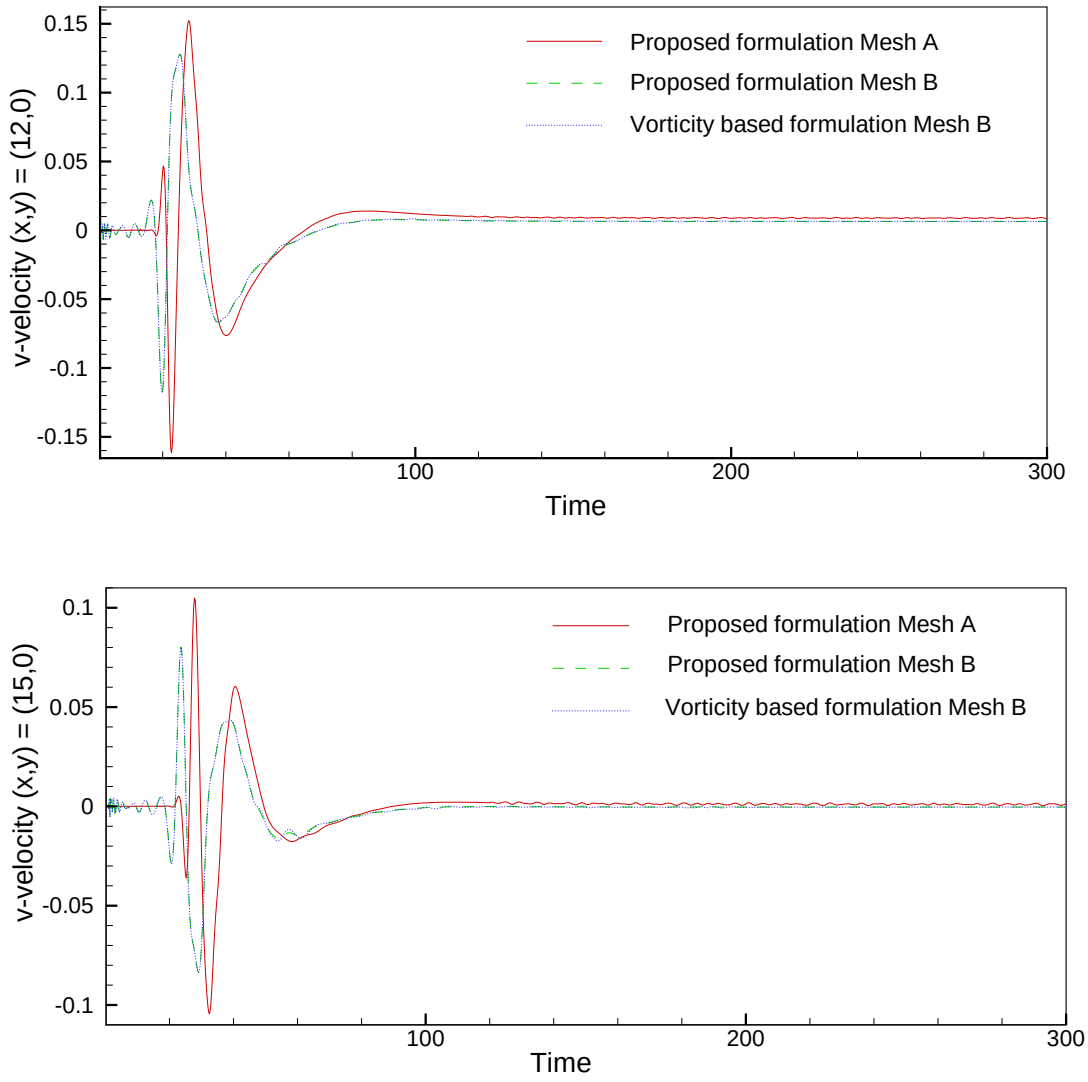

Fig. 68. Time history of the v-velocity component at two selected locations: Mesh C

CHAPTER VI

LEAST-SQUARES BASED FINITE ELEMENT FORMULATIONS FOR VISCOELASTIC FLUID FLOWS

A. Introduction

In the last two decades, much effort has been devoted to devising stable numerical algorithms for viscoelastic flows [47, 48, 49]. However, limits in the maximum attainable Weissenberg number, a parameter that characterizes the degree of viscoelasticity (memory effect), still exist. The mathematical model of viscoelastic flows consists of the continuity equation, momentum equations, and constitutive equations relating stress to strain. Constitutive equations for viscoelastic fluids can be differential equations or integral equations. Generally, due their simplicity, differential constitutive equations are used, which have hyperbolic character [50]. Coupling these hyperbolic constitutive equations to the elliptic momentum equations leads to a system of equations with mixed character.

The constitutive equations are, in general, nonlinear, and the nonlinearity depends on a nondimensional number called Weissenberg number, which is a measure of the memory of the fluid. Most numerical algorithms fail to converge above a critical value of this parameter [51]. Stabilization techniques have been used to remove numerical instabilities in order to extend the range of Weissenberg number over which converged solution can be obtained. For steady-state viscoelastic flow problems, it has been demonstrated that with some kind of stablizing measures, such as elastic viscous stress split (EVSS) [52] and adaptive viscous stress split (AVSS) [53], numerical stability can be improved. The idea is to enhance the elliptic character of the momentum equation by making elliptic operator as strong as possible. Some successful techniques are described in [54]. Fietier and Deville [55] investigated the source of numerical instabilities occurring in the simulation of

time-dependent flows of viscoelastic fluids by direct numerical simulations.

Finite element formulations have achieved success in the past for solving viscoelastic flows. For incompressible Navier-stokes, there exist a compatibility condition also known as the LBB condition on the approximation spaces for velocity and pressure. Likewise, the addition of the constitutive equation, Eq. 6.18, imposes compatibility constraints on the interpolation of the velocity field, pressure, and stresses [48]. The hyperbolic character of the constitutive equation is often handled with some upwinding. Marchal and Crochet [56] used streamline upwinding while Fortin and Fortin [57] used upwinding by discontinuous finite element formulation. Wapperom et al. [58] proposed hybrid finite element/finite volume scheme where they integrated finite element and finite volume methods.

As demonstrated in the previous chapters, the least-squares based finite element formulations are good alternative to the weak form finite element formulations of the incompressible Navier-stokes equations. It is well known that least-squares formulations circumvent the compatibility conditions (LBB conditions) between approximating spaces. Also least-squares based formulations produce symmetric positive definite coefficient matrix, and robust matrix solver can be used to solve resultant algebraic equations. These properties hold for viscoelastic flows also. Surana et al. [59] presented least-squares formulation for steady viscoelastic flows. They showed that Galerkin method with weak form remains variationally inconsistent where as least-squares process always yields variationally consistent integral forms. They used k-version least-squares formulation with C^k $(k \geq 1)$ continuous functions; i.e., derivatives order k are made continuous between elements. It is well know that a two- or three-dimensional C^1 basis functions constructed by taking the tensor product of a one-dimensional C^1 basis cannot enforce C^1 continuity when the elements are geometrically distorted, making it difficult to generate two- and three-dimensional C^k functions. In another study, Garritsma [60] used direct minimization of the discontinuous least-squares method, C^0-continuous functions were used and C^1-continuity is imple-

mented in weak sense through least-squares functional. This formulation suffers from the problem of bad conditioning of coefficient matrix and increase in degrees of freedom in spite of the fact that auxiliary variables are not introduced [14]. Both of these studies were concerned with steady viscoelastic flows.

In this chapter, we present least-squares based finite element formulations for unsteady viscoelastic flows. We use Oldroyd-B constitutive equation. Unlike Surana et al. [59] and Garritsma [60], where they minimize the least-squares functional of the original second-order equations directly, we recast the second-order governing equations as a set of first-order equations by introducing stresses as independent variables. An alternative first-order system can be formed by introducing vorticity as an independent variable. For incompressible Navier-Stokes equations, it has been observed that pressure evolution was not well behaved in traditional least-squares method, and Prabhakar and Reddy [6, 41] have developed penalty based least-squares formulations (refer to the previous chapters for details). In this study, we extend the penalty least-squares formulation to viscoelastic flows. Pressure is eliminated using the penalty approach and least-squares functional is formed in terms of velocity field, stresses, and extra stresses. Transient flow in a channel is used as benchmark problem to test the formulations developed here.

The present chapter is organized as follows. In Section B, the least-squares finite element model for the viscoelastic flows is presented. The penalty least-squares formulation is presented in Section C, and numerical results are discussed in Section D. Transient flow in a channel is used as a benchmark problem. Results are presented for Weissenberg number of 1 and 10 and Reynolds number of 0.1 and 1. The effect of channel length on flow characteristics is also investigated by analyzing for channel lengths of 16, 32 and 64.

B. Governing equations

For isothermal incompressible viscoelastic flows governing equations in nondimensional form can be stated as:

find the velocity $\mathbf{u}(\mathbf{x})$, pressure $p(\mathbf{x})$ and extra-stress tensor $\underline{\mathbf{A}}$ such that

$$\nabla \cdot \mathbf{u} = 0 \qquad \text{in } \Omega \tag{6.1}$$

$$\mathrm{Re}\,\frac{\partial \mathbf{u}}{\partial t} + \mathrm{Re}\mathbf{u} \cdot \nabla \mathbf{u} + \nabla p + \nabla \cdot \left[\frac{\mu_2}{\mu}((\nabla \mathbf{u}) + (\nabla \mathbf{u})^{\mathrm{T}})) + \underline{\mathbf{A}}\right] = \mathbf{0} \qquad \text{in } \Omega \times (0, \tau] \tag{6.2}$$

$$\mathrm{We}\,\frac{\partial \underline{\mathbf{A}}}{\partial t} + \mathrm{We}\,\mathbf{u} \cdot \nabla \underline{\mathbf{A}} - \frac{\mu_1}{\mu}\left[(\nabla \mathbf{u}) + (\nabla \mathbf{u})^{\mathrm{T}}\right] - \mathrm{We}\,(\underline{\mathbf{L}} \cdot \underline{\mathbf{A}} + \underline{\mathbf{A}} \cdot \underline{\mathbf{L}}^{\mathrm{T}}) + \underline{\mathbf{A}} = \underline{\mathbf{0}} \qquad \text{in } \Omega \times (0, \tau] \tag{6.3}$$

where $\underline{\mathbf{L}}^T = \nabla \mathbf{u}$. The total viscosity μ is split into Newtonian solvent (μ_2) and polymeric contribution (μ_1) such that $\mu = \mu_1 + \mu_2$. Here Reynolds and Weissenberg numbers are given by

$$Re = \rho U L/\mu, \qquad We = \lambda U/L$$

where U and L are characteristic velocity and length scales of the flow, and λ is the relaxation time.

1. The velocity-stress-extra stress first-order system

The momentum equations are second-order equations while the continuity equation and constitutive equations are first-order equations. To make the whole system first order, we introduce stress tensor components as independent variables.

Then the problem can be stated as one of finding the velocity vector $\mathbf{u}(\mathbf{x})$, , pressure

$p(\mathbf{x})$, Eulerian rate of deformation tensor $\underline{\mathbf{T}}$ and extra-stress tensor $\underline{\mathbf{A}}$ such that

$$\nabla \cdot \mathbf{u} = 0 \qquad \text{in } \Omega \tag{6.4}$$

$$\text{Re}\,\frac{\partial \mathbf{u}}{\partial t} + \text{Re}\mathbf{u} \cdot \nabla \mathbf{u} + \nabla p + \nabla \cdot \left(\frac{\mu_2}{\mu}\underline{\mathbf{T}} + \underline{\mathbf{A}}\right) = \mathbf{0} \qquad \text{in } \Omega \times (0, \tau] \tag{6.5}$$

$$\underline{\mathbf{T}} - \left[(\nabla \mathbf{u}) + (\nabla \mathbf{u})^{\mathrm{T}}\right] = \underline{\mathbf{0}} \qquad \text{in } \Omega \tag{6.6}$$

$$\text{We}\,\frac{\partial \underline{\mathbf{A}}}{\partial t} + \text{We}\,\mathbf{u} \cdot \nabla \underline{\mathbf{A}} - \frac{\mu_1}{\mu}\,\underline{\mathbf{T}} - \text{We}\,(\underline{\mathbf{L}} \cdot \underline{\mathbf{A}} + \underline{\mathbf{A}} \cdot \underline{\mathbf{L}}^{\mathrm{T}}) + \underline{\mathbf{A}} = \underline{\mathbf{0}} \qquad \text{in } \Omega \times (0, \tau] \tag{6.7}$$

a. L_2 least-squares formulation

The least-squares functional of the problem can be set up by summing up the squares of the residuals of the new set of equations. In this study, we use space-time decoupled formulation, in which discretization in space and time are carried out independently. Generally, the temporal operators are represented by truncated Taylor series expansions in time. We use the Crank-Nicholson or a backward multi-step scheme (BDF2) in this study. Least-square functional for backward multi-step schemes can be written as

$$\begin{aligned}
\mathcal{J}(\mathbf{u}, D, \boldsymbol{\omega}; \mathbf{f}) = \frac{1}{2}\Big(& \Big\| \text{Re}\big(\frac{\gamma_0}{\Delta t}\mathbf{u}^{s+1} - \sum_{q=0}^{M_\alpha}\frac{\beta_q}{\Delta t}\mathbf{u}^{s-q}\big) + \text{Re}\mathbf{u} \cdot \nabla \mathbf{u} + \nabla p \\
& + \nabla \cdot \left(\frac{\mu_2}{\mu}\underline{\mathbf{T}} + \underline{\mathbf{A}}\right) \Big\|^2_{0,\Omega\times(0,\tau]} + \Big\| \underline{\mathbf{T}} - \left[(\nabla \mathbf{u}) + (\nabla \mathbf{u})^{\mathrm{T}}\right] \Big\|^2_{0,\Omega\times(0,\tau]} \\
& + \Big\| \text{We}\,\big(\frac{\gamma_0}{\Delta t}\underline{\mathbf{A}}^{s+1} - \sum_{q=0}^{M_\alpha}\frac{\beta_q}{\Delta t}\underline{\mathbf{A}}^{s-q}\big) + \text{We}\,\mathbf{u} \cdot \nabla \underline{\mathbf{A}} - \frac{\mu_1}{\mu}\,\underline{\mathbf{T}} \\
& - \text{We}\,(\underline{\mathbf{L}} \cdot \underline{\mathbf{A}} + \underline{\mathbf{A}} \cdot \underline{\mathbf{L}}^{\mathrm{T}}) + \underline{\mathbf{A}} \Big\|^2_{0,\Omega\times(0,\tau]} \Big)
\end{aligned} \tag{6.8}$$

where $\gamma_0 = \sum_{q=0}^{M_\alpha} \beta_q$ for consistency, β_q are weights associated with a particular multi-step scheme, $\Delta t = t_{s+1} - t_s$ is the time increment.

Considering the homogeneous pure velocity boundary condition case, the least-squares principle for functional (6.8) can be stated as:

find $(\mathbf{u}, p, \underline{\mathbf{T}}, \underline{\mathbf{A}}) \in \mathbf{X}$, $\mathbf{u}(\mathbf{x}, 0)=\mathbf{u}_0(\mathbf{x})$, and $\underline{\mathbf{A}}(\mathbf{x}, 0)=\underline{\mathbf{A}}_0(\mathbf{x})$ such that

$$\mathcal{J}\left(\mathbf{u}, p, \underline{\mathbf{T}}, \underline{\mathbf{A}}; \mathbf{f}\right) \leq \mathcal{J}\left(\tilde{\mathbf{u}}, \tilde{p}, \underline{\tilde{\mathbf{T}}}, \underline{\tilde{\mathbf{A}}}; \mathbf{f}\right) \qquad \forall \ \left(\tilde{\mathbf{u}}, \tilde{p}, \underline{\tilde{\mathbf{T}}}, \underline{\tilde{\mathbf{A}}}\right) \in \mathbf{X} \tag{6.9}$$

where we use the space

$$\mathbf{X} = \left\{ (\mathbf{u}, p, \underline{\mathbf{T}}, \underline{\mathbf{A}}) \in \mathbf{H}_0^1(\Omega) \times H^1(\Omega) \cap \bar{L}_2(\Omega) \times \mathbf{H}^1(\Omega) \times \mathbf{H}^1(\Omega) \right\}$$

The variational problem (after linearization using Newton's method) corresponding to the least-squares principle is given by: find $(\mathbf{u}, p, \underline{\mathbf{T}}, \underline{\mathbf{A}}) \in \mathbf{X}$, $\mathbf{u}(\mathbf{x}, 0)=\mathbf{u}_0(\mathbf{x})$, and $\underline{\mathbf{A}}(\mathbf{x}, 0)=\underline{\mathbf{A}}_0(\mathbf{x})$ such that

$$\mathcal{B}\left((\mathbf{u}, p, \underline{\mathbf{T}}, \underline{\mathbf{A}}), \left(\tilde{\mathbf{u}}, \tilde{p}, \underline{\tilde{\mathbf{T}}}, \underline{\tilde{\mathbf{A}}}\right)\right) = \mathcal{F}\left(\left(\tilde{\mathbf{u}}, \tilde{p}, \underline{\tilde{\mathbf{T}}}, \underline{\tilde{\mathbf{A}}}\right)\right) \qquad \forall \ \left(\tilde{\mathbf{u}}, \tilde{p}, \underline{\tilde{\mathbf{T}}}, \underline{\tilde{\mathbf{A}}}\right) \in \mathbf{X} \tag{6.10}$$

Let $\mathbf{X}_{hp}$ denote a finite-dimensional subspace of $\mathbf{X}$. Then the least-squares discretized model of the Navier-Stokes equations is defined by the following discrete variational problem: find $(\mathbf{u}^{hp}, p^{hp}, \underline{\mathbf{T}}^{hp}, \underline{\mathbf{A}}^{hp}) \in \mathbf{X}_{hp}$, $\mathbf{u}(\mathbf{x}, 0)=\mathbf{u}_0(\mathbf{x})$, and $\underline{\mathbf{A}}(\mathbf{x}, 0)=\underline{\mathbf{A}}_0(\mathbf{x})$ such that

$$\begin{aligned}\mathcal{B}\left(\left(\mathbf{u}^{hp}, p^{hp}, \underline{\mathbf{T}}^{hp}, \underline{\mathbf{A}}^{hp}\right), \left(\tilde{\mathbf{u}}^{hp}, \tilde{p}^{hp}, \underline{\tilde{\mathbf{T}}}^{hp}, \underline{\tilde{\mathbf{A}}}^{hp}\right)\right) =& \mathcal{F}\left(\left(\tilde{\mathbf{u}}^{hp}, \tilde{p}^{hp}, \underline{\tilde{\mathbf{T}}}^{hp}, \underline{\tilde{\mathbf{A}}}^{hp}\right)\right) \\ & \forall \ \left(\tilde{\mathbf{u}}^{hp}, \tilde{p}^{hp}, \underline{\tilde{\mathbf{T}}}^{hp}, \underline{\tilde{\mathbf{A}}}^{hp}\right) \in \mathbf{X}_{hp}\end{aligned} \tag{6.11}$$

2. Expansion bases

In this study, we use both low and high order basis functions. We use bilinear basis functions with one point Gauss quadrature, which is equivalent to adopting a least-squares collocation approach [14]. For details on standard finite element computer implementation,

such as mapping $\bar{\Omega}_e \rightleftarrows \hat{\Omega}_e$, numerical integration in $\hat{\Omega}_e$, and assembly using the direct stiffness approach, see Reddy [27, 28]. For linearization, we use Newton's method, details of which can be found in [31].

C. Penalty least-squares formulation

In the penalty method, pressure is eliminated from the Navier-Stokes equations using the following relation, which follows from the application of the penalty method to the Navier-Stokes equations with the divergence-free constraint (see [27], [28], and [29]):

$$p = -\gamma(\nabla \cdot \mathbf{u}) \tag{6.12}$$

Gunzberger [13] proposed an iterative penalty method

$$p^n = p^{n-1} - \gamma(\nabla \cdot \mathbf{u}) \tag{6.13}$$

Find the velocity $\mathbf{u}(\mathbf{x})$, and extra-stress tensor $\underline{\mathbf{A}}$ such that

$$\mathrm{Re}\,\frac{\partial \mathbf{u}}{\partial t} + \mathrm{Re}\mathbf{u}\cdot\nabla\mathbf{u} - \gamma\nabla(\nabla\cdot\mathbf{u}) + \nabla\cdot\left[\frac{\mu_2}{\mu}((\nabla\mathbf{u}) + (\nabla\mathbf{u})^{\mathrm{T}}) + \underline{\mathbf{A}}\right] = -\nabla p^{n-1} \qquad \text{in } \Omega\times(0,\tau] \tag{6.14}$$

$$\mathrm{We}\,\frac{\partial \underline{\mathbf{A}}}{\partial t} + \mathrm{We}\,\mathbf{u}\cdot\nabla\underline{\mathbf{A}} - \frac{\mu_1}{\mu}\left[(\nabla\mathbf{u}) + (\nabla\mathbf{u})^{\mathrm{T}}\right] - \mathrm{We}\,(\underline{\mathbf{L}}\cdot\underline{\mathbf{A}} + \underline{\mathbf{A}}\cdot\underline{\mathbf{L}}^{\mathrm{T}}) + \underline{\mathbf{A}} = \underline{\mathbf{0}} \qquad \text{in } \Omega\times(0,\tau] \tag{6.15}$$

To make the system first order, we introduce extra-stress tensor components as independent variables.

Then the problem can be stated as one of finding the velocity vector $\mathbf{u}(\mathbf{x})$, Eulerian

rate of deformation tensor $\underline{\mathbf{T}}$ and extra-stress tensor $\underline{\mathbf{A}}$ such that

$$\mathrm{Re}\,\frac{\partial \mathbf{u}}{\partial t} + \mathrm{Re}\mathbf{u}\cdot\nabla\mathbf{u} - \gamma\nabla\big[\frac{1}{2}\,\mathrm{tr}(\underline{\mathbf{T}})\big] + \nabla\cdot\Big(\frac{\mu_2}{\mu}\underline{\mathbf{T}} + \underline{\mathbf{A}}\Big) = -\nabla p^{n-1} \qquad \text{in } \Omega\times(0,\tau] \tag{6.16}$$

$$\underline{\mathbf{T}} - \Big[(\nabla\mathbf{u}) + (\nabla\mathbf{u})^{\mathrm{T}}\Big] = \underline{\mathbf{0}} \qquad \text{in } \Omega \tag{6.17}$$

$$\mathrm{We}\,\frac{\partial \underline{\mathbf{A}}}{\partial t} + \mathrm{We}\,\mathbf{u}\cdot\nabla\underline{\mathbf{A}} - \frac{\mu_1}{\mu}\,\underline{\mathbf{T}} - \mathrm{We}\,(\underline{\mathbf{L}}\cdot\underline{\mathbf{A}} + \underline{\mathbf{A}}\cdot\underline{\mathbf{L}}^{\mathrm{T}}) + \underline{\mathbf{A}} = \underline{\mathbf{0}} \qquad \text{in } \Omega\times(0,\tau] \tag{6.18}$$

The L_2 least-squares formulation and finite element model development proceed in a similar manner to that described earlier.

D. Numerical results

In this section, numerical results obtained with the present least-squares finite element models are presented. The problem considered here is the transient flow in a channel for which analytical results exist [61]. For all the cases considered here, nonlinear convergence is declared when the relative norm of the residual, $\|\Delta\mathbf{U}\|/\|\mathbf{U}\|$ is less than 10^{-3} unless mentioned, where $\mathbf{U}$ is the solution vector (includes all degrees of freedom at a node). Convergence of conjugate gradient is declared when L_2-norm of error is less than 10^{-6}.

The boundary conditions used are on velocity field and extra-stresses. Velocity is imposed at both inlet and outlet through the analytical profiles of Waters and King [61] for the Oldroyd-B model. At inlet, extra-stress boundary condition is also imposed using the analytical solution. On side walls, no-slip boundary condition is used. Geometry and boundary conditions are shown in fig 1. Velocity values are reported at point A (along the centerline) and extra-stress values are reported at point B. These points are $L/8$ distance away from the exit of the channel. Os and Phillips [51] observed that stability of numerical

algorithm (spectral element method) depended on the channel length also. Problem has been solved for channel length of $L = 16, 32$ and 64. Velocity values are reported at point A while extra-stress values are reported at point B (see Fig. 69).

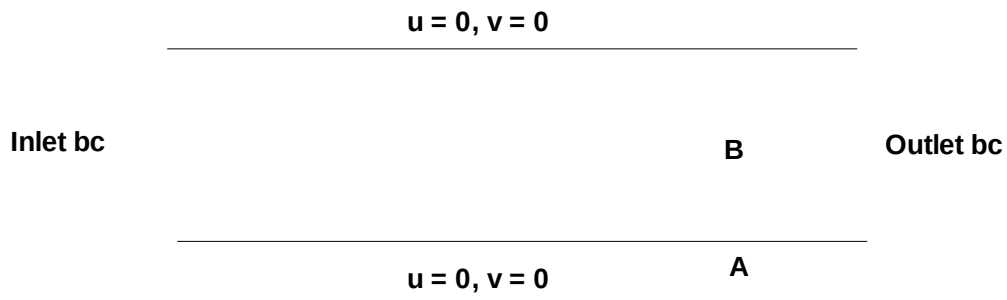

Fig. 69. Geometry and boundary conditions

Weissenberg number considered in this study varies between 1 to 10. Problems are solved for low Reynolds number varying between 0.1 to 1. Value of parameter β is taken to be $1/9$. The performance of the algorithm is shown by solving the transient channel flow problem for various values of Weissenberg number and Reynolds number.

1. Results for We=1

A time increment of 0.01 is used for all of the simulations for We = 1. For larger values of Δt solution is not sufficiently accurate. Fig. 70 shows evolution of velocity, extra-stress tensor components A_{xx} and A_{xy} with time for We = 1 and Re = 1 for channel length of L=16. Mesh used for this simulation is 32×8 bilinear elements. Numerical results are compared with the analytical results, and there is good agreement between them. The flow reaches steady state and no instability is observed. Next, Reynolds number is decreased to 0.1 with all other parameters held constant (We, channel length, and mesh). Results

are plotted in Fig. 71. Again we see good agreement between the numerical results and analytical solutions.

Next, we investigate the effect of channel length on the stability of the numerical algorithm. Channel length is increased to 32. A 64×8 mesh is used for this computation. Simulation converges and good agreement is found between numerical and analytical solutions. The problem is then solved for channel length of 64 with 64×8 mesh for Re=1. Again, the flow field converges. These cases indicate, unlike the spectral element method of Os and Phillips [51], the channel length has no effect on the stability in the present formulation.

In this chapter we also proposed penalty least-squares finite element formulation for viscoelastic flows. It has been observed that pressure evolution is not well behaved in traditional least-squares formulations [45] when implemented in context of incompressible Navier-Stokes equations. Penalty based formulations fix this problem [6, 41]. For this simple geometry (flow in a channel), pressure is well behaved so penalty method does not offer any advantages but for complicated geometries, we expect penalty method to perform better than traditional least-squares formulation.

2. Results for We=10

For We=10, smaller time increment (Δt) is required. We use Δt of 0.005 to 0.001 for this Weissenberg number. For such small Δt, the condition number of the coefficient matrix becomes high [45] and preconditioned conjugate gradient (PCG) solver converges slowly. It takes 50,000 PCG iterations to converge. Slow PCG convergence coupled with small Δt makes the computation time intensive. Pontaza [45] proposed scaling of momentum equations by Δt to fix high conditioning number problem and it worked very well for incompressible Navier-Stokes equation. This procedure essentially reduces weight of momentum equations (which is equivalent to increasing weight of the continuity equation).

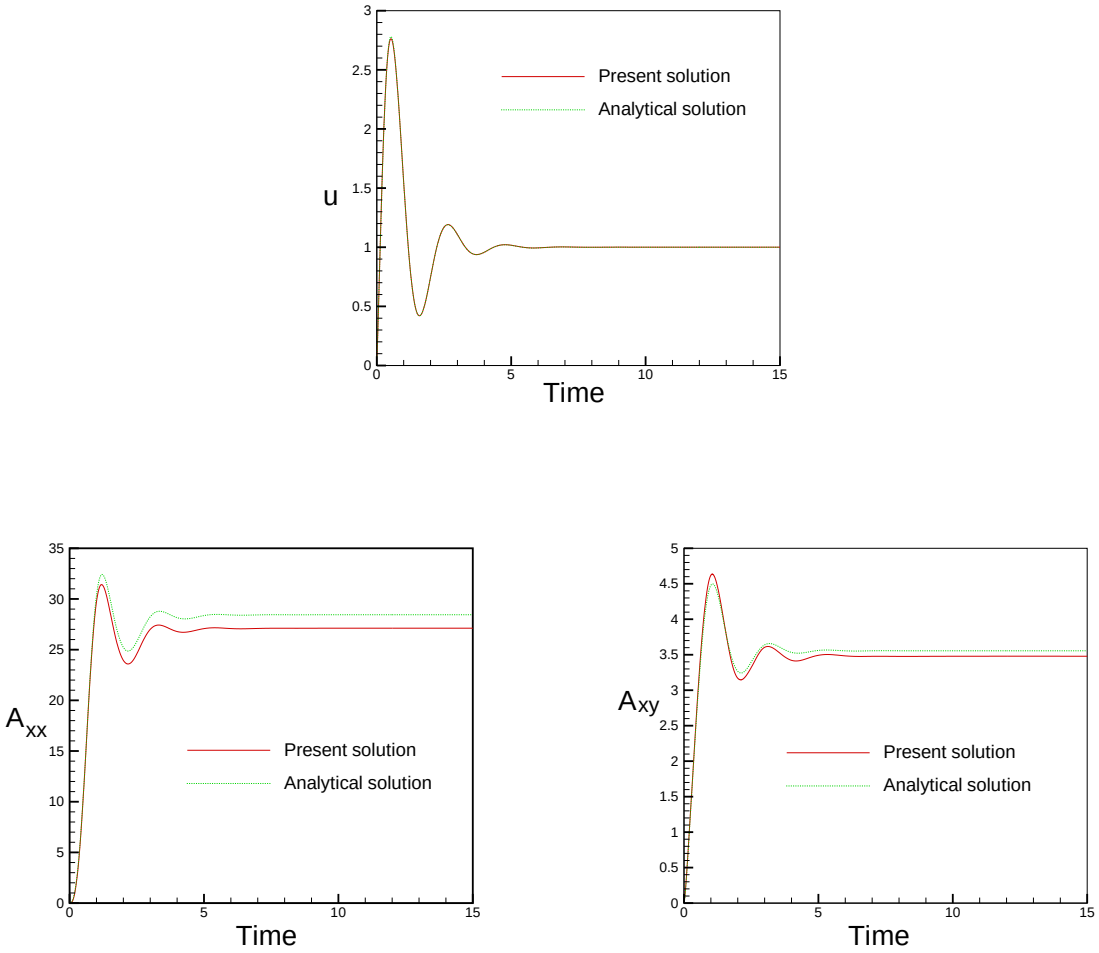

Fig. 70. Transient solution for channel flow: We=1, Re=1

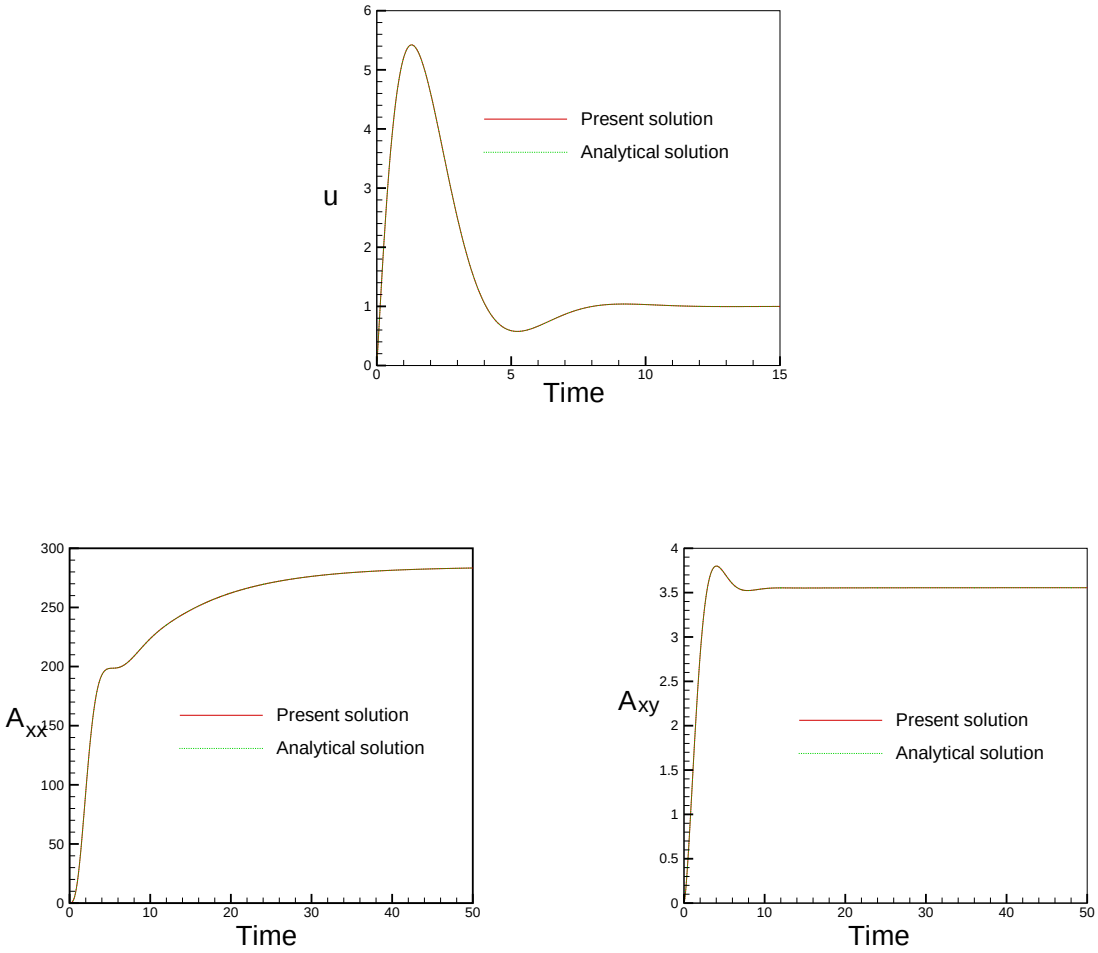

Fig. 71. Transient solution for channel flow: We=1, Re=0.1

In the case of viscoelastic flows, this procedures (time scaling of momentum and constitutive equations to reduce conditioning number) does not work. Scaling momentum and constitutive equations by Δt fixes conditioning number of the coefficient matrix and PCG converges in 1000 iterations but accuracy of solution is poor, as shown in Fig. 72 (simulation diverges). This is mainly because of presence of constitutive equations. The scaling reduces weight associated with constitutive equations.

Fig. 73 shows evolution of velocity and extra-stress tensor components A_{xx} and A_{xy} with time for We=10 and Re=1 for channel length of $L = 16$. Mesh used for this simulation is 32×8 bilinear elements. The time increment used is 0.005. Numerical results are in good agreement with the analytical solutions. The simulation could not be carried out to steady state because of the high computational cost.

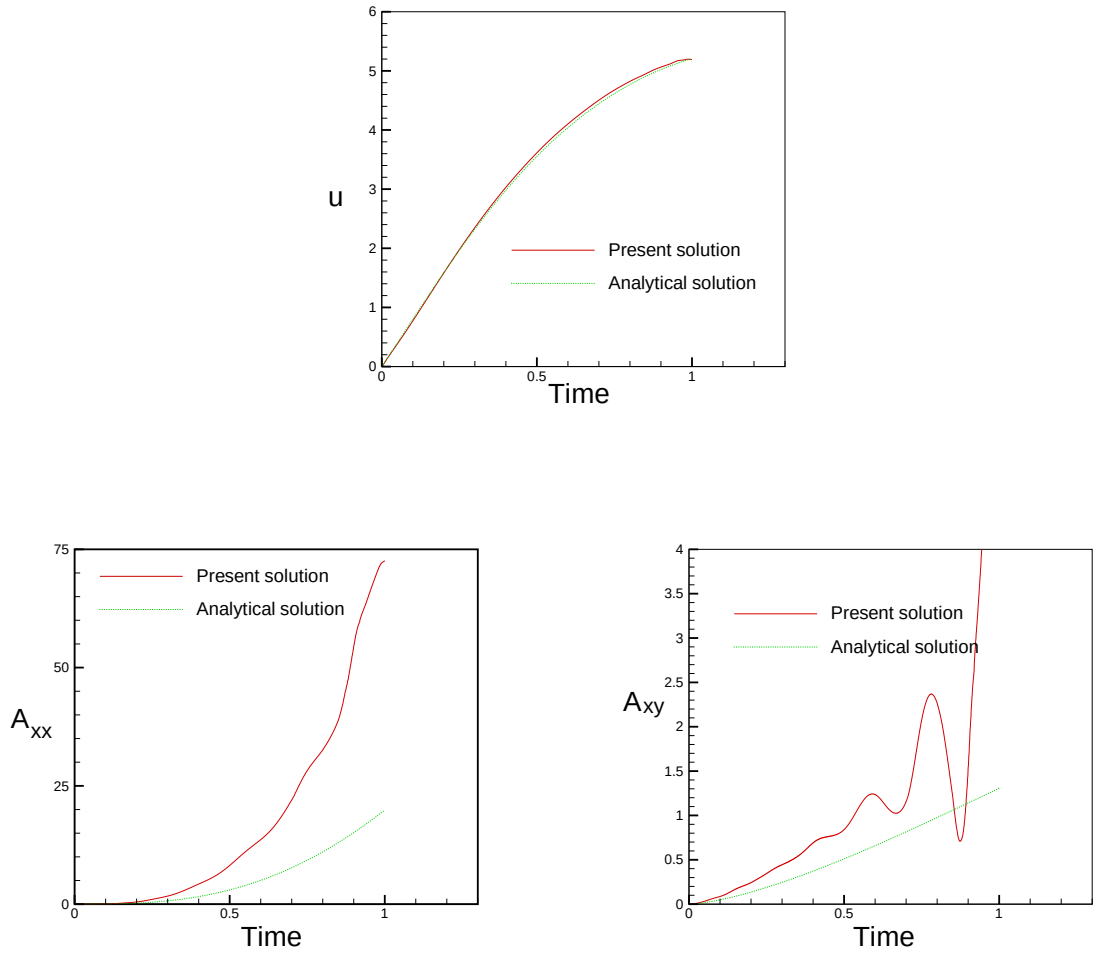

Fig. 72. Transient solution for channel flow: We=10, Re=1, with time scaling of momentum equations

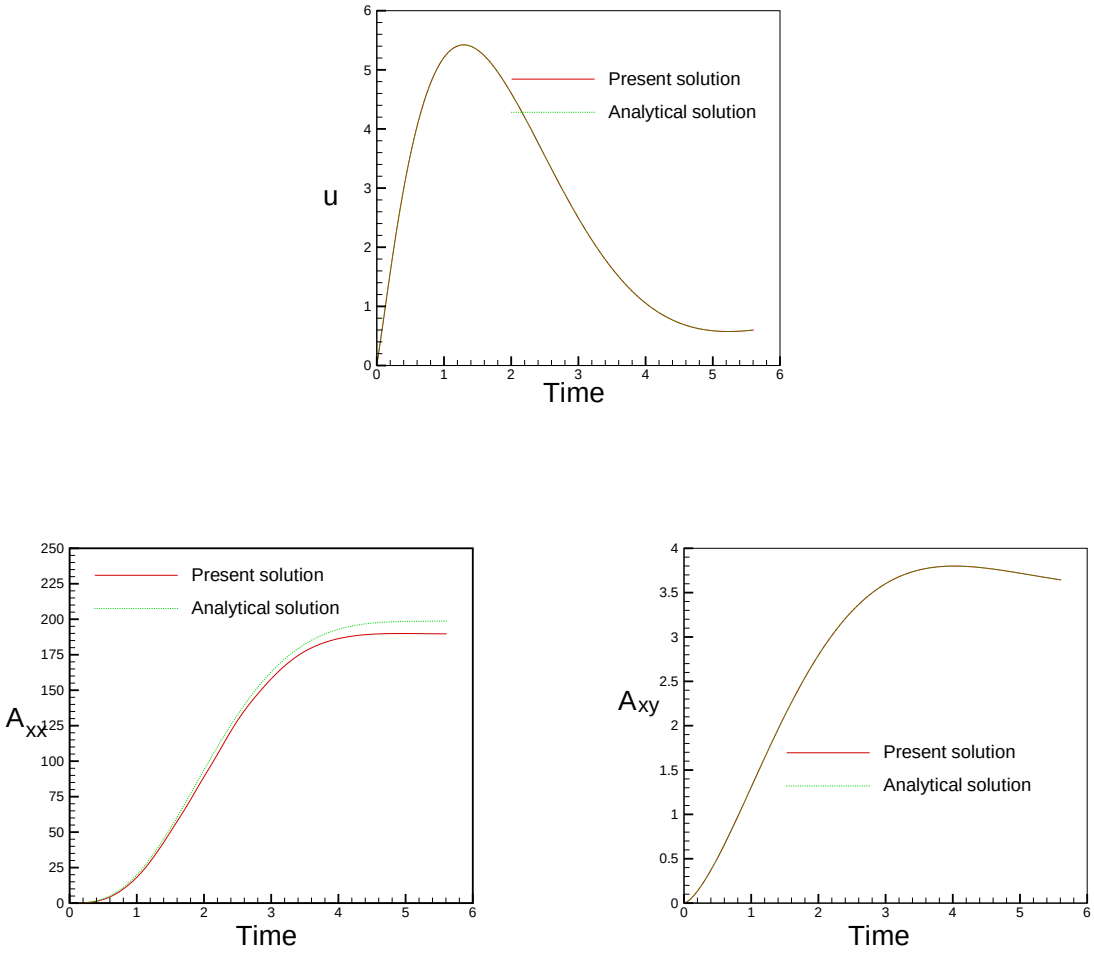

Fig. 73. Transient solution for channel flow: We=10, Re=1

CHAPTER VII

ORTHOGONALITY OF MODAL BASES IN HP FINITE ELEMENT MODELS

A. Introduction

The past two decades have witnessed a great deal of progress in the area of computational fluid dynamics. A large number of methods have been proposed for the numerical solution of the Navier-Stokes equations governing flows of viscous incompressible fluids. Direct discretization includes finite difference and finite volume techniques, mixed finite element methods using conformal and nonconformal elements, and spectral methods. Finite element method and its derivatives (e.g., least-squares finite element model, spectral/hp finite element model) have gained popularity in the recent times.

In the finite element method, we select basis functions to approximate dependent variables and perform coordinate transformation to evaluate the coefficient matrices. On the basis of polynomial order used, the finite element models can be divided into two groups: low-order expansions (order less than three) and high-order expansion (order higher than three). Most of the finite element implementations use low order expansions because they require less computational time per degree of freedom, and convergence is achieved by refining the mesh. On the other hand, high order expansions demonstrate exponential convergence. If high accuracy is required then we can justify using high-order expansions by the fact that the error will converge at a faster rate than the increase in the operation count. Therefore, ultimately it is more efficient to use high-order methods. Nevertheless, the cross-over point between the required accuracy and relative cost of low and high-order methods for a given application is a point of much debate. A further argument presented for using high-order methods is the numerical diffusion and the enhanced phase properties that these schemes demonstrate [12, 30].

In the context of least-squares finite element models, low-order nodal expansions have been found to lock and reduced integration is used to obtain acceptable numerical results. In this case, resulting coefficient matrix is nearly singular. Furthermore, the numerical solution may not be smooth at the nodes and post-processing is needed to recover nodal values from the reduced integration points. Pontaza and Reddy [5, 12] presented spectral/hp least-squares finite element models and Prabhakar and Reddy [6] presented spectral/hp penalty least-squares finite element models. They combined the idea of least-squares method with spectral/hp methods, and the models performed well in solving Navier-Stokes equations.

Having outlined the need for high-order expansion basis, we need to decide the types of expansion bases used. Many types of high-order expansion bases can be found in the literature. Peano [62] constructed a hierarchial triangular basis using area coordinates. A variation of this construction was later developed by [63] that introduces Legendre polynomials to avoid round-off error for high-order p-expansions. However, both approaches require special integration rules which are quite complicated at high polynomial order. Dubiner [64] first developed an alternative hierarchical basis for triangular domains that is based on cartesian coordinates. Dubiner's basis was implemented by [65] using a Galerkin finite element model of the Navier-Stokes equations, and it was found to be competitive in cost with the nodal basis on quadrilaterals employed in the spectral element method [66]. Warburton et al. [67] developed a unified description of hybrid basis functions. They developed five types of basis functions that are either modal, nodal or mixed, and which may or may not be hierarchical.

In this chapter, we implement hierarchical modal bases. Hierarchical bases can lead to better conditioning of mass and coefficient matrices [15]. We implement these bases in the context of least-squares finite element model of the Navier-Stokes equations [5, 12]. As described earlier, high-order expansions require more work per degree of freedom (during Gauss quadrature). In this chapter we exploit orthogonality of Jacobi polynomials, and

calculate integrals without using any numerical quadrature rule. We recast the terms of the coefficient matrix using the properties of Jacobi polynomial and evaluate them exactly. For rectangular elements, coefficient matrix entries are written in alternative forms and analytical expressions are developed to calculate them exactly. It is to be mentioned that multidimensional shape functions are constructed using tensor product of one-dimensional shape functions. Limitation of the procedure developed here is that it can be used for rectangular elements.

The present chapter is organized as follows. In section B, we review the least-squares finite element formulation for the steady incompressible Navier-Stokes equations. The Navier-Stokes equations are recast as first-order system using vorticity as additional dependent variable, and then the finite element formulation for these first-order systems is presented. In section C, we present a couple of properties associated with Jacobi polynomials and use them to evaluate the entries of coefficient matrix. Then in sections D and E we recast entries of coefficient matrix for one-dimensional and multidimensional cases and evaluate them analytically. We implement primary boundary conditions by inverting mass matrix, description of which is given in section F. In section G, we present space-time decoupled least-square formulation. Numerical results are presented in section H. The spectral convergence is verified using the Kovasznay flow solution. Numerical results are presented for transient 2-D flow over a backward-facing step. We compare results with the benchmark solution of Gartling [24] and Pontaza and Reddy [5]. Lastly, we consider the flow past a circular cylinder at low Reynolds number and compare the predicted surface pressure distribution with the experimental measurements of Grove et al. [25].

B. Least-squares finite element formulation

The steady incompressible Navier-Stokes equations in dimensionless form can be written as follows:

$$(\mathbf{u}\cdot\nabla)\,\mathbf{u}+\nabla p-\frac{1}{\mathrm{Re}}\,\nabla\cdot\left[(\nabla\mathbf{u})+(\nabla\mathbf{u})^{\mathrm{T}}\right]=\mathbf{f}\qquad\text{in }\Omega\tag{7.1}$$

$$\nabla\cdot\mathbf{u}=0\qquad\text{in }\Omega\tag{7.2}$$

$$\mathbf{u}=\mathbf{u}^{s}\qquad\text{on }\Gamma_{u}\tag{7.3}$$

$$\hat{\mathbf{n}}\cdot\underline{\boldsymbol{\sigma}}=\mathbf{f}^{s}\qquad\text{on }\Gamma_{f}\tag{7.4}$$

where $\mathbf{u}(\mathbf{x})$ is the velocity vector, $p(\mathbf{x})$ is the pressure, $\underline{\boldsymbol{\sigma}}=-p\,\underline{\mathbf{I}}+1/\mathrm{Re}\left[(\nabla\mathbf{u})+(\nabla\mathbf{u})^{\mathrm{T}}\right]$ is the total stress, $\mathbf{f}$ is a dimensionless force, $\hat{\mathbf{n}}$ is the outward unit normal on the boundary of Ω, $\mathbf{u}^{s}$ is the prescribed velocity on the boundary Γ_{u}, and $\mathbf{f}^{s}$ is the prescribed boundary stress on the boundary Γ_{f}, $\Gamma=\Gamma_{u}\cup\Gamma_{f}$ and $\Gamma_{u}\cap\Gamma_{f}=\emptyset$, and Re is the Reynolds number.

To reduce the system to first order, we introduce vorticity vector as an independent variable. We make use of the vector identity

$$\nabla\times\nabla\times\mathbf{u}=-\nabla^{2}\mathbf{u}+\nabla(\nabla\cdot\mathbf{u})$$

Then determining the solution of the stationary Navier-Stokes equations, Equations. (7.1)-(7.4), can now be stated as:

find the velocity $\mathbf{u}(\mathbf{x})$, pressure $p(\mathbf{x})$, and vorticity $\boldsymbol{\omega}(\mathbf{x})$ such that

$$(\mathbf{u}\cdot\nabla)\,\mathbf{u}+\nabla p+\frac{1}{\mathrm{Re}}\nabla\times\boldsymbol{\omega}=\mathbf{f} \qquad \text{in } \Omega \tag{7.5}$$

$$\boldsymbol{\omega}-\nabla\times\mathbf{u}=\mathbf{0} \qquad \text{in } \Omega \tag{7.6}$$

$$\nabla\cdot\mathbf{u}=0 \qquad \text{in } \Omega \tag{7.7}$$

$$\nabla\cdot\boldsymbol{\omega}=0 \qquad \text{in } \Omega \tag{7.8}$$

$$\mathbf{u}=\mathbf{u}^s \qquad \text{on } \Gamma_u \tag{7.9}$$

$$\boldsymbol{\omega}=\boldsymbol{\omega}^s \qquad \text{on } \Gamma_\omega \tag{7.10}$$

The L_2 least-squares functional associated with the velocity-pressure-vorticity equations presented above is given by

$$\mathcal{J}(\mathbf{u},p,\boldsymbol{\omega};\mathbf{f})=\frac{1}{2}\Big(\left\|(\mathbf{u}\cdot\nabla)\,\mathbf{u}+\nabla p+\frac{1}{\mathrm{Re}}\nabla\times\boldsymbol{\omega}-\mathbf{f}\right\|_0^2+\|\,\boldsymbol{\omega}-\nabla\times\mathbf{u}\,\|_0^2 + \|\,\nabla\cdot\mathbf{u}\,\|_0^2+\|\,\nabla\cdot\boldsymbol{\omega}\,\|_0^2\Big) \tag{7.11}$$

The least-squares principle can be stated as one of finding $(\mathbf{u},p,\boldsymbol{\omega})\in\mathbf{X}$ such that for all $(\mathbf{v},q,\boldsymbol{\psi})\in\mathbf{X}$

$$\mathcal{J}(\mathbf{u},p,\boldsymbol{\omega};\mathbf{f})\le\mathcal{J}(\mathbf{v},q,\boldsymbol{\psi};\mathbf{f}) \tag{7.12}$$

holds, where

$$\mathbf{X}=\left\{(\mathbf{u},p,\boldsymbol{\omega})\in\mathbf{H}_0^1(\Omega)\times H^1(\Omega)\cap\bar{L}_2(\Omega)\times\mathbf{H}^1(\Omega)\right\}$$

The Euler-Lagrange equations associated with this minimum principle are equivalent to the following variational problem: find $(\mathbf{u},p,\boldsymbol{\omega})\in\mathbf{X}$ such that for all $(\mathbf{v},q,\boldsymbol{\psi})\in\mathbf{X}$

$$\mathcal{B}((\mathbf{u},p,\boldsymbol{\omega}),(\mathbf{v},q,\boldsymbol{\psi}))=\mathcal{F}((\mathbf{v},q,\boldsymbol{\psi})) \tag{7.13}$$

where

$$\mathcal{B}\left(\left(\mathbf{u},p,\boldsymbol{\omega}\right),\left(\mathbf{v},q,\boldsymbol{\psi}\right)\right) =$$

$$\int_{\Omega}\left(\left(\mathbf{u_0}\cdot\nabla\right)\mathbf{u}+\nabla p+\frac{1}{\mathrm{Re}}\nabla\times\boldsymbol{\omega}\right)\cdot\left(\left(\mathbf{u_0}\cdot\nabla\right)\mathbf{v}+\nabla q+\frac{1}{\mathrm{Re}}\nabla\times\boldsymbol{\psi}\right)d\Omega$$

$$+\int_{\Omega}\left(\boldsymbol{\omega}-\nabla\times\mathbf{u}\right)\cdot\left(\boldsymbol{\psi}-\nabla\times\mathbf{v}\right)d\Omega+\int_{\Omega}\left(\nabla\cdot\mathbf{u}\right)\left(\nabla\cdot\mathbf{v}\right)d\Omega$$

$$+\int_{\Omega}\left(\nabla\cdot\boldsymbol{\omega}\right)\left(\nabla\cdot\boldsymbol{\psi}\right)d\Omega$$

and

$$\mathcal{F}\left(\left(\mathbf{v},q,\boldsymbol{\psi}\right)\right)=\int_{\Omega}\mathbf{f}\cdot\left(\left(\mathbf{u_0}\cdot\nabla\right)\mathbf{v}+\nabla q+\frac{1}{\mathrm{Re}}\nabla\times\boldsymbol{\psi}\right)d\Omega$$

We have used Picard method, where we linearize equations first and then minimize the least-squares functional.

1. Finite element model

The finite element model is obtained by restricting (7.13) to a finite-dimensional subspace $\mathbf{X}_{hp}$ of the space $\mathbf{X}$. Then the discrete least-squares finite element model for the incompressible Navier-Stokes equations is given by the following discrete variational problem: find $\left(\mathbf{u}^{hp},p^{hp},\boldsymbol{\omega}^{hp}\right)\in\mathbf{X}_{hp}$ such that for all $\left(\mathbf{v}^{hp},q^{hp},\boldsymbol{\psi}^{hp}\right)\in\mathbf{X}_{hp}$

$$\mathcal{B}\left(\left(\mathbf{u}^{hp},p^{hp},\boldsymbol{\omega}^{hp}\right),\left(\mathbf{v}^{hp},q^{hp},\boldsymbol{\psi}^{hp}\right)\right)=\mathcal{F}\left(\left(\mathbf{v}^{hp},q^{hp},\boldsymbol{\psi}^{hp}\right)\right) \tag{7.14}$$

For details, see Pontaza and Reddy [5]. This procedure leads to the following system of equations:

$$\begin{pmatrix} [S^{11}+S^{22}] & [S^{12}-S^{21}] & [0] & [S^{20}] \\ [S^{21}-S^{12}] & [S^{11}+S^{22}] & [0] & -[S^{10}] \\ [0] & [0] & [S^{11}+S^{22}] & \frac{1}{Re}[S^{12}-S^{21}] \\ [S^{02}] & -[S^{01}] & \frac{1}{Re}[S^{21}-S^{12}] & \frac{1}{Re^2}[S^{11}+S^{22}]+[S^{00}] \end{pmatrix} \begin{pmatrix} \{v_x\} \\ \{v_y\} \\ \{P\} \\ \{\omega_z\} \end{pmatrix}$$

$$+ \begin{pmatrix} [C^{00}(\mathbf{v})] & [0] & [C^{01}(\mathbf{v})] & \frac{1}{Re}[C^{02}(\mathbf{v})] \\ [0] & [C^{00}(\mathbf{v})] & [C^{02}(\mathbf{v})] & -\frac{1}{Re}[C^{01}(\mathbf{v})] \\ [C^{10}(\mathbf{v})] & [C^{20}(\mathbf{v})] & [0] & [0] \\ \frac{1}{Re}[C^{20}(\mathbf{v})] & -\frac{1}{Re}[C^{10}(\mathbf{v})] & [0] & [0] \end{pmatrix} \begin{pmatrix} \{v_x\} \\ \{v_y\} \\ \{P\} \\ \{\omega_z\} \end{pmatrix} = \begin{pmatrix} \{F^1\} \\ \{F^2\} \\ \{F^3\} \\ \{F^4\} \end{pmatrix}$$

$$C_{ij}^{00}(\mathbf{v}) = \int_{\Omega^e} \mathcal{C}_i \mathcal{C}_j \, dx \, dy, \qquad \mathcal{C}_i = v_x \frac{\partial \psi_i}{\partial x} + v_y \frac{\partial \psi_i}{\partial y}$$

$$C_{ij}^{01}(\mathbf{v}) = \int_{\Omega^e} \mathcal{C}_i \frac{\partial \psi_j}{\partial x} \, dx \, dy, \qquad C_{ij}^{02}(\mathbf{v}) = \int_{\Omega^e} \mathcal{C}_i \frac{\partial \psi_j}{\partial y} \, dx \, dy$$

$$C_{ij}^{10}(\mathbf{v}) = \int_{\Omega^e} \frac{\partial \psi_i}{\partial x} \mathcal{C}_j \, dx \, dy, \qquad C_{ij}^{20}(\mathbf{v}) = \int_{\Omega^e} \frac{\partial \psi_i}{\partial y} \mathcal{C}_j \, dx \, dy$$

$$S_{ij}^{00} = \int_{\Omega^e} \psi_i \psi_j \, d\Omega$$

$$S_{ij}^{01} = \int_{\Omega^e} \psi_i \frac{\partial \psi_j}{\partial x} \, dx dy, \qquad S_{ij}^{02} = \int_{\Omega^e} \psi_i \frac{\partial \psi_j}{\partial y} \, dx dy$$

$$S_{ij}^{10} = \int_{\Omega^e} \frac{\partial \psi_i}{\partial x} \psi_j \, dx dy, \qquad S_{ij}^{20} = \int_{\Omega^e} \frac{\partial \psi_i}{\partial y} \psi_j \, dx dy$$

$$S_{ij}^{11} = \int_{\Omega^e} \frac{\partial \psi_i}{\partial x} \frac{\partial \psi_j}{\partial x} \, dx \, dy, \qquad S_{ij}^{22} = \int_{\Omega^e} \frac{\partial \psi_i}{\partial y} \frac{\partial \psi_j}{\partial y} \, dx \, dy$$

$$S_{ij}^{12} = \int_{\Omega^e} \frac{\partial \psi_i}{\partial x} \frac{\partial \psi_j}{\partial y} \, dx \, dy, \qquad S_{ij}^{21} = \int_{\Omega^e} \frac{\partial \psi_i}{\partial y} \frac{\partial \psi_j}{\partial x} \, dx \, dy$$

$$
\begin{aligned}
F_i^1 &= \int_{\Omega^e} \mathcal{C}_i \, f_x \, dxdy \\
F_i^2 &= \int_{\Omega^e} \mathcal{C}_i \, f_y \, dx \, dy \\
F_i^3 &= \int_{\Omega^e} \left(\frac{\partial \psi_i}{\partial x} f_x + \frac{\partial \psi_i}{\partial y} f_y \right) \, dx \, dy \\
F_i^4 &= \int_{\Omega^e} \frac{1}{Re} \left(\frac{\partial \psi_i}{\partial y} f_x - \frac{\partial \psi_i}{\partial x} f_y \right) dx \, dy
\end{aligned}
$$

We proceed to develop a discrete problem by choosing appropriate finite element subspaces for the velocity, pressure and vorticity. There are no restrictive compatibility conditions on the discrete spaces, so we choose the same finite element subspace for each of the primary variables. The only requirement on the approximating spaces is that we choose continuous piecewise polynomials.

Modal expansion: In the standard interval $\Omega_{st} = \{\xi | -1 < \xi < 1\}$ modal expansions are defined as

$$
\psi_i(\xi) = \begin{cases} \frac{1-\xi}{2} & i = 1 \\ \left(\frac{1-\xi}{2}\right) \left(\frac{1+\xi}{2}\right) P_{p-2}^{\alpha,\beta} & 2 \leq i \leq p, \ p \geq 2 \\ \frac{1+\xi}{2} & i = p+1 \end{cases} \tag{7.15}
$$

In definition (7.15), $P_p^{\alpha,\beta}$ are the Jacobi polynomials of order p. We use ultraspheric polynomials corresponding to the choice $\alpha = \beta = 1$. Multidimensional modal expansions are constructed by taking tensor product of one-dimensional modal expansions. An important property of Jacobi polynomials is their orthogonal relationship given by the following equation:

$$
\int_{-1}^{1} (1-x)^{\alpha} (1+x)^{\beta} \, P_p^{\alpha,\beta}(x) \, P_q^{\alpha,\beta}(x) \, dx = C \, \delta_{pq} \tag{7.16}
$$

where the value of C depends on α, β, and p, and it has the value

$$C = \frac{2^{\alpha+\beta+1}}{2p+\alpha+\beta+1} \frac{\Gamma(p+\alpha+1)\Gamma(p+\beta+1)}{p!\Gamma(p+\alpha+\beta+1)} \tag{7.17}$$

Other notable property is that the multidimensional shape functions are constructed by taking tensor product of one-dimensional shape functions. These two properties make the computation of coefficient matrix very fast. The shape functions in two dimensions are given below.

Interior modes:

$$\phi_{mn}^{interior} = \Big(\frac{1+\xi}{2}\Big)\Big(\frac{1-\xi}{2}\Big) P_{m-1}^{1,1}(\xi) \Big(\frac{1+\eta}{2}\Big)\Big(\frac{1-\eta}{2}\Big) P_{n-1}^{1,1}(\eta)$$

Vertex modes:

$$\begin{aligned}
\phi^{vertex_1} &= \Big(\frac{1-\xi}{2}\Big)\Big(\frac{1-\eta}{2}\Big) \\
\phi^{vertex_2} &= \Big(\frac{1+\xi}{2}\Big)\Big(\frac{1-\eta}{2}\Big) \\
\phi^{vertex_3} &= \Big(\frac{1+\xi}{2}\Big)\Big(\frac{1+\eta}{2}\Big) \\
\phi^{vertex_4} &= \Big(\frac{1-\xi}{2}\Big)\Big(\frac{1+\eta}{2}\Big)
\end{aligned}$$

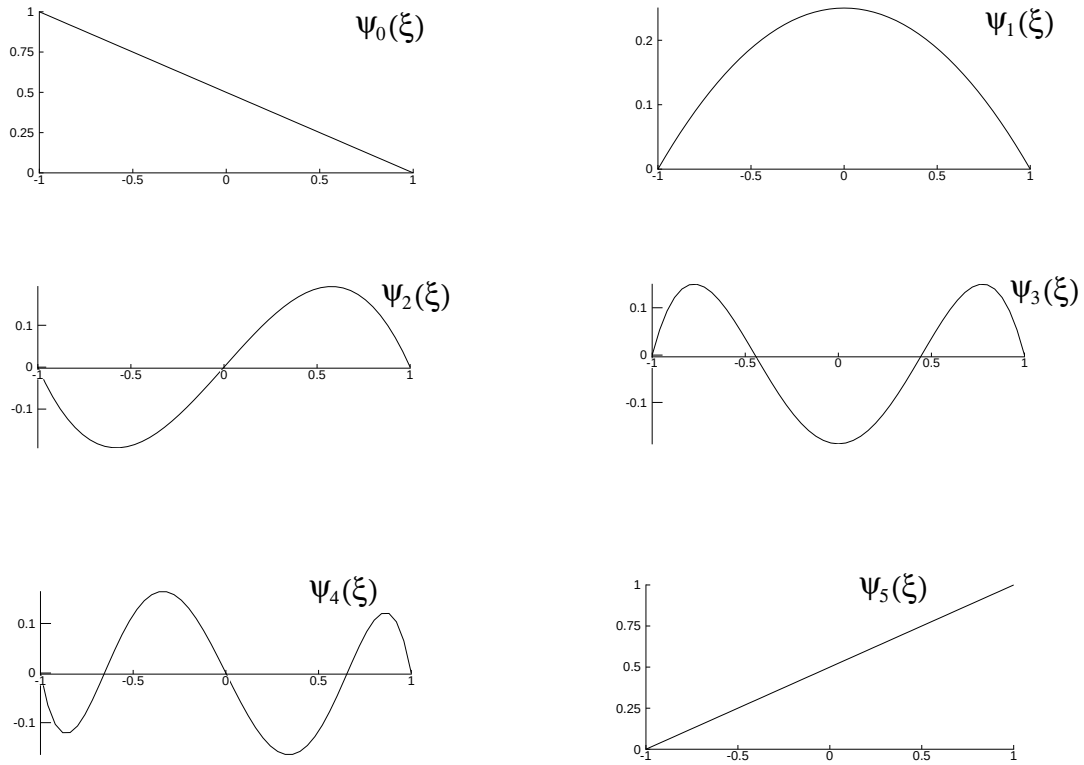

Fig. 74. Shape of modal expansion modes for a polynomial order of $P = 5$

Edge modes:

$$\phi_m^{edge_1} = \Big(\frac{1+\xi}{2}\Big)\Big(\frac{1-\xi}{2}\Big)P_{m-1}^{1,1}(\xi)\Big(\frac{1-\eta}{2}\Big)$$
$$\phi_n^{edge_2} = \Big(\frac{1+\xi}{2}\Big)\Big(\frac{1-\eta}{2}\Big)\Big(\frac{1+\eta}{2}\Big)P_{n-1}^{1,1}(\eta)$$
$$\phi_m^{edge_3} = \Big(\frac{1+\xi}{2}\Big)\Big(\frac{1-\xi}{2}\Big)P_{m-1}^{1,1}(\xi)\Big(\frac{1+\eta}{2}\Big)$$
$$\phi_n^{edge_4} = \Big(\frac{1-\xi}{2}\Big)\Big(\frac{1-\eta}{2}\Big)\Big(\frac{1+\eta}{2}\Big)P_{n-1}^{1,1}(\eta)$$

Fig. 74 shows 1-D modal expansions of order 5. Expansion modes ψ_0 and ψ_P are the same as the linear finite element expansion. These are boundary modes since they are the only modes which have magnitude at the ends of the interval. The remaining interior

modes are zero at the ends of the interval and increase in polynomial order as is typical in a hierarchial expansion. This setting helps implementing boundary conditions.

C. Orthogonality of Modal bases

Modal bases defined above consist of Jacobi polynomials which are orthogonal polynomials satisfying the condition (7.16). In Fig. 75 non-zero entries of $(\psi_i\,,\psi_j)$, $(\psi_i\,,d\psi_j/d\xi)$ and $(d\psi_i/d\xi\,,d\psi_j/d\xi)$ in 1-D for $P=9$ are plotted, where

$$(\psi_i\,,\psi_j)=\int \psi_i\psi_j d\xi \tag{7.18}$$

etc; $(\psi_i\,,\psi_j)$ has 32 non-zero entries out of 100. Rest of the entries are zero by the virtue of orthogonality of Jacobi polynomials; $(\psi_i\,,d\psi_j/d\xi)$ has 22 non-zero entries while $(d\psi_i/d\xi\,,d\psi_j/d\xi)$ has 12 non-zero entries. Analytical expressions will be developed to compute these non-zero entries without using any quadrature rule.

In Fig. 76 non-zero entries of $(\psi_i\,,\psi_j)$, $(\psi_i\,,\partial\psi_j/\partial\xi)$, $(\partial\psi_i/\partial\xi\,,\partial\psi_j/\partial\eta)$, $(\partial\psi_i/\partial\xi\,,\partial\psi_j/\partial\xi)$ in 2-D for $P=9$ are plotted. In 2-D, $(\psi_i\,,\psi_j)$, $(\psi_i\,,\partial\psi_j/\partial\xi)$, $(\partial\psi_i/\partial\xi\,,\partial\psi_j/\partial\eta)$, $(\partial\psi_i/\partial\xi\,,\partial\psi_j/\partial\xi)$ have 1024, 704 , 484 and 384 non-zero entries, respectively, out of 10,000. These entries can be computed analytically for rectangular elements.

To exploit these orthogonality relationships while computing coefficient matrix, we need to recast stiffness matrix entries in a slightly different form. We will first state following relationships which will be useful later. For a proof of these equalities, see [68].

Relation 1: All Jacobi polynomials, $P_n^{\alpha,\beta}(x)$, satisfy a three-term recurrence relation of the form

$$xP_n^{\alpha,\beta}(x)=a_{n-1,n}^{\alpha,\beta}P_{n-1}^{\alpha,\beta}(x)+a_{n,n}^{\alpha,\beta}P_n^{\alpha,\beta}(x)+a_{n+1,n}^{\alpha,\beta}P_{n+1}^{\alpha,\beta}(x) \tag{7.19}$$

where $a^{\alpha,\beta}$ depends only on α,β and n. For $\alpha=\beta=1$, $a_{n,n}^{\alpha,\beta}$=0 and above equation can be

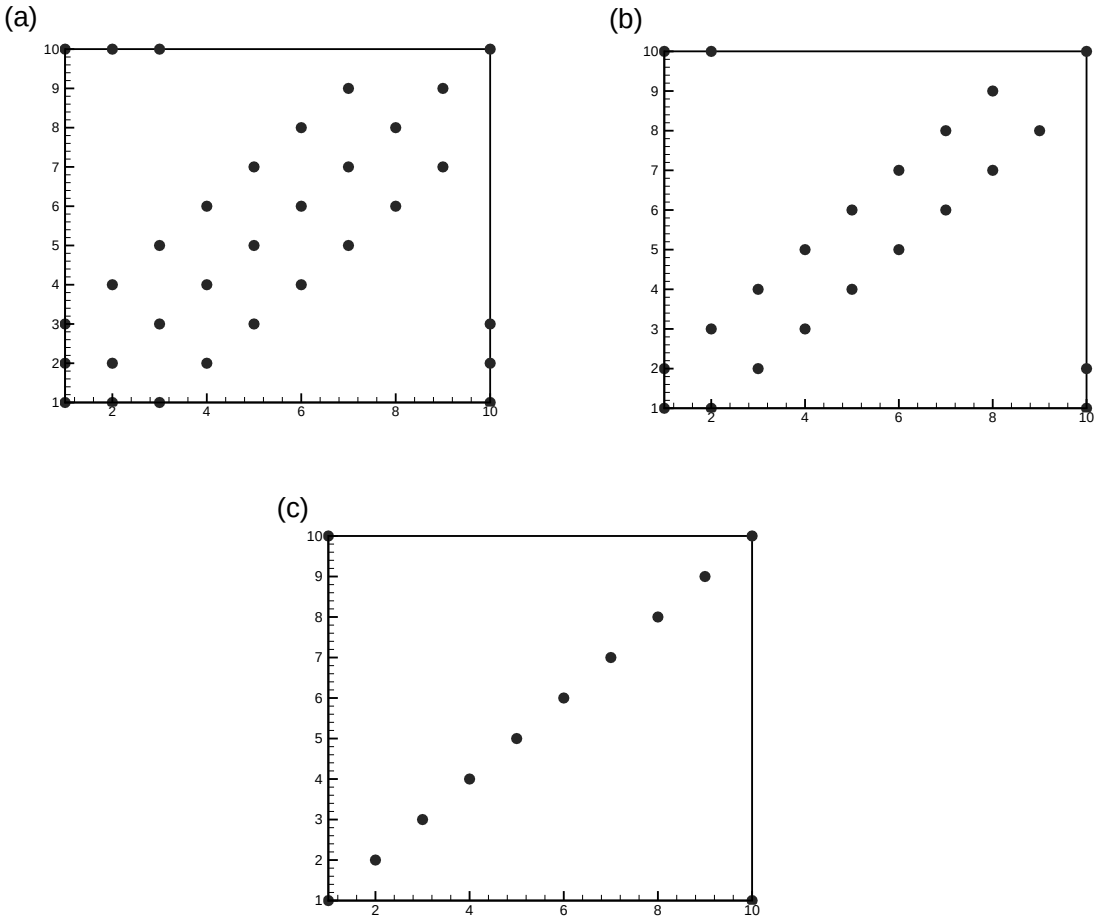

Fig. 75. Nonzero entries of (a) $\psi_i\ \psi_j$ (b) $\psi_i\ d\psi_j/d\xi$(c) $d\psi_i$ / $d\xi$ $d\psi_j$ / $d\xi$

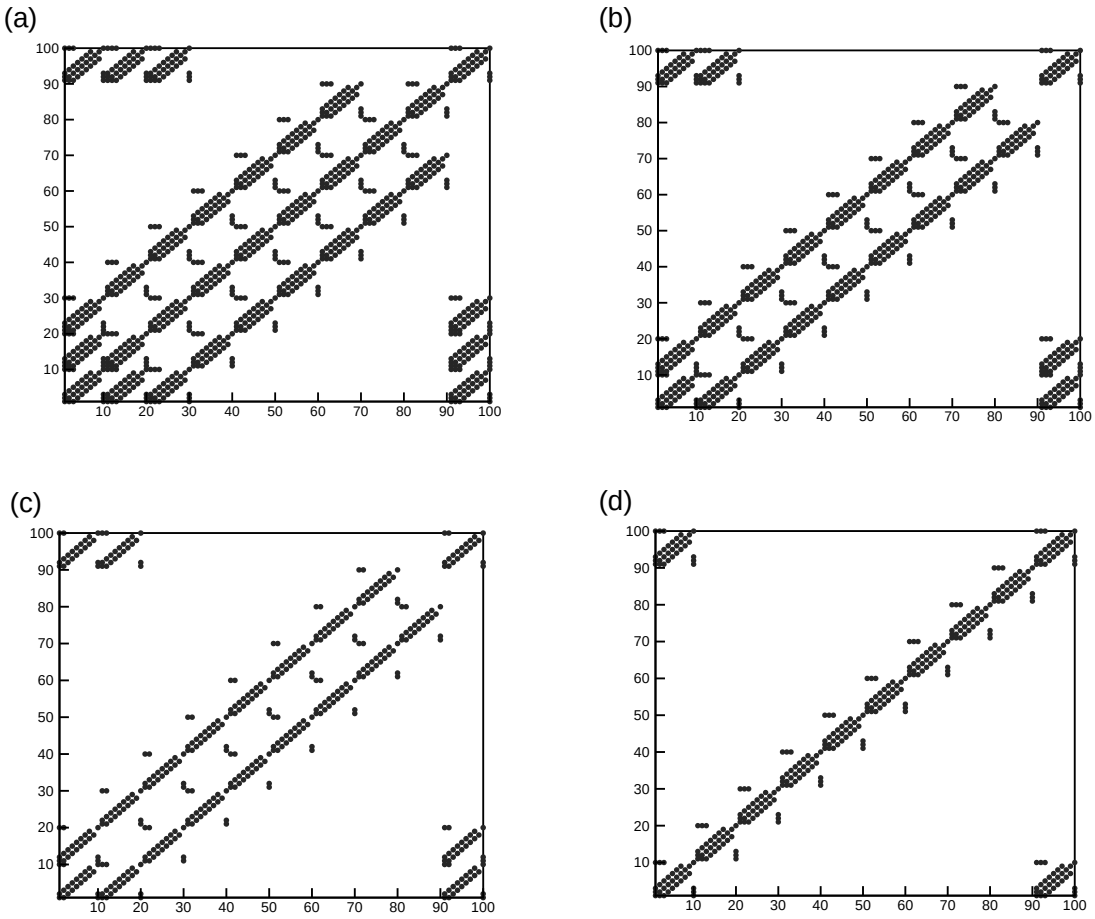

Fig. 76. Nonzero entries of (a) $\psi_i \ \psi_j$ (b) $\psi_i \, d\psi_j/d\xi$(c)$d\psi_i$ / $d\xi$ $d\psi_j$ / $d\eta$ (d)$d\psi_i/d\xi$ $d\psi_j/d\xi$

written as

$$xP_n^{\alpha,\beta}(x) = a_{n-1,n}^{\alpha,\beta} P_{n-1}^{\alpha,\beta}(x) + a_{n+1,n}^{\alpha,\beta} P_{n+1}^{\alpha,\beta}(x) \tag{7.20}$$

or, for the sake of compactness, we rewrite above equation by dropping α and β as we consider $\alpha = \beta = 1$ only

$$xP_n(x) = a_1(n)P_{n-1}(x) + a_2(n)P_{n+1}(x) \tag{7.21}$$

where

$$a_1(n) = \frac{n+1}{2n+3} \tag{7.22}$$

and

$$a_2(n) = \frac{(n+1)(n+3)}{(n+2)(2n+3)} \tag{7.23}$$

Relation 2: All Jacobi polynomials, $P_n^{\alpha,\beta}(x)$, satisfy a three-term recurrence relation of the form

$$(1-x^2)\frac{dP_n^{\alpha,\beta}(x)}{dx} = c_{n-1,n}^{\alpha,\beta} P_{n-1}^{\alpha,\beta}(x) + c_{n,n}^{\alpha,\beta} P_n^{\alpha,\beta}(x) + c_{n+1,n}^{\alpha,\beta} P_{n+1}^{\alpha,\beta}(x) \tag{7.24}$$

where $c^{\alpha,\beta}$ depends only on α,β and n. For $\alpha = \beta = 1$, $c_{n,n}^{\alpha,\beta}$=0 and above equation can be written as

$$(1-x^2)\frac{dP_n^{\alpha,\beta}(x)}{dx} = c_{n-1,n}^{\alpha,\beta} P_{n-1}^{\alpha,\beta}(x) + c_{n+1,n}^{\alpha,\beta} P_{n+1}^{\alpha,\beta}(x) \tag{7.25}$$

Again, for the sake of compactness, we rewrite above equation by dropping α and β and considering $\alpha = \beta = 1$ only

$$(1-x^2)\frac{dP_n(x)}{dx} = c_1(n)P_{n-1}(x) + c_2(n)P_{n+1}(x) \tag{7.26}$$

where

$$c_1(n) = \frac{(n+1)(n+3)}{(2n+3)} \tag{7.27}$$

and

$$c_2(n) = \frac{2n(n+1)(n+3)}{(2n+3)(2n+4)} \tag{7.28}$$

D. One-dimensional case

Let us recast entries of coefficient matrix using these relationships.

$$\begin{aligned}\int \psi_p \psi_q d\xi &= \int \frac{(1-\xi)}{2}\frac{(1+\xi)}{2} P_p \frac{(1-\xi)}{2}\frac{(1+\xi)}{2} P_q d\xi \\ &= \frac{1}{16}\int (1-\xi)(1+\xi) P_p P_q d\xi - \int (1-\xi)(1+\xi)\xi^2 P_p P_q d\xi\end{aligned}$$

$$\begin{aligned}\xi^2 P_q &= \xi[\xi P_q] \\ &= [a_1(q)\xi P_{q-1} + a_2(q)\xi P_{q+1}] \\ &= a_1(q)[a_1(q-1)P_{q-2} + a_2(q-1)P_q] + a_2(q)[a_1(q+1)P_q + a_2(q+1)P_{q+2}] \\ &= a_1(q)a_1(q-1)P_{q-2} + [a_1(q)a_2(q-1) + a_2(q)a_1(q+1)]P_q + \\ &\quad a_2(q)a_2(q+1)P_{q+2}\end{aligned}$$

$$\begin{aligned}\int (1-\xi)(1+\xi)\xi^2 P_p P_q d\xi = a_1(q)a_1(q-1)\delta_{p,q-2}C_1 + \\ [a_1(q)a_2(q-1) + a_2(q)a_1(q+1)]\delta_{p,q}C_2 + \\ a_2(q)a_2(q+1)\delta_{p,q+2}C_3\end{aligned}$$

$$\begin{aligned}\int \psi_p \frac{d\psi_q}{d\xi} d\xi &= \frac{1}{16}\int (1-\xi)(1+\xi) P_p \frac{d[(1-\xi^2)P_q]}{d\xi} \\ &= \frac{1}{16}\int (1-\xi)(1+\xi) P_p [(1-\xi^2)\frac{dP_q}{d\xi} - P_q 2\xi] d\xi \\ &= \frac{1}{16}\int (1-\xi)(1+\xi) P_p (1-\xi^2)\frac{dP_q}{d\xi} d\xi \\ &\quad - \frac{2}{16}\int (1-\xi)(1+\xi) P_p \xi P_q d\xi\end{aligned}$$

$$
\begin{aligned}
A &= \int (1-\xi)(1+\xi) P_p [c_1(q) P_{q-1} + c_2(q) P_{q+1}] d\xi \\
&= c_1(q)\delta_{p,q-1} C_1 + c_2(q)\delta_{p,q+1} C_2 \\
B &= \int (1-\xi)(1+\xi) P_p [a_1(q) P_{q-1} + a_2(q) P_{q+1}] d\xi \\
&= a_1(q)\delta_{p,q-1} C_1 + a_2(q)\delta_{p,q+1} C_2
\end{aligned}
$$

$$
\int \psi_p \frac{d\psi_q}{d\xi} d\xi = \frac{A - 2B}{16}
$$

Here C_1, C_2 and C_3 are given by Equation (7.17) .We calculate ($d\psi/d\xi\,, d\psi/d\xi$) term using the Gauss quadrature.

E. Multidimensional case

One of the notable property of modal bases used here is that multidimensional basis functions are constructed by taking tensor product of one-dimensional basis functions. So they can be separated. Separation is particularly easy when we use orthogonal grid. For rectangular elements jacobian matrix is of the form (see Reddy [27, 28])

$$
J = \begin{pmatrix} \frac{h_1}{2} & 0 \\ 0 & \frac{h_2}{2} \end{pmatrix}
$$

and global derivatives of shape functions are

$$
\begin{pmatrix} \frac{\partial \psi_i^e}{\partial x} \\ \frac{\partial \psi_i^e}{\partial y} \end{pmatrix} = J^{-1} \begin{pmatrix} \frac{\partial \psi_i^e}{\partial \xi} \\ \frac{\partial \psi_i^e}{\partial \eta} \end{pmatrix} = \begin{pmatrix} \frac{2}{h_1} \frac{\partial \psi_i^e}{\partial \xi} \\ \frac{2}{h_2} \frac{\partial \psi_i^e}{\partial \eta} \end{pmatrix}
$$

where $\frac{\partial \psi_i^e}{\partial \xi}$, and $\frac{\partial \psi_i^e}{\partial \eta}$ are local derivatives of shape functions. We will use this representation to develop analytical expressions of entries of coefficient matrix.

Multidimensional shape functions are constructed by taking the tensor product of one-

dimensional shape function.

$$\phi_i(\xi,\eta) \rightarrow \phi_{p,q}(\xi,\eta) = \psi_p(\xi)\psi_q(\eta)$$
$$\phi_j(\xi,\eta) \rightarrow \phi_{r,s}(\xi,\eta) = \psi_r(\xi)\psi_s(\eta)$$
$$\phi_k(\xi,\eta) \rightarrow \phi_{m,n}(\xi,\eta) = \psi_m(\xi)\psi_n(\eta)$$

The entries of the coefficient matrix can now be rewritten as

$$\begin{aligned}\int \phi_i\phi_j dx\,dy &= \int \phi_i(\xi,\eta)\phi_j(\xi,\eta)J\,d\xi\,d\eta \\ &= J\int \psi_p(\xi)\psi_r(\xi)d\xi \int \psi_q(\eta)\psi_s(\eta)d\eta\end{aligned}$$

$$\begin{aligned}\int \phi_i\frac{\partial\phi_j}{\partial x}dx\,dy &= \int \phi_i(\xi,\eta)\frac{2}{h_1}\frac{\partial\phi_j(\xi,\eta)}{\partial\xi}J\,d\xi\,d\eta \\ &= J\,\frac{2}{h_1}\int \psi_p(\xi)\frac{\partial\psi_r(\xi)}{\partial\xi}d\xi \int \psi_q(\eta)\psi_s(\eta)d\eta\end{aligned}$$

$$\begin{aligned}\int \frac{\partial\phi_i}{\partial x}\frac{\partial\phi_j}{\partial x}dx\,dy &= \int \frac{2}{h_1}\frac{\partial\phi_i(\xi,\eta)}{\partial\xi}\frac{2}{h_1}\frac{\partial\phi_j(\xi,\eta)}{\partial\xi}J\,d\xi\,d\eta \\ &= J\,\frac{4}{h_1^2}\int \frac{\partial\psi_p(\xi)}{\partial\xi}\frac{\partial\psi_r(\xi)}{\partial\xi}d\xi \int \psi_q(\eta)\psi_s(\eta)d\eta\end{aligned}$$

$$\begin{aligned}\int \frac{\partial\phi_i}{\partial x}\frac{\partial\phi_j}{\partial y}dx\,dy &= \int \frac{2}{h_1}\frac{\partial\phi_i(\xi,\eta)}{\partial\xi}\frac{2}{h_2}\frac{\partial\phi_j(\xi,\eta)}{\partial\eta}J\,d\xi\,d\eta \\ &= J\,\frac{4}{h_1h_2}\int \frac{\partial\psi_p(\xi)}{\partial\xi}\psi_r(\xi)d\xi \int \psi_q(\eta)\frac{\partial\psi_s(\eta)}{\partial\eta}d\eta\end{aligned}$$

All these 1-D integrals can be calculated analytically using expressions developed in the previous section.

Non-linear term $C_{ij}^{02}(\mathbf{v})$ can be written as

$$\begin{aligned}\int C_i \frac{\partial \phi_j}{\partial y} dxdy &= \int (U \frac{\partial \phi_i}{\partial x} + V \frac{\partial \phi_i}{\partial y}) \frac{\partial \phi_j}{\partial y} dxdy \\ &= \int (U \frac{\partial \phi_i}{\partial \xi} \frac{2}{h_1} + V \frac{\partial \phi_i}{\partial \eta} \frac{2}{h_2}) \frac{\partial \phi_j}{\partial \eta} \frac{2}{h_2} J d\xi d\eta \\ &= \int \sum U_k \phi_k \frac{\partial \phi_i}{\partial \xi} \frac{2}{h_1} \frac{2}{h_2} \frac{\partial \phi_j}{\partial \eta} J d\xi d\eta + \int \sum V_k \phi_k \frac{\partial \phi_i}{\partial \eta} \frac{2}{h_2} \frac{2}{h_2} \frac{\partial \phi_j}{\partial \eta} J d\xi d\eta\end{aligned}$$

$$\int \sum U_k \phi_k \frac{\partial \phi_i}{\partial \xi} \frac{\partial \phi_j}{\partial \eta} d\xi d\eta = \sum \Big(U_k \int \psi_m \frac{\partial \psi_p}{\partial \xi} \psi_r d\xi \int \psi_n \psi_q \frac{\partial \psi_s}{\partial \eta} d\eta \Big)$$

All these 1-D integrals are evaluated using the 1-D Gauss quadrature rule.

We have recast all the entries of coefficient matrix except $\mathcal{C}_{ij}^{00}$, which we calculate using the 2-D Gauss quadrature.

1. Computer implementation

In multidimensions, shape functions are constructed by taking tensor product of one-dimensional shape functions. To use orthogonality we again separate them into one-dimensional shape functions. In one-dimension we have vertex and interior modes. All the derivation presented earlier is for interior modes consisting of Jacobi polynomials. Shape functions for the vertex modes can be written as

$$\Big(\frac{1-\xi}{2} \Big) = \frac{1}{2} \Big(P_0^{1,1} - \frac{P_1^{1,1}}{2} \Big)$$

Thus, vertex modes in one-dimension can be written as $\frac{1}{2}(P_0^{1,1} - \xi_i \frac{P_1^{1,1}}{2})$, where ξ_i takes the values of ± 1. Now previous derivations can be used for vertex modes also.

F. Implementation of boundary conditions

Since the modal basis functions do not satisfy interpolation and partition of unity properties, boundary conditions must be interpolated using some technique. Here the boundary conditions are implemented using the least-squares method. Suppose $u = f(x)$ on Γ. We approximate $f(x)$ with $g(x)$ such that

$$f(x) \approx g(x) = \sum_{j=0}^{n} C_j \phi_j(x)$$

where ϕ_j are the same shape functions that are used to interpolate dependent variables in our formulation. Above equation is written for an element boundary Γ_e that coincides with domain boundary Γ. We assemble global coefficient matrix obtained by this equation

$$E = g(x) - f(x)$$
$$E^2 = (C_j\phi_j - f, C_k\phi_k - f)$$

We minimize the square of the error with respect to C_j and obtain

$$\frac{\partial (E)^2}{\partial C_k} = 2(C_j\phi_j - f, \phi_k) = 0$$
$$\Rightarrow \qquad (C_j\phi_j, \phi_k) = (f, \phi_k) \quad \Rightarrow \qquad \underline{A}\, C = B$$

where

$$A_{kj} = (\phi_k\phi_j) = \int \phi_j(x)\phi_k(x)dx$$
$$B_k = (f, \phi_k) = \int f(x)\phi_k(x)dx$$

G. Time dependent problems

For time integration, space-time coupled or space-time decoupled methods can be used. Here we consider space-time decoupled formulations. In space-time decoupled formula-

tions, discretization in space and time are carried out independently. Generally, the time derivatives are represented by a truncated Taylor series in time. Least-square functional for backward multi-step scheme of order M_α can be written as

$$\mathcal{J}\left(\mathbf{u},p,\boldsymbol{\omega};\mathbf{f}\right)=\frac{1}{2}\Big(\Big\|\frac{\gamma_0}{\Delta t}\mathbf{u}^{s+1}-\sum_{q=0}^{M_\alpha-1}\frac{\beta_q}{\Delta t}\mathbf{u}^{s-q}+\left(\mathbf{u}_0\cdot\nabla\right)\mathbf{u}+\nabla p+\frac{1}{\mathrm{Re}}\nabla\times\boldsymbol{\omega}$$
$$-\mathbf{f}\Big\|^2_{0,\Omega\times(0,\tau]}+\Big\|\boldsymbol{\omega}-\nabla\times\mathbf{u}\Big\|^2_{0,\Omega\times(0,\tau]}+\Big\|\nabla\cdot\mathbf{u}\Big\|^2_{0,\Omega\times(0,\tau]}\Big) \tag{7.29}$$

where $\gamma_0=\sum_{q=0}^{M_\alpha-1}\beta_q$ for consistency, β_q are weights associated with a particular multi-step scheme, $\Delta t=t_{s+1}-t_s$ is the time increment.

H. Numerical examples

In this section, we present numerical results obtained with the proposed formulation. First, we verify spectral convergence. Next, we present results for the transient two-dimensional flow over a backward facing step and steady flow past a circular cylinder at low Reynolds number.

1. Verification : Kovasznay flow

The benchmark problem to be used for the purpose of verification of the least-squares based finite element models is an analytical solution to the two-dimensional steady incompressible Navier-Stokes due to Kovasznay [34]. Domain of interest is $\bar{\Omega}=[-0.5,1.5]\times[-0.5,1.5]$. The solution is given by

$$u=1-e^{\lambda x}\,\cos(2\pi y) \tag{7.30}$$

$$v=\frac{\lambda}{2\pi}\,e^{\lambda x}\,\sin(2\pi y) \tag{7.31}$$

$$p = p_0 - \frac{1}{2}\, e^{2\lambda x} \tag{7.32}$$

where $\lambda = \mathrm{Re}/2 - (\mathrm{Re}^2/4 + 4\pi^2)^{1/2}$ and p_0 is a reference pressure (an arbitrary constant).

We perform a p-refinement study. We fix spatial discretization and systematically increase the order of polynomial used in each element. The discretization is a non-uniform mesh of 8 quadrilateral finite elements. We choose the L_2 least-squares functional as error measure. Convergence of this measure to zero implies that the L_2 norm of the governing equations converges to zero.

We use 8 non-uniform quadrilateral elements for spatial discetization. The exact solution given by Equations (7.30) and (7.31) is used to prescribe Dirichlet boundary conditions. The system is linearized using Picard's method (Direct iteration method) and resulting symmetric positive-definite (SPD) system of equations are solved using conjugate gradient method with Jacobi preconditioner. Nonlinear convergence is declared when $\sum_{n=1}^{ndf} \|\Delta \mathbf{U}_n\| / \|\mathbf{U}_n\|$ is less than 10^{-4}, where ndf is total number of degrees of freedom in the mesh and **U** is the solution vector (includes all degrees of freedom at a node). Convergence of conjugate gradient is declared when error is less than 10^{-6}.

Fig. 77(a) shows streamlines for Kovasznay flow and Fig. 77(b) shows pressure contours. To verify spectral convergence, we plot L_2 norm of least-square functional $\mathcal{J}$ against polynomial order for vorticity based first-order formulation in Fig. 78. On logarithmic-linear scale we get almost straight line showing exponential decay of least-squares functional.

2. Transient flow over a backward-facing step

We next consider a two-dimensional flow over a backward-facing step at $\mathrm{Re} = 800$. The geometry and boundary conditions are taken from the benchmark solution of Gartling [24] and they are shown in Fig. 79. No-slip boundary condition is imposed on all walls. Bound-

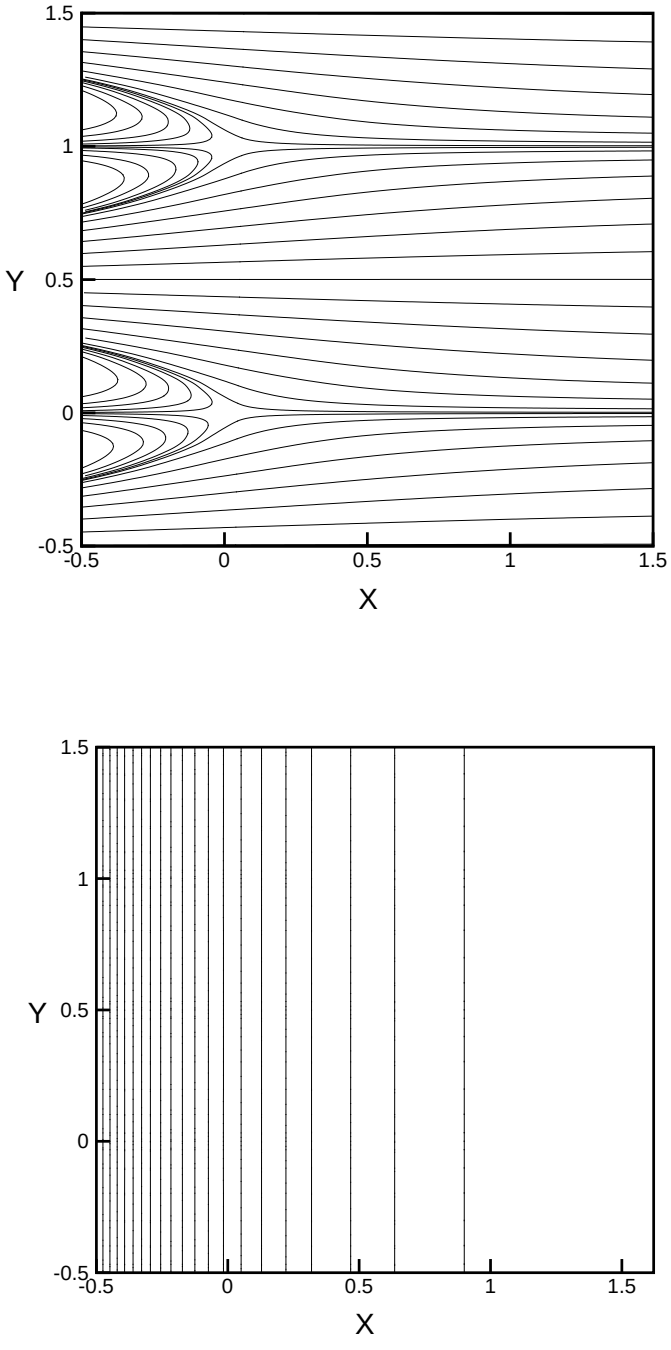

Fig. 77. Kovasznay flow (a) Streamlines (b) Pressure contours for $Re = 40$

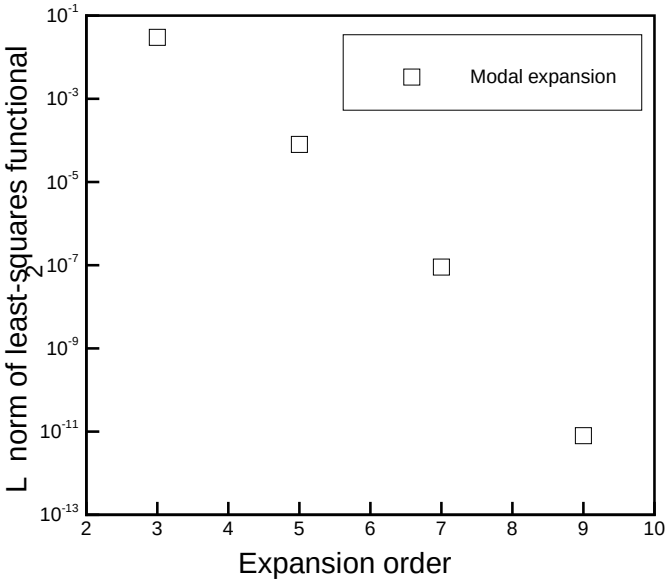

Fig. 78. Decay of least squares functional with polynomial order

ary condition of $u(y) = 0$ is imposed for $-0.5 \leq y \leq 0.0$. A parabolic velocity profile given by $u(y) = 24y(0.5 - y)$ is specified at the inlet for $0.0 \leq y \leq 0.5$. This produces a maximum inflow velocity of $u_{max} = 1.5$ and a mean inflow velocity of $u_{avg} = 1.0$. The Reynolds number is based on the mean inflow velocity. We impose outflow boundary condition in a weak sense through the least-squares functional [5]. For long domains, the strong outflow boundary condition $p = 0$ also gives good results. However, we prefer the weak imposition of outflow boundary conditions. Initial condition is zero velocity everywhere in the domain.

The domain, $\bar{\Omega} = [0, 25] \times [-0.5, 0.5]$, is discretized using 22 finite elements as shown in Figure 6. To accurately resolve primary and secondary circulation zones, we use a non-uniform grid. A 9^{th} order modal expansion is used in each element, resulting in a total of 7600 degrees of freedom in the mesh. The resulting discrete model is linearized using Picard's method. At each Picard step, the linear system of equations, involving a symmetric

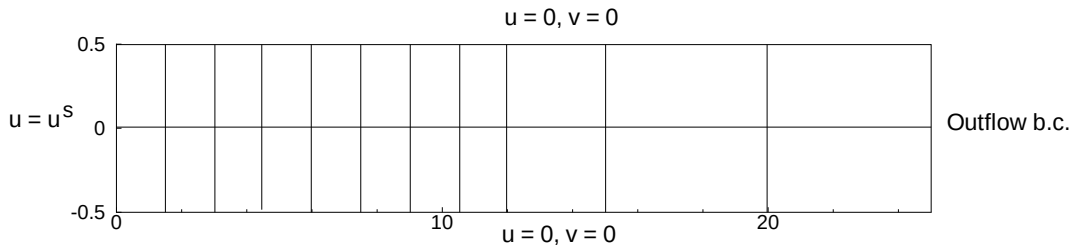

Fig. 79. Mesh and boundary conditions for flow over a backward facing step

positive-definite coefficient matrix, is solved using the conjugate gradient method with a Jacobi preconditioner. Convergence of the conjugate gradient method is declared when the norm of the residual is less than 10^{-6}. Nonlinear convergence is declared when the relative norm of the residual in solution vector is less than 10^{-4}. A time increment of 0.2 is used to march in time.

Fig. 80(a) shows the streamlines and pressure contours for $0 \leq x \leq 15$, where most of the phenomena of interest occur. The primary reattachment length is approximately 6.10, while the secondary separation and reattachment lengths approximately 4.9 and 10.4 respectively. Fig. 80(b) shows the pressure contours. After reattachment of the upper wall eddy, the flow slowly recovers towards a fully developed Poiseuille flow. The flow is almost fully developed at the exit with no pressure gradient in y direction. This is because outlet boundary condition of $p = 0$ also gives identical results.

Fig. 81 shows evolution of velocity field with time. The main flow coming from the inlet follows a sinuous path, forming a series of eddies along the upper and lower wall. Initial velocity field is taken to be zero everywhere in the domain. At $t = 400$ the relative norm of the residual in velocities between two consecutive time steps was less than 10^{-4}, indicating that a steady state was achieved.

Fig. 82 shows a plot of the L_2 least-squares functional as a function of time. Initially there is some fluctuation but fluctuations damp with time and the functional stabilizes at a

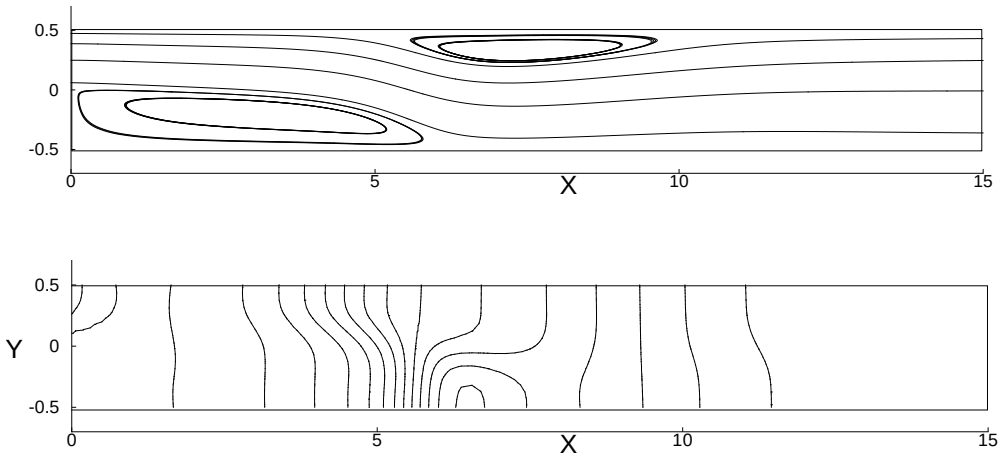

Fig. 80. Flow over a backward facing step at $Re = 800$ (a) Streamlines (b) Pressure contours

value of 3×10^{-3}.

3. Steady flow past a circular cylinder at low Reynolds number

Next, we consider steady two-dimensional flow of an incompressible fluid past a circular cylinder. The Reynolds number is taken to be 40, for which a steady-state solution exists. Domain of interest is $[-10.0, 15.0] \times [-10.0, 10.0]$. The x-component of inlet velocity (u) is specified to be 1.0 and the y-component (v) is set to zero. Symmetry boundary conditions, $\omega_z = 0$ and $v = 0$, are imposed on the top and bottom walls. The outflow boundary conditions are imposed in a weak sense through the least-squares functional.

Fig. 83 contains a close-up view of the geometric discretization around the circular cylinder. We generate orthogonal grid (rectangular elements) everywhere in the domain except around the cylinder. One layer of body fitting grid is generated around the cylinder. In order to accurately represent the curved boundary, we implement an isoparametric formulation; i.e., we use the same expansion order to interpolate dependent variables and the geometry.

We use two-dimensional steady incompressible Navier-Stokes equations in the vorticity-

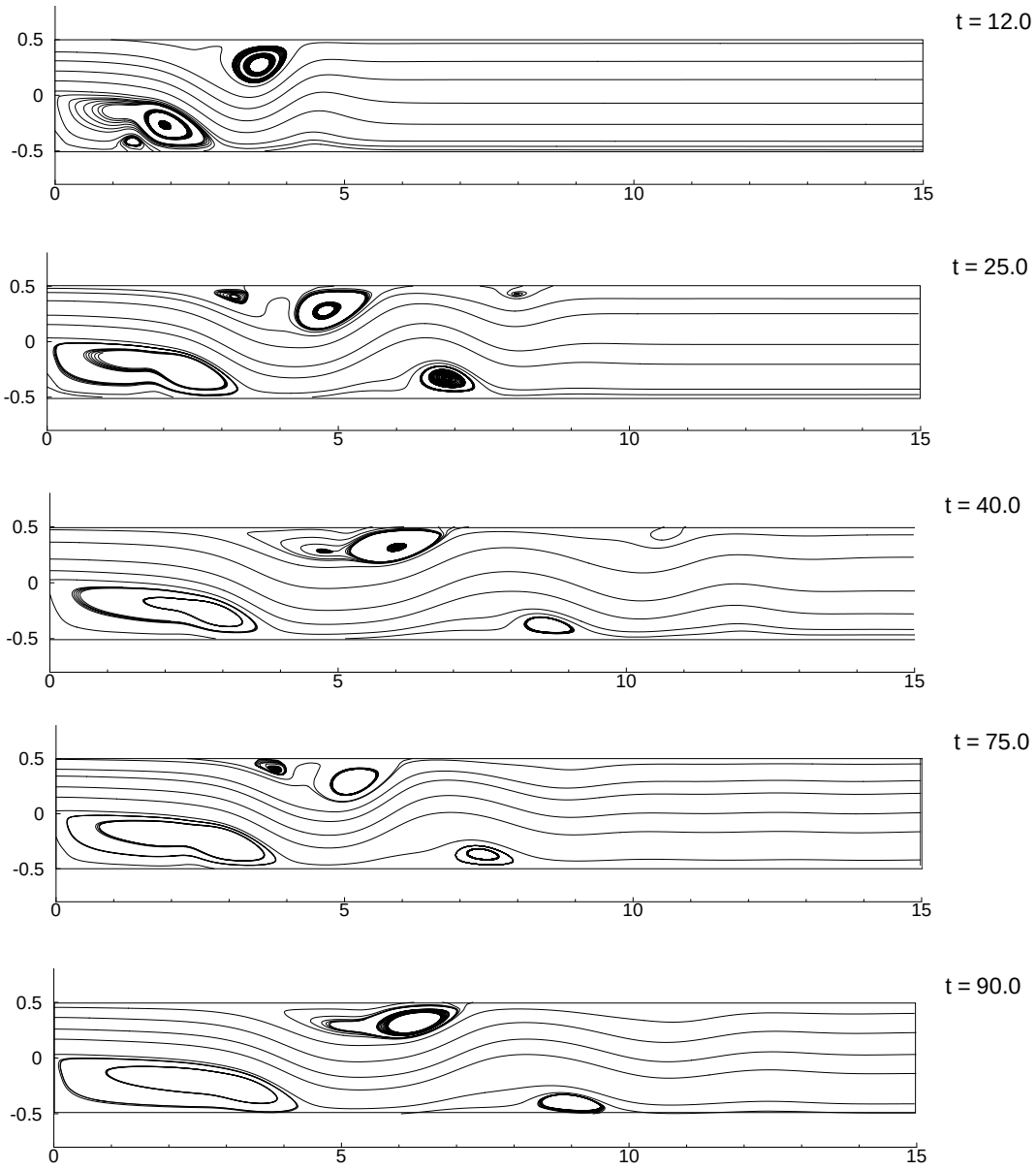

Fig. 81. Time history streamline plots for flow over a backward facing step at Re = 800.

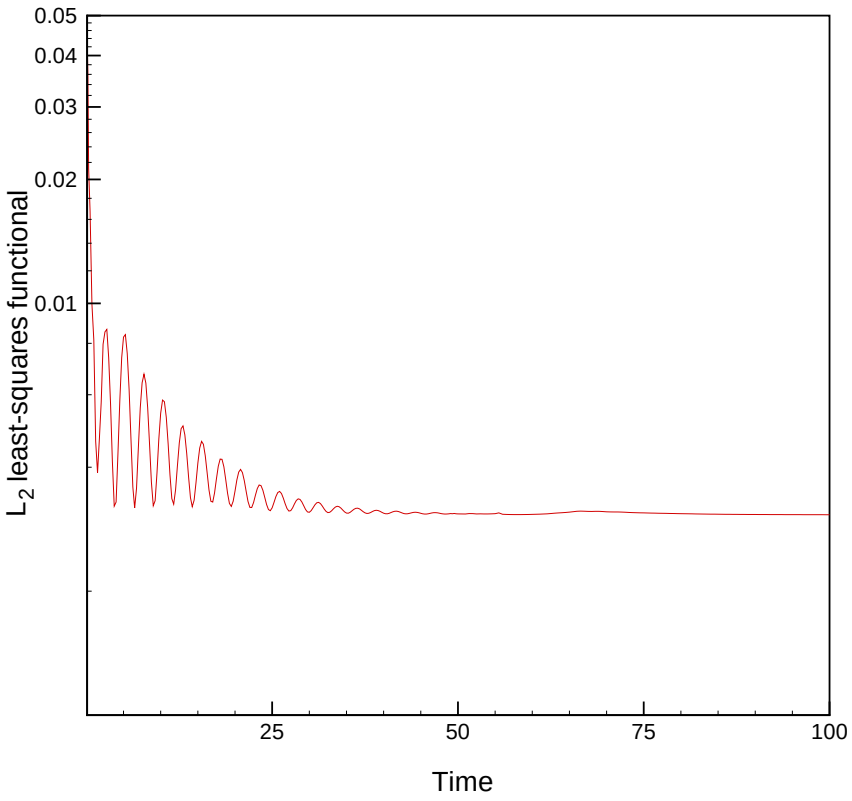

Fig. 82. Time history of the L_2 least squares functional

based first-order form and with a 9^{th} order modal expansions in each element. The resulting discrete model consists of a total of 209,196 degrees of freedom. The value of the L_2 least-squares functional remains below 10^{-4}.

Figs. 84 and 85 contain plots of the contours of streamlines and pressure, respectively, in the wake region for Re $= 40$. The value of the recirculation length is found to be 4.55 cylinder radii. The present result is in good agreement with the numerical value of 4.55 cylinder radii by Pontaza and Reddy [5]. Dennis and Chang [38] reported a recirculation length of 4.69 cylinder radii.

A comparison of the experimental values of the surface pressure coefficient distribu-

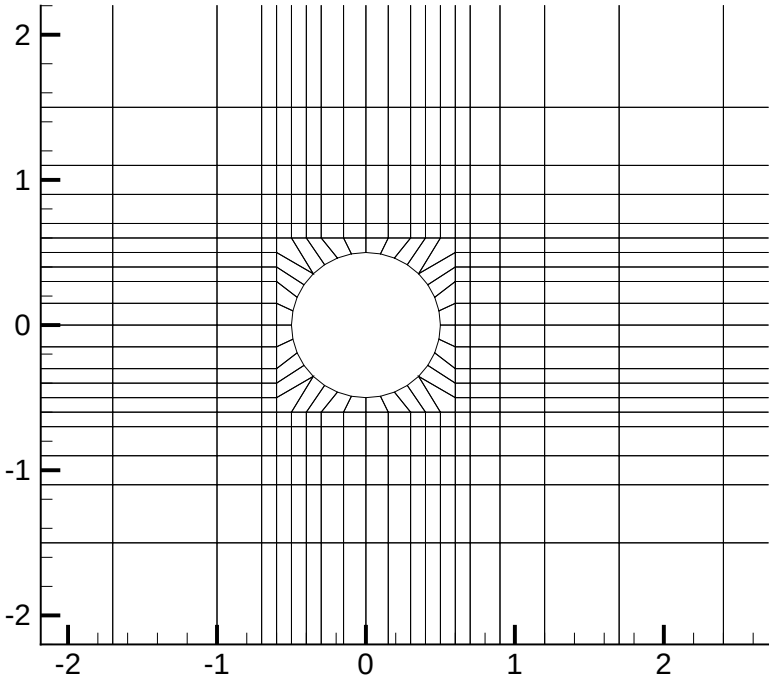

Fig. 83. Closeup view of geometric discretization the cylinder

tion along the cylinder surface with the computed values is shown in Fig. 86. Experimental values are taken from Grove et al. [25]. The present results are in good agreement with the experimental measurements. Drag coefficient is calculated to be $C_D = 1.55$, which is in good agreement with the published results of Tritton [39], who reported a value of 1.56.

Actual CPU time depends on the implementation (data-structure, node numbering etc.) and vary from one implementation to other. To give the reader a feeling of the algorithmic performance, we report the speed-up obtained by using proposed orthogonal modal bases in Table VII.

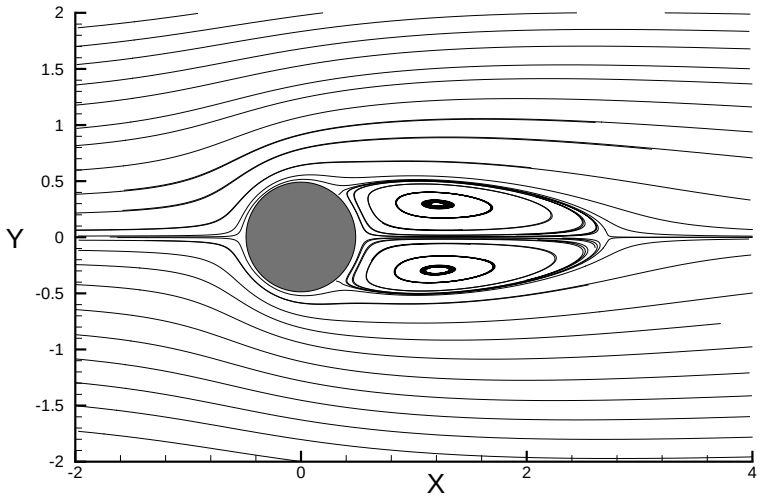

Fig. 84. Streamlines in the wake region for flow past a circular cylinder at $Re = 40$

Table VII. Speed up for various values of polynomial order.

Polynomial order (P)	Speed-up($t_{non\text{-}ortho}/t_{ortho}$)
7	2.1
9	3.1
11	4.5

At this point, we want to remind the reader that we recast all the terms of coefficient matrix except $\mathcal{C}_{ij}^{00}$ term associated with rectangular elements. We evaluated $\mathcal{C}_{ij}^{00}$ using the 2-D Guass quadrature. Calculation of other non-linear terms $\mathcal{C}_{ij}^{01}, \mathcal{C}_{ij}^{02}, \mathcal{C}_{ij}^{10}, \mathcal{C}_{ij}^{20}$ is also computationally expensive as they involve do-looping even though we calculate them by performing 1-D Gauss quadrature. Most of the time is consumed in computing these terms only. For curved elements, we performed 2-D Guass quadrature for all the terms of coefficient matrix.

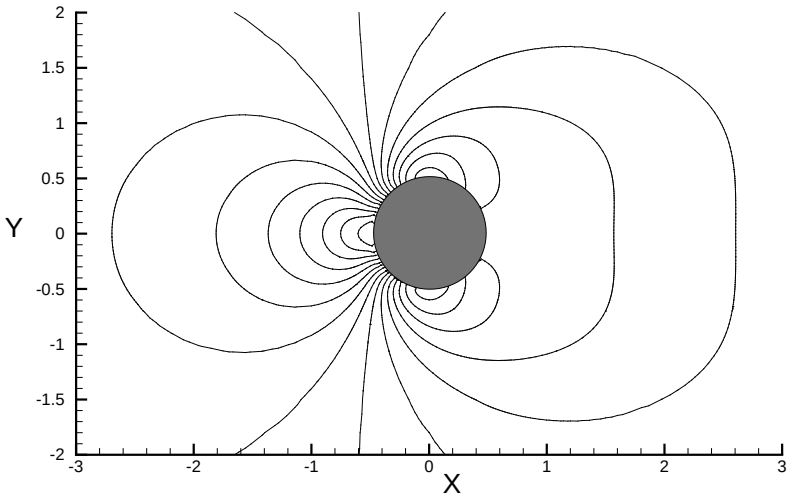

Fig. 85. Pressure contours for flow past a circular cylinder at $Re = 40$

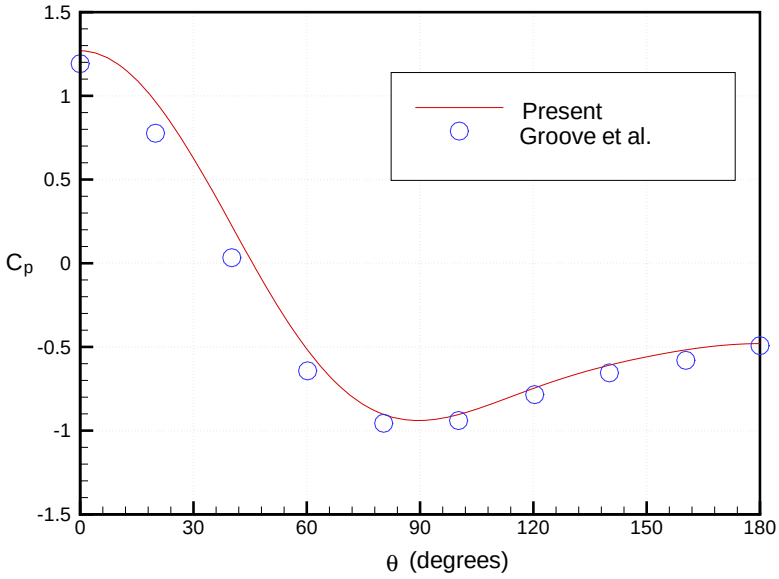

Fig. 86. Pressure coefficient distribution along the cylinder surface for flow past a circular cylinder at $Re = 40$

CHAPTER VIII

LEAST-SQUARES FINITE ELEMENT FORMULATION FOR MOVING BOUNDARY FLOWS

A. Introduction

Numerical simulation of moving boundary, multi-fluid flows presents a challenge, because the boundary changes and fluid properties are discontinuous across the fluid interface. There are essentially two techniques for simulating moving boundaries: Lagrangian (front tracking) and Eulerian (front capturing) schemes. The former schemes employ a moving mesh system, in which mesh moves with the interface. On the other hand, the Eulerian methods use a fixed mesh. While Lagrangian techniques are superior for small deformations of the interfaces, Eulerian techniques are usually preferred for highly distorted, complex interfaces.

Front tracking methods, e.g., Fritt and Boris [75] and Fyfe et al. [76], explicitly treat the interface as a discontinuity. The advantage in these methods is that interface conditions are easy to impose as interface always coincides with mesh. The nodes of the mesh are moved according to the fluid velocity, and thus the mesh is severely distorted and remeshing becomes unavoidable. Arbitrary Lagrangian–Eulerian methods remedy this situation by allowing the internal nodes to move independently from the fluid velocity. However, the selection of the mesh velocity is nontrival for complex flows.

In the second category, the computational grid is fixed throughout the simulation. An additional unknown variable (volume fraction, color function) is used to identify interface. Example of such methods are the level set method proposed by Zhu and Sethian [69], volume of fluid (VOF) by Hirt and Nichols [70], and the marker and cell (MAC) method by Harlow and Welch [71]. In the conventional MAC method, the interface is represented

by Lagrangian marker particles advected by the local velocity. As a result, it can not accurately define an interface, especially for three-dimensional flow, nor properly conserves mass. However, one favored feature of this method is that, unlike many other methods, no numerical diffusion exists. In the recent time, VOF algorithms based on Hirt and Nichols [70] and level set methods have gained popularity . The common problem of front capturing method is the inaccurate representation of surface tension force which is concentrated on the interface. This difficulty can be alleviated by using a continuum surface force (CSF) model proposed by Brackbill et al. [74]. The CSF model interprets surface tension as a continuous, three-dimensional body force across an interface, rather than as a boundary condition on the interface. For details see [1].

In this chapter, we use the VOF method to simulate moving boundary flows. The main advantages of this method are that the interface shape is not constrained, changes in topology are handled automatically, and the mass of each component is conserved exactly. The interface location is captured as it moves through the grid by tracking the local volume fraction. We use CSF method to model surface tension force. The two-dimensional Navier-Stokes equations are expressed as an equivalent set of first-order equations by introducing stresses as additional dependent variables. The hp least-squares method is used to develop the finite element model. We solve the broken dam problem to test this method and compare results with the benchmark results of Martin and Moyce [16].

B. Numerical method

The motion of both fluids is governed by a Newtonian incompressible fluid flow model. We consider the solution of the unsteady Navier-Stokes equations governing incompressible flow, which in dimensionless form can be stated as follows:

Find the velocity $\mathbf{u}(\mathbf{x})$ and pressure $p(\mathbf{x})$ such that

$$\frac{\partial \mathbf{u}}{\partial t} + (\mathbf{u} \cdot \nabla)\,\mathbf{u} + \nabla p - \frac{1}{\mathrm{Re}}\,\nabla \cdot \left[(\nabla \mathbf{u}) + (\nabla \mathbf{u})^{\mathrm{T}}\right] = \mathbf{f} \qquad \text{in } \Omega \tag{8.1}$$

$$\nabla \cdot \mathbf{u} = 0 \qquad \text{in } \Omega \tag{8.2}$$

$$\mathbf{u} = \mathbf{u}^s \qquad \text{on } \Gamma_u \tag{8.3}$$

$$\hat{\mathbf{n}} \cdot \boldsymbol{\sigma} = \mathbf{f}^s \qquad \text{on } \Gamma_f \tag{8.4}$$

where $\Gamma = \Gamma_u \cup \Gamma_f$ and $\Gamma_u \cap \Gamma_f = \emptyset$, Re is the Reynolds number, $\boldsymbol{\sigma} = -p\,\mathbf{I} + 1/\mathrm{Re}\,\left[(\nabla \mathbf{u}) + (\nabla \mathbf{u})^{\mathrm{T}}\right]$, $\mathbf{f}$ is a dimensionless force, $\hat{\mathbf{n}}$ is the outward unit normal on the boundary of Ω, $\mathbf{u}^s$ is the prescribed velocity on the boundary Γ_u, and $\mathbf{f}^s$ are the prescribed tractions on the boundary Γ_f. We assume that the problem is well posed and that a unique solution exists.

We recast this set of equations into a set of first order-equations using stresses as independent variables, details of which can be found in [5].

The fluids are identified by different values of the color function C, which is convected by the flow field:

$$\frac{\partial C}{\partial t} + (\mathbf{u} \cdot \nabla)\,C = 0 \tag{8.5}$$

Fluid properties such as the density and the viscosity are assumed to be distributed in the same manner as C, i.e.

$$\rho = \rho_1 + \frac{\rho_2 - \rho_1}{C_2 - C_1}(C - C_1) \tag{8.6}$$

$$\mu = \mu_1 + \frac{\mu_2 - \mu_1}{C_2 - C_1}(C - C_1) \tag{8.7}$$

The governing equations are discretized using the least-squares finite element formulation [5]. High-order expansions are used to construct the discrete model. The discrete

model thus obtained is linearized by Newton's method. We obtain a symmetric positive definite matrix which is solved using PCG method. Nonlinear convergence is declared when the relative norm of the residual in velocities, $\|\Delta \mathbf{u}^{hp}\|/\|\mathbf{u}^{hp}\|$, was less than 10^{-4}. Convergence of conjugate gradient is declared when error is less than 10^{-5}.

C. Numerical results

The formulation is tested by solving the broken dam problem. This problem has been used by many researchers as a test case for simulating moving boundary flows. Experimental data for this case is available in [16]. The problem is solved as a two-fluid problem involving water and air. Initially, water occupies a 1×1 area at the bottom left corner. Right wall breaks at $t = 0$ and the water starts flowing under the effect of gravity. The nondimensional gravitational acceleration, g, is taken to be unity. The densities for water and air are 1 and 0.001, respectively.

A 29×22 mesh, shown in Fig. 87, is used for this simulation. P-level of 3 is used. For time marching Crank-Nicholson scheme is used with delta t of 0.005.

Fig. 88 shows the location of water front with time. We compared the present results with the benchmark results of Martin and Moyce [16] and found very good agreement.

Fig. 89 shows the pressure contours at $t = 0.5$, 1.0, 1.5, 2.0 and 2.5. There is a sharp pressure variation across the boundary. Pressure contours give good feel of the interface.

Fig. 90 contains plots of streamlines and pressure contours at $t = 0.75$. There is a circulation zone near the interface on the air side. As the water flows, it drags the air and this creates circulatory flow.

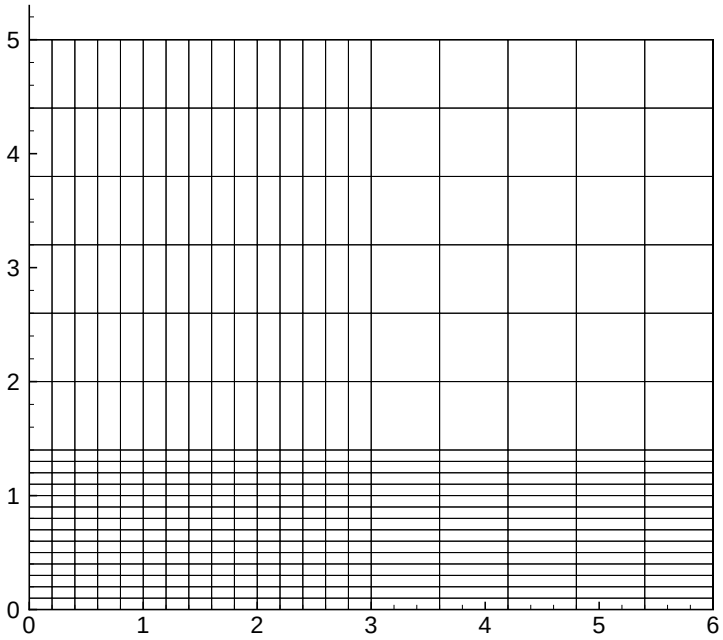

Fig. 87. Mesh for broken dam problem

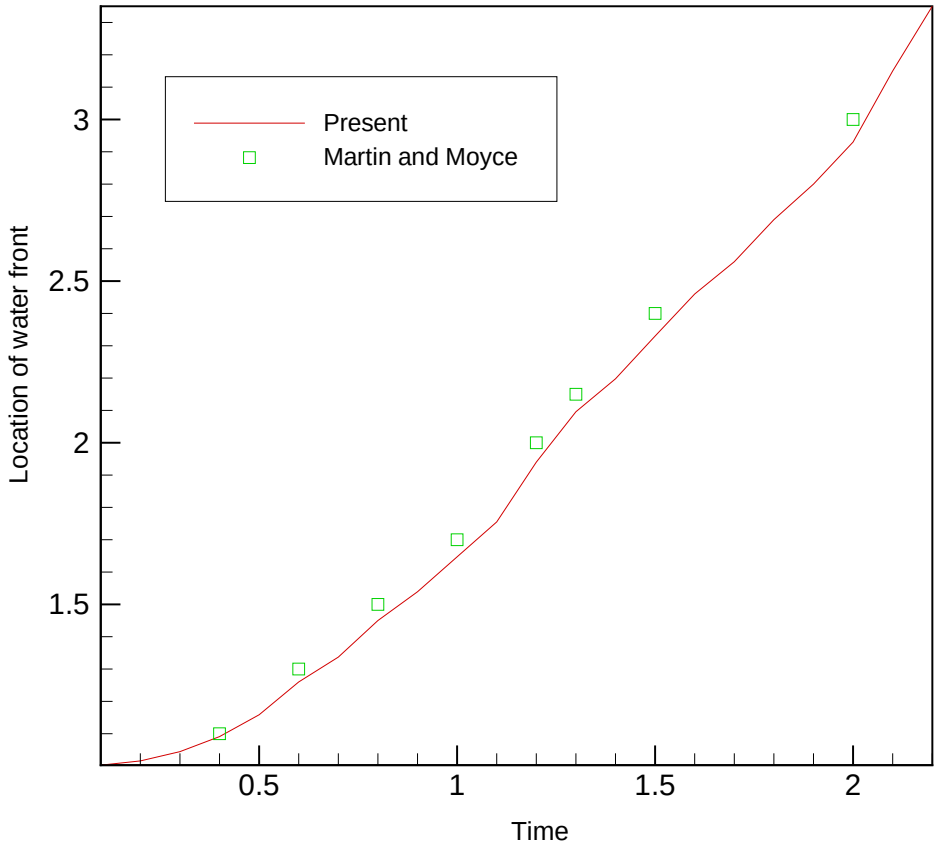

Fig. 88. Water front location with time: comparison with Martin and Moyce [16]

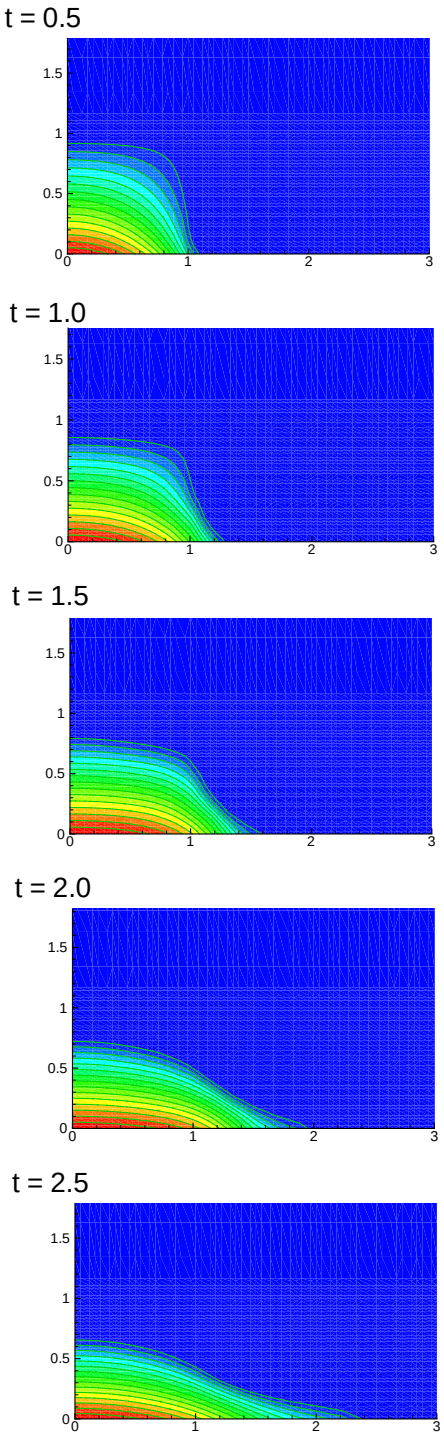

Fig. 89. Pressure contours at various times for the broken dam problem

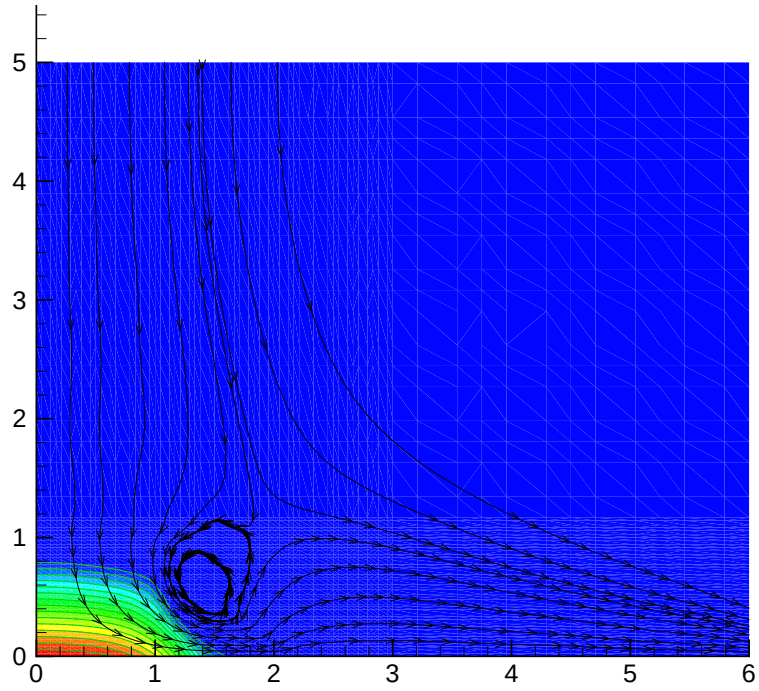

Fig. 90. Pressure contour and streamlines at t=0.75 for the broken dam problem

CHAPTER IX

CONCLUSION

A. Summary and Concluding Remarks

In this work, we presented least-squares based finite element formulations and their applications to flows of viscous fluids. These formulations offer several theoretical and computational advantages. Most notably, such formulations circumvent the inf-sup condition of Ladyzhenskaya-Babuska-Brezzi (LBB). Therefore, the choice of approximating spaces is not subject to any condition, and a single continuous piecewise polynomial space can be used for the approximation of all variables. They also yield symmetric positive-definite coefficient matrix and robust iterative solvers can be used to solve the resulting system of linear equations. In this work, we developed penalty based least-squares formulations where the pressure variable is eliminated using the penalty approach. It is demonstrated through numerical example that these formulations perform well in practical implementation.

Following the introduction, in chapter II, we presented spectral/hp penalty least-squares finite element formulation for the steady incompressible Navier-Stokes equations and its validation and applications to a variety of benchmark problems. Continuity equation was treated as a constraint on velocity field and this constraint was imposed using the penalty method, eliminating pressure from the formulation. The pressure is postcomputed from the known velocity field. Spectral convergence of the L_2 least-squares functional was verified using the Kovasznay flow solution to the incompressible Navier-Stokes equations. Both vorticity-dilatation and stress based first-order systems achieved spectral convergence for all the variables including pressure. Numerical results for incompressible 2D lid driven cavity flow, flow over a backward-facing step, steady flow past a circular cylinder, flow

past a large circular cylinder in a channel, and buoyant flow inside a square enclosure were presented. In all cases, the present results were found to be in excellent agreement with benchmark solutions available in the literature. For all numerical examples, the effect of penalty parameter on the accuracy was investigated thoroughly and it was concluded that the present model gives very accurate results even for small values of the penalty parameter ($10 - 40$).

We presented the penalty least-squares formulation as an alternative of spectral/hp least-squares finite element formulation of Pontaza and Reddy [5, 12], where the continuity residual is retained in the least-squares functional and enforced in a least-squares sense. In the present formulation, the incompressibility condition can be satisfied to any extent by a suitable value for the penalty parameter. Present formulation carries equal number of independent variables as spectral/hp least-squares [5] carries. We presented PCG convergence history of all the problems solved and plots showed that coefficient matrix was well conditioned. We compared PCG history with that of spectral/hp least-squares [5] and found similar convergence.

The present penalty least-squares finite element model is also a better alternative to traditional weak form penalty finite element model. Advantage of the present model is that it gives very accurate results for very low penalty parameters. In addition, there is no need to under-integrate penalty terms of the coefficient matrix. We computed pressure for all the problems solved herein and compared with the results of benchmark problems whenever available. We note that the computed pressure fields are continuous in this formulation as opposed to the weak form penalty finite element formulation, and their values are found to be in excellent agreement with published results. This penalty least-squares formulation produces a symmetric positive-definite coefficient matrix while the weak form penalty finite element formulation produces unsymmetric coefficient matrix.

In chapter III, we presented spectral/hp penalty least-squares finite element formu-

lation for the unsteady incompressible Navier-Stokes equations. The least-squares model was formed in terms of velocity, vorticity and dilatation. Space-time decoupled formulations were used for time discretization. Second order accuracy of time integration scheme was verified using method of manufactured solution. Numerical results were presented for impulsively started lid-driven cavity and flow over a backward facing step problem. For these numerical examples, the effect of penalty parameter on the accuracy was investigated thoroughly and it was concluded that the present model produces accurate results even for low penalty parameters (10-50). We presented this formulation as an alternative to traditional least-squares formulation, which has problems with pressure evolution. Pressure evolved smoothly in this formulation as verified through numerical examples.

In chapter IV, we presented a collocation penalty least-squares finite element formulation for incompressible flows. The least-squares model was formed in terms of velocity, vorticity, and dilatation. The h-convergence was verified using the exact solution of Kovasznay flow. Numerical results were presented for a number of benchmark problems. For all numerical examples, the effect of penalty parameter on the accuracy was investigated thoroughly and it was concluded that the present model produces accurate results even for low penalty parameters (10-100). We solved problems on coarser meshes also for various values of penalty parameters and found results to be 'equally inaccurate' for all the penalty parameters used, showing that inaccuracy was not because of low values of penalty parameters but because of inadequate mesh resolution.

In chapter V, we presented a stress based least-squares finite element formulation for the solution of incompressible Navier-Stokes equations. Stress components were introduced as independent variables to make the system first order. Continuity equation became an algebraic equation and was eliminated from the system with suitable modifications. This formulation carried one less degree of freedom compared to existing stress based first order formulations [46]. The h and p convergence were verified using the exact solution of

Kovasznay flow. Steady flow past a large circular cylinder in a channel was solved to check mass conservation and we found good mass conservation. Transient flow over a backward facing problem was solved on three different meshes and accuracy was investigated. We compared results obtained by proposed formulation with that obtained by vorticity based formulation and found that proposed formulation was less affected with mesh coarsening.

In chapter VI, we presented least-square based finite element formulations for viscoelastic fluid flows. We used Oldrolyd-B constitutive equations. First we presented velocity-pressure-stress-extra stress least-squares formulation. Transient channel flow was considered as benchmark problem to test the formulation. Formulation performed well for low Weissenberg number (1-5). For higher Weissenberg numbers (≥ 10) very small time step was required ($\sim$ O(10^{-3}))and simulation could not be carried for long time (solution was accurate till simulations were carried out). Next we presented penalty based least-squares formulation. Governing equations were recast as first order system in terms of velocity-extra stress. Pressure was eliminated from governing equations using penalty method approach.

In chapter VII, a method to exploit orthogonality of modal bases in order to avoid numerical integration and have a fast computation, was presented. The entries of coefficient matrix were calculated analytically. The properties of Jacobi polynomials were used and most of the entries of coefficient matrix were recast so that they can be evaluated analytically. This strategy was implemented in the context of least-square finite element model, although this procedure can be used in other finite element formulations. The equations were linearized using direct iteration method (Picard method). Analytical expressions were developed for rectangular elements. Spectral convergence of the L_2 least-squares functional was verified using the exact solution of the Kovasznay flow. Numerical results were presented for unsteady flow over a backward-facing step. Also the steady flow past a circular cylinder was analyzed and it showed reduction in computational cost.

All the terms of coefficient matrix were recast except $\mathcal{C}_{ij}^{00}$ term. This term was evaluated using the 2-D Guass quadrature. Also the 1-D Gauss integration was performed for $(\frac{\partial\psi}{\partial\xi}\ \frac{\partial\psi}{\partial\xi})$, which was quite fast as it was 1-D integration, and 2-D and 3-D expressions $(\frac{\partial\psi}{\partial\xi}\ \frac{\partial\psi}{\partial\xi})$ can be calculated by making use of the 1-D expression without the use of numerical integration. Other than these two Gauss quadratures, no numerical integration was used to evaluate the coefficients. Limitation of this procedure is that it can be used only for rectangular elements. For skew elements, it is not possible to separate multidimensional integrals (entries) into 1-D integrals. Therefore, one may choose to use analytical expressions to evaluate entries for rectangular elements and use quadrature for curved elements.

Finally, in chapter VIII, we presented hp least-squares finite element formulation to simulate the moving boundary flows. We used VOF method to track the interface, which is very similar to the *level set method*. The CSF (continuum surface force) model was used to treat surface tension effects in the VOF. We solved the broken dam problem to test our formulation and found very good agrement with the benchmark results.

In summary, we have amply demonstrated that the least-squares based finite element formulations perform well in practical problems. One big advantage of the least-squares formulations is their universality, i.e., the basic formulation is the same irrespective of the differential equation. In future we expect the least-squares based finite element formulations to be potential candidates for solving partial differential equations numerically irrespective of their origin and physics involved in it.

REFERENCES

[1] B. N. Jiang, *The Least-Squares Finite Element Method*. 1st ed. Berlin: Springer, 1998.

[2] B. N. Jiang, "On the least-squares method," *Computer Methods in Applied Mechanics and Engineering*, vol. 152, pp. 239-257, 1997.

[3] P. V. Bochev and M. D. Gunzburger, "Finite element methods of least-squares type," *SIAM Review*, vol. 40, pp. 789-837, 1998.

[4] M. M. J. Proot and M. I. Gerritsma, "Least-squares spectral elements applied to the Stokes problem," *Journal of Computational Physics*, vol. 181, pp. 454-477, 2002.

[5] J. P. Pontaza and J. N. Reddy, "Spectral/hp least-squares finite element formulation for the Navier-Stokes equations," *Journal of Computational Physics*, vol. 190, pp. 523-549, 2003.

[6] V. Prabhakar and J. N. Reddy, "Spectral/hp penalty least-squares finite element formulation for the steady incompressible Navier-Stokes equations," *Journal of Computational Physics*, vol. 215, pp. 274-297, 2006.

[7] V. Prabhakar and J. N. Reddy, "A stress based least-squares finite element formulation for the Incompressible Navier-Stokes equations," *International Journal for Numerical Methods in Fluids* (in review).

[8] C. L. Chang and J. J. Nelson, "Least-squares finite element method for the Stokes problem with zero residual of mass conservation," *SIAM Journal on Numerical Analysis*, vol. 34, pp. 480-489, 1997.

[9] P. Bolton and R. W. Thatcher, "On mass conservation in least-squares methods," *Journal of Computational Physics*, vol. 203, pp. 287-304, 2005.

[10] J. M. Deang, M. D. Gunzburger, "Issues related to least-squares finite element methods for the Stokes equations," *SIAM Journal on Scientific Computing*, vol. 20, pp. 878-906, 1998.

[11] P. Bolton, R. W. Thatcher, "A least-squares finite element method for the Navier-Stokes equations," *Journal of Computational Physics*, vol. 213, pp. 174-183, 2006.

[12] J. P. Pontaza and J. N. Reddy, "Space-time coupled spectral/hp least-squares finite element formulation for the incompressible Navier-Stokes equations," *Journal of Computational Physics*, vol. 197, pp. 418-459, 2004.

[13] M. D. Gunzburger, "iterated penalty methods for the Stokes and Navier-Stokes equations," in *Finite Element Analysis in Fluids, Proc. 7th Internat. Conf. on Finite Element Methods in Flow Problems*, T. J. Chung, G. R. Karr, Eds. (University of Alabama Press) 1989 , pp. 1040-1045.

[14] J. P. Pontaza and J. N. Reddy, "Least-squares finite element formulations for viscous incompressible and compressible fluid flows," *Computer Methods in Applied Mechanics and Engineering*, vol. 195, pp. 2454-2494, 2006.

[15] O. C. Zienkiewicz and R. L. Taylor, *The Finite Element Method*, Vol. 1, New York: McGraw-Hill, 1989.

[16] J. C. Martin and W. J. Moyce, "An experimental study of the collapse of liquid columns on a horizontal plane," *Philosophical Transations of the Royal Society of London. A*, vol. 244, pp. 312-324, 1952.

[17] I. Babuska, "Errors bounds for finite element method," *Numerical Mathematics*, vol. 16, pp. 322-333, 1971.

[18] F. Brezzi and K. J. Bathe, “A discourse on the stability conditions for mixed finite element formulations,” *Computer Methods in Applied Mechanics and Engineering*, vol. 82, pp. 27-57, 1990.

[19] D. S. Malkus and T. J. R. Hughes, “Mixed finite element methods - reduced and selective integration techniques: a unification of concepts,” *Computer Methods in Applied Mechanics and Engineering*, vol. 15, pp. 63-81, 1978.

[20] T. J. R. Hughes and W. K. Liu, “Finite element analysis of incompressible viscous flows by the penalty function formulation,” *Journal of Computational Physics*, vol. 30, pp. 1-60, 1979.

[21] P. Bochov and M. D. Gunzburger, “Least-squares finite-element methods for optimization and control problems for the Stokes equations,” *Computers and Mathematics with Applications*, vol. 48, pp. 1035-1057, 2004.

[22] J. S. Hesthaven, “Spectral penalty methods,” *Applied Numerical Mathematics*, vol. 33, pp. 23-41, 2000.

[23] P. J. Diamessis, J. A. Domaradzki and J. S. Hesthaven, “A spectral multidomain penalty method model for the simulation of high Reynolds number localized incompressible stratified turbulence,” *Journal of Computational Physics*, vol. 202, pp. 298-322, 2005.

[24] D. K. Gartling, “A test problem for outflow boundary conditions - flow over a backward-facing step,” *International Journal for Numerical Methods in Fluids*, vol. 11, pp. 953-967, 1990.

[25] A. S. Grove, F. H. Shair, E. E Petersen and A. Acrivos, “An experimental investigation of the steady separated flow past a circular cylinder,“ *Journal of Fluid Mechanics*, vol.

19, pp. 60-80, 1964.

[26] G. D. V. Davis, "Natural convection of air in a square cavity: a bench mark numerical solution," *International Journal for Numerical Methods in Fluids*, vol. 3, pp. 249-264, 1983.

[27] J. N. Reddy, *An Introduction to the Finite Element Method*. 3rd ed., New York: McGraw-Hill, 2006.

[28] J. N. Reddy, *Introduction to Nonlinear Finite Element Analysis*. Oxford: Oxford University Press, 2004.

[29] J. N. Reddy and D. K. Gartling, *The Finite Element Method in Heat Transfer and Fluid Dynamics*. 2nd ed., New York: CRC Press, 2001.

[30] G. E. Karniadakis and S. J. Sherwin, *Spectral/hp Element Methods for CFD*. Oxford: Oxford University Press, 1999.

[31] B. C. Bell and K. S. Surana, "A space-time coupled p-version least squares finite element formulation for unsteady two-dimensional Navier-Stokes equations," *International Journal for Numerical Methods in Engineering*, vol. 39, pp. 2593-2618, 1996.

[32] W. Couzy and M. O. Deville, "A fast schur complement method for the spectral element discretization of the incompressible Navier-Stokes equations," *Journal of Computational Physics*, vol. 116, pp. 135-142, 1995.

[33] G. H. Golub and C. F. V. Loan, *Matrix Computation*. 3rd ed., Baltimore: The Johns Hopkins University Press, 1996.

[34] L. S. G. Kovasznay, "Laminar flow behind a two-dimensional grid," *Mathematical Proceedings of the Cambridge Philosophical Society*, vol. 44, pp. 58-62, 1948.

[35] Y. Saad, *Iterative Methods for Sparse Linear Systems*. Boston: PWS Publishing Company, 1996.

[36] B. N. Jiang, T. L. Lin and L. A. Povinelli, "Large-scale computation of incompressible viscous flow by least-squares finite element method," *Computer Methods in Applied Mechanics and Engineering*, vol. 114, pp. 213-231, 1994.

[37] M. Kawaguti and P. Jain, "Numerical study of a viscous fluid past a circular cylinder," *Journal of the Physical Society of Japan*, vol. 21, pp. 2055-2062, 1966.

[38] S. C. R. Dennis, G. Z. Chang, "Numrical solutions for steady flow past a circular cylinder at Reynolds numbers up to 100," *Journal of Fluid Mechanics*, vol. 42, pp. 471-489, 1970.

[39] D. J. Tritton, "Experiments on the flow past a circular cylinder at low Reynolds numbers," *Journal of Fluid Mechanics*, vol. 6, pp. 547-567, 1959.

[40] J. N. Reddy, "Penalty-finite-element analysis of 3-D Navier-Stokes equations," *Computer Methods in Applied Mechanics and Engineering*, vol. 35, pp. 87, 1982.

[41] V. Prabhakar, J. P. Pontaza and J. N. Reddy, "A collocation penalty least-squares finite element formulation for incompressible flows," *Computer Methods in Applied Mechanics and Engineering* (in review).

[42] U. Ghia, K. Ghia and C. T. Shin, "High-Re solutions for incompressible flow using the Navier-Stokes equations and a multigrid method," *Journal of Computational Physics*, vol. 48, pp. 387-411, 1982.

[43] P. M. Gresho, D. K. Gartling, J. R. Torczynski, K. A. Cliffe, K. H. Winters, T. J. Garrat, A. Spence and J. W. Goodrich, "Is the steady viscous incompressible two-

dimensional flow over a backward-facing step at Re = 800 stable?," *International Journal for Numerical Methods in Fluids*, vol. 17, pp. 501-541, 1993.

[44] J. R. Torczynski, "A grid refinement study of two-dimensional transient flow over a backward-facing step using a spectral element method," in *Separated Flows*, J. C. Duuton, L. P. Purtell, Eds., vol. 149, ASME 1993, pp.44-62.

[45] J. P. Pontaza, "A least-squares finite element formulation for the unsteady incompressible flows with improved velocity-pressure coupling," *Journal of Computational Physics*, vol. 217, pp. 563-588, 2006.

[46] P. V. Bochev and M. D. Gunzburger, "Least-squares methods for the velocity-pressure-stress formulation of the Stokes equations," *Computer Methods in Applied Mechanics and Engineering*, vol. 126, pp. 267-287, 1995.

[47] R. Keunings, "Simulation of viscoelastic flow," in *Computer modeling for polymer processing*,C. L. Tucker (Ed.), Hanser, Munich, 1989, pp. 404-469.

[48] F. T. P. Baaijens, "Mixed finite element methods for viscoelastic flow analysis: a review," *Journal of Non-Newtonian Fluid Mechanics*, vol. 79, pp. 361-385, 1998.

[49] K. Walters and M. F. Webster, "The distinctive CFD challenges of computational rheology," ECCOMAS Swansea 2001, *International Journal for Numerical Methods in Fluids*, vol. 45, pp. 577-596, 2003.

[50] C. D. Eggleton, T. N. Pulliam and J. H. Ferziger, "Numerical simulation of viscoelastic flow using flux difference splitting at moderate Reynolds numbers," *Journal of Non-Newtonian Fluid Mechanics*, vol. 64, pp. 269-298, 1996.

[51] R. G. M. van Os and T. N. Phillips, "Spectral element methods for transient viscoelastic flow problems," *Journal of Computational Physics*, vol. 201, pp. 286-314, 2004.

[52] D. Rajagopalan, R. C. Armstrong and R. A. Brown, “Finite element methods foe circulation of steady viscoelastic flow using constitutive equations with a Newtonian viscosity,” *Journal of Non-Newtonian Fluid Mechanics*, vol. 36, pp. 159-199, 1990.

[53] J. Sun, N. Phan-Tien and R. I. Tanner, “An adaptive viscoelastic stress splitting scheme and its application: AVSS/SI and AVSS/SUPG,” *Journal of Non-Newtonian Fluid Mechanics*, vol. 65, pp. 75-91, 1996.

[54] R. G. Owens and T. N. Phillips, *Computational Rheology*. London: Imperial College Press, 2002.

[55] N. Fietier and M. O. Deville, “Time-dependent algorithms for the simulation of viscoelastic flows with spectral element methods: applications and stability,” *Journal of Computational Physics*, vol. 186, pp. 93-121, 2003.

[56] J. M. Marchal and M. J. Crochet, “A new finite element for circulating viscoelastic flow,” *Journal of Non-Newtonian Fluid Mechanics*, vol. 26, pp. 77-114, 1987.

[57] M. Fortin and A. Fortin, “A new approach for the FEM simulation of viscoelastic flows,” *International Journal for Numerical Methods in Fluids*, vol. 32, pp. 295-310, 1989.

[58] P. Wapperom and M. F. Webster, “A second-order hybrid finite-element/volume method for viscoelastic flow,” *Journal of Non-Newtonian Fluid Mechanics*, vol. 79, pp. 405-431, 1998.

[59] K. S. Surana, A. Mohammed, J. N. Reddy and P. W. TenPas, “K-version of finite element method in 2-D polymer flows: Oldroyd-B constitutive model,” *International Journal for Numerical Methods in Fluids*, vol. 52, pp. 119-162, 2006.

[60] M. I. Gerritsma, “Direct minimization of the discontinuous least-squares spectral element method for viscoelastic fluids,” *Journal of Scientific Computing*, vol. 27, pp. 245-256, 2006.

[61] N. D. Waters and M. J. King, “Unsteady flow of an elastico-viscous liquid,” *Rheologica Acta*, Band 9: Heft 3, pp. 345-355, 1970.

[62] A. Peano, “Hierarchies of conforming finite elements for plane elasticity and plate bending,” *Computers & Mathematics with Applications*, vol. 2, pp. 211-224, 1976.

[63] B. A. Szabo and I. Babuska, *Finite Element Analysis*. New York: John Wiley & Sons, 1991.

[64] M. Dubiner, “Spectral methods on triangles and other domains,” *Journal of Scientific Computing*, vol. 6, pp. 345-390, 1991.

[65] S. J. Sherwin and G. E. Karniadakis, “A triangular spectral method; Applications to the incompressible Navier-Stokes equation,” *Computer Methods in Applied Mechanics and Engineering*, vol. 123, pp. 189-229, 1995.

[66] A. T. Patera, “A spectral method for fluid dynamics: Laminar flow in a channel expansion,” *Journal of Computational Physics*, vol. 54, pp. 468-488, 1984.

[67] T. C. Warburton, S. J. Sherwin and G. E. Karniadakis, “Basis functions for triangular and quadrilateral high-order elements,” *SIAM Journal on Scientific Computing*, vol. 20, pp. 1671-1695, 1999.

[68] Osilenker B, *Fourier Series in Orthogonal Polynomials*. New Jersy: World Scientific, 1999.

[69] J. Zhu and J. A. Sethian, “Projection methods coupled to level set interface techniques,” *Journal of Computational Physics*, vol. 102, pp. 128-138, 1992.

[70] C. W. Hirt and B. D. Nichols, “Volume of Fluid (VOF) method for the dynamics of free boundaries,” *Journal of Computational Physics*, vol. 39, pp. 201-225, 1981.

[71] F. H. Harlow and J. E. Welch, “Numerical calculation of time-dependent viscous incompressible flow of fluid with free surface,” *Physics of Fluids*, vol. 8, pp. 2182-2189, 1965.

[72] B. J. Daly, “A technique for including surface tension effects in hydrodynamic calculations,” *Journal of Computational Physics*, vol. 4, pp. 97-117, 1969.

[73] F. H. Harlow and J. P. Shannon, “The spalsh of a liquid drop” *Journal of Computational Physics*, vol. 38, pp. 3855-3866, 1967.

[74] J. U. Brackbill, D. B. Kothe and C. Zemach, “A continuum method for modeling surface tension,” *Journal of Computational Physics*, vol. 100, pp. 335-354, 1992.

[75] M. J. Fritt and J. P. Boris, “The Lagrangian solution of transient problems in hydrodynamics using a triangular mesh,” *Journal of Computational Physics*, vol. 31, pp. 173-215, 1979.

[76] D. E. Fyfe, E. S. Oran and M. J. Fritts, “Surface tension and viscosity with Lagrangian hydrodynamics on a triangular mesh,” *Journal of Computational Physics*, vol. 76, pp. 349-384, 1988.

VITA

Vivek Prabhakar was born in Uttar Pradesh, India in 1979. He received his baccalaureate (B.Tech.) degree in Mechanical Engineering from Indian Institute of Technology, Kanpur, India in May 2002. In August, 2002, he joined the Mechanical Engineering department of Texas A&M University for his graduate studies. Vivek Prabhakar's research at TAMU was concerned with least-squares based finite element formulations in context of fluid mechanics. He graduated with his Ph.D. degree in Mechanical Engineering in December 2006.

He can be reached at vivekwrites@gmail.com or by contacting Dr. J.N. Reddy, Department of Mechanical Engineering, Texas A&M University, College Station, TX-77843.

The typist for this dissertation was Vivek Prabhakar.